

# NUMERICAL ANALYSIS OF STRESS AND STRAIN IN SPECIMENS WITH RECTANGULAR CROSS-SECTION SUBJECTED TO TORSION AND BENDING WITH TORSION

Sebastian FASZYŃKA\*, Janusz LEWANDOWSKI\*, Dariusz ROZUMEK\*

\*Faculty of Mechanical Engineering, Department of Mechanics and Machine Design,  
Opole University of Technology, ul. Mikołajczyka 5, 45-271 Opole, Poland

[sebastian.faszynka@op.pl](mailto:sebastian.faszynka@op.pl), [janusz210@wp.pl](mailto:janusz210@wp.pl), [d.rozumek@po.opole.pl](mailto:d.rozumek@po.opole.pl)

received 4 May 2015, revised 12 December 2015, accepted 22 December 2015

**Abstract:** The paper presents an analysis of the state of stress and crack tip opening displacement (strain) in specimens with rectangular cross-section subjected to torsion and combined bending with torsion. The specimens were made of the EN AW-2017A aluminium alloy. The specimens had an external unilateral notch, which was 2 mm deep and its radius was 22.5 mm. The tests were performed at constant moment amplitude  $M_T = M_{BT} = 15.84$  N·m and under stress ratio  $R = -1$ . The exemplary results of numerical computations being obtained by using the FRANC3D software were shown in the form of stress and crack tip opening displacement (CTOD) maps. The paper presents the differences of fatigue cracks growth under torsion and bending with torsion being derived by using the FRANC3D software.

**Keywords:** Numerical Method, Fatigue Crack Growth, Torsion and Bending with Torsion

## 1. INTRODUCTION

Extremely fast development of technology causes that the current numerical methods often replace analytical methods and they reinforce the analysis of experimental research studies. The disadvantages associated with experimental tests are their time-consumption and costs for performing them. Nowadays, basic numerical methods being commonly used in engineering calculations are the finite element method (FEM) (Zienkiewicz and Taylor, 2000; Kleiber, 1995; Szusta and Seweryn, 2010) and the boundary element method (BEM) (Becker, 1992). Those methods allow achieving fast and relatively accurate solutions to many issues in the design of machines, which would be exceptionally difficult or even impossible when using analytical methods (Rusiński, 2002). Today, many large and medium-sized enterprises could not imagine starting production of a new product, before it undergoes positive verification by using numerical methods. These methods allow for modeling the maps of stress, displacement and strain in accordance with the analytical solution in terms of both, the linear and non-linear range. Moreover, they allow for calculation of many others parameters required by the user, such as: the stress intensity factor, the crack tip opening displacement or the J-integral (Rozumek and Macha, 2006; Döring et al., 2006). Using the numerical methods, it should be kept in mind that it is recommended to compare the obtained results with analytical calculations or experimental research carried out in the field, as far as it is possible. It should be considered that the results of numerical calculations describing the behavior of the complex model will be presented in an approximate manner. Moreover, it should be also note that these results are subject to a certain error. One method for solving such complex models is their transformation into several simplified models. The main purpose of the finite element method is to divide the continuous geometric model into finite elements being combined into the so-called nodes,

the result of which is the development of discrete geometric model. Boundary element method employs the fundamental solution (differential equations). Approximation takes place explicitly on the edge of the tested area of the body without any interference in the internal area. Finite (boundary) elements are interrelated in nodes, and this ensures the system parameters' continuity (Rozumek and Macha, 2006). The research paper (Derpeński and Seweryn, 2007) presents the results of numerical analysis of stress field and strain under tensile in notch type specimens. The specimens were made of the EN 2024 aluminum alloy. Moreover, the stress criterion of specimens cracks emanating from notched, considering the maximum values of plastic shear strain. The authors of the research paper (Duchaczek and Mańko, 2012) proposed methods for determining value of the stress intensity factor by using the FRANC2D software. The research work (Seweryn, 2002) indicates the accuracy of calculation of the stress intensity factor and the way in which the stress values near the crack tip are being changed.

The aim of the paper is the analysis of the state of stress and the crack tip opening displacement (strain) at the bottom of the notch, as well as presenting the changes in fatigue cracks growth behaviour under torsion and bending with torsion in specimens with rectangular cross-section.

## 2. SUBJECT OF STUDY

Specimens with rectangular cross-section and gross dimension 8x10 mm were the subject of numerical computations (Fig. 1). The specimens were made of the EN AW-2017A (PA6) aluminium alloy with mechanical properties shown in Tab. 1.

The specimens had an external unilateral notch, which was  $a_0 = 2$  mm deep and its radius was  $\rho = 22.5$  mm. The theoretical stress concentration factor in the specimen was estimated accord-

ing to the equation provided in the research work (Thum et al., 1960), which under bending was  $K_t = 1.04$ .

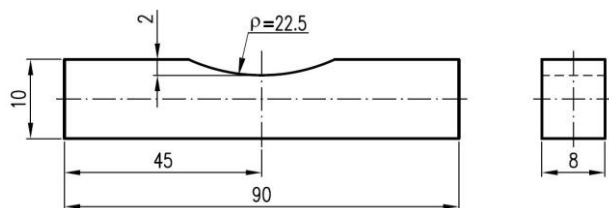


Fig. 1. Shape and dimensions of specimens for fatigue crack growth tests, dimensions in mm

Tab. 1. Mechanical properties of the EN AW-2017A aluminium alloy

| $\sigma_y$ (MPa) | $\sigma_u$ (MPa) | $E$ (GPa) | $\nu$ (-) |
|------------------|------------------|-----------|-----------|
| 382              | 480              | 72        | 0.32      |

Alloys of aluminium with copper and magnesium -that is du-ralumin- belong to alloys characterised by supreme strength properties. Chemical composition of the tested EN AW-2017A aluminium alloy shown in Table 2 (Rozumek and Macha, 2009). The longitudinal microsection shown in Fig. 2 indicate structures heavily dominated by elongated grains of the solid solution  $\alpha$  of various sizes and at width of approx. 50  $\mu\text{m}$ . Between large elongated grains clusters of very small equiaxed  $\alpha$  phase grains in the system band are visible, as well. On the base of solid solution  $\alpha$ , numerous precipitation of intermetallic phases, particularly  $\text{Al}_2\text{Cu}$ , as well as  $\text{Mg}_2\text{Si}$  and  $\text{AlCuMg}$  are seen. Precipitations of the  $\text{Al}_2\text{Cu}$  phase occur mainly in the chain system on grain boundaries of the solid solution, and their size does not exceed 5  $\mu\text{m}$  (Rozumek et al., 2015).

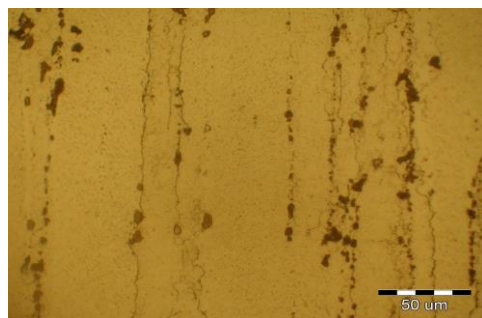


Fig. 2. Microstructure of the EN AW-2017A aluminium alloy, magnification 500x

Tab. 2. Chemical composition of the tested EN AW-2017A alloy (wt%)

|            |            |            |              |            |
|------------|------------|------------|--------------|------------|
| Cu - 4.15% | Mn - 0.65% | Zn - 0.50% | Mg - 0.69%   | Fe - 0.70% |
| Cr - 0.10% | Si - 0.45% | Ti - 0.20% | Al - Balance |            |

Numerical computations were carried out under torsion and proportional bending with torsion. Proportional bending with torsion was obtained through the ratio of torsional and bending moments, which amounted to  $M_T / M_B = \tan \alpha = 1$ . The computations were performed at constant moment amplitude  $M_T = M_{BT} = 15.84 \text{ N}\cdot\text{m}$ . The tests were performed at load frequency 28.4 Hz and stress ratio  $R = -1$ .

### 3. NUMERICAL COMPUTATIONS OF STATE OF STRESS AND CRACK TIP OPENING DISPLACEMENT

#### 3.1. Description of the software for numerical computations (FRANC3D)

The state of stress and crack tip opening displacement (strain) in the examined specimens was analysed with boundary element method with the FRANC3D software ([www.cfg.cornell.edu/software/software.htm](http://www.cfg.cornell.edu/software/software.htm)). Geometric model of the specimen was performed using the OSM software application. The work in the OSM application began with modeling specimens by introducing coordinates of points forming a flat figure with a notch. The next step was to transform the flat outline of the specimen into 3D object. Then, the work in the FRANC3D software was started with introduction of operating range (linear-elastic, elastic-plastic) and material data. After entering the above data, the required specimens surfaces needed to be confirmed. For the presented example of numerical computations, the specimens is fixed by one end (taking away the numbers of degrees of freedom of nodes) (Fig. 3). The next step is to determine the method and load value of the specimens. The specimens was subjected under torsion (Fig. 3a) and bending with torsion (Fig. 3b) in accordance with the directions of the  $x$ ,  $y$  and  $z$  axes.

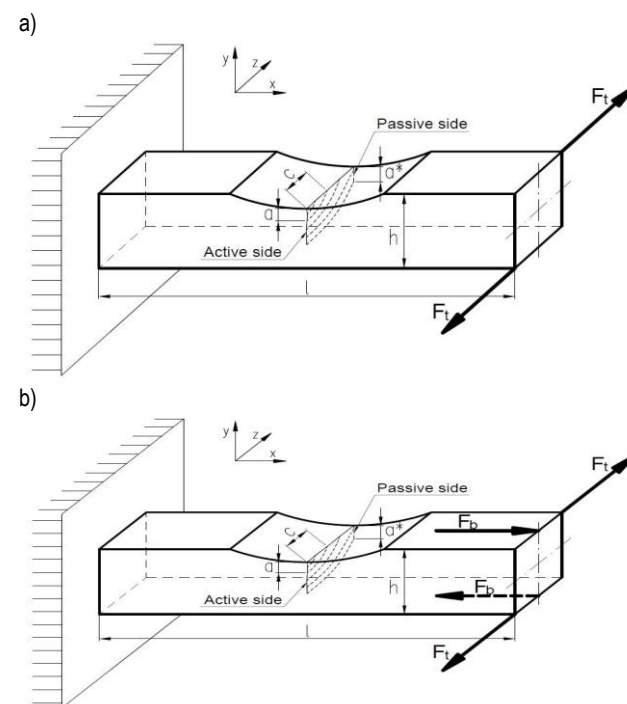


Fig. 3. The geometry of the specimen model with selected method of support and load for: a) torsion, b) bending with torsion

Bearing defined restrain and load, the boundary element mesh formation can be started. The size and shape of boundary elements depends on the division of section closing a given area (Faszynka and Rozumek, 2014). Fig. 4 shows networks of boundary elements for spatial model, consisting of 1209 triangular elements.

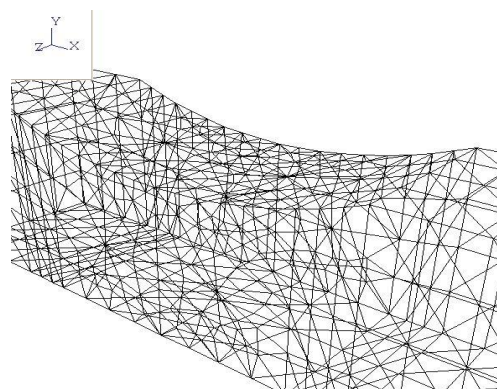


Fig. 4. Division into boundary elements of a specimen model around the bottom of the notch

First numerical computations of the state of stress without crack were performed on such a model of specimen. Furthermore, the next step of computations is the numerical analysis of stress and CTOD being performed around the crack tip opening displacement. In the calculation model, torsion crack were initiated in the form of the arc at the bottom of the notch with initial length of 0.1 mm on a side surface, and 0.1 mm on the upper surface. At the time of bending with torsion, the crack was initiated in the form of the arc of 0.1 mm length on the side surface, and of 0.3 mm on the upper surface. Introduced points were connected with curve in such a way that they enabled forming an edge of the crack. At the first steps of the crack growth, the FRANC3D software will form a surface of quarter-elliptic edge crack in the bottom of the notch, as shown in Fig. 5. Then, the crack goes across the specimen (various length of the crack at front and edge of the specimen), as shown in Fig. 6.

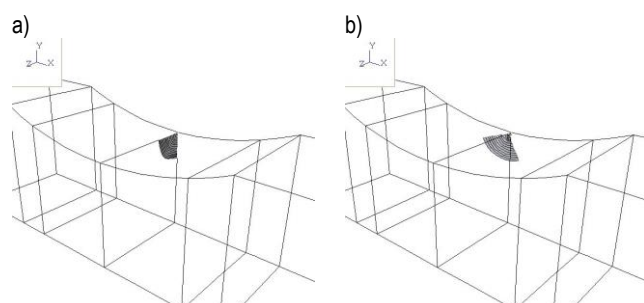


Fig. 5. Plane of quarter-elliptic crack at the edge of the notch: a) torsion, b) bending with torsion

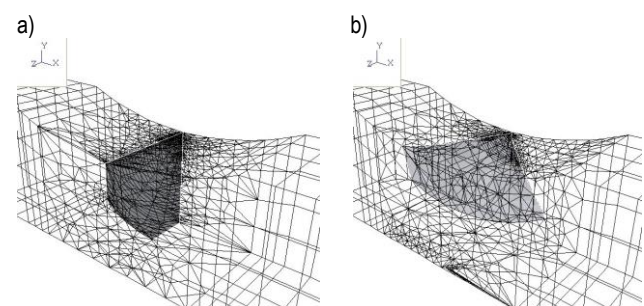


Fig. 6. Plane of through crack with division into boundary elements under: a) torsion, b) bending with torsion

The obtained plane of cracks should be divided into boundary elements. The method of division and the way in which the

boundary element mesh is made at the place of crack initiation are the same as at the time, when the mesh was generated for the whole model. The next step is to perform numerical computations. For further recalculations on the crack growth, numerical values of crack growth and the total length of the crack were introduced. After the crack growth is being accepted, the program automatically enlarges the crack by a predetermined value (the program itself will set the path of crack growth according to the given load). In order to perform numerical analysis of crack growth, new planes should be further divided into smaller surface and a mesh of boundary elements should be developed. The process of distribution of new plane into smaller surfaces should be repeated as long as the desired length of the crack will be obtained or as the complete destruction of the test specimen will be reached (Faszynka and Rozumek, 2014).

### 3.2. The results of numerical computations

The results of numerical computations were presented in the form of maps of stress and crack tip opening displacement (CTOD) for spatial model of the specimen. Fig. 7 shows a specimen model without crack.

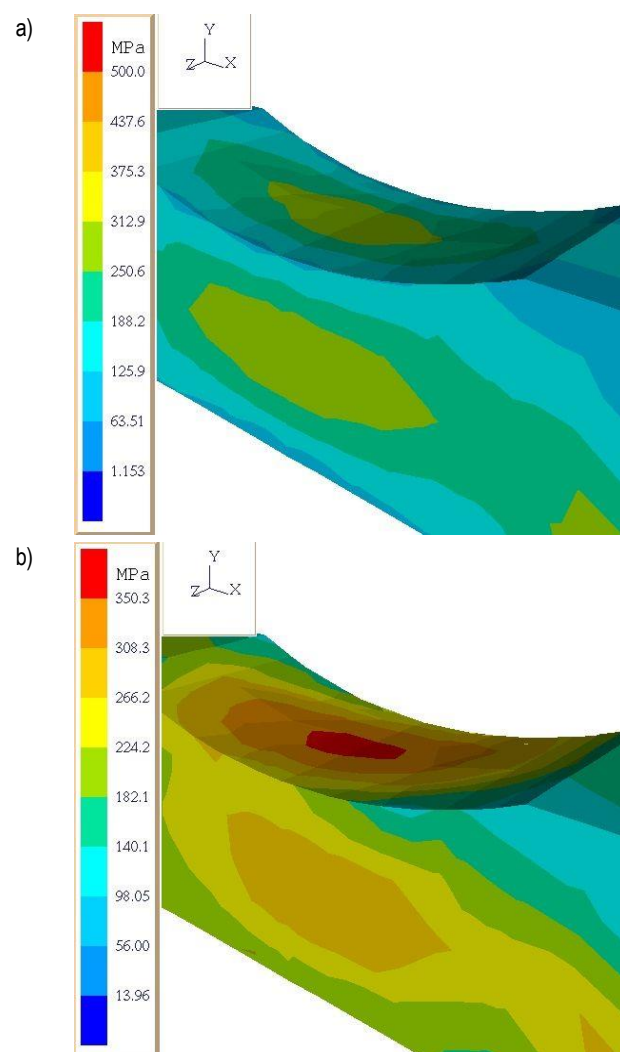
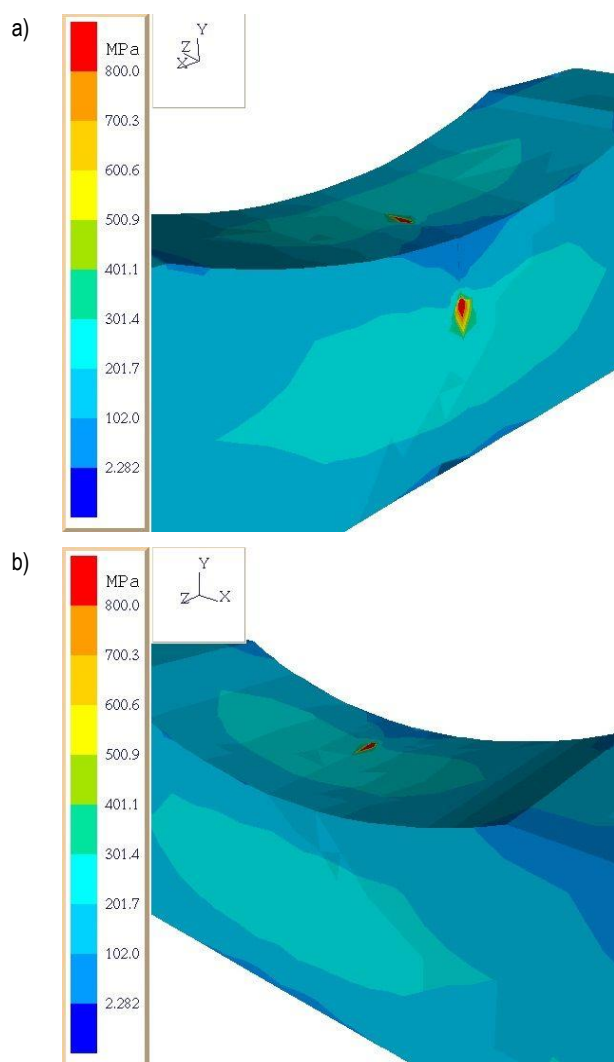


Fig. 7. Distribution of stresses in the specimen model (according to Huber-Mises) under: a) torsion, b) bending with torsion



Figs. 8÷11 present a model of the specimen with quarter-elliptic edge crack. While in Figs. 12÷15 a model of the specimen with a through the thickness crack. Computations were made for a specimen model under torsion (Fig. 3a) and proportional bending with torsion (Fig. 3b). The exemplary results of the numerical computations for the specimen model without crack are shown in Fig. 7a (torsion) and in Fig. 7b (bending with torsion) as stress maps. Numerical computations on the crack growth were performed by employing the incremental method for crack lengths, corresponding to the cracks obtained during experimental tests (Faszynka et al., 2015). A non-uniform fatigue cracks growth on both lateral surfaces of specimens (active side and passive side) was observed during experimental tests under torsion and bending with torsion. The development of fatigue cracks in the specimens was performed in two stages: at first, the quarter-elliptic edge cracks were observed and then they were transforming into the through the thickness crack. Fig. 8 shows the stress distribution in the model of the specimen (according to Huber-Mises Hypothesis) for load  $M_T = 15.84 \text{ N}\cdot\text{m}$  ( $R = -1$ ) under torsion, with a quarter-elliptic edge crack and the length of  $a = 2.00 \text{ mm}$  (lateral side of the specimen) and  $c = 2.20 \text{ mm}$  depth (at the notch root).



**Fig. 8.** Distribution of stresses in the specimen model (according to Huber-Mises) for quarter-elliptic edge crack length of  $a = 2.00 \text{ mm}$  and depth of  $c = 2.20 \text{ mm}$  under torsion: a) active side, b) passive side

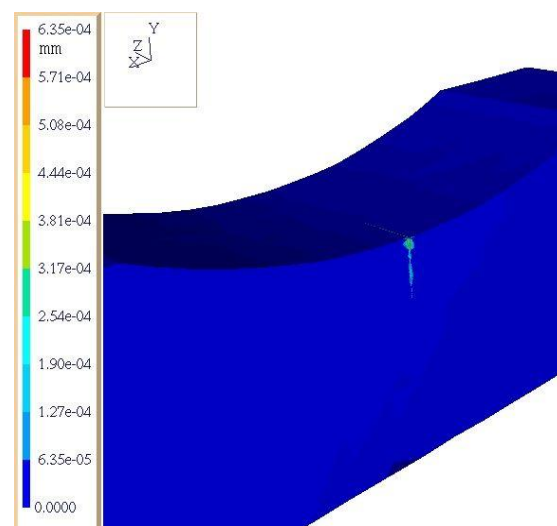


**Fig. 9.** Crack tip opening displacement maps for a quarter-elliptic edge crack length of  $a = 2.00 \text{ mm}$  and depth of  $c = 2.20 \text{ mm}$  (active side) under torsion

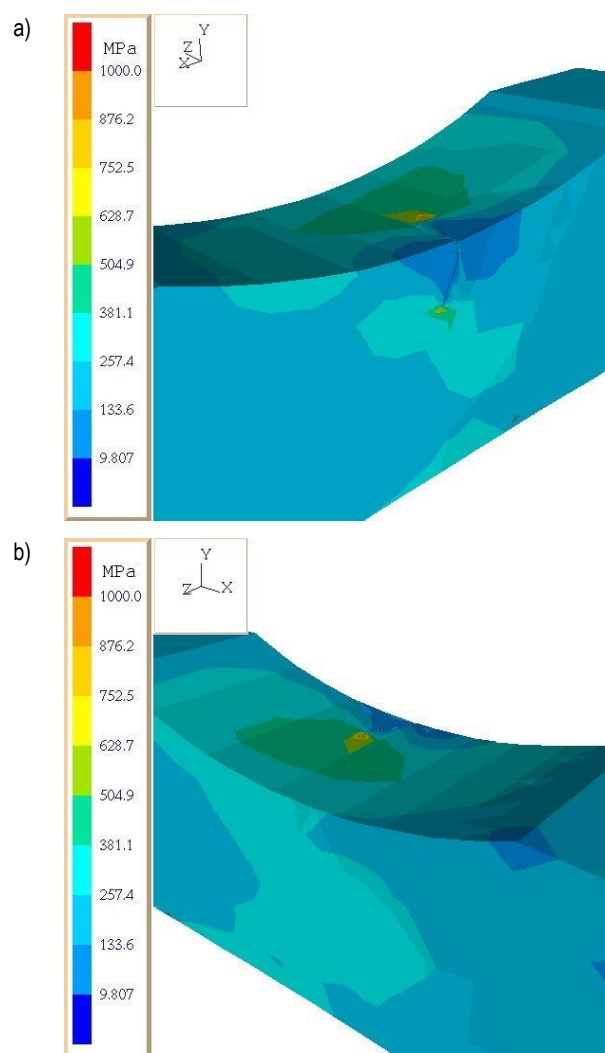


**Fig. 10.** Distribution of stresses in the specimen model (according to Huber-Mises) for quarter-elliptic edge crack length of  $a = 2.50 \text{ mm}$  and depth of  $c = 2.80 \text{ mm}$  under bending with torsion: a) active side, b) passive side

Fig. 9 presents the crack tip opening displacement (CTOD) at load  $M_T = 15.84 \text{ N}\cdot\text{m}$  ( $R = -1$ ) under torsion, with a quarter-elliptic edge crack with the length of  $a = 2.00 \text{ mm}$  (lateral side of the specimen) and  $c = 2.20 \text{ mm}$  depth (at the notch root).

Fig. 10 indicates distribution of stresses in the specimen model (according to Huber-Mises) for the load  $M_{BT} = 15.84 \text{ N}\cdot\text{m}$  ( $R = -1$ ) under bending with torsion, with a quarter-elliptic edge crack length of  $a = 2.50 \text{ mm}$  and depth of  $c = 2.80 \text{ mm}$ . Fig. 8 and 10 ensure that the highest value of stress are at the notch root than on the lateral side of the specimen (h peak values, Fig. 3). By comparing the Figs. 8 and 10 it can be noted that greater stress values in crack tip opening occur for bending with torsion than for torsion. Fig. 11 presents CTOD maps for the load  $M_{BT} = 15.84 \text{ N}\cdot\text{m}$  ( $R = -1$ ) under bending with torsion, for a quarter-elliptic edge crack length of  $a = 2.50 \text{ mm}$  and depth of  $c = 2.80 \text{ mm}$ . During comparison of Figs. 9 and 11, the greater CTOD values for bending with torsion rather than for torsion were observed.

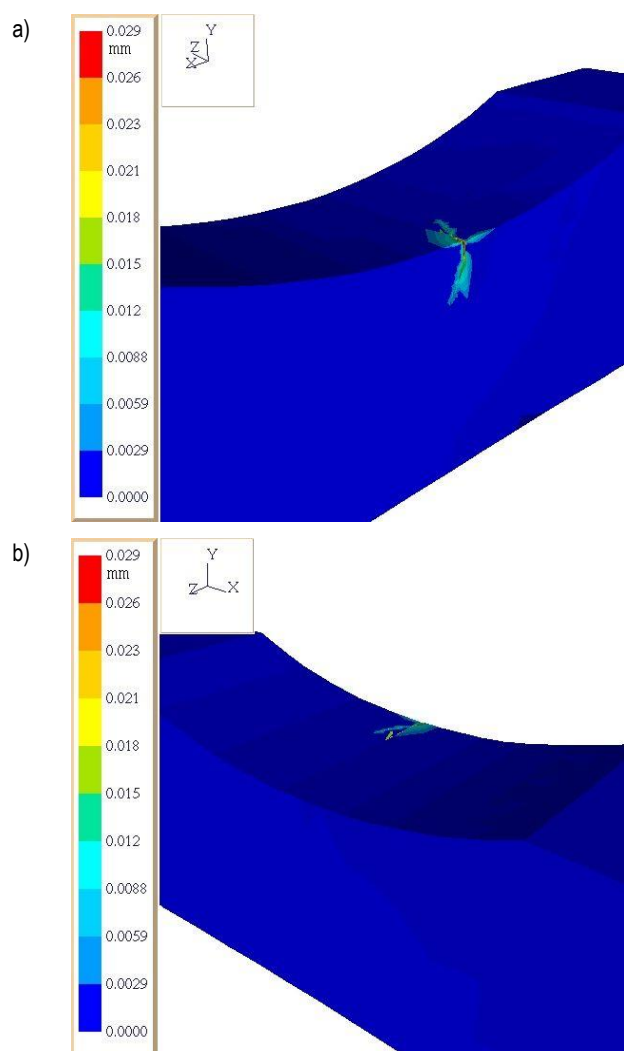


Fig. 11. Crack tip opening displacement maps for a quarter-elliptic edge crack length of  $a = 2.50 \text{ mm}$  and depth of  $c = 2.80 \text{ mm}$  under bending with torsion: a) active side, b) passive side

Figs. 12÷15 represent exemplary results of numerical computations for the specimen model with the through the thickness crack. Measurement of the crack length was carried out on both sides of specimens. On the active side (Fig. 12a) the

cracks were a greater than on the passive side (Fig. 12b). Larger crack length on the active side causes reduction of cross-section of the specimen without crack, which leads to stress increase. For calculations purposes, the greater lengths of cracks are assumed simple because they obtain the greatest stress values and have major impact on the specimen failure. On the active side, the crack lengths were marked with the letter "a", and on the passive side with the letter "a\*". Fig. 12 indicate distribution of stresses in the specimen model (according to Huber-Mises) for the load  $M_T = 15.84 \text{ N}\cdot\text{m}$  ( $R = -1$ ) under torsion, with the through the thickness crack length of  $a = 8.00 \text{ mm}$  (active side of the specimen) and the length of  $a^* = 2.50 \text{ mm}$  (passive side of the specimen).

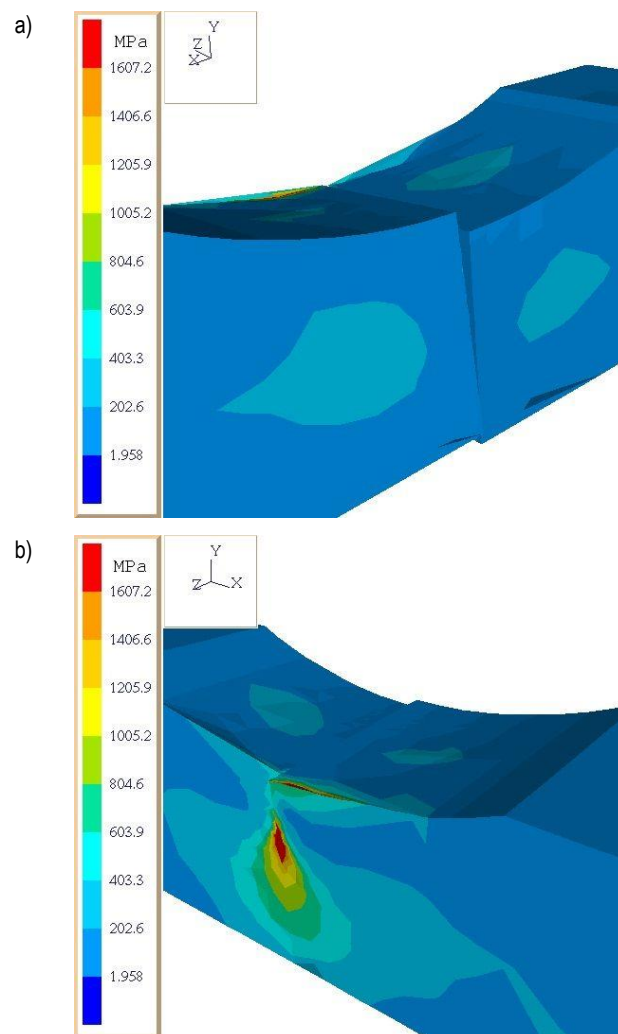


Fig. 12. Distribution of stresses in the specimen model (according to Huber-Mises) for through crack length of  $a = 8.00 \text{ mm}$  and the length of  $a^* = 2.50 \text{ mm}$  under torsion: a) active side, b) passive side

Fig. 13 presents crack tip opening displacement maps for the load  $M_T = 15.84 \text{ N}\cdot\text{m}$  ( $R = -1$ ) under torsion, with through the thickness crack length of  $a = 8.00 \text{ mm}$  and the length of  $a^* = 2.50 \text{ mm}$ .

Fig. 14 shows distribution of stresses in the specimen model (according to Huber-Mises) for the load  $M_{BT} = 15.84 \text{ N}\cdot\text{m}$  ( $R = -1$ ) under bending with torsion, with through the thickness crack length of  $a = 6.10 \text{ mm}$  and the length of  $a^* = 2.60 \text{ mm}$ . Comparing

Figs. 12 and 14, the various lengths of cracks at both sides of the specimen can be distinguished under torsion and under bending with torsion. Despite the  $M_B$  to  $M_T$  ratio being applied during the research tests, differences in length of crack growth on the active and passive side of the specimen could be always observed. By comparing Figs. 12 and 14 could be easily seen that greater stress in crack tip opening displacement are observed for torsion rather than for bending with torsion. Comparison of Figs. 8 and 12 with Figs. 10 and 14 shows that longer cracks indicate higher stress values.

Fig. 15 presents crack tip opening displacement maps for the load  $M_{BT} = 15.84$  N·m ( $R = -1$ ) under bending with torsion, for through the thickness crack length of  $a = 6.10$  mm and the length of  $a^* = 2.60$  mm. Crack tip opening displacement for the quarter-elliptic edge cracks and the through the thickness cracks is greater under bending with torsion than under torsion.

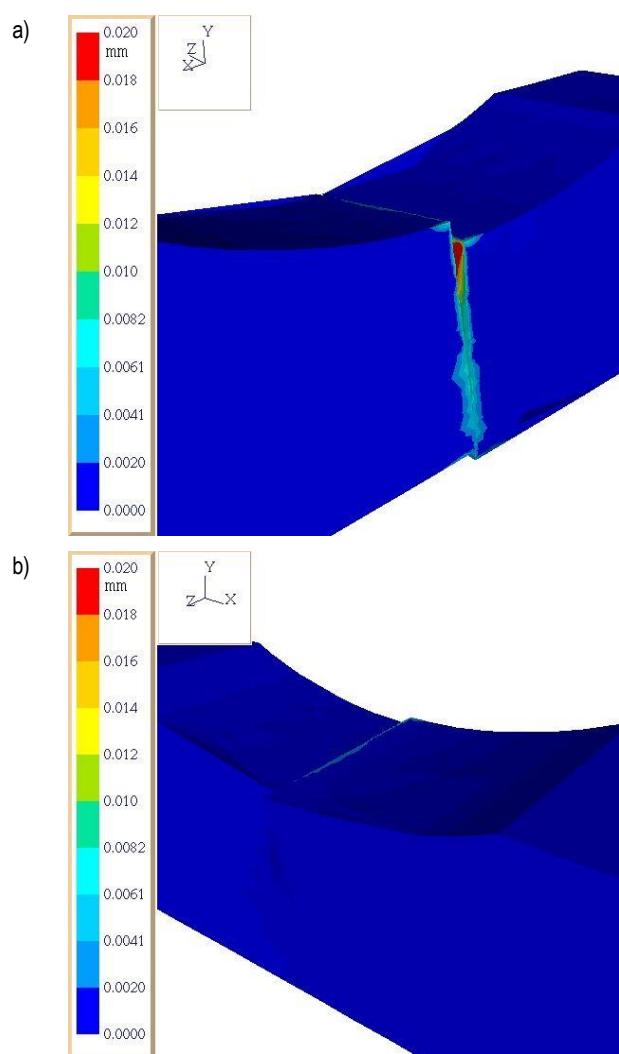


Fig. 13. Crack tip opening displacement maps for through the thickness crack length of  $a = 8.00$  mm and the length of  $a^* = 2.50$  mm under torsion: a) active side, b) passive side

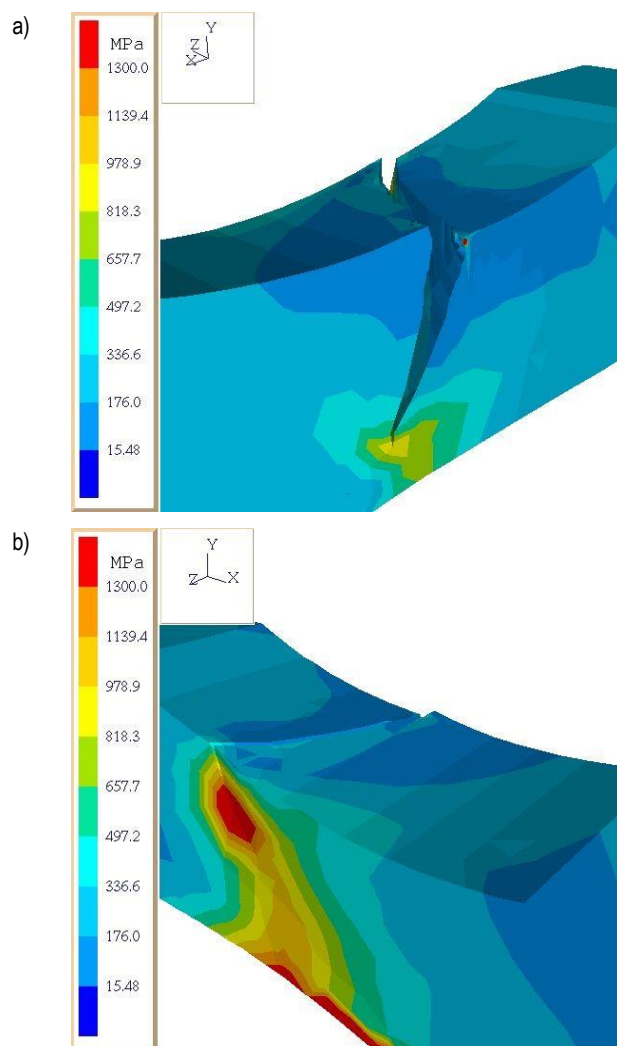


Fig. 14. Distribution of stresses in the specimen model (according to Huber-Mises) for through the thickness crack length of  $a = 6.10$  mm and the length of  $a^* = 2.60$  mm under bending with torsion: a) active side, b) passive side

During numerical computations, the observed track of crack growth (the quarter-elliptic edge and the through the thickness crack) under torsion and under bending with torsion was at the same direction as during experimental tests (Zappalorto et al., 2011; Brighenti et al., 2012). To illustrate it, the nominal stress values obtained by using the BEM method (numerical calculations) were compared to these values received from analytical calculations (Susmel and Taylor, 2007). The stress values for the active length quarter-elliptic edge cracks  $a = 2.00$  mm (for torsion) and  $a = 2.50$  mm (for bending with torsion) were  $\tau_n = 175.7$  MPa (for torsion) when using BEM method, and  $\tau_n = 162.1$  MPa when applying the analytical method. The stress values for bending with torsion were  $\sigma_n = 242.7$  MPa when using BEM method, and  $\sigma_n = 266.6$  MPa when applying the analytical method. By comparing both methods of computation for the presented example, it was marked that the relative error does not exceed 10%. Superiority of the BEM method over the analytical method is derived from the ability to obtain stress distribution near the crack tip opening displacement.



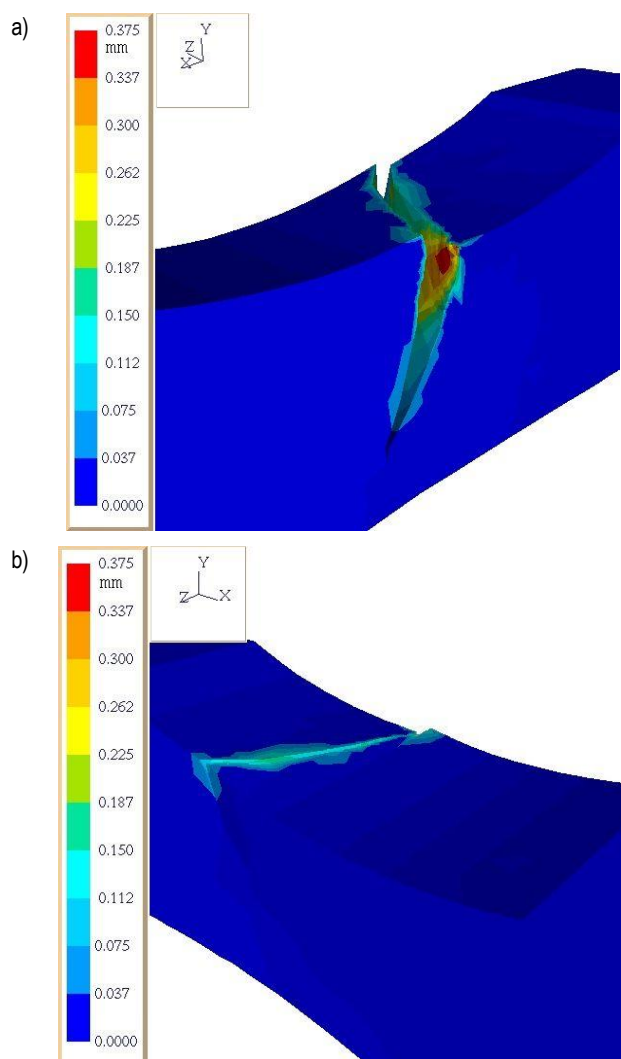


Fig. 15. Crack tip opening displacement maps for through crack length of  $a = 6.10$  mm and the length of  $a^* = 2.60$  mm under bending with torsion: a) active side, b) passive side

#### 4. CONCLUSIONS

Numerical computations for cracks growth allow for the following conclusions:

1. At quarter-elliptic edge cracks, the values of stresses are higher of approx. 9.5% for bending with torsion than for torsion.
2. At the through the thickness cracks, the values of stresses are higher of approx. 23.6% for torsion than for bending with torsion.
3. The FRANC3D software is one of the few programs that can be employed for numerical computations of cracks growth.

#### REFERENCES

1. Becker A.A. (1992), The boundary element method in engineering, McGraw – Hill International, New York.
2. Brighenti R., Carpinteri A., Vantadori S. (2012), Fatigue life assessment under a complex multiaxial load history: an approach based on damage mechanics, *Fatigue & Fracture of Engineering Materials & Structures*, Vol. 35, 141-153.
3. Derpeński Ł., Seweryn A. (2007), Numerical analysis of fracture for specimens with notches made of elasto-plastic material, *Acta Mechanica et Automatica*, Vol. 1 (1), 27-30 (in Polish).
4. Döring R., Hoffmeyer J., Seeger T., Vormwald M. (2006), Short fatigue crack growth nonproportional multiaxial elastic-plastic strains, *International Journal of Fatigue*, Vol. 28 (9), 972-982.
5. Duchaczek A., Mańko Z. (2012), Assessment of direct method of calculating stress intensity factor, *Journal of Science of the gen. Tadeusz Kosciuszko Military Academy of Land Forces*, No. 3 (165), 336-346 (in Polish).
6. Faszynka S., Rozumek D. (2014), Application of the FRANC3D software for crack growth calculations, *Mechanik*, No. 11, 932-934 (in Polish).
7. Faszynka S., Rozumek D., Lewandowski J. (2015), Crack growth path in specimens with rectangular section under bending with torsion, *Solid State Phenomena*, Vol. 224, 133-138.
8. Kleiber M. (1995), *Computational methods in mechanics of solids*, Warsaw, PWN (in Polish).
9. Rozumek D., Hepner M., Faszynka S. (2015), Fatigue tests of PA6 and PA7 alloys subjected to bending without and after precipitation hardening, *Mechanik*, No. 3, 246-249 (in Polish).
10. Rozumek D., Macha E. (2006), Elastic-plastic fatigue crack growth in 18G2A steel under proportional bending with torsion loading, *Fatigue & Fracture of Engineering Materials & Structures*, Vol. 29 (2), 135-145.
11. Rozumek D., Macha E. (2009), J-integral in the description of fatigue crack growth rate induced by different ratios of torsion to bending loading in AlCu4Mg1, *Mat.-wiss. u. Werkstofftech.*, Vol. 40 (10), 743-749.
12. Rusiński E. (2002), Design principles supporting structures of motor vehicles, *Oficyna Wydawnicza Politechniki Wrocławskiej*, Wrocław (in Polish).
13. Seweryn A., (2002), Modeling of singular stress fields using finite element method, *Int. Journal of Solids and Structures*, Vol. 39 (18), 4787-4804.
14. Susmel L., Taylor D. (2007), Non-propagating cracks and high-cycle fatigue failures in sharply notched specimens under in-phase Mode I and II loading, *Engineering Failure Analysis*, Vol. 14, 861-876.
15. Szusta J., Seweryn A. (2010), Fatigue damage accumulation modelling in the range of complex low-cycle loadings – The strain approach and its experimental verification on the basis of EN AW-2007 aluminium alloy, *International Journal of Fatigue*, Vol. 33 (2), 255-264.
16. Thum A., Petersen C., Swenson O. (1960), *Deformation, stress and notch effect*, VDI, Duesseldorf (in German).
17. Zappalorto M., Berto F., Lazzarin P. (2011), Practical expressions for the notch stress concentration factors of round bars under torsion, *International Journal of Fatigue*, Vol. 33 (3), 382-395.
18. Zienkiewicz O. C., Taylor R. L. (2000), *The finite element method*, Butterworth Heinemann, Vol. 1-3, Oxford.
19. www.cfg.cornell.edu/software/software.htm.

# ANALYSIS OF CORRELATION BETWEEN STRESSES AND FATIGUE LIVES OF WELDED STEEL SPECIMENS BASED ON REAL THREE-DIMENSIONAL WELD GEOMETRY

Przemysław STASIUK\*, Aleksander KAROLCZUK\*\*, Wiesław KUCZKO\*\*\*

\*Formopex Sp. z o.o., ul. Braci Prankel 1, 47-100 Strzelce Opolskie, Poland

\*\*Faculty of Mechanical Engineering, Department of Mechanics and Machine Design,  
Opole University of Technology, ul. Prószkowska 76, 45-758 Opole, Poland

\*\*\*Chair of Management and Production Engineering, Department of Mechanical Engineering and Management,  
Poznań University of Technology, Pl. M. Skłodowskiej-Curie 5, 60-965 Poznań, Poland

[przemyslaw.stasiuk@formopex.pl](mailto:przemyslaw.stasiuk@formopex.pl), [a.karolczuk@po.opole.pl](mailto:a.karolczuk@po.opole.pl), [wieslaw.kuczko@put.poznan.pl](mailto:wieslaw.kuczko@put.poznan.pl)

received 4 May 2015, revised 11 December 2015, accepted 22 December 2015

**Abstract:** Welded joints are areas of increased stresses in construction. The reason for this phenomenon is associated with the nonhomogeneous mechanical, structural and geometrical properties of the weld. In the article the correlations between locally raised stresses due to real geometry and fatigue lives of non-load carrying cruciform joints made from S355J2+N steel are analysed. Stresses were computed using Finite Element Method (FEM) based on real three-dimensional weld geometry obtained by 3D scanning. The specimens were experimentally tested under cyclic push-pull loading with a zero mean value of applied force. The correlation was analysed using Pearson's correlation coefficient and statistical hypotheses. It was shown that statistically significant correlation exists between maximum values of normal stresses and fatigue lives.

**Keywords:** 3D Topography of Weld Joint, Non-Load Carrying Cruciform Joints, FEM Analysis, Correlation Analysis

## 1. INTRODUCTION

Welding is a very popular method of joining steel elements. There are many possibilities to automate this process through the use of specialized equipment. It is not complicated in the case of long, straight welds but for small parts, where access could be problematic, automation could be expensive or sometimes impossible. Therefore, manual welding still remains an important element of technological processes. The shape of the manually welded seam is characterized, e.g. by varying the values of the angle of the face and the radius at the weld toe and also by existence of ripples. The welding operation causes residual stresses, changes in the structure of the material, forming a structural notch and also a geometry notch studied in (Nykänen et al., 2007; Barsoum et al., 2011; Blacha et al., 2011, 2013). The influence of these defects can be reduced by heat treatment (the heterogeneity of structure and residual stresses) and by machining (geometric notch) (Kirkhope et al., 1999; Ting et al. 2009). However, this type of treatment carries a considerable financial outlay. Popularity of welding makes attempts to find methods to better understanding the changes occurring in the material and the effect on the fatigue strength.

Analysis of a shape of the weld was taken into account by many researchers. In the works of (Williams et al., 1970) analysis of the influence of a welding geometry on the fatigue behavior of transverse butt welded joints in ASTM A36 steel and A441 (high-strength low-alloy structural manganese vanadium steel) was conducted. The analysis has shown that the height of the

crown of the weld better correlates with fatigue lives than radius at the toe of the weld. Along with the development of measuring method and equipment availability, geometry mapping was getting closer to real weld geometry. Measuring of a silicon mold of specimen were used to analyze non-load-carrying fillet welded cruciform joints in mild carbon SM490 steel (Lee et al., 2009). The analysis showed that fatigue lives increases with increasing the weld flank angle and the weld toe radius. Alam et al., (2010) analyzed the influence of surface geometry and topography on the fatigue cracking behavior of laser hybrid welded eccentric fillet joints (stainless steel SS2333). They have shown that the toe radius does not always dominate fatigue performance and the ripples can become more crucial.

3D scanning is the most accurate method to obtain weld seam geometry. This method gives a possibility to create real model of a weld joint. The method was used to calculate stress distribution by finite element method (FEM) in cross welded joints in high-strength low-alloy ASTM A572 steel (Hou, 2007) and in overlap and T-joint in S355MC construction steel (Kaffenberger et al., 2012). It was shown in (Hou, 2007) that not all crack started from the highest stress concentration points. Kaffenberger et al. (2012) successfully applied mean value of toe radius determined as 0.2 mm to correlate fatigue lives with calculated stress amplitudes.

This present paper aims to analyze correlation between experimentally observed fatigue lives and different types of stresses being the result of imperfect weld joint geometry. The analyzed stresses are: nominal stress amplitudes, maximum local values of normal stress amplitudes, maximum local values of superposed



normal stress amplitudes and mean values, averaged normal stresses (highly stressed volume approach). The analysis was performed on a non-load carrying cruciform joints made from S355J2+N steel. The shape of a weld was received by 3D scanning, as it was mentioned, this method allows to create a virtual model of a specimen and use it to calculate a stress distribution by FEM.

## 2. PREPARATION OF THE SPECIMENS

The welded plates were made from 6 mm thick metal (S355J2+N) sheets with the base plate dimensions 200x1000 mm and rib dimensions 30x1000. Plasma cutting was used to prepare elements. Parts were blasted after cutting. Edges of the plates were grinded in order to create correct joint. Welding was conducted by MAG method, with 1.2 mm wire, in Ar (92%) and CO<sub>2</sub> (8%) gas shield, without using clamps. Deformation of plates (deviation from flatness of main plate) after cooling reached 0.35 mm. The specimens were obtained from four welded plates (marked as numbers 1-4) with geometry presented in Fig. 1 by saw cutting. The specimens from one of plate (number 2) were subjected to the heat treatment (stress relief annealing).

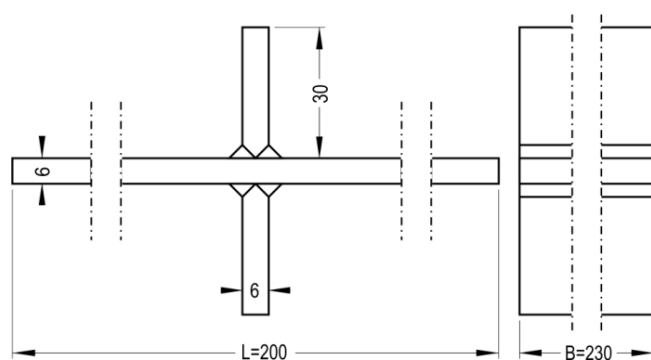


Fig. 1. Geometry of the welded plates

### 2.1. 3D scanning

The plates were scanned by using GOM ATOS device which applies refraction of white light bands on the element. Five scans for both sides of each plate were taken. The clouds of points were converted into a mesh of triangles and next into stereolithography (\*.stl). This allowed to mapping of the sample with 0.02 mm (distance between the points). Fig. 2 shows a comparison between measured points and output model.

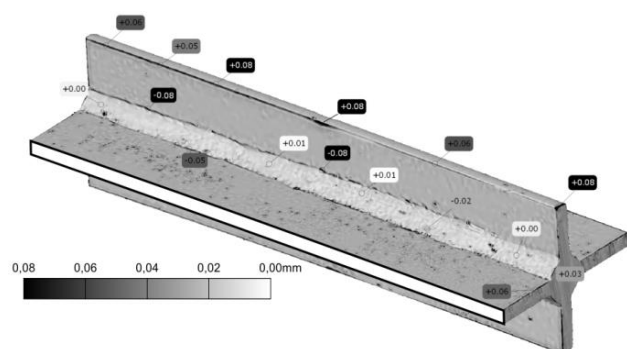


Fig. 2. Mapping of accuracy

## 3. EXPERIMENTAL TESTS

After scanning, the specimens for fatigue tests were prepared by saw cutting and milling. Thirteen specimens with B=24 mm width were received from plate (Fig. 1). The specimens were marked as "no1.no2", where no1 is a based plate (1-4), and no2 is a specimen number (1-9). The specimens were experimentally tested under cyclic push-pull loading with controlled nominal stress amplitude  $\sigma_{an}$  ( $153.1 \pm 5.9$  MPa). Tests were conducted until complete rupture of the specimens. Fatigue lives  $N_{exp}$  were summarized in Tab. 1.

Tab. 1. Results of experimental cyclic push-pull loading

| Specimen | $\sigma_{an}$ , MPa | $N_{exp}$ , cycles |
|----------|---------------------|--------------------|
| 1.1      | 154.7               | 191890             |
| 1.2      | 159.1               | 219650             |
| 1.4      | 153.5               | 230470             |
| 1.5      | 156.5               | 177650             |
| 2.3      | 154.7               | 104480             |
| 2.5      | 149.5               | 165980             |
| 2.6      | 151.6               | 76150              |
| 2.7      | 151.2               | 112710             |
| 2.8      | 152.8               | 109600             |
| 2.9      | 150.4               | 103040             |
| 4.1      | 156.9               | 174960             |
| 4.5      | 158.9               | 97680              |
| 4.8      | 141.2               | 114290             |

The stress relief annealing did not change significantly the fatigue lives of specimens. The reason could be seen in small width of specimens obtained by saw cutting or/and due to stress relaxation occurring under loading (Barsoum and Gustafsson, 2009). As result all data will be treated as one set. Fig. 3 presents an example of fatigue fracture surface.

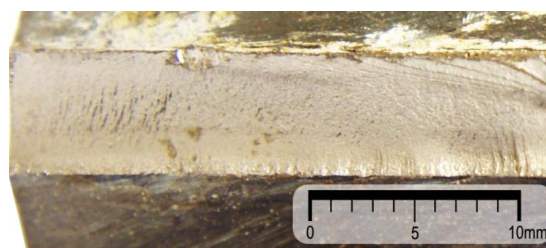


Fig. 3. Fatigue fracture

## 4. FEM ANALYSIS

The scanned models were converted into step file and imported into Solid Edge program in order to divide and prepare 24mm width specimen models. Preliminary analysis was conducted to determine the appropriate mesh size. Finally, the maximum length of finite element equal to 0.05mm in the welding toe was chosen. Fig. 4 presented mesh density used in FEM model.

Applied constrains and loads imitate fixing and testing in the fatigue machine with hydraulic grips under cyclic push-pul loading. Analysis were conducted in steps. At first (i) closing of thegrips were modeled. Straightening of a specimen associated with the

welding deformation was taking into account and stress tensor components were computed  $\sigma_{ij}^{(i)}(x, y, z)$ . In next step the models were subjected to tensile nominal stresses  $\sigma_{an}$  reported in Tab. 1 and stress tensor components  $\sigma_{ij}^{(ii)}(x, y, z)$  were determined. Static analysis was performed using a linear-elastic model of the body ( $E = 205\text{GPa}$ ,  $\nu = 0.3$ ). In Fig. 5 example (specimen 2.7) of maximum principal stress distribution is showed computed as superposition of steps (i) and (ii). The Fig. 5 clearly shows that stresses are highly concentrated in fusion line where all fatigue cracks were observed.

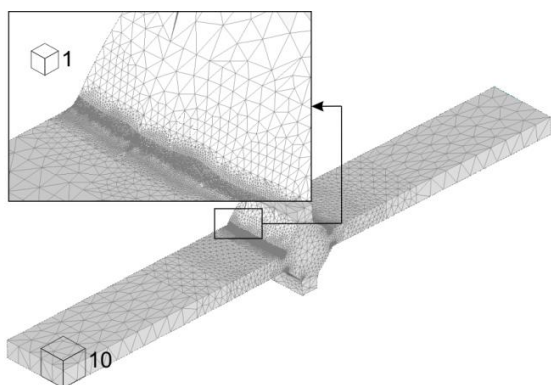


Fig. 4. Mesh density in the specimen model

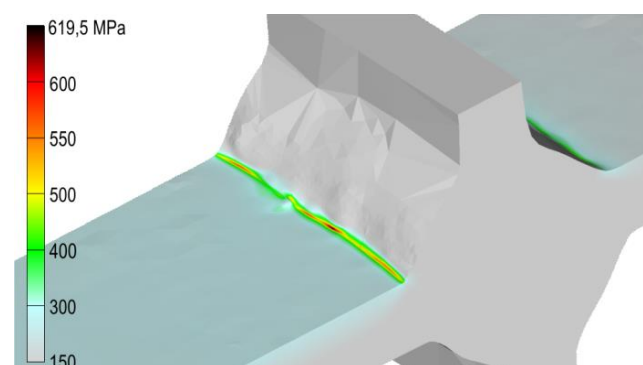


Fig. 5. Maximum principal stress  $\sigma_1$  (from superposition) distribution in specimen 2.7

Stresses resulting from straightening of the specimen due to jaw gripping do not vary in time. Hence, they can be treated as the mean value of stress courses. On the other hand, the stresses being the result only of the applied nominal stress amplitude  $\sigma_{an}$  (Tab. 1) can be treated as stress amplitudes. Finally, the following maximum normal stresses over each geometry model of specimens were calculated: (a) mean values of normal stress  $\sigma_m$  – from step (i); (b) amplitudes of normal stresses  $\sigma_a$  – from step (ii); (c) superposition of both steps (i)+(ii), i.e. maximum values  $\sigma_{max}$ . It must be notice that values of  $\sigma_{max}$  do not have to be sum of  $\sigma_m$  and  $\sigma_a$  since the normal stresses computed in steps (i) and (ii) could be on different planes and in different points.

Additionally, the hypothesis of the highly stressed volume proposed by Sosino at all., (1999) was applied to calculate stress denoted as  $\sigma_{V90}$ . According this hypothesis, the highly stressed volume is defined as the region where 90% of the maximum notch stress is exceeded (named as  $V_{90}$ ). In this case, value of a  $\sigma_{V90}$  was calculated as a mean stress value from this region. The stresses taken into this calculaion comes from  $\sigma_{max}$

(superposition). The basic material volume  $V_0$  was defined as a volume under the following condition  $\sigma_{max}(x, y, z) \geq \sigma_{an}$ . All determined and analysed stresses are presented in Tab. 2.

Tab. 2. Values of the analysed stresses

| Specimen | $\sigma_m$ , MPa | $\sigma_a$ , MPa | $\sigma_{max}$ , MPa | $\sigma_{V90}$ , MPa |
|----------|------------------|------------------|----------------------|----------------------|
| 1.1      | 147.0            | 562.9            | 591.1                | 265.8                |
| 1.2      | 35.8             | 443.2            | 443.6                | 225.4                |
| 1.4      | 115.2            | 408.1            | 466.1                | 240.5                |
| 1.5      | 127.3            | 415.3            | 481.9                | 254.4                |
| 2.3      | 194.5            | 519.6            | 704.8                | 269.9                |
| 2.5      | 143.7            | 431.1            | 573.4                | 253.3                |
| 2.6      | 141.2            | 448.3            | 589.6                | 245.6                |
| 2.7      | 162.6            | 469.9            | 619.5                | 251.7                |
| 2.8      | 150.4            | 445.4            | 582.9                | 253.6                |
| 2.9      | 41.8             | 393.4            | 410.3                | 217.7                |
| 4.1      | 86.7             | 463.0            | 549.6                | 242.7                |
| 4.5      | 101.8            | 491.4            | 578.6                | 265.6                |
| 4.8      | 147.1            | 409.2            | 515.0                | 254.9                |

## 5. CORRELATION ANALYSIS

Different stress types:  $\sigma_{an}$ ,  $\sigma_a$ ,  $\sigma_{max}$ ,  $\sigma_{V90}$  described in the previous paragraph were used in trials of correlation of the experimental fatigue lives. ASTM procedure (E739-91, 1998) was used to calculate the coefficients of regression line using double logarithmic scales:  $\log(N) - \log(\sigma)$ . Additionally, sample Pearson linear correlation coefficient  $r$  was determined for each applied stress types and fatigue lives:

$$r = \frac{\sum_{i=1}^n (x_i - \bar{x})(y_i - \bar{y})}{\sqrt{\sum_{i=1}^n (x_i - \bar{x})^2 \sum_{i=1}^n (y_i - \bar{y})^2}} \quad (1)$$

where  $y_i = \log(N_i)$ ,  $x_i = \log(\sigma_i)$ ,  $\bar{y}$ ,  $\bar{x}$  – mean values. Also the null hypothesis  $H_0$  was determined as: there is no correlation between stresses and fatigue lives ( $r=0$ ) against alternative hypothesis  $H_1$  that fatigue lives  $N$  decrease with stress values increase ( $r<0$ ).  $P$ -values using a Student's  $t$  distribution for a transformation of the correlation were calculated (MATLAB R2011b). The  $p$ -values describe the probability of rejection the true hypothesis  $H_0$  and acceptance of hypothesis  $H_1$ . The lower  $p$ -value then the correlation more statistically significantly differs from zero. Usually  $p$ -value lower than 0.05 causes rejection of the null hypothesis. For example Fig. 6 presents regression line with 0.95 probability intervals for nominal stress amplitudes  $\sigma_{an}$  and fatigue lives  $N$ . The computed correlation coefficient  $r$  is small and the more important positive which would means that increasing nominal stress amplitude the fatigue life also increases and this is against our understanding of fatigue mechanism. As a result the  $p$ -value is very high.

In Figs. 7-9 correlation between fatigue lives and the following stresses  $\sigma_a$ ,  $\sigma_{max}$ ,  $\sigma_{V90}$  are presented, respectively. Summarised values of the correlation coefficient  $r$ ,  $p$ -values and additionally the coefficients of determination  $r^2$  are presented in Tab. 3. The coefficient of determination  $r^2$  in % informs us how many points could be explained by linear relation. For example, in the  $\log(\sigma_a) - \log(N)$  relation 17.7 % of fatigue lives  $N$  is explained by linear relation with stress amplitude  $\sigma_a$ . And, taking into ac-

count the mean values  $\sigma_m$ . i.e. influence of initial deformation of specimens improves the correlation and in the  $\log(\sigma_{max}) - \log(N)$  relation. 23.7 % of fatigue lives  $N$  is explained by linear relation with maximum stresses  $\sigma_{max}$ .

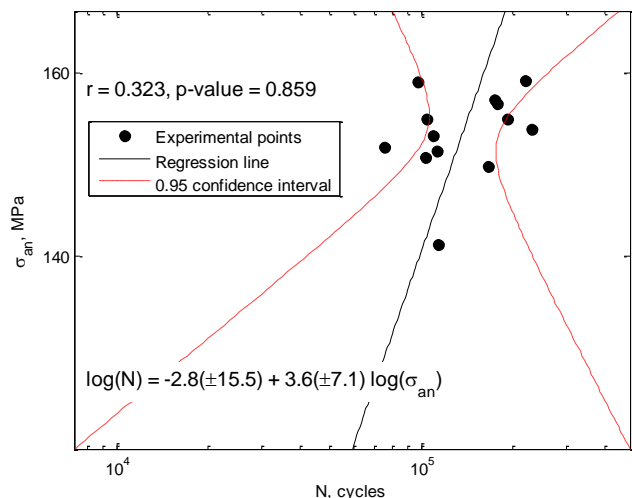


Fig. 6. Correlation between nominal stress amplitudes  $\sigma_{an}$  and fatigue lives  $N$

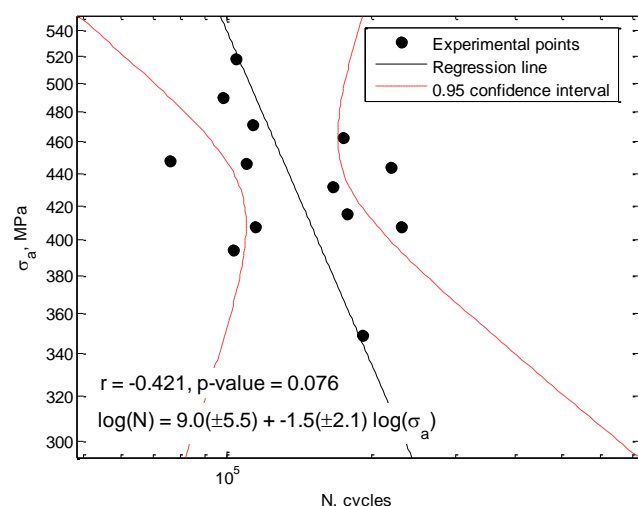


Fig. 7. Correlation between stress amplitudes  $\sigma_a$  and fatigue lives  $N$

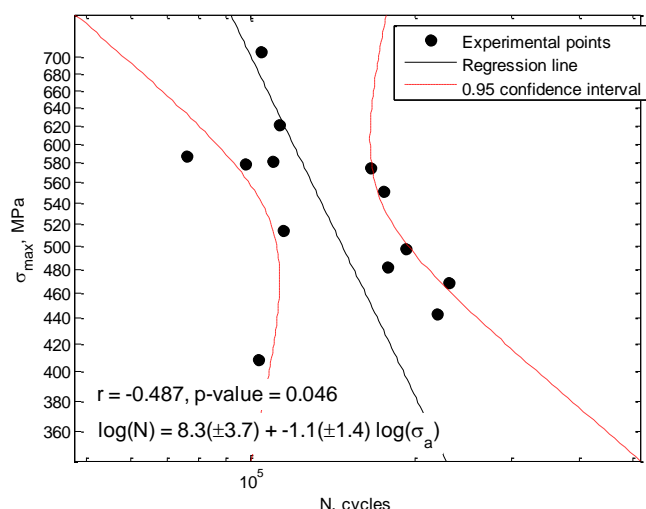


Fig. 8. Correlation between stresses  $\sigma_{max}$  and fatigue lives  $N$

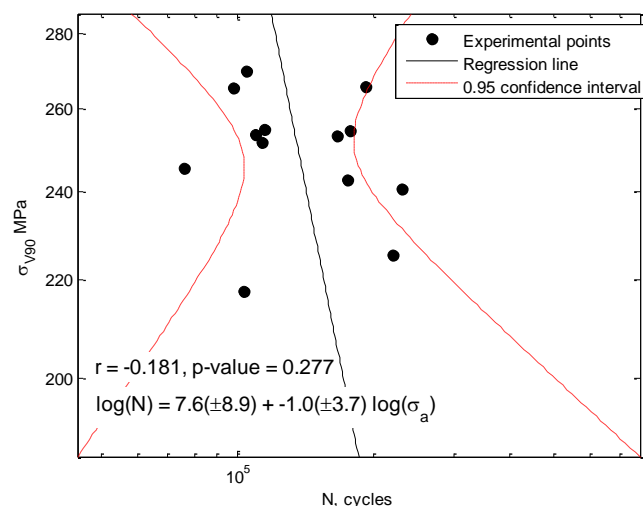


Fig. 9. Correlation between  $\sigma_{v90}$  stresses and fatigue lives  $N$

Tab. 3. Values of Pearson's correlation coefficient.  $p$ -values and coefficient of determination

| Case (log scales)            | $r$           | $p$ -value   | $r^2$ , %   |
|------------------------------|---------------|--------------|-------------|
| $\sigma_{an}$ vs. $N_{exp}$  | 0.323         | 0.859        | 10.4        |
| $\sigma_a$ vs. $N_{exp}$     | -0.421        | 0.076        | 17.7        |
| $\sigma_{max}$ vs. $N_{exp}$ | <b>-0.487</b> | <b>0.046</b> | <b>23.7</b> |
| $\sigma_{v90}$ vs. $N_{exp}$ | -0.181        | 0.277        | 3.3         |

Taking into account simple non-local method. i.e. highly stress volume approach in which averaged stress over the volume of with 10% of the highest stresses is computed did not result in sufficient correlation.

## 6. SUMMARY

- There is no correlation between nominal stress amplitudes (153.1±5.9 MPa) and fatigue lives.
- Application of maximum normal stress amplitudes values  $\sigma_a$  over the whole specimen volume  $V$  improves the correlation with fatigue lives  $N$ .
- The best and statistically significant correlation was obtained between maximum values of normal stresses  $\sigma_{max}$  and fatigue lives  $N$ . The hypothesis of non-correlation in this case is rejected at significance level  $\alpha=0.05$ .
- The correlation of fatigue lives and averaged values of normal stresses over the 10% of the highest stresses is very weak  $r=-0.181$ .
- Finally, it can be stated that local maximum values of stresses influence the fatigue life of non-load carrying cruciform steel weld joints by around 23.7%. However, for more reliable analysis the number of specimens must be increased.

## REFERENCES

1. Alam M.M., Barsoum Z., Jonsén P., Kaplan A.F.H., Häggblad H.A. (2010). The influence of surface geometry and topography on the fatigue cracking behaviour of laser hybrid welded eccentric fillet joints. *Applied Surface Science*. 256. 1936–1945.



2. **ASTM E739-91**(1998). Standard Practice for Statistical Analysis of Linear or Linearized Stress-Life (S-N) and Strain-Life ( $\epsilon$ -N) Fatigue Data. ASTM Int West Conshohocken PA 1998;03.01.
3. **Barsoum Z., Gustafsson M.** (2009). Fatigue of high strength steel joints welded with low temperature transformation consumables. *Engineering Failure Analysis*. 16. 2186–2194.
4. **Barsoum Z., Jonsson B.** (2011). Influence of weld quality on the fatigue strength in seam welds. *Engineering Failure Analysis*. 18. 971–979.
5. **Blacha Ł., Karolczuk A., Bański R., Stasiuk P.** (2013). Application of the weakest link analysis to the area of fatigue design of steel welded joints. *Engineering Failure Analysis*. 35. 665–677.
6. **Blacha Ł., Karolczuk A., Łagoda T.** (2011). Modeling of stress in welded joints under consideration of plastic strains in fatigue life calculations. *Materials Testing*. 53. 339–343.
7. **Hou C-Y.** (2007). Fatigue analysis of welded joints with the aid of real three-dimensional weld toe geometry. *International Journal of Fatigue*. 29. 772–785.
8. **Kaffenberger M., Malikoutsakis M., Savaidis G., Vormwald M.** (2012). Fatigue resistance of weld ends. *Computational Materials Science*. 52. 287–292.
9. **Kirkhoph K.J., Bell R., Caron L., Basu R.I., Ma K.-T.** (1999). Weld detail fatigue life improvement techniques. Part 1: review. *Marine Structures*. 12. 447–474.
10. **Lee C-H., Chang K-H., Jang G-C., Lee C-Y.** (2009). Effect of weld geometry on the fatigue life of non-load-carrying fillet welded cruciform joints. *Engineering Failure Analysis*. 16. 849–855.
11. **MATLAB R2011b** (2011). Statistics toolbox. version 7.6.
12. **Nykänen T., Marquis G., Björk T.** (2007) Fatigue analysis of non-load-carrying fillet welded cruciform joints. *Engineering Fracture Mechanics*. 74. 399–415.
13. **Sonsino C.M., Radaj D., Brandt U., Lehrke H.P.** (1999) Fatigue assessment of welded joints in AlMg 4.5Mn aluminium alloy (AA 5083) by local approaches. *International Journal of Fatigue*. 21. 985–999.
14. **Ting W., Dongpo W., Lixing H., Yufeng Z.** (2009) Discussion on fatigue design of welded joints enhanced by ultrasonic peening treatment (UPT). *International Journal of Fatigue*. 31. 644–650.
15. **Williams H.E., Ottsen H., Lawrence F.V., Munse W.H.** (1970) The effects of weld geometry on the fatigue behavior of welded connections. *Civil Engineering Studies*. University of Illinois Urbana. Illinois. Structural Research Series No.366.

## TESTING OF COMPOSITE PANELS USED AS COMPONENTS OF A FREIGHT WAGON BY THERMOVISION

Andrzej WRÓBEL\*, Marek PŁACZEK\*, Andrzej BUCHACZ\*

\*Faculty of Mechanical Engineering, Silesian University of Technology,  
ul. Konarskiego 18A, 44-100 Gliwice, Poland

[andrzej.wrobel@polsl.pl](mailto:andrzej.wrobel@polsl.pl), [marek.placzek@polsl.pl](mailto:marek.placzek@polsl.pl), [andrzej.buchacz@polsl.pl](mailto:andrzej.buchacz@polsl.pl)

received 22 September 2014, revised 14 December 2015, accepted 22 December 2015

**Abstract:** In this paper research methods for detection of laminate panels damage were presented. The most common damage is: matrix cracking laminate interlayer damage to joints, connecting cracks, delamination and fiber breakage. The tested laminates will be used as assemblies and sub-assemblies of freight wagon. Other methods of modeling of machines by means of transducers are shown in Placzek (2012, 2015) and Białas (2010). As part of the project authors were collaborated with specialists from other research centers and scientific research (Bocian and Kulisiewicz, 2013). As a part of future work the places where we will be able to replace the standard materials by parts made of laminate will be shown. Layered composites despite many advantages have also disadvantages. From last mentioned it is a relatively low resistance to transverse impact. When the laminate is used as a decorative element, its small damage is not a problem. The problems start when the composite satisfies more responsible tasks such as: is a part of the technical means for example of a railway wagon. Aspect of continuous monitoring of the technical state of the laminate is very important. Current technology provides numerous opportunities for non-destructive methods of technical inspections. In this paper method for testing of large areas, completely non-contact, based on the methods of thermography, was presented. It consists heating by using the composite tubes and examining it through a thermal imaging camera. Length of heating, and consequently the temperature to which the laminate is heated mostly were chosen experimentally. During the measurements, the camera measures the intensity of radiation, not temperature. Received thermogram is not always a precise representation of the actual temperature, because the camera does not reach only the radiation from tested object, but also reaches the radiation coming from the environment and reflected objects etc. As part of the research authors also we undertook other work related to Mechanical Engineering (Wróbel et al., 2008, 2010, 2012, 2013, 2015; Placzek et al., 2014). Cooperation with other national and European centers has contributed to many publications of authors for example Tuma et al. (2013, 2014) and Jamrozak and Kosobudzki (2014).

**Key words:** Thermovision, Components, Testing, Panels, Imaging Method

### 1. PRODUCTION OF THE TEST PANELS

There are several basic groups of laminates:

- one-sided: only one side has a certain esthetic values, and the second is not visible, such as for example a sink,
- double-sided: both sides must meet certain esthetic requirements, such as for example boat,
- standard: used for gluing different types of elements,
- postforming: used in the manufacture of kitchen worktops, or parts of furniture,
- floor: floor panels manufacture (Buchacz et al., 2013)

The method of production is selected depending on the type of laminate and technology, which possess a manufacturing plant. Hand lamination is the most popular method for the production of laminates among amateur applications. It is used a form, which shape is the negative of the expected shape. This form is prepared by polishing, afterwards the separatory layer is applied. For this purpose, several substances are used, the most popular is a polyvinyl alcohol (PVA), and various types of paste based on natural waxes. The application of PVA is easier and less time consuming, but during laminating the alcohol layer forms a very thin film, which can influence the surface structure. In case when

the final element is to be perfectly smooth, it is necessary to apply the wax. This operation is time consuming because of the need to impose several layers (6-7), and requirement that, after each of layer the polishing is needed. However, in case of the reuse of the form, it is sufficient only wax "refresh", by applying one or two layers. The next step is to apply the gel coat with the addition of a hardener. It is a colored resin, which imparts an aesthetic appearance and protects the laminate center from water and sunlight. This process can be done manually by brushing, or by spraying. Partial gelation of the gel coat is followed by the resin layered application, alternating with fiber glass (alternatively fiber carbon) in a form of mat or fabric. The whole should be rolled with a special knurled roller in order to remove air bubbles. If this activity is neglected, there is a high risk of delamination. After application of a certain number of layers, hardening process occurs. After a total transition into the solid state, inner layer is covered by so-called topcoat, which performs functions similar to the gel coat layer, but is no longer not so even and smooth. The final step is to split the element from the form. The method is dependent on the imagination of the operator, usually this is done with a wooden wedge and hammer.

## 2. THERMAL IMAGING METHOD

The thermal imaging method is used to examine large areas, completely non-contact, based on thermography methods. It involves heating by using the lamp of certain composite and examining it using a thermal imaging camera. Time of heating, and consequently the temperature to which the laminate is heated mostly were chosen experimentally. It depends inter alia on the thickness of laminate, reinforcement and matrix.

Thermal imaging is based on infrared radiation. The range can be divided into smaller bands contractually defined:

- near-infrared (0,75-3  $\mu\text{m}$ ),
- average infrared (3-6  $\mu\text{m}$ ),
- far infrared (6-15  $\mu\text{m}$ ),
- very far infrared (15-100  $\mu\text{m}$ ).

Thermographic studies generally use the far infrared range. During the measurements, the camera measures the radiation intensity, not temperature. By this, thermogram is not always an accurate representation of the actual temperature. These inaccuracies arise from the fact that the camera does not reach only the radiation from the test object, but also reaches the radiation coming from the environment and those reflected by the other surfaces, etc. On the quality of the measurement has also influence temperature, in which the tests are conducted. The higher, the more reliable the thermogram is. In case of advanced cameras are possible measurements up to  $-20^{\circ}\text{C}$ , but while being owner of cheaper thermal imaging camera the limit temperature is about  $-5^{\circ}\text{C}$ . In order to minimize the impact of other objects and the environment during the test, a number of camera settings should be introduced, i.e.: object emissivity, humidity, ambient temperature, the distance from an object to the camera. After introducing those information, a number of camera settings must be also changed:

- temperature range (the smaller range the more accurate differences will be seen),
- setting of the optical focal length,
- compensation of the image,
- level (expected temperature).

When there is no possibility of testing from both sides, there is a possibility to set the camera and flash from one side. In this case the way of interpretation of the results should be changed, because part of the damages in the first set is seen as stains of lower temperature, and with the other set of the camera, the same place will be seen as a stain of the higher temperature. Significant impact on the results of the research has a way of heating.

For this purpose is applied the heating:

- pulse - surface is uniformly heated by thermal pulse ,
- modulating - intensity of the heat pulse varies sinusoidally,
- pulse-phase – connection of pulse and modulation methods.

The tested element must not only be heated by lamps or radiators. For this purpose also vibrating methods are used. The tested laminate is subjected to vibrations, which through friction change the temperature (Szczepanik et al. 2008).

## 3. THERMAL IMAGING TEST OF LAMINATED PANEL

The aim of the study was to carry out non-destructive thermal imaging testing of laminate and determination of influences of the laminate properties for their analysis. The results are affected by

many factors, such as frame emissivity (color and type of surface), which carries a panel, the environment, the type of lighting and form the same panel shape, method of molding).

The present work includes several variants of the study and at the final stage, it was concluded that the factors have the most significant impact on the effect of thermal imaging diagnosis. Research has characteristics of the typical comparative method, because the goal is not to designate a specific temperature, but to determine the difference in temperature between the places where damage exists, and the places where does not. Preparation of test-bench and testing was carried out in a two-person team. Three plates with dimensions of 400x500mm with polyester matrix were performed:

### Panel no 1:

- a) Type of fiber: fiberglass mat 300g/m<sup>2</sup>,
- b) number of layers: 3
- c) the top layer: black polyester gelcoat, polished,
- d) panel thickness: 1,8 mm,
- e) the type of damage:
  - delamination resulting from the production process (bad rolling)
  - delamination created by the stroke,
  - cracks,
  - bad separation of form from the element (damage of the divider layer),
  - uneven distribution of gel coat,
  - too strong gelcoat rolling.

### Panel no. 2:

- a) Type of fiber: glass roving fabric 150g/m<sup>2</sup>,
- b) number of layers: 3
- c) the top layer: black polyester gelcoat, matt,
- d) panel thickness: 1,7 mm ,
- e) the type of damage:
  - delamination created after the stroke,
  - cracks,
  - uneven distribution of the gel coat.

### Panel no 3:

- a) Type of fiber: fiberglass mat 300g/m<sup>2</sup>,
- b) number of layers: 4,
- c) the top layer: No gelcoat,
- d) board thickness: 1,6mm,
- e) the type of damage:
  - stratification resulting from the production process (bad rolling)
  - delamination created after the stroke,
  - cracks,
  - local saturation and the unsaturation of the resin.

While preparing panels intentional errors were done. They should copy damages, that most frequently occur in laminates.

On the first panel, a number of defects associated with the uneven distribution of gel coat, scratches and small pores on the gel coat layer, formed due to poor separation of the form, are shown. Photo of the panel no. 1 from the back of the panel shows a diagonal shallow crack, some delamination and local unsaturation with resin. On the front side of the panel no 2 is not visible any defect with the naked eye, but on the back side can be seen one small delamination, from which propagate cracks. In addition,




the connections of fabric are visible and piece of the loose fiber, which was laminated as an imitation of another layer. The first panel has a shiny structure, while the second was matted by sandpaper with grit of P400. Panel no. 3 does not contain a gel coat layer, which imparts gloss, but the resin itself confers a semi-gloss structure. As a device for pulse heating halogen bulb of 500W was used. It was placed in a special housing. Lamp during the measurements was either in a stand, or was held in a hand, in order to obtain different heating method. During the study a thermal imaging camera of FLIR brand, model I7 was used.

#### 4. RESEARCH METHODOLOGY

The research was conducted using thermal imaging camera type "FLIR I7", the parameters of this camera are contained in Tab. 1.

Tab. 1. Camera "FLIR I7" parameters

| Parameter         | Value             |  |
|-------------------|-------------------|--|
| Resolution        | 140 x 140 pixels  |  |
| Sensitivity       | < 0.1°C           |  |
| Precision         | +/- 2% lub 2°C    |  |
| Temperature range | od -20°C do 250°C |  |
| Field of view     | 29° x 29°         |  |

The tested samples were inserted to the black chamber made of an open cell polyurethane foam, length of 1 meter and a width of 0.5 meter, presented in Fig. 1.



Fig. 1. The laboratory stand with tested sample placed in the black chamber

A few steps were carried out in order to eliminate measurement errors:

- a stable temperature of 21 degrees Celsius was set in the room during the measurements,
- the samples were measured in a darkened chamber (where there was no access to sunlight),
- surfaces of the samples were dry and tested samples were placed in the chamber 24 hours before testing,

- the emissivity value was exactly set.

Emissivity was calculated by using the camera. Samples were coated with a black paint with a known emissivity of 0.95. After that the surface temperature (in painted place) using a thermal imaging camera with known emissivity was measured. Indicated temperature was the reference temperature. Then the emissivity of the camera had been setting up until the temperature measurement using the thermal imager had the same effect for the area covered and uncovered paint as paint was adjusted. So the emissivity corresponded to the emissivity of the surface plate. Experiments were repeated 4 times for each sample and the results were reproducible. Because of the large number of camera images in only a few thermograms are presented in the article.

#### 5. TEST RESULTS

In case of studies with the division of laminate for parts (Fig. 2a,b.), it may be noticed more damages. Basic damage that thermography method detects is a delamination. They are visible in the case of heating from both, the front and back side, but the manner of their representation is different. If you set the lamp on the same side as the camera, delamination is seen as spots of higher temperature than the area around the damage. When the back of the laminate is heated, the thermograms show that delamination of a surface part of lower temperature. The thermogram (Fig.2) shows them as places with higher temperatures, but in addition it is surrounded by surface with lower temperature. The photos do not show the large transverse crack. It is too shallow.

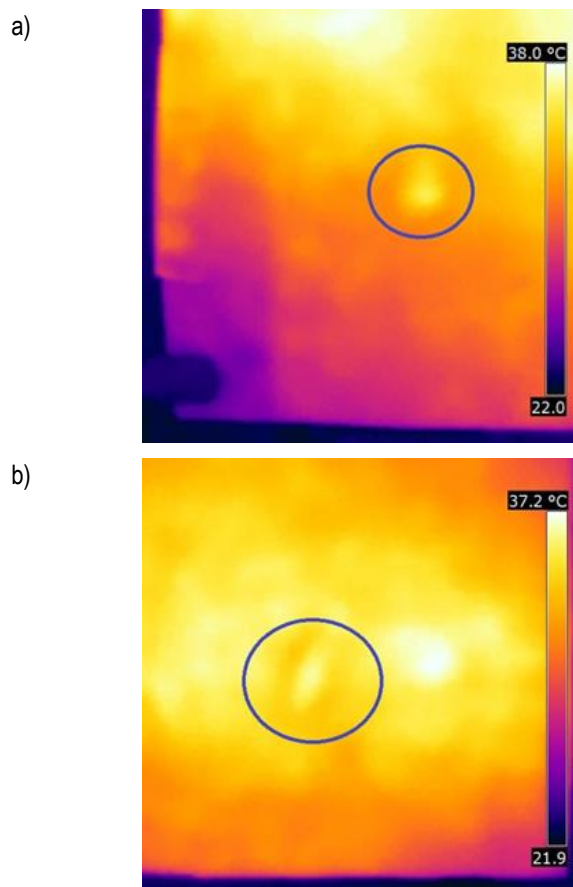
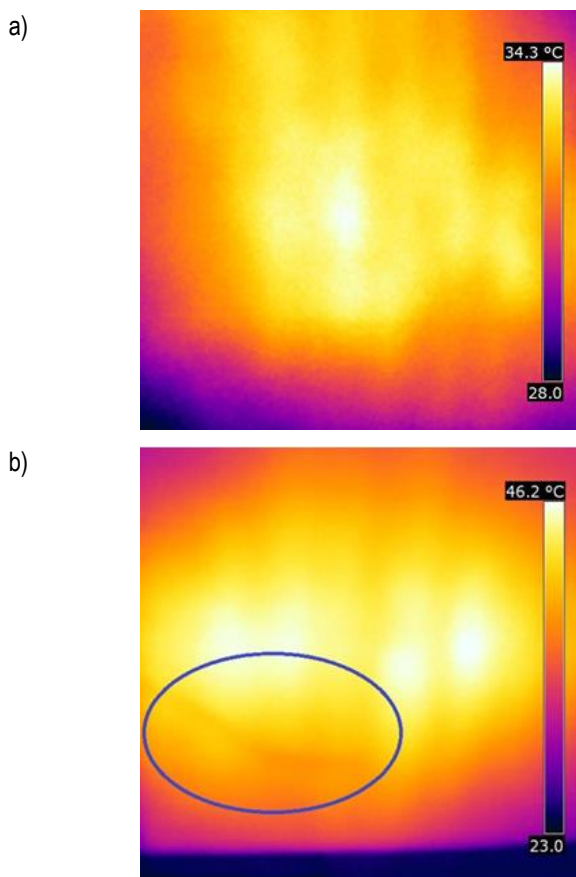


Fig. 2. The thermograms obtained while panel's testing 1: a) III quarter heated from the front, b) IV quarter heated from the front



**Fig. 3.** The thermograms obtained through the test of panel no 2:  
a) III quarter heated from back, b) IV quarter heated from back side

The thermograms shown in Fig. 3. describing a case of studies of the panel no. 2, similarly as in the case of the laminate no 1, the defects cannot be located by using photos of the entire panels. Defects are visible only in the case of the panel heating, divided into four parts. On the thermograms vertical stripes of lower temperature are visible. These are the effects of applying a gel coat with a brush. On the side edges of the paintbrush, band of the higher thickness of the gel coat were formed, which afterward were heated less. Furthermore, the thermogram presented on Fig. 3 b) shows a small delamination, but the cracks are already noticeable around it. In addition to these defects, the infrared method gives the feasibility of a change in a number of layers. An example of this is the thermogram of Fig. 3b) where it is clearly visible thin band running across the panel. This is part of the fiber that had to imitate change in the number of layers. Panel no. 2 was of much better quality than panel no 1 and for this reason, there is much less damage visible through the thermal camera.

On the thermograms obtained from testing of panel no 3, contrary to appearances, and previous studies, most can be identified on the basis of photos of sub-paragraph 3. b). It can be observed on it the band of lower temperature running on the bottom. This is an area where the amount of resin was correct. However above this place, it was too much of resin. Furthermore, the laminate no 3 contained defects in the form of the local, too small saturation of resin and it is also shown on termographs depicting the entire panels. Apart from these defects, images obtained in the case of heating from the back side, show some minor delamination. Panel damage of this panel was much more, but low emission of plate made it impossible to obtain accurate results.

The thermograms obtained while heating the front side differ from those heated from the back. This is due to the difference in emissivity of the surface, because the front was shinier (smooth) than the back. The measurement results are reproducible. During the heating and cooling plates, temperature measurement error in all the samples of the same batch does not exceed 8%.

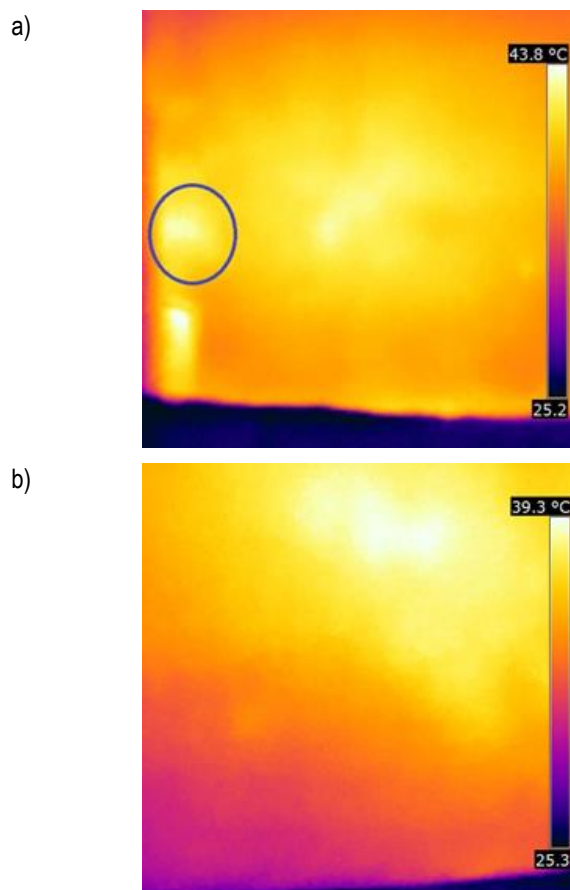


**Fig. 4.** The thermograms obtained with the test panel no 3: a) III quarter heated from back, b) IV quarter heated from back side

## 6. SUMMARY

Research of laminated panels by using thermal imaging method proved to be effective, because it was possible to determine the most places of damage. However, this method has many disadvantages, one of them is a method of heating. If you use an ordinary halogen lamp, the results can be affected, because the heat flux spreads evenly on the panel. In this situation the smartest solution would be to use an infrared lamp. These devices are designed specifically for uniform heating. Such devices often can be found in the painting workshops, where freshly painted parts placed on a special frame, are exposed on the action of several radiators. This speeds up the drying process, which enables faster processing. Optionally, for the heating purpose can be used larger number of lamps. Wise solution, in the case of the test panels with dimensions close to the analyzed samples, would be to use four lamps. In addition to equipment changes in heating appliances are used and changes of the heating method. For this purpose instead of pulse heating, modulation methods, which rely on oscillatory change of element heat can be used. It would not completely remove of uneven heating, but it would reduce its size. Heating

could be also made through the excitation of the laminate vibration, but it carries behind the need of purchasing of expensive equipment. Another disadvantage of thermal imaging studies is the fact, that at the time of the study, the element must be excluded from use. Apart from this, it is important its purity, because each dirt in a form of dust, grease, etc. may cause misrepresentation of results.

On the result of thermal testing the most significant impact had not only panel's properties itself, but the manner of trials execution and the equipment used to them. Heating of a large surface area worked only in the case of panel no 3, where it was possible to notice differences in saturation of the resin. Heating from the distance resulted in a uniformly warming up of the panel, but the process required a longer duration of lamp action. With this method of heating, the entire panel, including the center heat up evenly and it was not possible to locate the places of damage.

In the case of study of elements used in the industry, it would be wiser to use the vibration methods, where the damage is detected based on the analysis of changes in vibrations that occur when the device is in working order and when damaged. It would be necessary to laminate the piezoelectric elements to measure and control the subsequent oscillations both, passively (without additional excitation) and actively (with additional forcing).

## REFERENCES

1. **Białas K.** (2010), Passive and Active Elements in Reduction of Vibrations of Torsional Systems, *Mechatronic Systems and Materials: Mechatronic Systems and Robotics*, *Solid State Phenomena*, Vol.164, 260-264.
2. **Bocian M., Kulisiewicz M.** (2013), Method of identifying nonlinear characteristic of energy dissipation in dynamic systems with one degree of freedom, *Archives of Civil and Mechanical Engineering*, Vol. , 14 (3), pages 354-359.
3. **Buchacz A., Wróbel A.** (2010), Computer-aided analysis of piezoelectric plates, *Solid State Phenomena*, Vol. 164, 239-242.
4. **Buchacz A., Banaś W., Płaczek M.** (2015), Influence of the excitation parameters of the mechanical subsystem on effectiveness of energy harvesting system, *IOP Conf. Series: Materials Science and Engineering*, 95, pages 1-6.
5. **Buchacz A., Płaczek M.** (2014), Modelling of passive vibration damping using piezoelectric transducers – the mathematical model, *Eksploatacja i Niezawodność*, Vol. 16 (2), 301–306.
6. **Buchacz A., Płaczek M., Wróbel A.** (2013), Control of characteristics of mechatronic systems using piezoelectric materials, *Journal of Theoretical and Applied Mechanics*, Vol. 51, 225-234.
7. **Dymarek A., Dzitkowski T.** (2005), Modelling and synthesis of discrete – continuous subsystems of machines with damping, *Journal of Materials Processing Technology*, Vol. 164-165, 1317-1326.
8. **Jamroziak K., Kosobudzki M.** (2012), Determining the torsional natural frequency of underframe of off-road vehicle with use of the procedure of operational modal analysis, *Journal of Vibroengineering*, Vol. 14(2), 472-476.
9. **Kłarecki K., Hetmańczyk M., Rabsztyń D.** (2015), Influence of the selected settings of the controller on the behavior of the hydraulic servo drive, *Mechatronics - Ideas for Industrial Application. Advances in Intelligent Systems and Computing*, Vol. 317, 91-100.
10. **Ociepka P., Herbuś K., Gwiazda A.** (2014), Application of the method basing on engineering knowledge and experience for adding the hexapod design process, *Advanced Materials Research*, Vol. 1036, 1005-1010.
11. **Płaczek M.** (2012), Dynamic characteristics of a piezoelectric transducer with structural damping, *Solid State Phenomena*, Vol. 198, 633-638.
12. **Płaczek M.** (2015), Modelling and investigation of a piezo composite actuator application, *Int. J. Materials and Product Technology*, Vol. 50(3/4), 244-258.
13. **Płaczek M., Wróbel A., Baier A.** (2015), Computer-aided strength analysis of the modernized freight wagon, *IOP Conf. Series: Materials Science and Engineering*, 95, pages. 1-6.
14. **Szczepanik M., Stabik J., Wróbel G., Wierzbicki Ł.** (2008), The use of thermal imaging systems for testing of polymeric materials, *Modelowanie Inżynierskie*, 5(36), 279-286 (in Polish).
15. **Tuma J., Mahdal M., Suranek P.** (2013), Simulation Study of the non-colocated control of a cantilever beam, *Mechanics and Control*, Vol. 32, 110-116.
16. **Tuma J., Simek J., Skuta J., Los J.** (2013), Active vibration control of journal bearings with the use of piezoactuators, *Mechanical Systems and Signal Processing*, Vol. 36, 618-629.
17. **Tuma T., Suranek P., Mahdal M., Babiuch M.** (2014), Simulation of the parametric excitation of the cantilever beam vibrations, *15th International Carpathian Control Conference (ICCC)*, Velke Karlovice, Czech Republic.
18. **Wróbel A.** (2012), Kelvin Voigt's model of single piezoelectric plate, *Journal of Vibroengineering*, Vol. 14(2), 534-537.
19. **Wróbel A.** (2015), Analysis of possibility of applying the PVDF foil in industrial vibration sensors, *IOP Conf. Series: Materials Science and Engineering*, 95, pages 1-5.
20. **Wróbel A., Płaczek M., Buchacz A., Majzner M.** (2015), Study of mechanical properties and computer simulation of composite materials reinforced by metal, *Int. J. Materials and Product Technology*, Vol. 50(3/4), 259-275.
21. **Wróbel A., Langer P.** (2015), Designing of robotic production lines using CAx software, *IOP Conf. Series: Materials Science and Engineering*, 95 (2015), pages 1-6.

The work was carried out under the project number PBS2/A6/17/2013 agreement implemented under the Applied Research Program, founded by the National Centre for Research and Development.



## ACCELERATED DETERMINATION OF THE FATIGUE LIMIT AND THE S-N CURVE BY MEANS OF THE THERMOGRAPHIC METHOD FOR X5CrNi18-10 STEEL

Adam LIPSKI\*

\*Faculty of Mechanical Engineering, Department Laboratory for Research on Materials and Structures,  
UTP University of Science and Technology, Al. Prof. S. Kaliskiego 7, PL 85-796 Bydgoszcz, Poland

[Adam.Lipski@utp.edu.pl](mailto:Adam.Lipski@utp.edu.pl)

*received 8 May 2015, revised 4 February 2016, accepted 8 February 2016*

**Abstract:** A new thermographic method that enables simultaneous accelerated determination of the fatigue limit and the S-N curve was presented in this paper. The fatigue limit determination method was based on a constant rate of temperature rise occurring in second phase of the specimen fatigue life. The S-N curve determination method was based on energetic parameter with assumption of its dependency on the stress amplitude. The tests made on X5CrNi18-10 steel under reversed bending revealed that the fatigue limit value obtained from accelerated thermographic tests as compared to the value obtained from full test differs by 5.0 %. The S-N curve obtained by accelerated thermographic method fits inside 95 % confidence interval for the S-N curve obtained from full test.

**Key words:** Fatigue Limit, S-N Curve, IR Thermography

### 1. INTRODUCTION

Thanks to modern, fast and high sensitivity thermographic cameras it is possible to record surface temperature distribution of the tested object (specimen) and thus obtain among other things a new information about physical phenomena connected with loading and the change of strain state in structural members. This research focuses on phenomena related to temperature changes induced by monotone tension and compression load (i.e. Litwinko and Oliferuk, 2009; Lipski, 2014a; Lipski and Boroński, 2012) and fatigue load under both uniaxial and multi-axial loading (i.e. Doudard et al., 2007; Poncelet et al., 2010; Lipski and Skibicki, 2012; Skibicki et al., 2013). Based on these and other works it is possible to introduce new strength testing methods, including those related to the fatigue of materials and structures.

The S-N curve and the fatigue limit are basic parameters defining fatigue strength properties of the material under cyclic load, particularly in case of so called stress approach. The fatigue tests are long-lasting and expensive. For example the minimum number of specimens required to obtain the S-N curve depends on the type of test program conducted and ranges from 12 to 24 for data on design allowables or reliability data (ASTM E 739-91 (Reapproved, 2004)). The fatigue limit can be determined using the Up-and-Down method (also known as Staircase method) widely used all over the world. That method involves consecutive testing of several dozen specimens at 2-10 million cycles, which significantly influences duration of tests. A test of an individual specimen can last even several days, thus making it expensive as well. Hence researchers struggle to develop new or to improve existing methods for accelerated determining of fatigue limit. Thanks to those methods it is possible to significantly cut cost of fatigue tests by reduction of the quantity of specimens and shortening test duration.

One of proven and recognized methods of fatigue limit testing is the Locati method. Using that method it is theoretically possible to estimate fatigue limit based on a single specimen, which is gradually loaded until its failure. Analytical (computational) part of that method is based on the Palmgren-Miner's linear cumulative damage rule. However, the slope of the S-N curve must be known. The new method of fatigue limit calculation by Locati method where the slope of the S-N curve is determined on the same specimen by thermographic method was presented by Lipski (2014b).

Effects of temperature changes induced by fatigue loading can be used for development of accelerated methods for determining fatigue limit and fatigue curves. The researcher who first used thermography to explore the a surface temperature distribution of a specimen and thereby determine the fatigue limit in year 1986 was Risitano (La Rosa and Risitano, 2000). This method was used or modified, among others, in the works of Luong (1995, 1998), Cura et al. (2005) and Galietti et al. (2014). According to a similar concept, the fatigue limit is determined using the Lock-In method (Li et al, 2012, Kordatos, 2013). In these studies the fatigue limit is determined as a rule for axial load based on the assumption that there is temperature stabilization period in phase 2 of the fatigue life (Fig. 1 – line A). Luong also used Risitano methodology to determine the fatigue limit of XC55 steel under four-point rotating bending with 100 Hz of loading frequency.

The thermography can be also used to rapid determination of the fatigue curve. Fargione et al. (2002) proposed that the integration of the area under the temperature rise over the entire number of cycles of a specimen (area under line A – Fig. 1, especially under line A in phase 2) remains constant and is independent of the stress amplitude, thus representing a characteristic of the material. Amiri and Khonsari (2010a, 2010b) used the rate of temperature rise in phase 1 for prediction of fatigue failure.

However not all materials show temperature stabilization period during fatigue life in phase 2. This fact significantly limited the use of previously developed thermographic methods of rapid determination of the fatigue limit.

A new thermographic method for simultaneous determination of the fatigue limit and the S-N curve was presented in this paper. The fatigue limit determination method based on a constant rate of temperature rise occurring in phase 2 of fatigue life (Fig. 1 - line B). The S-N curve determination method is based on the parameter proposed by Fargione et al. (2002) with assumption of its dependency on the stress amplitude. Because this parameter is proportional to energy dissipated under cyclic load which is dependent on the stress level (Golański and Mroziński, 2012) then this assumption seems to be more appropriate.

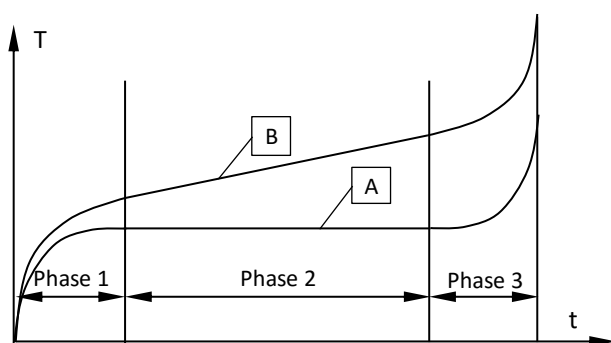


Fig. 1. The change in the temperature  $T$  during the fatigue test for material featuring phase 2 temperature stabilization (line A) and a constant rate of temperature rise (line B)

## 2. TEST DESCRIPTION

### 2.1. Test station

The tests were performed in the Department Laboratory for Research on Materials and Structures (certified by the Polish Centre for Accreditation – PCA AB 372) of the Faculty of Mechanical Engineering at the UTP University of Science and Technology using the reversed bending fatigue testing machine (with rotational frequency of 77 Hz).

The main item of the test station was the thermographic camera CEDIP Silver 420M (FLIR SC5200) equipped with high sensitivity InSb matrix cooled using Stirling pump.

Main parameters of the camera:

- resolution of sensor: 320x256 pixels, pitch 30  $\mu\text{m}$ ,
- spectral range 3.6÷5.0  $\mu\text{m}$ ,
- sensitivity below 20 mK (available: 8 mK),
- maximum frequency 140 Hz for the entire matrix (up to 25 kHz at lower resolution).

The thermographic camera recorded (at the constant frequency from 100 to 450 Hz depending on load level) the surface temperature distribution of the tested object (specimen) fixed in the testing machine. Camera images were transmitted via USB interface to PC with appropriate software, where they were digitally stored directly on HDD in form of PTW format files.

The following software was installed in the computer:

- VirtualCAM allowing two-way communication between PC and the thermographic camera via USB 2.0 interface,
- CIRBUS Front End which was the user interface used to

control the CEDIP camera,

- ALTAIR allowing downloading, storage and advanced processing of thermographic images.

### 2.2. Test specimen

Test specimens were made of cold-drawn bars from corrosion resistant austenitic X5CrNi18-10 (1.4301) steel. The proof stress for this steel  $R_{p0.2}$  is 706 MPa and the ultimate tensile strength  $R_m$  is 798 MPa.

Chemical composition of the specimen material is specified in Tab. 1.

Tab. 1. Chemical composition of the specimen material (wt %)

|                               | C     | Mn   | Si   | P      | S      | Cr      | Ni     | N     |
|-------------------------------|-------|------|------|--------|--------|---------|--------|-------|
| Acc. to PN-EN 10088-1:2014-12 | ≤0.07 | ≤2   | ≤1   | ≤0.045 | ≤0.015 | 17÷19.5 | 8÷10.5 | ≤0.11 |
| For tested specimens          | 0.02  | 1.53 | 0.61 | 0.07   | 0.016  | 18.75   | 8.22   | -     |

The geometry of applied specimens is shown in Fig. 2.

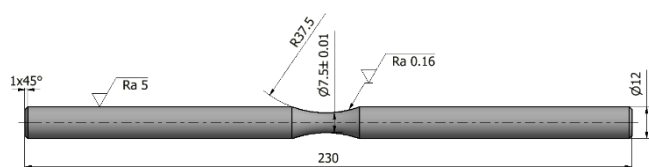


Fig. 2. Geometry of specimens used for tests

## 3. FULL TEST RESULTS

### 3.1. Fatigue limit

The fatigue limit was obtained by Staircase method assuming the base of  $10^7$  cycles. 35 specimens were tested (Fig. 3). The lowest alternating stress level  $S_0$  was 260 MPa and the stress increment  $\Delta S$  was 5 MPa. The fatigue limit obtained from Dixon & Mood relations  $S_e$  is 278.2 MPa with standard deviation  $S_s$  = 7.4 MPa.

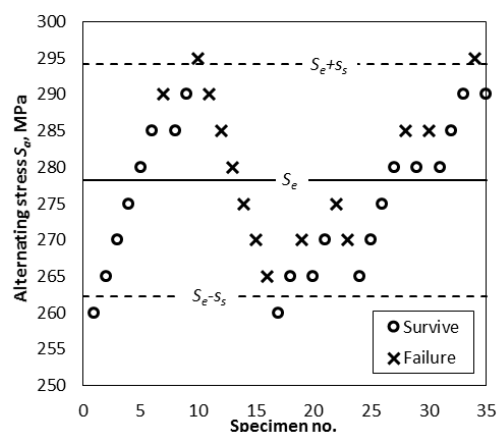


Fig. 3. The Staircase data for X5CrNi18-10 steel under reversed bending

### 3.2. S-N curve

18 specimens at 6 load levels were tested for the fatigue S-N curve determination. The lowest alternating stress level  $S_a$  was 320 MPa, the highest was 495 MPa. The test results and the S-N curve with confidence interval for the significance level  $\alpha = 0.05$  were presented in Fig. 4.

The Basquin relationship obtained from linear regression ( $R^2 = 0.98$ ) of test results is

$$S_a^m \cdot N = C, \quad (1)$$

where  $m = 10.38$  and  $C = 5.12 \cdot 10^{31}$ .

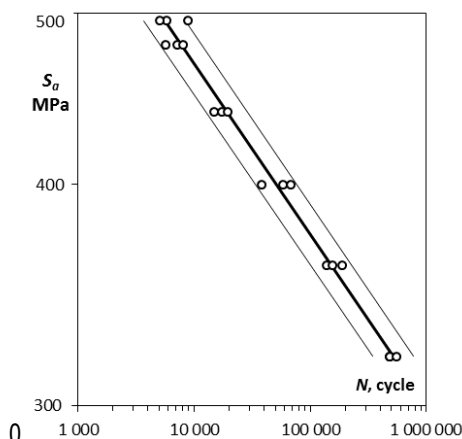


Fig. 4. The S-N curve for X5CrNi18-10 steel under reversed bending

### 3.3. Thermographic tests

12 specimens at 5 load levels were tested using thermographic camera in constant amplitude loading conditions. The lowest alternating stress level  $S_a$  was 320 MPa, the highest was 480 MPa. The change of the surface temperature of selected specimens during tests were presented in Fig. 5 where  $T = 0^\circ\text{C}$  for  $N = 0$  corresponds to initial specimen temperature of 23-25°C.

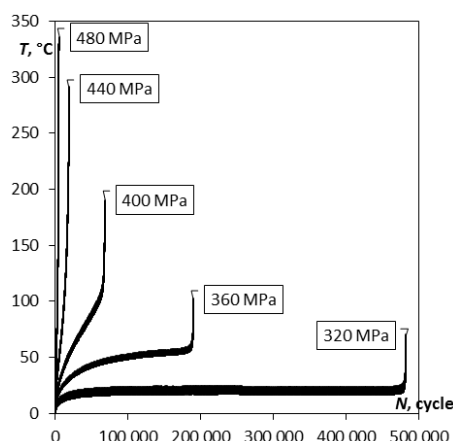


Fig. 5. Samples of the  $T - N$  curves for X5CrNi18-10 steel under reversed bending

The specimen mean temperature changes presented in Fig. 5 were generated by internal energy increase which can be estimated based on the following relation:

$$\Delta I = c_v \cdot \rho \int_0^{N_{failure}} T(N) \cdot dN, \quad (2)$$

where:  $c_v$  – specific heat at constant volume;  $\rho$  – density;  $dN$  – cycle increment;  $N_{failure}$  – number of loading cycles until fatigue failure. Because  $c_v$  and  $\rho$  are constant for specimens from the same material the internal energy change can be taken into account as the area under  $T = f(N)$  curve (Fig. 10):

$$\Phi = \int_0^{N_{failure}} T(N) \cdot dN. \quad (3)$$

The dependence of energy-related parameter  $\Phi$  on load level  $S_a$  were presented in Fig. 6. The Basquin-similar relationship obtained from linear regression ( $R^2 = 0.93$ ) of test results is:

$$S_a^k \cdot \Phi = B, \quad (4)$$

where  $k = 6.91$  and  $B = 4.03 \cdot 10^{22}$ .

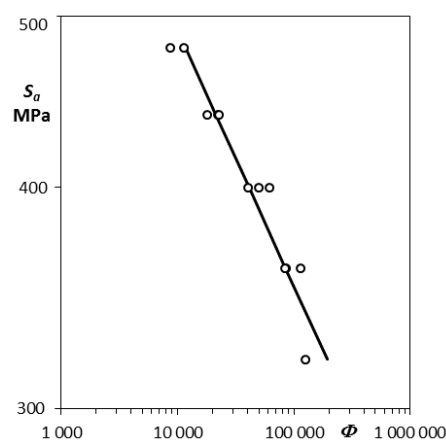


Fig. 6. The dependence of  $\Phi$  parameter on load level  $S_a$  for X5CrNi18-10 steel under reversed bending

## 4. ACCELERATED TEST RESULTS

The fatigue limit and the S-N curve were determined in one gradually increasing loading test. The lowest alternating stress level  $S_{a1}$  was 230 MPa and the stress increment  $\Delta S$  was 10 MPa.  $\Delta N$  for each load level was 30 000 cycles. The test was made at the same load frequency of 77 Hz as the full test. The change of the surface temperature of selected specimen during test was presented in Fig. 7 where  $T = 0^\circ\text{C}$  for  $N = 0$  corresponds to initial specimen temperature 19°C.

Tab. 2. Summary of fatigue life for the individual specimens from X5CrNi18-10 steel under reversed bending in the accelerated tests

|                           |       | Specimen |         |         |
|---------------------------|-------|----------|---------|---------|
|                           |       | No. 1    | No. 2   | No. 3   |
| Fatigue failure level     | $i$   | 18       | 17      | 16      |
| Failure stress, MPa       | $S_k$ | 400      | 390     | 380     |
| Total fatigue life, cycle | $N_c$ | 518 400  | 487 300 | 457 600 |

Theoretically accelerated test can be made using only one specimen, but in practice tests on three samples can increase the accuracy of estimates. Tab. 2 shows total fatigue life achieved by each sample.



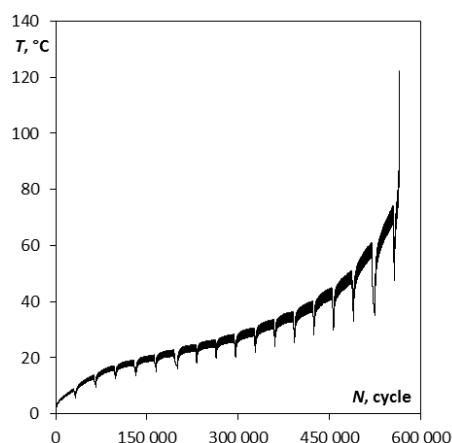


Fig. 7. Sample of the  $T - N$  curve for X5CrNi18-10 steel under accelerated test

The T-N curve (Fig. 7) obtained from gradually increasing loading test was cut into individual T-N curves for the different

load levels (Fig. 8). The reference level of the temperature was the initial temperature of the specimen.

## 5. ANALYSIS OF THE ACCELERATED TEST RESULTS

### 5.1. Fatigue limit

T-N curves for each load level  $S_a$  (Fig. 8) were examined for the temperature change rate  $\Delta T / \Delta N$ . For the period of its stabilization its average value was determined and plotted on  $\Delta T / \Delta N - S_a$  plot (Fig. 9). It can be noted that these results are characterized by the minimum that can be connected with the fatigue limit. Close to the fatigue limit the other processes of material degradation significantly affect the energy balance of the whole specimen, so that less energy will raise the temperature of the specimen. Once the fatigue limit value is exceeded, there is increase of the specimen. The temperature change rate for failure level was excluded from the analysis concerning the fatigue limit.

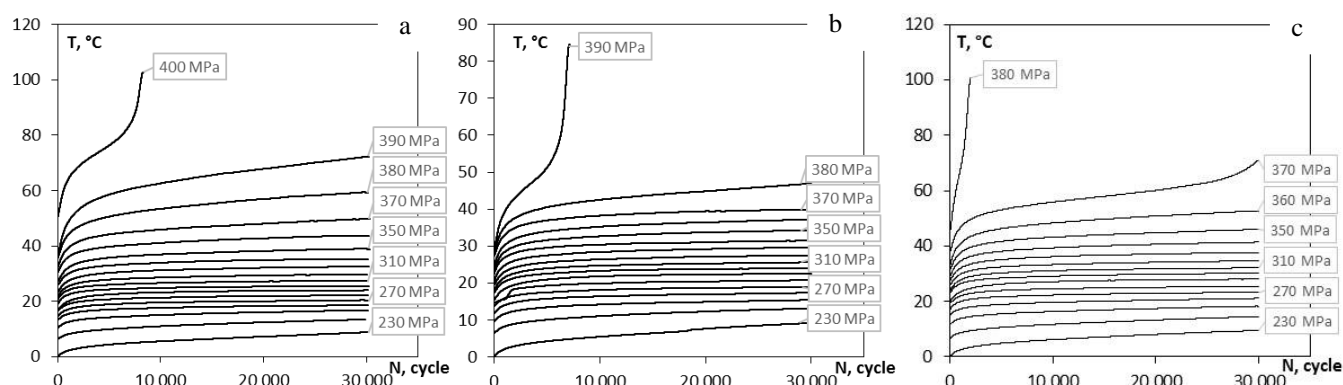


Fig. 8. Cut T-N curves for different load levels for each specimen: a) Specimen No. 1, b) Specimen No. 2, c) Specimen No. 3

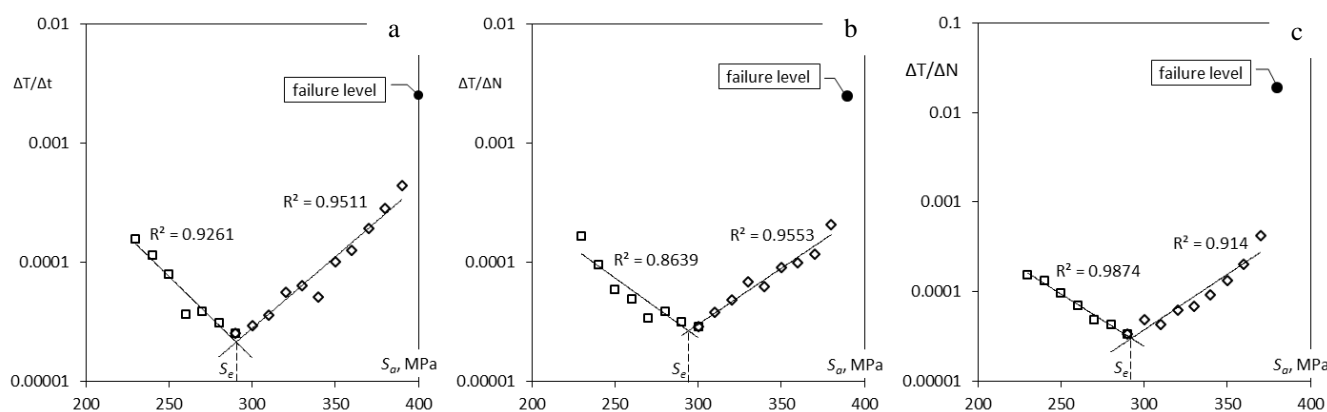


Fig. 9. The  $\Delta T / \Delta N - S_a$  plots for fatigue limit  $S_e$  determination: a) Specimen No. 1, b) Specimen No. 2, c) Specimen No. 3

Tab. 3 shows the fatigue limit obtained by the thermographic method on the base of Fig. 9 for each specimen.

Value of the fatigue limit obtained from the accelerated thermographic tests in relation to the value obtained from the full test differs by 5.0 %.

Tab. 3. Fatigue limit obtained for the individual specimens of X5CrNi18-10 steel under reversed bending in the accelerated thermographic tests

|                    |       | Specimen |       |       |
|--------------------|-------|----------|-------|-------|
|                    |       | No. 1    | No. 2 | No. 3 |
| Fatigue limit, MPa | $S_e$ | 290.4    | 294.3 | 292.4 |
|                    |       | 292.4    |       |       |

## 5.2. S-N curve

The same data used for the fatigue limit determination (Fig. 8) was used for the S-N curve determination. It was assumed that under the gradually increasing loading test at each load level only part of the total internal energy represented by parameter  $\varphi$  was measured (Fig. 10):

$$\varphi = \int_0^{N_{step}} T(N) \cdot dN, \quad (5)$$

where:  $N_{step} = \Delta N = 30\,000$  cycles.

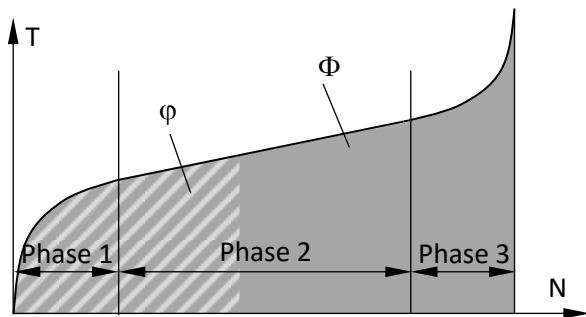


Fig. 10. Schematic representation of energy-related parameter  $\Phi$  and  $\varphi$

The Palmgren-Miner's hypothesis in its energy-related version can assume the following form (Kaleta, 1998):

$$\sum_{i=1}^q \frac{\varphi_i}{\Phi_i} = 1 \quad \text{for } S_{ai} \geq S_e. \quad (6)$$

Assuming that the relationship between energy related parameter  $\Phi_i$  for full test and load  $S_{ai}$  on level  $i$  is described by formula (4):

$$S_{ai}^k \cdot \Phi_i = B \Rightarrow \Phi_i = \frac{B}{S_{ai}^k} \quad (7)$$

and putting (7) into (6):

$$\sum_{i=1}^q \frac{\varphi_i}{\frac{B}{S_{ai}^k}} = 1 \Rightarrow \sum_{i=1}^q S_{ai}^k \cdot \varphi_i = B \quad (8)$$

is obtained:

$$\sum_{i=1}^q S_{ai}^k \cdot \varphi_i - B = 0. \quad (9)$$

where: there are two unknown parameters  $B$  and  $k$  of the  $S_a = f(\Phi)$  curve which can be determined numerically. Then it is possible to determine the values of  $\Phi_i$  at the level  $i$  by using equation (7).

Fatigue life on level  $i$  can be estimated based on the following proportions:

$$\frac{\varphi_i}{\Phi_i} = \frac{n_i}{N_i} \Rightarrow N_i = \frac{\varphi_i}{\Phi_i} \cdot n_i. \quad (10)$$

Tab. 4 shows parameters (equations (1) and (4)) obtained by presented method.

The  $S - N$  curves estimated for the individual specimens were presented in Fig. 11.

The individual estimated fatigue life data obtained from equation (10) for all three specimens has been used as a data to estimate one S-N curve (Fig. 12). It can be observed that the S-N curve obtained by the accelerated thermographic method fits inside the 95 % confidence interval for the S-N curve developed based on full test which proves good consistency of the results of

presented method.

Tab. 4. Parameters obtained for the individual specimens of X5CrNi18-10 steel under reversed bending in the accelerated thermographic tests

|                  | k     | B                    | m      | C                    |
|------------------|-------|----------------------|--------|----------------------|
| Full test        | 6.914 | $4.03 \cdot 10^{22}$ | 10.377 | $5.12 \cdot 10^{31}$ |
| Specimen No. 1   | 6.408 | $4.00 \cdot 10^{21}$ | 10.157 | $2.63 \cdot 10^{31}$ |
| Specimen No. 2   | 6.500 | $4.10 \cdot 10^{21}$ | 9.196  | $6.75 \cdot 10^{28}$ |
| Specimen No. 3   | 6.500 | $4.00 \cdot 10^{21}$ | 9.456  | $2.30 \cdot 10^{29}$ |
| Specimen No. 1-3 | -     | -                    | 9.603  | $5.87 \cdot 10^{29}$ |

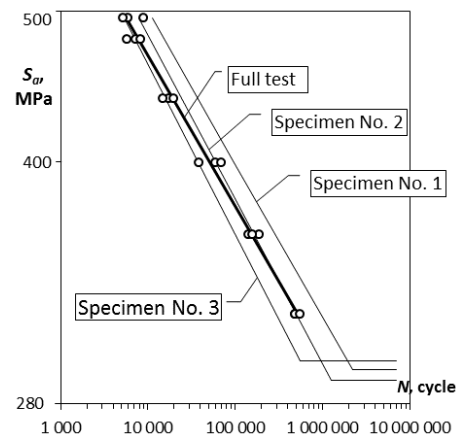


Fig. 11. The S-N curves estimated for individual specimens on the background of the full test results

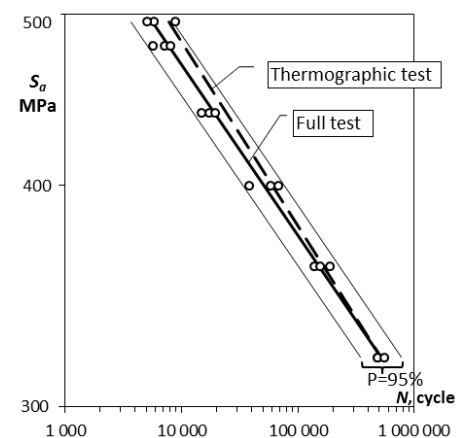


Fig. 12. Comparison of estimated S-N curve obtained by the accelerated thermographic method and the S-N curve obtained from full test

## 6. SUMMARY

The presented new thermographic method enables accelerated simultaneous determination of the fatigue limit and the S-N curve. The fatigue limit determination method is based on a constant rate of temperature rise occurring in phase 2 of the fatigue life. The S-N curve determination method is based on the energy-related parameter with the assumption of its dependency on the stress amplitude.

The tests made on X5CrNi18-10 steel under reversed bending revealed that the fatigue limit value obtained from the accelerated thermographic tests as compared to the value obtained from full test differs by 5.0 %. The S-N curve obtained by accelerated ther-

thermographic method fits inside the 95 % confidence interval for the S-N curve obtained from full test.

## REFERENCES

1. **Amiri M., Khonsari M.M.** (2010a), Life prediction of metals undergoing fatigue load based on temperature evolution, *Materials Science and Engineering A*, Vol. 527, No. 6, 1555–1559.
2. **Amiri M., Khonsari M.M.** (2010b), Rapid determination of fatigue failure based on temperature evolution: Fully reversed bending load, *International Journal of Fatigue*, Vol. 32, No. 2, 382–389.
3. **Cura F., Curti G., Sesana R.** (2005), A new iteration method for the thermographic determination of fatigue limit in steels, *International Journal of Fatigue*, Vol. 27, No. 4, 453–459.
4. **Doudard C., Poncelet M., Calloch S., Boue C., Hild F., Galtier A.** (2007), Determination of an HCF criterion by thermal measurements under biaxial cyclic loading, *International Journal of Fatigue*, Vol. 29, No. 4, 748–757.
5. **Fargione G., Geraci A., La Rosa G., Risitano A.** (2002), Rapid determination of the fatigue curve by the thermographic method, *International Journal of Fatigue*, Vol. 24, No. 1, 11–19.
6. **Galietti U., Palumbo D., De Finis R., Ancona F.** (2014), Fatigue limit evaluation of martensitic steels with thermal methods. The 12th International Conference of Quantitative Infrared Thermography, *QIRT*, Bordeaux.
7. **Golański G., Mroziński S.** (2012), Fatigue life of GX12CrMoVNbN9-1 cast steel in the energy-based approach, *Advanced Materials Research*, Vols. 396-398, 446-449.
8. **Kaleta J.** (1998), *The experimental foundations of energetical fatigue hypothesis formulation*, Wrocław University of Technology, Wrocław (in Polish).
9. **Kordatos E.Z., Dassios K.G., Aggelis D.G., Matikas T.E.** (2013), Rapid evaluation of the fatigue limit in composites using infrared lock-in thermography and acoustic emission, *Mechanics Research Communications*, Vol. 54, 14–20.
10. **La Rosa G., Risitano A.** (2000), Thermographic methodology for rapid determination of the fatigue limit of materials and mechanical components, *International Journal of Fatigue*, Vol. 22, No. 1, 65–73.
11. **Li X.D., Zhang H., Wu D.L., Liu X., Liu J.Y.** (2012), Adopting lock-in infrared thermography technique for rapid determination of fatigue limit of aluminum alloy riveted component and affection to determined result caused by initial stress, *International Journal of Fatigue*, Vol. 36, No. 1, 18–23.
12. **Lipski A.** (2014a), Impact of the Strain Rate During Tension Test on 46Cr1 Steel Temperature Change, *Key Engineering Materials*, Vol. 598, 133-140.
13. **Lipski A.** (2014b), Determination of Fatigue Limit by Locati Method using S-N Curve Determined by Means of Thermographic Method, *Solid State Phenomena*, Vol. 223, 362-373.
14. **Lipski A., Boroński D.** (2012), Use of Thermography for the Analysis of Strength Properties of Mini-Specimens, *Materials Science Forum*, Vol. 726, 156-161.
15. **Lipski A., Skibicki D.** (2012), Variations Of The Specimen Temperature Depending On The Pattern Of The Multiaxial Load - Preliminary Research, *Materials Science Forum*, Vol. 726, 162-168.
16. **Litwinko R., Oliferuk W.** (2009), Yield Point Determination Based On Thermomechanical Behaviour Of Polycrystalline Material Under Uniaxial Loading, *Acta Mechanica et Automatica*, Vol. 3, No. 4, 49-51.
17. **Luong M.P.** (1995), Infrared thermographic scanning of fatigue in metals, *Nuclear Engineering and Design*, Vol. 158, No. 2-3, 363-376.
18. **Luong M.P.** (1998), Fatigue limit evaluation of metals using an infrared thermographic technique, *Mechanics of Materials*, Vol. 28, No. 1, 155–163.
19. **Poncelet M., Doudard C., Calloch S., Weber B., Hild F.** (2010), Probabilistic multiscale models and measurements of self-heating under multiaxial high cycle fatigue, *Journal of Mechanics and Physics of Solids*, Vol. 58, No. 4, 578–593.
20. **Skibicki D., Sempruch J., Lipski A., Pejkowski Ł.** (2013), Fatigue Life, Fractographic and Thermographic Analysis of Steel X2CrNiMo17-12-2 for Proportional and Non-Proportional Loads, *The Tenth International Conference on Multiaxial Fatigue & Fracture*, Kyoto (Japan).

The publication financed by The Polish National Centre for Research and Development in the framework of the INNOTECH – IN-TECH program identified as the project No. INNOTECH-K3/IN3/32/227826/NCBR/14.

## A GROUND CONTROL STATION FOR THE UAV FLIGHT SIMULATOR

Sławomir ROMANIUK\*, Zdzisław GOSIEWSKI\*, Leszek AMBROZIAK\*

\*Department of Automatic Control and Robotics, Faculty of Mechanical Engineering, Białystok University of Technology,  
ul. Wiejska 45C, 15-351 Białystok, Poland

[s.romaniuk@doktoranci.pb.edu.pl](mailto:s.romaniuk@doktoranci.pb.edu.pl), [z.gosiewski@pb.edu.pl](mailto:z.gosiewski@pb.edu.pl), [l.ambroziak@pb.edu.pl](mailto:l.ambroziak@pb.edu.pl)

received 13 July 2015, revised 3 February 2016, accepted 8 February 2016

**Abstract:** In the paper implementation of a ground control station for UAV flight simulator is shown. The ground control station software is in cooperation with flight simulator, displaying various aircraft flight parameters. The software is programmed in C++ language and utilizes the windows forms for implementing graphical content. One of the main aims of the design of the application was to simplify the interface, simultaneously maintaining the functionality and the eligibility. A mission can be planned and monitored using the implemented map control supported by waypoint list.

**Key words:** Ground Control Station, Flight Simulator

### 1. INTRODUCTION

Having miniaturized wide scope of measurement and communication devices and reduced costs of propelling devices, relatively cheap Unmanned Aerial Vehicles (UAVs) development has intensified. Trend of utilizing autopilot's capabilities for performing different applications of UAVs is arising. Contemporary autopilot systems are able to stabilize object's rotary motion along all three axes corresponding to pitch, roll and yaw angles. Those basic abilities allows implementing more complicated routines such as autonomous starting and landing, navigation through desired waypoints, circulation around given point. Furthermore unmanned aerial vehicles may be equipped with many different measurement devices, cameras, and miscellaneous sensors. Hence by the aggregation of mentioned elements it is possible to plan different UAV's missions for many modern appliances e.g. searching for lost. Although a number of adoptions is possible, there is additional necessity for some kind of supplementary system which would give final user the eventuality of planning, monitoring and controlling the UAV. This system may be represented by ground control station (GCS).

Ground control station may have many different capabilities, however there are few that are usually implemented. One of the requirement that GCS is usually bound to fulfill is acquiring and displaying data relating UAV flight parameters, which may be showed as text or visualized through different graphical elements. Furthermore ground control station should have the possibility of steering the UAV behavior by sending appropriate configuration and control commands to it.

As the one of the main components of any Unmanned Aerial System (UAS), ground control station serves as the device, the user can monitor and control UAV through. Hence it has to be as intuitive and clear as possible, to decrease the overall operator workload and improve operational parameters such as reaction time of the operator.



Fig. 1. The "FlightGear" application (Zachary et al., 2013)

There is unextinguished work to increase the functionality of ground control station, since they are reliable for successful mission accomplishment of unmanned aerial vehicles. Hence the adoption of multimodality has occurred in order to improve the interaction quality between the operator and GCS. Elements like text-to-speech synthesis, voice recognition, three dimensional



projection may be useful in decreasing the operators workload and effort. Nevertheless addition of such communication channels should be properly designed, otherwise it can redound to undesirable overload of incoming information (Perez et al., 2013).

There are commercial ground control stations like the one by Airware (<http://www.airware.com/>). Likewise they are quite a few open-source projects like OpenPilot Ground Control Station (<http://www.openpilot.org/>) or the QGroundControl (<http://www.qgroundcontrol.org/>). However usage of aforementioned ground control station projects has disadvantages. One of the problem that arises, involves adapting them into system performing assumed tasks.

The direct implementation of ground control station for chosen autopilot system would be time demanding, awkward and weather dependent, since programming of such software requires constant interaction with target device. Furthermore many changes would have to be verified during the flight, causing additional inconveniences. Hence ground control station depicted hereafter is based on the flight simulator. This approach excludes the need of using communication devices, because both, the ground control station and the flight simulator may run on the same computer. Moreover by means of using flight simulator it is possible to achieve aerial situations that are dangerous, hard to perform or even unreachable with real objects.

## 2. SYSTEM ARCHITECTURE

The flight simulator software, a ground control station software and the computer those programs run on, are the elements of the validation system.

FlightGear (<http://www.flightgear.org/>) is the program used as the flight simulator component. It is an open-source program, that has different versions supporting many popular platforms (Windows, Linux, Mac). FlightGear was created as the simulation tool that can be used as the pilot training software, industry engineering tool. Nevertheless it can be used in the academic applications due to its implementation of many different aircrafts dynamic models. Furthermore FlightGear allows communication with individual software programs as well as external devices through network socket connection. This simulator allows previewing the flight from both inside and outside of the aircraft (Fig. 1). Moreover adverse weather effects such as wind may be simulated, giving the potentiality of aircraft's behavior assessment in the extreme conditions (<http://www.flightgear.org/>).

Ground control station is basing on the data acquired from the flight simulator. These programs are utilizing the TCP in order to communicate each other. The ground control station starts first before the flight simulator for the creation of a server. In the next step the starting flight simulator connects to the previously created server. Followed by the connection of the GCS to the flight simulator. When the connection is successfully established, FlightGear sends output data in the predefined form. It can output many various parameters ranging from the position and orientation ones through gear and onboard systems states, engines speeds, control surface positions ending with velocities and accelerations. Parameters that are demanded at the output may be arbitrarily adjusted according to the current needs, by means of the configuration file. Moreover there is possibility of modifying the frequency at which the program actualizes the output. It was necessary to implement adequate class, which is responsible for TCP connection and packets recognition for data acquisition.

## 2.1. Transmission Control Protocol

Transmission Control Protocol (TCP) is the transport layer protocol. TCP is responsible for the correctness of transmitted data. It is situated just above a basic Internet Protocol (IP). TCP utilizes IP for sending and receiving variable-length segments of information. Furthermore internet protocol provides ability of reassembling fragmented TCP segments, assuring delivery through multiple networks (<http://www.tools.ietf.org/html/rfc793>, <http://www.students.mimuw.edu.pl/SO/Linux>). In the following work TCP is used to maintain communication between the application of ground control station and the flight simulator.

## 3. GROUND CONTROL STATION DESIGN

The ground control station was designed in order to improve operator's awareness of UAV's current situation. Moreover the system was aimed to be operated by a single user, enabling him to control UAV missions with little effort. The overall design of the graphical interface had to be kept on the simple form. It was achieved by placing constituent elements in the organized form, which simultaneously display as well as visualize a set of important flight parameters.

In the proposed design of ground control station, many different elements presenting basic flight parameters are included. Some of these parameters are visualized, in order to increase their eligibility, while the rest of them are displayed in the form of numbers.

The ground control station software was programmed in the C++ language utilizing the standard WinApi libraries. This approach gave possibility of running the mentioned program on Windows class systems. Well documented WinApi libraries allow convenient development of various application providing access to many basic system resources including file systems, devices, network services, graphical user interfaces, error handling (<http://msdn.microsoft.com/en-us/library>). However the graphical content of WinApi provides functions for drawing some basic geometric figures, hence there was necessity of writing own classes for creating and updating controls that visualize current orientation and position of the monitored aircraft.

Ground control station window is divided into two main areas, each of which contains a set of different controls.

### 3.1. Aircraft area

Aircraft area that is located at the left side of GCS window presents some basic information of the aircraft's current orientation and position. Attitude of the object is presented in the three consequent indicators that visualize pitch, roll and yaw respectively. Pitch and roll indicators look similarly. They consist out of an circle inside of which aircraft's graphical visualization is presented. At the outside of that circle, short lines with adequate numbers are placed in order to preview the aircraft's inclination. Numbers are placed in the way that their center of symmetry covers the center of the previously mentioned circle.

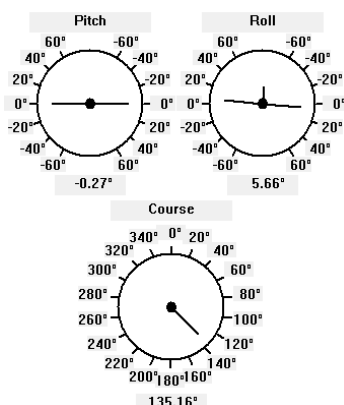


Fig. 2. Pitch, roll and yaw indicators

That approach increases the user awareness of the current aircraft orientation, by enabling him indicating the pitch and roll angles from both sides respectively. At the bottom of each indicator the field displaying amending value of pitch and roll angles respectively is placed. The general yaw indicator outlook is almost the same as pitch and roll ones except that, the numbers indicating the course angle are ranged from 0° up to 360°.

In the next section of the aircraft's area, parameters of the aircrafts orientation and position are displayed in the form of list.

At the first, pitch, roll and yaw angles are presented. They are displayed both in the degrees and in the radians, however angles with degrees units are slightly less precisely presented than in the foregoing indicators. Subsequently the velocity values are displayed both in the km/h and in the m/s units. Values of latitude, longitude and height are displayed at the end of the list alternately. Latitude and longitude are shown in two forms: degrees only one and degrees, minutes, seconds alternative one.

| Parameters |             |    |                |
|------------|-------------|----|----------------|
| Pitch:     | -0.3 °      | -> | -0.00 rad      |
| Roll:      | 5.7°        | -> | 0.10 rad       |
| Yaw:       | 135.2°      | -> | 2.36 rad       |
| Velocity:  | 276.1 km/h  | -> | 76.7 m/s       |
| Latitude:  | 37.71488°   | -> | 37° 42' 53"    |
| Longitude: | -122.31856° | -> | -122° -19' -6" |
| Height:    | 1151.6 m    |    |                |

Fig. 3. Aircraft's flight parameters section

Afterwards values of elevator, ailerons, rudder and flaps position are presented in the last section of the aircraft area. These values are ranged from -100 % to 100% and are representing maximum deflection in opposite directions. Number of digits that are displayed may be adjusted in order to increase or decrease the precision.

| Control surface positions |        |
|---------------------------|--------|
| Elevator:                 | 6.6 %  |
| Ailerons:                 | 27.6 % |
| Rudder:                   | -3.6 % |
| Flaps:                    | 0.0 %  |

Fig. 4. Aircraft's control surface positions section

## 3.2. Map area

Map area contains, as the name suggests, the visualized waypoints, but it is not the only one element displayed. Additionally this area includes the list of waypoints, three fields to type in new coordinates and a button for adding a new waypoint.

On the edges of the map, latitude and longitude in the degrees form is presented respectively at the left side and at the bottom of the map. On opposite sides of the map, those parameters represented in the meters units are shown. Map is displaying two types of points. First of them is black thick circle with a black short line. Those show current position and course of the aircraft. The other type of point is a red thin circle. A set of this points represents the position of inflicted waypoints. While the aircraft moves, it leaves a black thick line on the map which is drew to indicate aircraft's travelled path.

The map visualization allows planning aircrafts route. Moreover it is possible to add new waypoints by right-clicking on the map, which is an alternative to adding the waypoints by typing their coordinates in.

Below the map list of existing waypoints is presented. List has elements that consist of latitude, longitude and height values, given in degrees and meters units respectively, separated by comma character. List of the waypoints is aided with three fields that allow specifying latitude, longitude and height of newly created waypoint, and the button that is used to confirm addition of the new waypoint. New waypoint is placed at the end of the list of waypoints.

All the waypoints are managed by the autopilot. Application of the ground control station sends requests, with coordinates, to the autopilot in order to add new waypoint.

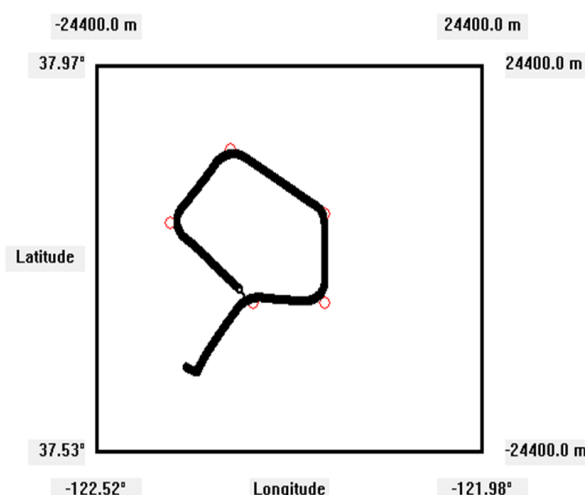


Fig. 5. Ground control station's map

In the navigation section parameters according control of the UAV route are presented. An alpha angle is the angle to the previous waypoint from the current one, whilst the beta angle is the angle to the next waypoint determined from the current waypoint. Gamma angle is the bisector of the alpha and beta angles. Phi angle is the sum of two angles. First one is the value calculated from the characteristic point placed on the bisector to the current position of aircraft, while the other one is  $\pi/2$ . Distance is determined from the current aircraft position to the current waypoint.

|         |           |          |
|---------|-----------|----------|
| 37.800, | -122.100, | 1150.000 |
| 37.800, | -121.800, | 1000.000 |
| 38.100, | -121.800, | 1250.000 |
| 38.321, | -122.136, | 1500.000 |
| 38.022, | -122.393, | 1500.000 |

|     |     |     |
|-----|-----|-----|
| 0.0 | 0.0 | 0.0 |
|-----|-----|-----|

**ADD WAYPOINT**

Fig. 6. List of the set waypoints with controls for adding new one

Presented GCS has the possibility of logging achieved data into file. Basing on the information from this file it is possible to further analyze, post-process the flight parameters of the aircraft.

#### 4. GROUND CONTROL STATION TESTING

In order to examine and present the capabilities of designed GCS, test flight has been performed. The chosen aircraft model was Diamond DA40, which model can be adopted as the UAV platform. It is an 8.1 m long, 1.98 m high civil aircraft which can cruise at the speeds of up to 279 km/h, and has range of around 1341 km and wingspan of 11.9 m (<http://www.diamondaircraft.com/>).

The aircraft has flew along the arranged route, which was defined by means of waypoints. Preview of the preset waypoints is presented on the map while their coordinates are detailed in the waypoint list. Three of the waypoints were predefined in the software, while the other were added using the ground control station interface. First two were inserted utilizing the ability of map right click addition. Rest of them were configured by typing in their coordinates in three corresponding fields rightly and confirming with adequate button. Having configured the path, "START" button was pressed to commence the flight.

When the aircraft started it became apparent that change in monitored object course as well as position is visible on the map. When the aircraft flew along the desired route it left marks on the map indicating a history of its antecedent positions. Additionally the precise information of aircrafts position and attitude was on an ongoing basis actualized. Test evidenced that graphical content representing pitch, roll and yaw angles, is helpful in raising the awareness of aircrafts attitude. Besides the control surface position area is useful in understanding the correlation between them and the movement of the aircraft and may be useful in future development of autopilot system. Some of parameters are displayed with two different units increasing their usefulness.

#### 5. CONCLUSIONS

The presented design of ground control station allows not only monitoring current position and attitude of the aircraft through utilization of different controls, but planning the aircrafts route and

adding new waypoint to it as well. The favorable side of the design lies on both, visualization and display of the monitored parameters. While the visualization gives coarse but swiftly and effortlessly understandable information, distinct controls display it in more precise way.

Having accomplished the design of ground control station it is possible to further improve its content by editing or adding new elements. It is possible to add three dimensional map which will increase the functionality of existing one by adding the information of the height (Siebert and Teizer, 2014). Furthermore 3D map gives the opportunity of visualizing modeled objects like buildings, trees and other obstacles which role is significant in the context of route planning. If the autopilot will be concerned, the possibility of adding features such as controller gains tuning window and graphs plotting window is arising. Likewise the performed ground control station may be helpful in the development process of an autopilot system for the needs of flight simulator (Cetin et al., 2011).

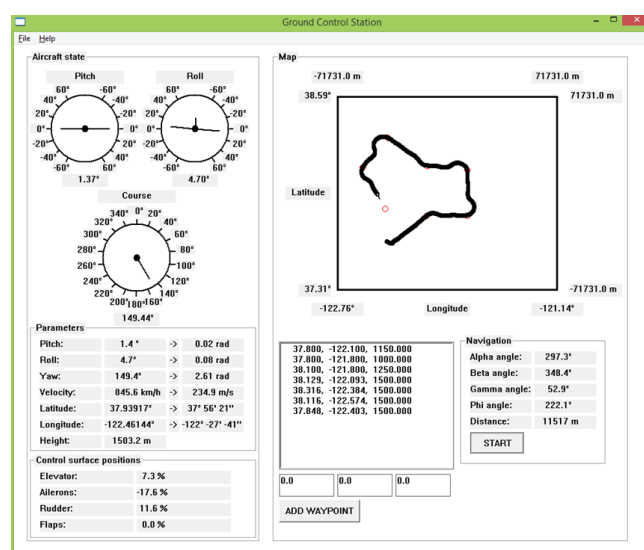


Fig. 7. Ground control station during the testing

Created GCS on the basis of flight simulator, may be further easily adopted to cooperate with real aircrafts, allowing taking control over their autopilots. This alteration may be a significant step in creating a complex unmanned aerial system consisting of aircraft, its autopilot and GCS itself. Aforementioned software may be further developed to suit specific mission requirements (Han et al., 2013). The adaptation can involve extension of the GCS functionalities to video stream handling, sensor data visualization, control over auxiliary onboard devices, cooperation with terrestrial system.

Future work may also be based on the conception of multi UAV systems, extending the capabilities of the presented ground control station for monitoring and controlling several of them (Boccalatte et al., 2013; Zheng et al., 2004; Dydek et al., 2013; Garcia et al., 2010; Sahingoz et al. 2014). The maximum number of different UAVs that can be supervised is limited by the operators workload capabilities and the design of ground control station. Systems that consist of multi unmanned aerial vehicles can hasten the mission realization, decrease the influence of time-dependent factors e.g. weather and increase the success plausibility. Furthermore this approach gives the possibility of realizing tasks that can't be performed by single UAV, or assuring mission

continuity in the case of low energy level of operating unmanned aerial vehicle (Damilano et al., 2013; Maza et al., 2010; Perez et al., 2013).

## REFERENCES

1. **Boccalatte M., Brogi F., Caltafamo F., Maddaluno S., Martino M., Mellano V., Rosazza P. P., Solitro F., Torasso P., Torta G.** (2013), A multi-UAS cooperative mission over non-segregated civil areas, *Journal of Intelligent and Robotic Systems*, 70, 275-291.
2. **Cetin O., Kurnaz S., Kaynak O.** (2011), Fuzzy logic based approach to design of autonomous landing system for unmanned aerial vehicles, *Journal of Intelligent and Robotic Systems*, 61, 239-250.
3. **Damilano L., Guglieri G., Quagliotti F., Sale I., Lunghi A.** (2013), Ground control station embedded mission planning for UAS, *Journal of Intelligent and Robotic Systems*, 69, 241-256.
4. **Dydek Z. T., Annaswamy A. M., Lavretsky E.** (2013), Adaptive configuration control of multiple UAVs, *Control Engineering Practice*, 21, 1043-1052.
5. **Garcia R., Barnes L.** (2010), Multi-UAV simulator utilizing X-Plane, *Journal of Intelligent and Robotic Systems*, 57, 393-406.
6. **Jinlu H., Yaojin X., Long D., YangQuan C.** (2013), Low-cost multi-UAV technologies for contour mapping of nuclear radiation field, *Journal of Intelligent and Robotic Systems*, 70, 401-410.
7. **Maza I., Kondak K., Bernard M., Ollero A.** (2010), Multi-UAV Cooperation and Control for Load Transportation and Deployment, *Journal of Intelligent and Robotic Systems*, 57, 417-449.
8. **Perez D., Maza I., Caballero F., Scarlatti D., Casado E., Ollero A.** (2013), A ground control station for a multi-UAV surveillance system, *Journal of Intelligent and Robotic Systems*, 69, 119-130.
9. **Sahingoz O. K.** (2014), Generation of Bezier Curve-Based Flyable Trajectories for multi-UAV systems with Parallel Genetic Algorithm, *Journal of Intelligent and Robotic Systems*, 74, 499-511.
10. **Siebert S., Teizer J.** (2014), Mobile 3D mapping for surveying earthwork projects using an Unmanned Aerial Vehicle (UAV) system, *Automation in Construction*, 41, 1-14.
11. **Zheng C., Ding M., Zhou C., Li L.** (2004), Coevolving and cooperating path planner for multiple unmanneed air vehicles, *Engineering Applications of Artificial Intelligence*, 17, 887-896.
12. <http://msdn.microsoft.com/en-us/library>
13. <http://www.airware.com/>
14. <http://www.diamondaircraft.com/>
15. <http://www.flightgear.org/>
16. <http://www.openpilot.org/>
17. <http://www.qgroundcontrol.org/>
18. <http://www.students.mimuw.edu.pl/SO/Linux>
19. <http://www.tools.ietf.org/html/rfc793>

Acknowledgements: The researchers are financed by Bialystok University of Technology as the own work (No. MB/WM/16/2014).



# PLASTIC MECHANISMS FOR THIN-WALLED COLD-FORMED STEEL MEMBERS IN ECCENTRIC COMPRESSION

Viorel UNGUREANU<sup>\*,\*\*</sup>, Maria KOTELKO<sup>\*\*\*</sup>, Jan GRUDZIECKI<sup>\*\*\*</sup>

<sup>\*</sup>Department of Steel Structures and Structural Mechanics, Politehnica University of Timisoara, Ioan Curea 1, 300224 Timisoara, Romania

<sup>\*\*</sup>Laboratory of Steel Structures, Romanian Academy – Timisoara Branch, Mihai Viteazu 24, 300223 Timisoara, Romania

<sup>\*\*\*</sup>Department of Strength of Materials, Łódź University of Technology, ul. Stefanowskiego 1/15, 90-924 Łódź, Poland

[viorel.ungureanu@upt.ro](mailto:viorel.ungureanu@upt.ro), [maria.kotelko@p.lodz.pl](mailto:maria.kotelko@p.lodz.pl), [jan.grudziecki@p.lodz.pl](mailto:jan.grudziecki@p.lodz.pl)

received 20 October 2015, revised 8 February 2016, accepted 10 February 2016

**Abstract:** The Eurocode 3 concerning thin-walled steel members divides members subjected to compression into four classes, considering their ductility. The representatives of the class C4 are short bars, for which the load-capacity corresponds to the maximum compression stresses less than the yield stress. There are bars prone to local buckling in the elastic range and they do not have a real post-elastic capacity. The failure at ultimate stage of such members, either in compression or bending, always occurs by forming a local plastic mechanism. This fact suggests the possibility to use the local plastic mechanism to characterise the ultimate strength of such members. The present paper is based on previous studies and some latest investigations of the authors, as well as the literature collected data. It represents an attempt to study the plastic mechanisms for members in eccentric compression about minor axis and the evolution of plastic mechanisms, considering several types of lipped channel sections.

**Key words:** Plastic Mechanism, Eccentric Compression

## 1. INTRODUCTION

Eurocode 3 (1993) concerning thin-walled steel members divides members subjected to compression into four classes, considering their ductility. Class C1 concerns bars, in which global plastic hinges may develop entirely, so that they have a relatively large redundancy of the load-capacity above the fully plastic moment  $M_p$  of the total cross-section. To class C2 belong bars, for which load-capacity is slightly higher than the fully plastic moment, to class C3 – bars, for which the load-carrying capacity is situated in the elasto-plastic range. It means, that their load-capacity is determined by the “first yield criterion” ( $M_{pl}$ ).

The code distinguishes also the class C4 of short bars, for which the load-capacity corresponds to the maximum compression stresses less than the yield stress. There are bars prone to local buckling in the elastic range.

It is very well known that thin-walled cold-formed steel structures (TWCFSS) are usually made of thin-walled members of class 4 sections and they are characterised by a reduced post-elastic strength and by a reduced ductility. Since these sections are prematurely prone to local or distortional buckling and they do not have a real post-elastic capacity, a failure of such members is initialized by the local-global interactive buckling of plastic-elastic type, not an elastic-elastic one. Thus, the failure at ultimate stage of those members, either in compression or bending, always occurs by forming a local plastic mechanism (Eurocode 3, 1993) – Fig. 1. This fact suggests the possibility to use the local plastic mechanism analysis to characterise the ultimate strength of such members (their load-carrying capacity). Load-capacity of such members subjected to simple states of loading (pure bending or pure axial compression) is relatively well determined

(with high accuracy) both on the basis of the theory of thin-walled structures and in the code specifications. However, determination of the load-capacity of TWCFSS members subjected to combined load, particularly eccentric compression) is still an open question and the code specifications for that case should be improved.

The yield line mechanism analysis has been widely used to study steel members and connections that involve local collapse mechanisms. This method can be used to study post-elastic behaviour, load-carrying capacity, ductility, rotation capacity and energy absorption. A detailed history of yield line mechanism theory has been presented by Zhao (2003). An art review of the application of yield line analysis to cold-formed members has been presented by Hiriyur and Schafer (2004) and Ungureanu et al. (2010) make an inventory, classify and range geometrical and analytical models for the local-plastic mechanisms aiming to characterize the ultimate capacity of some of the most used cold-formed steel sections in structural applications.

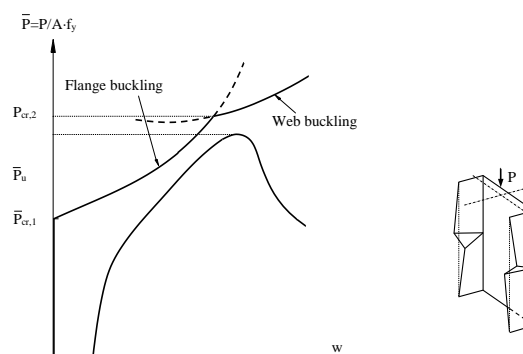


Fig. 1. Structural behavior of short TWCFSS member and exemplary plastic mechanism of failure

## 2. SUBJECT AND OBJECTIVES OF THE ANALYSIS

Subject of the analysis are TWCFSS members subjected to eccentric compression about minor axis, namely lipped channel section columns (Fig.2.). Positive and negative eccentricities along the symmetry axis are investigated, i.e.  $e = -10$  mm,  $-5$  mm,  $-2$  mm,  $-1$  mm,  $0$  mm,  $+1$  mm,  $+2$  mm,  $+5$  mm,  $+10$  mm and  $+20$  mm.

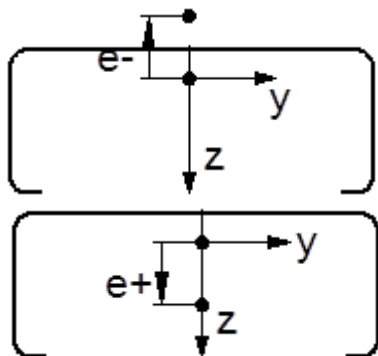


Fig. 2. Lipped channel section with examples of considered eccentricities

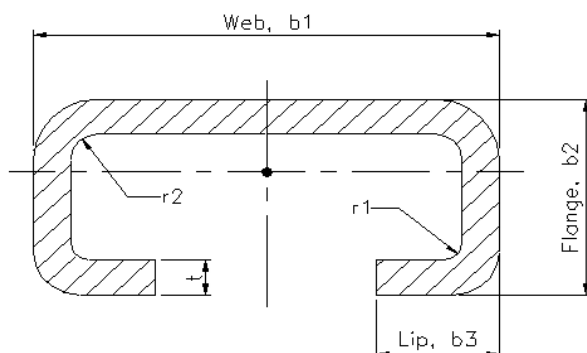


Fig. 3. Lipped channel cross section column dimensions:  $b_1 = 150$  mm,  $b_2 = 60$  mm,  $b_3 = 20$  mm,  $r_1 = 1$  mm,  $r_2 = 1$  mm,  $t = 1$  mm

Columns of length  $L = 450$  mm were investigated, made of structural steel of yield stress  $\sigma_Y = 355$  MPa and with the cross section shown in Fig. 3.

Present paper is based on previous studies and some latest investigations of authors, as well as the literature collected data. It represents an attempt to study the plastic mechanisms for members in eccentric compression.

The approach is a numerical one (FE analysis), in order to identify the plastic mechanisms of members subjected to eccentric compression about minor axis and the evolution of plastic mechanisms, considering several different eccentricities, which cause either flange or web compression and lead to an evolution of different local plastic mechanisms.

## 3. PLASTIC MCHANISMS – STATE OF ART REVIEW

As was mentioned, the yield line mechanism analysis has been widely used since the 60ties of the XXth Century. Experiments carried out by many researchers on beams or columns built from plate strips, subjected to uniform compression, show, that in such members some simple plastic mechanisms can be distin-

guished, which have been termed in Królak (1990) as basic mechanisms. Simultaneously, results of experiments performed, among others, by Murray and Khoo (1981) confirmed, that even a very complex mechanisms can be described as superposition of some simple basic mechanisms. Murray and Khoo (1981)] developed and classified 8 basic plastic mechanisms in plate strips under uniform compression. They also derived for them relations, determining the failure equilibrium path (load versus deflection). These mechanisms and corresponding relations are also described in details in Kotelko (2010).

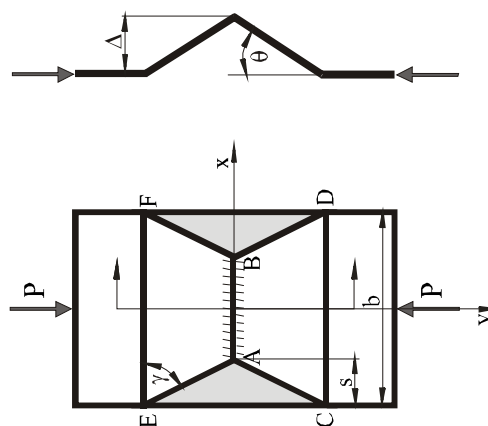


Fig. 4. Local plastic mechanisms in thin plates: – pitched-roof mechanisms, Mahendran (1997)

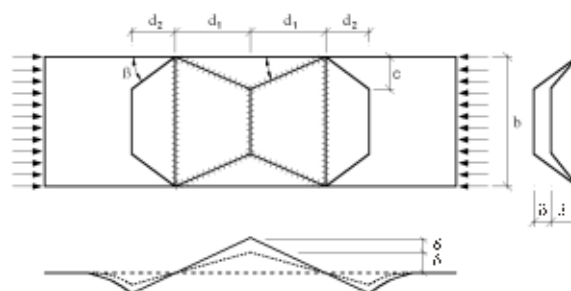


Fig. 5. Local plastic mechanisms in thin plates: – roof mechanism, Ungureanu (2006)

In plates subjected to uniform compression, at symmetrical boundary conditions, which corresponds to the case of column web in compression, a pitched-roof mechanism (Fig. 4) or roof mechanisms (Fig. 5) can develop. The pitched-roof mechanism has been described by some researchers, i.e. Kato (1965), Korol and Sherbourne (1972), Davies et al. (1994) as well as Sin (1985) and Mahendran (1997). Modifications of pitched-roof mechanisms (mainly roof mechanism) were developed by Rondal and Maquoi (1985) and Kragerup (1982). The roof mechanism was also described in details by Ungureanu (2006). All the mechanisms mentioned above, in plate strips and plates under compression are described in details together with corresponding relations for failure equilibrium path (load versus deflection) in Kotelko (2010).

Five plastic mechanisms of failure in channel section columns subjected to axial compression were originally developed by Murray and Khoo (1981). They were also analysed by Mahendran (1997), Dubina and Ungureanu (2002) and Ungureanu and Dubina (2004), who described mechanism CW2 and Rassmussen and Hancock (1991), who analysed mechanisms CF2 and CF3. Mechanisms CW1 and CW2 correspond to the case of the web

in compression, while mechanisms CF1, CF2 and CF3 – to the case of the flange in compression. In all papers, mentioned above, the yield strip equilibrium method (Kotelko and Mania, 2008; Kotelko, 2010) has been applied.

The equilibrium strip method treats the plastic mechanism as a compatible collection of strips of infinitesimal or unit width parallel to the direction of applied force. On the basis of free-body diagram of a separated strip an equilibrium equation is formulated and then, those equations are integrated across walls of the plastic mechanism, in order to obtain simultaneous equilibrium equation for the mechanism as a whole.

An alternative is the energy method (Kotelko and Mania, 2008; Kotelko, 2010). Using the energy method one applies the Principle of Virtual Velocities of the general following form:

$$P \cdot \dot{\delta} = \int_V \sigma_{ij} \dot{\varepsilon}_{ij}^p(\beta, \chi) dV, \quad (1)$$

where:  $\delta$  – is the global generalized displacement,  $\dot{\delta}$  – is the rate of change of the global generalized displacement,  $\beta$  – is the vector of kinematical parameters of the plastic mechanisms (kinematically admissible displacements),  $\chi$  – is the vector of geometrical parameters of the plastic mechanisms,  $\dot{\varepsilon}_{ij}^p$  – is the strain rate tensor.

As a result, a load – deformation relation is obtained, the graphical representation of which is a failure equilibrium path. In the case of a plate in compression the Principle (1) takes form

$$\delta W_{ext} = \delta W_b + \delta W_m, \quad (2)$$

where:  $W_b$  is a bending strain energy,  $W_m$  – a membrane strain energy.

From equation (2) a current force  $P$  in terms of deflection (failure equilibrium path) is obtained. In the case of true mechanisms, eg. CF1 or CF3 (Kotelko, 2010), the bending strain energy takes form:

$$W_p(\delta) = m_p \sum_{i=1}^n l_i' \beta_i, \quad (3)$$

where:  $l_i$  – length of  $i^{th}$  yield line,  $\beta_i$  – angle of rotation at  $i^{th}$  yield line,  $m_p$  – fully plastic moment.

After derivation of (3) with respect to rotation angle of the global mechanism, the failure equilibrium path is obtained.

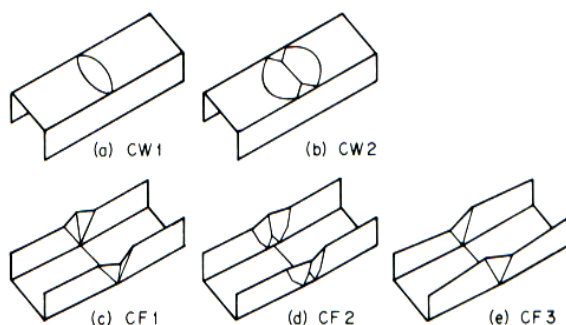


Fig. 6. Basic plastic mechanisms in channel – section columns

#### 4. IDENTIFICATION OF PLASTIC MECHANISMS IN COLUMNS UNDER ECCENTRIC COMPRESSION

In order to identify the plastic mechanisms of columns subjected to eccentric compression about minor axis leading to an

evolution of different local plastic mechanisms, depending on the position of eccentricity, finite element simulations have been performed for lipped channel section columns described in chapter 2. Failure patterns obtained from FE calculations are shown in Fig. 7 and 8.

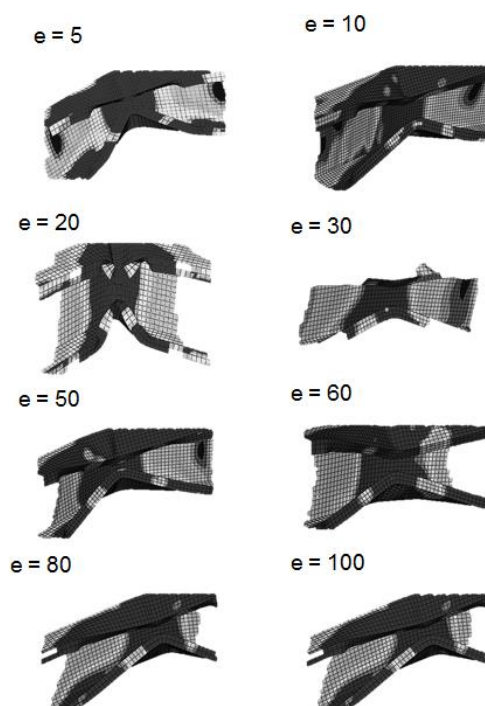


Fig. 7. FE failure patterns for positive eccentricities (flange in compression)

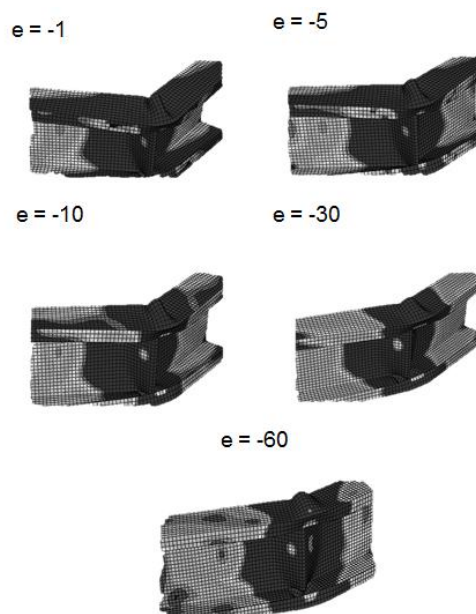


Fig. 8. FE failure patterns for negative eccentricities (web in compression)

On the basis of FE simulations one can state, that a shape of the plastic mechanism strongly depends on the eccentricity value. For positive eccentricities (flange in compression) we observe mechanisms similar to those, shown in Fig. 6. For negative eccentricities (web in compression) one can observe mechanisms similar to mechanisms in plates subjected to uniform compression

(Fig.5). However, in that case yield lines occur also in flanges and lips, so that the actual mechanism is more complex. Moreover, within those two main cases (flange or web in compression), mechanisms differ, depending on a magnitude of the eccentricity.

According to FE results, four simplified types of plastic mechanisms have been identified. The first (Fig. 9) is a mechanism similar to CF1. It is typical for small positive eccentricities. For larger positive eccentricities the enhanced mechanism CF2 has been identified Fig.10). For small negative eccentricities (web in compression) the V-shaped mechanism was developed (Fig.11), similar to the mechanism for beams in bending (Kotelko, 2010).

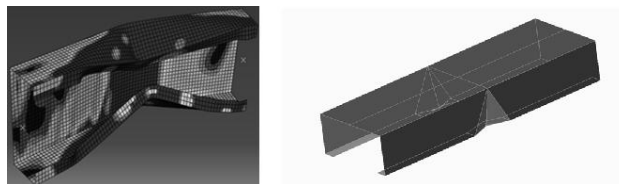


Fig. 9. Enhanced three-hinge mechanism CF1 for positive eccentricities  $e = 5, 10$  mm (flange in compression)

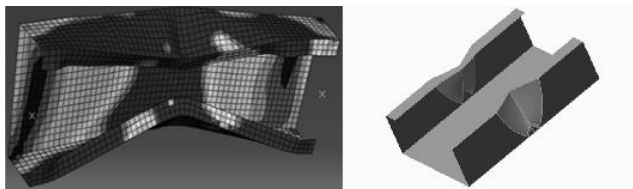


Fig. 10. Enhanced mechanisms CF2 for positive eccentricities  $e = 20 - 100$  mm, (flange in compression)

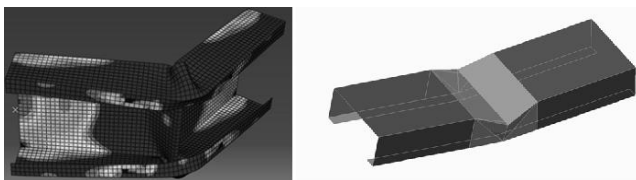


Fig. 11. V-shaped mechanisms for negative eccentricities  $e = (-1) - (-10)$  mm

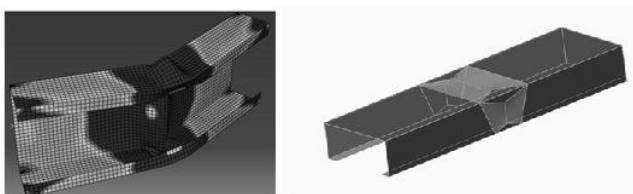


Fig. 12. Pitched-roof mechanism for negative eccentricities  $e = (-30) - (-60)$  mm, (web in compression)

For large negative eccentricities the mechanism shown in Fig. 12 has been identified, consisting of the pitched-roof mechanism in the web and additional yield lines and tension fields in the flanges.

Preliminary theoretical calculations based on the mechanisms models shown above have been performed. Selected results of these calculations, compared with FE results are presented in Fig. 13 and 14. In Fig. 13 the failure equilibrium paths obtained for CF1 mechanism are compared with corresponding FE results. The yield line analysis was carried out using the energy method

(rel. (3)). Although the mechanism model does not count for yield lines in lips, the agreement with FE results is relatively good.

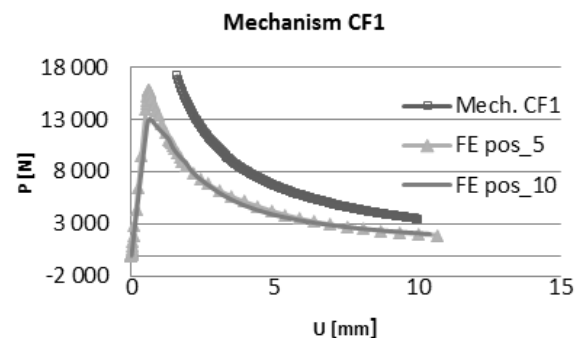


Fig. 13. Comparison of numerical results for small positive eccentricities (flange in compression)

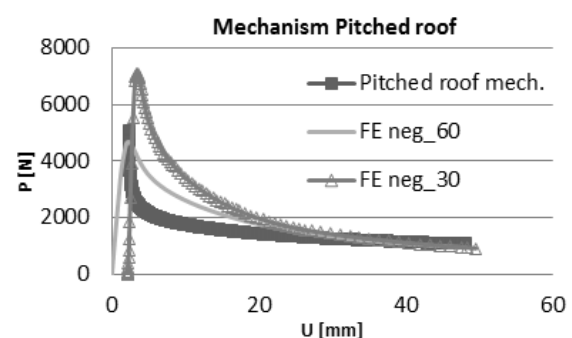


Fig. 14. Comparison of numerical results for large negative eccentricities (web in compression)

The energy method (rel. (2)) was used to obtain failure equilibrium path for mechanism, shown in Fig.12. In relation (2) only the plastic strain energy dissipated in the web (for pitched-roof mechanism) was taken into account. In that case the agreement with FE results is poor, except the last stage of failure.

## 5. FINAL REMARKS

The FE simulation results show, that for short TWCF members subjected to compression or eccentric compression, all elastic phenomena become plastic. Thus, the yield line analysis (plastic mechanism) approach is of aid in the estimation of the load-capacity of such members. However, even if plastic mechanisms are identified for compression and bending separately, in the case of eccentric compression, this is far from a linear superposition of basic mechanisms.

The plastic mechanisms models presented in the paper are the first approximation and should be completed, taking into account tension fields and traveling lines (Kotelko, 2010).

## REFERENCES

1. Davies J.M., Leach P. (1994), First order generalized beam theory, *Journal of Construction. Steel research*, 39,187-220.
2. Dubina D., Ungureanu V. (2002), Plastic strength of thin-walled members, *Sixteenth Int. Specialty Conference on Cold-Formed Steel Structures, Orlando, Florida*, 324-332.



3. **Eurocode 1993-1-3:** Eurocode 3: Design of steel structures, Part 1-3: General Rules.
4. **Hiriyur B.K.J., Schafer B.W.** (2004), Yield-line analysis of cold-formed steel members, *International Journal of Steel Structures*, 5(1), 43-54.
5. **Kato B.** (1965), Buckling strength of plates in the plastic range, *International Association of Bridge and Structural Engineering*, 25,127-141.
6. **Korol R.M., Sherbourne A.N.** (1972), Strength prediction of plates in uniaxial compression, *Journal of Structural Division*, 98, 1965-1986.
7. **Kotelko M.** (2010), Load-carrying capacity and mechanisms of failure of thin-walled structures, (in Polish), WNT Warszawa.
8. **Kotelko M., Mania J.R.** (2008), Alternative solution of the problem of load-capacity of thin-walled plated structures, *Mechanics and Mechanical Eng.*, 12(4), 323-336.
9. **Kragerup J.** (1982), Five notes on plate buckling, *Technical University of Denmark, Department of Structural Engineering, Series R, Nr 143*.
10. **Królak M. [ed.]** (1990), Post-buckling and load-capacity of thin-walled girders of flat walls (in Polish), PWN Warszawa-Łódź.
11. **Mahendran M.** (1997), Local plastic mechanisms in thin steel plates under in-plane compression, *Thin-Walled Structure, Elsevier Appl. Sci*, 27, 245-261.
12. **Murray N.W., Khoo P.S.** (1981), Some basic plastic mechanisms in thin-walled steel structures, *Int. J. Mech. Sci.*, 23(12), 703-713.
13. **Rasmussen K.J.R., Hancock G.J.** (1991), Nonlinear analyses of thin-walled channel-section columns, *Thin-Walled Structures*, 13(1,2) 145-176.
14. **Rondal J., Maquoi R.** (1985), Stub-column strength of thin-walled square and rectangular hollow sections, *Thin-Walled Structures*, 3, 15-34.
15. **Sin K.W.** (1985), *The collapse behaviour of thin-walled sections*, PhD Thesis, Dept. of Mechanical Engineering, University of Strathclyde, Glasgow.
16. **Ungureanu D.V.** (2006), Light steel structures made of cold-formed steel profiles, (in Romanian), *Ed. Orizonturi Universitare Timisoara*.
17. **Ungureanu V., Dubina D.** (2004), Post-elastic strength and ductility of cold-formed steel sections, *Proc. of Int. Conference on Thin-Walled Structures, Loughborough, Thin-Walled Structures*, 283-294.
18. **Ungureanu V., Kotelko M., Mania R.J., Dubina D.** (2010), Plastic mechanisms database for thin walled cold-formed steel members in compression and bending, *Thin-Walled Structures*, 48(10-11) 818-826.
19. **Zhao X.-L.** (2003), Yield line mechanism analysis of steel members and connections, *Prog. Struct. Engng Mater.*, 5, 252-262.

The work has been presented over the XIVth Symposium on Stability of Structures, Zakopane, Poland, June 2015.

## DEFORMATION PROPERTIES OF TAILOR-WELDED BLANK MADE OF DUAL PHASE STEELS

Alexander SCHREK\*, Pavol ŠVEC\*, Veronika GAJDOŠOVÁ\*

\*Faculty of Mechanical Engineering, Slovak University of Technology in Bratislava, Institute of Technologies and Materials,  
Pionierska 15, 831 02 Bratislava, Slovakia[alexander.schrek@stuba.sk](mailto:alexander.schrek@stuba.sk), [pavol.svec@stuba.sk](mailto:pavol.svec@stuba.sk), [veronika.gajdosova@stuba.sk](mailto:veronika.gajdosova@stuba.sk)

received 2 November 2015, revised 18 February 2016, accepted 22 February 2016

**Abstract:** The paper is dedicated to forming and properties of passenger car's B-pillar reinforcement drawn from simple blank and alternatively tailor-welded blank (TWB). Drawn part is characterised by a place with a large strain, while forming process simulation did not confirm the creation of crack using the TWB consisting of dual phase HCT980X instead of previous HCT600 steel. It is because HCT980X steel has higher strength and lower ductile properties. The analysis of properties of drawn parts is focused on the simulated crash test in Dynaform software. Obtained sizes of drawn forces in simulated frame of the drawn parts and their comparison proved the possibility of the replacement the 1.2 mm thick simple blank from HCT600 steel with the 1 mm thick TWB consisting of HCT600 and HCT980X steel. The changed thickness of the simple blank caused 20% weight saving while containing the same properties of the drawn part.

**Keywords:** Dual Phase Steels, Tailor-Welded Blank, Drawn Part, Crash Test Simulation, Reaction Force

## 1. INTRODUCTION

In several industries (e.g. the automotive and aerospace industries), the need for lightweight and cost-effective products with exceptional performance is essential for success. Tailor welded blanks (TWBs) offer an excellent means to meet these competing and seemingly contradictory demands. They are used for forming of parts with special strength, stiffness and operational deformation properties (Kinsey and Wu, 2011; Evin and Tomáš, 2012; Bilik et al., 2015; Fracz et al., 2014; Reisgen et al., 2012). With the use of materials with different stress-strain properties or different thicknesses we can achieve higher strength and stiffness while lower weight of the drawn parts or even the whole construction (Słota et al., 2014; Evin, 2013; Fracz et al., 2013; Bilik et al., 2010; Evin et al., 2015; Merklein et al., 2014). On the other hand, these differences cause uneven material flow into the die area, which result in several forming problems, e.g. weld line displacement or sheet thickness reduction of more ductile material. These effects should be minimised in the preparation process by means of special design of forming tool or optimising of blankholder forces distribution (Sinha et al., 2013; Zhong-Qin et al., 2007; Reisgen et al., 2010).

The aim of the experiment was to analyse the manufacturing possibility and comparison of the deformation properties of the B-pillar reinforcement of the car bodywork from two types of blanks. First researched solution is simple blank made of dual phase steel and the second one is TWB consisting of dual phase steel in boundary areas and dual phase steel with significantly different (higher) stress and (lower) ductile properties in the middle area of the part. Simulation software based on finite element method (FEM) is a common solution for dealing with specifics of forming of TWBs. Dynaform was specially developed for crash testing. This paper presents the result of the experiment simulating crash

test of the chosen B-pillar by the deformation tool (Padmanabhan et al., 2007; Chena et al., 2008; Groche and Metz, 2006; Daxin et al., 2008). We were evaluating the sizes and diagrams of reaction forces in simulated frames of the drawn parts in the both variants, their time dependence differences and the prediction of application possibility while decreasing weight of the car bodywork.

## 2. EXPERIMENT

The material of the real B-pillar drawn part was dual phase steel HCT600. The conditions analysis of the simple blank formability was the basis for the comparison with TWB formability.

Chemical composition and stress-strain parameters are in Tabs. 1, 2. In the simulation we used material model defined by the tensile test.

Tab. 1. Chemical composition of the steel HCT600

| C [%] | Si [%] | Mn [%] | P [%] | S [%] | Al [%] | N [%] | Cr+Ni +Cu [%] |
|-------|--------|--------|-------|-------|--------|-------|---------------|
| 0.12  | 0.5    | 1.4    | 0.08  | 0.008 | 0.04   | 0.009 | 1.3           |

Tab. 2. Basic mechanical properties of steel HCT600

| $R_{p0.2}$ [MPa] | $R_m$ [MPa] | $A_{80}$ [%] |
|------------------|-------------|--------------|
| 390              | 650         | 26.6         |

The blank shape (Fig. 1) was optimised while forming tool construction using Dynaform software with the aim of minimisation of strain and wall thickness reduction. Sheet thickness of simple blank was 1.2 mm.



Fig. 1. Shape of the simple blank (blue colour signalled  $\varphi = 0$ )

Simulation of technological process of deep drawing is based on the geometry of the tool function part which is the same as the real tool used for the manufacturing of structural body part – B-pillar reinforcement. The die is the moving part with the simulated speed of 1 m/s and die displacement of 0.5 m. The use of such speed is a condition for the use of simulation solver, which, as a dynamic software, easily and accurately solves dynamic operations. The punch is defined as a stationary member. Model of the drawing tool is shown in Fig. 2. „Mesh scaling” or „velocity scaling” are used for shortening of computational time, since solver converges towards the process result faster.

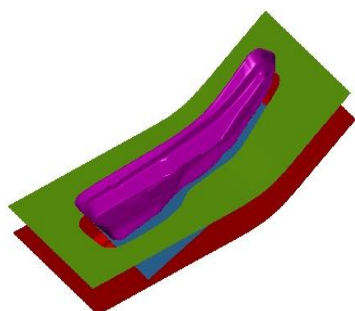


Fig. 2. Model of the drawing tool created in Dynaform software

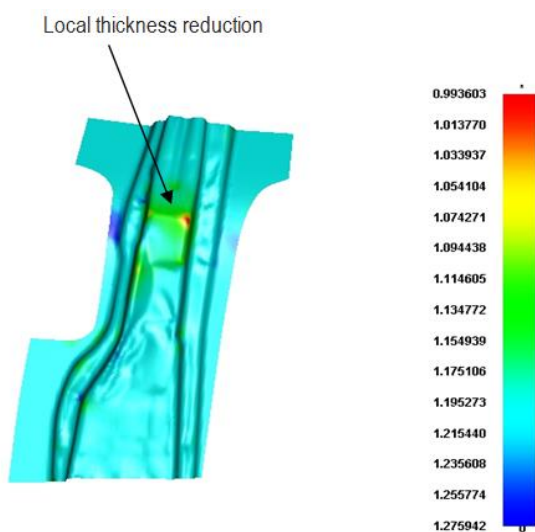


Fig. 3. Simulation of drawing of the B-pillar from the simple blank

Fig. 3 shows the example of the B-pillar reinforcement drawing simulation from the simple blank, with marked critical area with the largest strain and local thickness reduction (-0.2 mm). The size of the blankholder force was optimised on the value 250 kN during the forming process.

Fig. 4 shows drawn part with the areas highlighted by color corresponding to the strain values given by FLD - diagram. By comparing the true values of logarithmic strain in critical areas of the part to the strain values in various areas of FLD - diagram, technological safety of the operation can be obtained given by the area of limit deformations. The greatest stress concentration is shown in green, which according to the diagram in Fig. 5 is still in the safe zone, and does not cause crack of the part.



Fig. 4. B-pillar drawn from the simple blank with highlighted strain areas

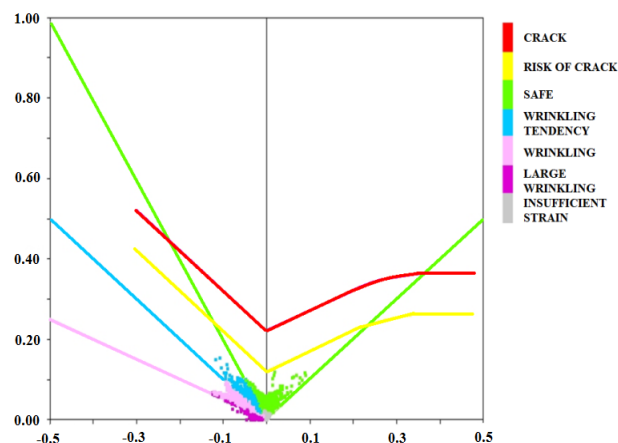


Fig. 5. Forming Limit Diagram - FLD with a color legend for the B-pillar drawn from simple blank

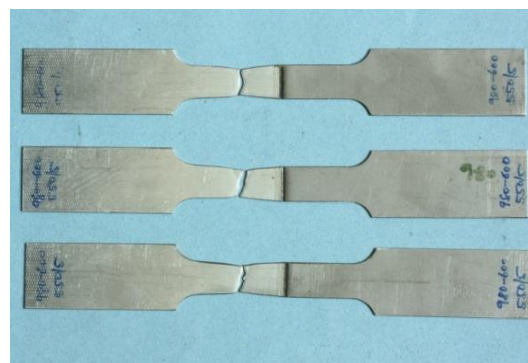


Fig. 6. Examples of the TWB specimen with the weld joint in HCT980X – HCT600 combination after tensile test (welding power 550W, rate 5mm/s)

TWB was made of 1mm thick sheet, consisting of dual phase steels HCT600 a HCT980X. The joint produced by laser welding has sufficient strength - the crack of the specimen in the tensile test of the weld joint was not created in the weld interface area or thermally influenced area but on the side of the steel HCT600 (Fig. 6) (Reisgen, 2012).

The weld interface position on the blank was chosen according to the expected load in the crash test and also the formability analysis of the critical area of the drawn part considering lower ductile properties of the steel HCT980X. Its properties are in Tab. 3 and 4. In the simulation we used material model defined by the tensile test.

Tab. 3. Chemical composition of steel HCT980X

| C[%]     | Si [%]  | Mn [%]  | P [%]    | S [%]     | V [%]    | Al [%] | B [%]     | [%]                   |
|----------|---------|---------|----------|-----------|----------|--------|-----------|-----------------------|
| Max 0.23 | Max 0.8 | Max 2.2 | Max 0.08 | Max 0.015 | Max 0.22 | Max 2  | Max 0.005 | Cr+Mo<1<br>Nb+Ti<0.15 |

Tab. 4. Basic mechanical properties of steel HCT980X

| R <sub>p0.2</sub> [MPa] | R <sub>m</sub> [MPa] | A <sub>80</sub> [%] |
|-------------------------|----------------------|---------------------|
| 620                     | 980                  | 12.2                |

The TWB shape with s marked weld interfaces is shown in Fig. 7. Blue and yellow colours signalise steel HCT600, purple one steel HCT980X.

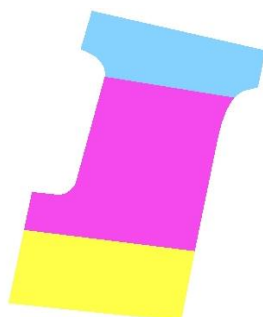


Fig. 7. Shape and composition of the TWB

Local thickness reduction

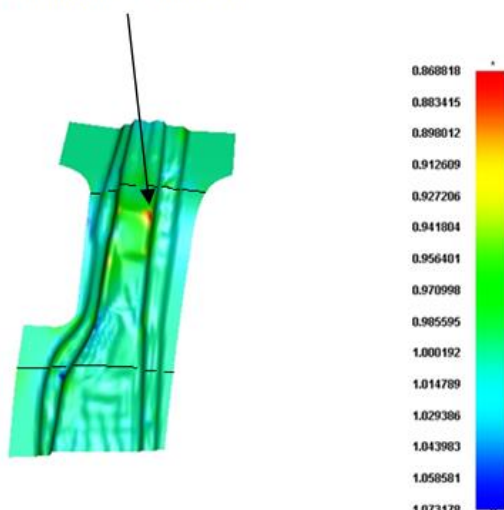


Fig. 8. Simulation of drawing of the B-pillar from TWB

Fig. 8 shows the example of the B-pillar reinforcement drawing simulation from the TWB, with marked critical area with the largest strain and local thickness reduction (-0.11 mm). To reduce the risk of cracks and because of significantly different strength and strain properties of steel HCT980X, we optimised size of the blankholder force on the value 200 kN at the beginning of the drawing process and 180 kN at its end.

Simulation of TWB drawing in FLD diagram in Fig. 9 shows a safe strain for which there are no cracks or nucleus to cracks. Similar to Fig. 5, when comparing true values of logarithmic strain in critical areas of the part drawn from TWB to strain values in FLD - diagram in Fig. 10, we can obtain technological safety given by the area of limit deformations.

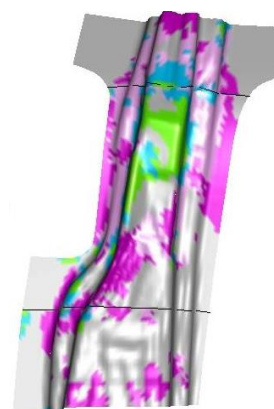


Fig. 9. B-pillar drawn from the TWB with highlighted strained areas

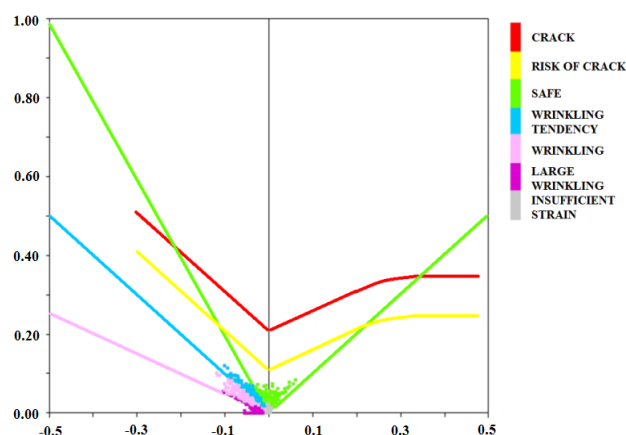


Fig. 10. Forming Limit Diagram - FLD with a color legend for the B-pillar drawn from the TWB

## 2.1. Simulation of the crash tests of the drawn parts

Analysis objective was to observe the strain properties of the B-pillar reinforcement drawn from the simple blank during crash test (side crash test of the automobile). Simulation software Dynaform (Slota et al., 2014), enabling this type of analysis, was used for definition of the position of B-pillar reinforcement with the frame on the boundary, marked with red colour in Fig. 11 and 12. Model motion rate of the deformation part with 200 mm diameter was 27 km/h in the both variants. We have been observing the sizes of the reaction forces in frame areas. The size of the maximal reaction force in analysis of the drawn part from HCT600



simple blank was  $F_R = 62.77\text{kN}$ . The size of the maximal reaction force in analysis of the drawn part from TWB consisting of steels HCT980X and HCT600 was  $F_R = 61.485\text{kN}$ . The time depended diagrams and sizes of the simulated crash tests in the same conditions (rate and size of the deformation part) were almost the same, the drawn parts has comparable properties (Fig. 13 and 14).

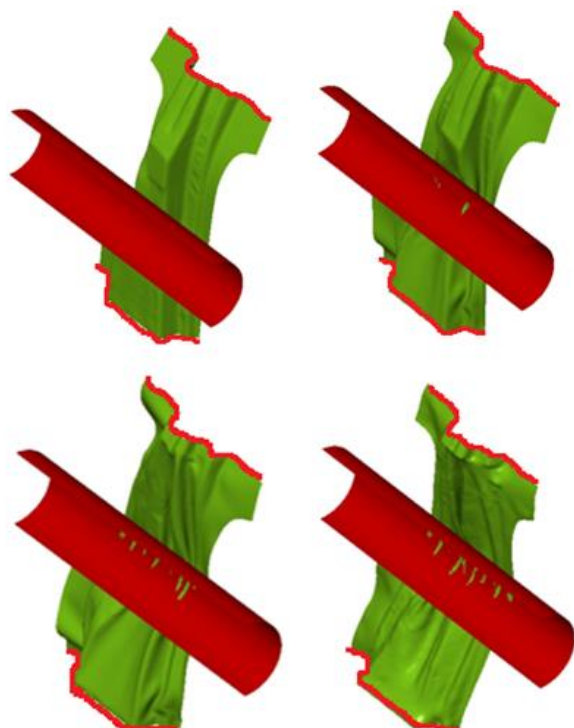


Fig. 11. Time evolution of the simulated crash of the deformation part towards drawn part from the simple blank

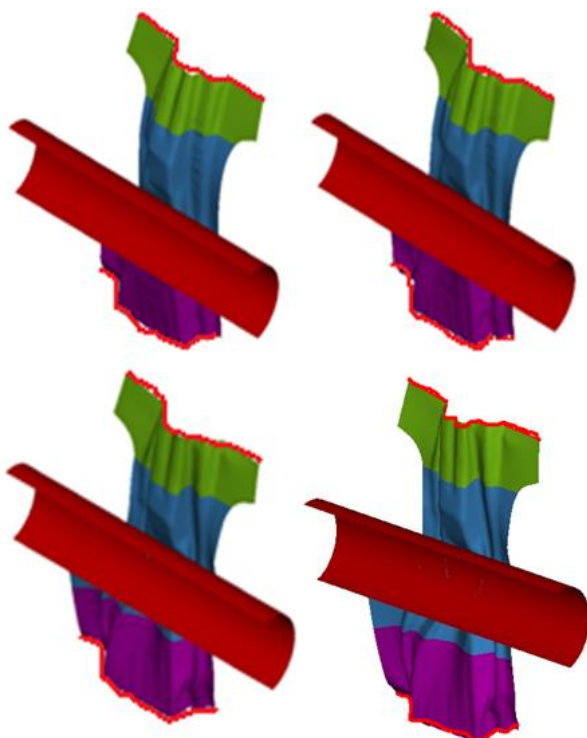


Fig. 12. Time evolution of the simulated crash of the deformation part

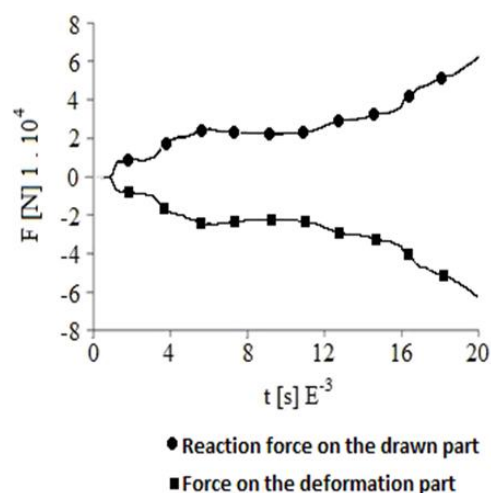


Fig. 13. Diagram of the reaction forces on the drawn part caused by the deformation part in simulated crash – simple blank

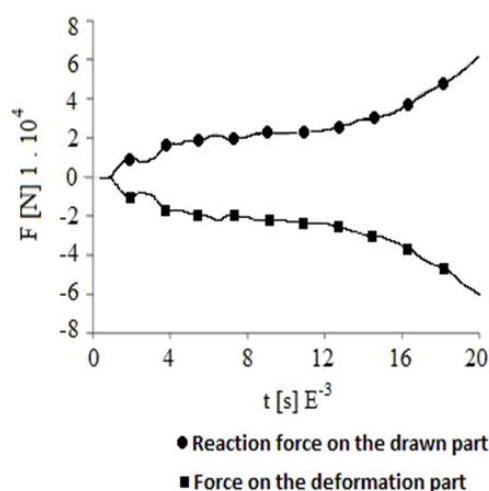


Fig. 14. Diagram of the reaction forces on the drawn part caused by the deformation part in simulated crash – tailor welded blank

Tab. 5. The measured values of reaction forces in different time intervals with their differences

| Measure ment | Time [s] | Simple blank part F[kN] | TWB F[kN] | Difference F[kN] |
|--------------|----------|-------------------------|-----------|------------------|
| 1            | 0.0018   | 7.7                     | 9.97      | 2.27             |
| 2            | 0.0035   | 15.785                  | 15.513    | 0.272            |
| 3            | 0.005    | 23.426                  | 19.229    | 4.197            |
| 4            | 0.007    | 23.192                  | 19.247    | 3.945            |
| 5            | 0.009    | 22.303                  | 22.508    | 0.205            |
| 6            | 0.01     | 23.076                  | 23.013    | 0.063            |
| 7            | 0.012    | 28.591                  | 24.934    | 3.657            |
| 8            | 0.014    | 32.254                  | 29.593    | 2.661            |
| 9            | 0.016    | 40.522                  | 37.371    | 3.151            |
| 10           | 0.018    | 51.647                  | 46.506    | 5.141            |
| 11           | 0.02     | 62.770                  | 61.485    | 1.285            |

The sizes of the reaction forces in the same time period and their differences for the both blank types are in Tab. 5.

The analysis of the simple blank and TWB formability using deep-drawing simulation software Dynaform on the basis of the optimisation of blank shape, blankholder force and blankholder force-displacement curve shows the possibility of the manufacturing of the chosen drawn part also with the material with higher stress and lower ductile properties in the critical area. During the manufacturing of the part by deep drawing process, we observed the local thickness reduction without any crack creation due to the sheet thickness change from 1.2 to 1mm.

Simulated crash test shew almost the same properties of the drawn parts from the simple blank and TWB, due to the usage of HCT 980X material in TWB in the area with the biggest bending moment. The sizes of the reaction forces in simulated frames of the drawn parts reached minimal differences for both variants. However, the sheet thickness change of the TWB from 1.2 to 1mm enabled significant weight reduction of the chosen drawn part by 20%.

The experiment confirmed the utilisation possibilities of modern materials and TWBs with the aim of weight reduction of steel car bodyworks.

## REFERENCES

1. Bilič J., Balážová M., Kršiaková L., Šuba R. (2010), The analysis of properties and forming duplex steel DP 450, *Hutnícke listy*, Vol. 63, No. 4, 74-77.
2. Bilič J., Ertel J., Bárta J., Marónek M., Šugárová J. (2015), The analysis of properties and forming of laser welded superduplex steel SAF 2507, *Hutník-WH*, Vol. 82, No. 9, 627-631.
3. Chena, W., Linb, G.S., Hub, S.J. (2008), A comparison study on the effectiveness of stepped binder and weld line clamping pins on formability improvement for tailor-welded blanks, *Journal of materials processing technology* 207, 204-210.
4. Daxin E., Takaji M., Zhiguo L. (2008), Stress analysis of rectangular cup drawing, *Journal of Materials Processing Technology*, Vol. 205, 469-476.
5. Evin E. (2013), Design of dual phase high strength steels sheet for auto body, *Metal 22<sup>nd</sup> International Conference on Metallurgy and Materials, Conference Proceedings*.
6. Evin E., Antoszewski B., Tomáš M., Tkáčová J., Draganovská D. (2015), Tribological Properties of Coatings for Sheet Metal Stamping Dies, *Materials Science Forum*, Vol. 818, 69-73.
7. Evin E., Tomáš M. (2012), Comparison of deformation properties of steel sheets for car body parts, *Procedia Engineering*, Vol. 48, 115-122.
8. Fracz W., Stachowicz F., Pieja T. (2013) Aspects of verification and optimization of sheet metal numerical simulations process using the photogrammetric system, *Acta Metallurgica Slovaca*, Vol. 19, 51-59.
9. Fracz W., Stachowicz F., Trzepieciniski T., Pieja T. (2014), Forming limit of the heat resistant AMS 5599 sheet metal, *Hutník-WH*, Vol. 81, No. 7, 442-445.
10. Groche P., Metz C. (2006), Investigation of active-elastic blank holder systems for high-pressure forming of metal sheets, *International Journal of Machine Tools & Manufacture*, Vol. 46, 1271-1275.
11. Kinsey L.B., Wu X. (2011), *Tailor-welded blanks for advanced manufacturing*. Woodhead publishing, Cambridge.
12. Merklein M., Johanes M., Lechner M., Kuppert A. (2014), A review on tailored blanks – Production, applications and evaluation, *Journal of Materials Processing Technology*, Vol. 214, 151-164.
13. Padmanabhan R., Baptista A.J., Olivieira M.C., Menezes L.F. (2007), Effect of anisotropy on the deep-drawing of mild steel and dual-phase steel tailor-welded blanks, *Journal of Materials Processing Technology*, Vol. 184, 288-293.
14. Reisgen U., Schleser M., Mokrov O., Ahmed E. (2010), Uni- and bi-axial deformation behavior of laser welded advanced high strength steel sheets, *Journal of Materials Processing Technology*, Vol. 210, 2188-2196.
15. Reisgen U., Schleser M., Mokrov O., Ahmed E. (2012), Statistical modelling of laser welding of DP/TRIP steel sheets, *Optics & Laser Technology*, Vol. 44, 92-101.
16. Sinha, A.K., Kim, D.Y., Ceglarek, D. (2013), Correlation analysis of the variation of weld seam and tensile strength in laser welding galvanized steel, *Optics and Laser in Engineering*, 51, 1143-1152.
17. Slota J., Jurčišin M., Spišák E. (2014), Experimental and numerical analysis of local mechanical properties of drawn part, *Key Engineering Materials*, Vol. 586, 245-248.
18. Zhong-Qin L., Wu-Rong W., Guan-Long C. (2007), A new strategy to optimize variable blank holder force towards improving the forming limits of aluminum sheet metal forming, *Journal of Materials Processing Technology*, Vol. 183, 339-346.

**Acknowledgement:** This work was supported by the Slovak Research and Development Agency under the contract No. APVV-0281-12 and by the Ministry of Education, Science, Research and Sport of the Slovak Republic under project VEGA 1/0149/13.

# SOME CONSIDERATIONS ON AN UNDERWATER ROBOTIC MANIPULATOR SUBJECTED TO THE ENVIRONMENTAL DISTURBANCES CAUSED BY WATER CURRENT

Waldemar KOŁODZIEJCZYK\*

\*Faculty of Mechanical Engineering, Department of Automatic Control and Robotics, Białystok University of Technology,  
ul. Wiejska 45c, 15-351 Białystok, Poland

[w.kolodziejczyk@pb.edu.pl](mailto:w.kolodziejczyk@pb.edu.pl)

received 31 July 2015, revised 19 February 2016, accepted 22 February 2016

**Abstract:** The objective of this paper is to discuss some of the issues associated with environmental load on the three-link serial manipulator caused by underwater current. We have conducted CFD simulations to investigate hydrodynamic effects induced by changing current direction and changing with time current speed in order to better understand the physics of the problem. The results are presented in terms of moments of hydrodynamic forces plotted against relative position of the current and the robotic arm. Time history of hydrodynamic loads according to periodically changing current speed is presented and discussed.

**Key words:** Underwater Manipulator, CFD, Current Disturbances

## 1. INTRODUCTION

Underwater manipulators constitute subsystems of remotely operated vehicles (ROVs) or autonomous underwater vehicles (AUVs), making the jobs of exploration, construction, inspection, and recovery possible. Manipulators enable the robots to replicate the function of human arm in carrying out operations such as picking up objects from the bed, placing and joining assembly parts, drilling, cutting, however, the overall performance of underwater manipulation is greatly affected by interaction with the water environment, particularly in position/motion control of the end-effector with respect to the given target position.

Land-based manipulators operate in the air, which is much lighter than a solid body, and consequently, their models of dynamics, usually, do not include environmental contributions, as though they move in vacuum, not meeting any resistance at all. In underwater applications the impact of the environment cannot be neglected, and in consequence, quantifying of hydrodynamic loads is necessary, especially, in determining controllability of the system. Moreover, the underwater robotic arms have to be designed to withstand the hydrodynamic forces exerted by the surrounding fluid.

Underwater manipulators consist of rigid links connected in series by pin joints. The joint torques for generating the motion of the links have to overcome the weight and payload along with the hydrodynamic load induced by relative motion of the arm and the fluid. A moving solid body immersed in flowing water is subjected to the pressure and shear stress distributions resulting from their relative motion. In the equations of motion of the multibody system this hydrodynamic load is usually decoupled into independently computed inertia, friction damping and lift contributions, although these phenomena are strongly coupled according to basic continuum mechanics principles.

Currents represent important ambient flow conditions in a changeable and uncertain aquatic environment. Ocean cur-

rents are caused by tidal movements, wind, heat exchange, the salinity differences, and the Coriolis force due to the rotation of the Earth. Furthermore, the refresh of water in structured environment may be strong enough to induce additional hydrodynamic loads on the underwater system. Usually the current effect on the underwater manipulator is modeled (if at all) in a simplified way as a constant disturbance by assuming the current to be irrotational and unchanged (Fossen, 1994; Antonelli, 2006). Real ocean currents are often multi-directional and irregular, spatially and time variable.

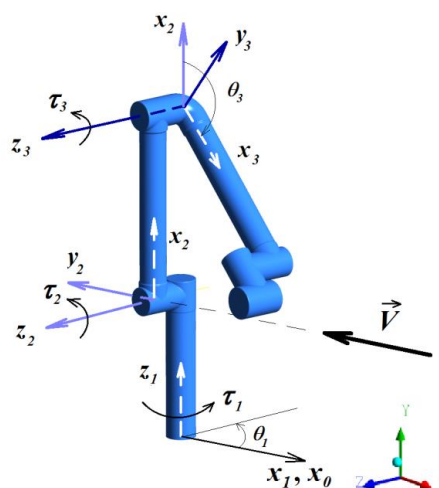


Fig. 1. Coordinate frame arrangement of the robotic arm (external and local reference frames)

In this paper some aspects of hydrodynamic load on the underwater robotic arm caused by current of water are considered and analyzed by using the CFD modeling tools in order to get more insight to the physics of the problem. The power of CFD

simulations enabled us to observe the effects of disturbances such as changes in the direction of the current velocity and its magnitude on the moments experienced by the manipulator joints.

This paper is organized as follows. The second section is devoted to the modeling of water environmental impact on the manipulator considered as a lumped mechanical system. In the third section the continuum mechanics approach and CFD modeling of water flow around the robotic arm is described. The next section provides results of calculations and discussion, and the last section – conclusions.

## 2. MECHANICAL ASPECTS

The main purpose to model a robot manipulator is to compute the forces and torques required to drive the joints given the requested end-effector position. The other purpose is to simulate the motion of the robotic arm in order to define control strategies. The hydrodynamic effects have to be assessed in advance to reproduce in a proper way the dynamical behavior of the robotic arm, otherwise the control may be significantly deteriorated. Recently, it is increasingly performed in specialized virtual prototyping environments, utilizing lumped approximations to hydrodynamic forces. Some of these environments were described in Wang (2012).

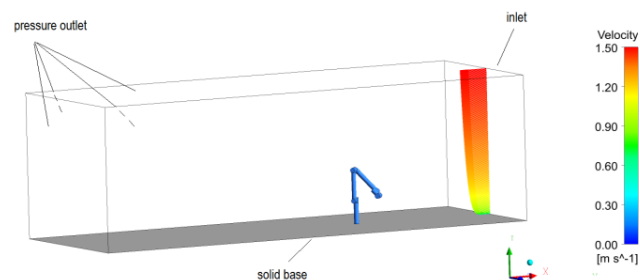


**Fig. 2.** Manipulator, computational domain, types of boundary conditions and velocity profile at the inlet to the domain

The robotic arm considered in this study is a serial manipulator (Fig. 1). It is composed of three links with diameters of 8.4 cm. The lowest link is 0.43 m long, the middle one – 0.45m, and the upper link has the cylindrical part of the length of 0.4m. The configuration of the arm was kept unchanged at the position of the third upper link inclined at an angle  $\theta_3 = 135^\circ$  with respect to the middle vertical link (Fig. 1).

Industrial or, more generally, land-based manipulators operate in the air, and consequently their equations of motion do not have to include environmental contributions. Hydrodynamics matters in underwater applications. In the lumped modeling of the dynamics of the rigid body in water environment the additional inertia resistance due to the accelerated fluid is taken into account through the concept of added mass and added moments of inertia, depending on the shape of the body and its ability to carry along the fluid (Fossen, 1994; Antonelli, 2006).

The lumped model of dynamics of an underwater manipulator, considered as a rigid multibody system consists of equations of motion derived by using law of conservation of momentum. In case of underwater applications it is usually written in the following form (Antonelli, 2006; Herman, 2009; Pazmino et al., 2011):

$$M\dot{v} + C(v)v + D(v)v + g(v) = \tau_v, \quad (1)$$

where:  $v$  – is the velocity vector. The symbols:

$$M = M_m + M_a, \quad C(v) = C_m(v) + C_a(v) \quad (2)$$

denote as follows:  $M_m$  and  $C_m(v)$  are the rigid body mass matrix, and the Coriolis/centripetal matrix, respectively, whilst  $M_a$  denotes the added mass matrix and  $C_a(v)$  – the added Coriolis/centripetal matrix.  $D(v)$  stands for the drag matrix,  $g(v)$  – is the resultant vector of gravity and buoyancy;  $\tau_v$  – is the resultant input vector of forces and moments influencing the manipulator.

A number of works have been conducted in order to model underwater manipulator dynamics. Richard and Levesque (1996) developed the dynamic model of subsea manipulator for a non-deterministic fluid environment in order to deal with stochastic buoyancy effects for partially immersed arm. McLain and Rock (1998) and Leabourne and Rock (1998) have estimated added mass and drag contributions using and developing potential flow theory and experimental tests. Vossoughi et al. (2004) investigated the dynamics of underwater robotic arm incorporating results obtained by McLain and Rock (1998) for modeling hydrodynamic effects in order to design velocity control system. Santhakumar and Kim (2012) developed indirect adaptive control system for Underwater Vehicle Manipulator System (UVMS) in order to compensate disturbances caused, inter alia, by currents.

The added terms are computed as the extra forces and moments, needed to accelerate the fluid, divided by the accelerations – linear or angular, respectively. They are usually expressed in terms of hydrodynamic coefficients.

The part of hydrodynamic force on the body, dependent on the relative velocity is usually decomposed into an in-line force, called the drag force, and a transverse force – the lift force. They are expressed in terms of hydrodynamic coefficients as well. Drag coefficients depending on the shape and configuration of the manipulator, and the type of the flow characterized by Reynolds number, are computed as a superposition of a constant part representing laminar flow and a velocity-depending part accounting for turbulent effects.

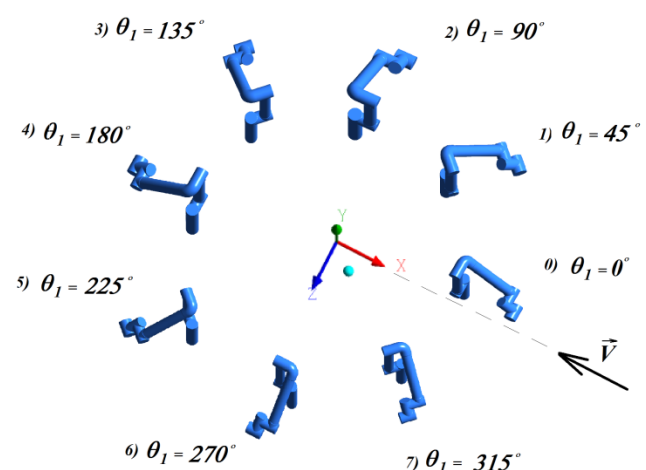


**Fig. 3.** The relative positions of the robotic arm and current velocity  $\vec{V}$

The hydrodynamic added inertia and drag coefficients are commonly computed from the strip theory coming from potential flow background for 2D inviscid flows, and extended semi-empirically to three dimensions (McLain and Rock, 1998). In this



approach, the solid body is divided into multiple narrow slices, which can be considered as airfoils. Viscous effect of the fluid has to be incorporated into a model via additional drag and lift coefficients.

Water currents are usually assumed to be irrotational and constant and their effects are modeled as constant disturbances included into added inertia, added Coriolis/centripetal and damping terms of the model (Fossen, 1994; Antonelli, 2006).

The equations of motion are highly nonlinear due to hydrodynamic forces (Fossen, 1994). They contain uncertainties associated with hydrodynamic coefficients, estimated only approximately from simplified theories, experimental studies and empirical relations.

### 3. HYDRODYNAMIC MODELING

In the lumped approach, presented in the previous section, the hydrodynamic effect on the body completely immersed in water is decomposed into forces and moments depending on acceleration and velocity in relative motion between water and manipulator, which results in added inertia, added Coriolis/centripetal and damping contributions, taken into considerations independently, although in real flows these flow phenomena are strongly coupled, according to the fundamental conservation laws of continuum mechanics. In continuum mechanics approach all hydrodynamic forces and moments acting on the submerged manipulator are the result of pressure and shear stress distributions around the body, occurring in the flow.

Furthermore, in solid body mechanics the effect of the underwater current on the submerged body is commonly considered as being constant and irrotational, but real flow even far away from boundary layer on the body is always rotational and turbulent. This is another premise to employ the continuum mechanics approach and numerical simulations in the present considerations.

Tab. 1. Grid independence study

| Sl. No.<br><i>i</i> | Number<br>of cells<br><i>N</i> | Torques [N m] |          |          | Grid independence factor |            |            |
|---------------------|--------------------------------|---------------|----------|----------|--------------------------|------------|------------|
|                     |                                | $\tau_1$      | $\tau_2$ | $\tau_3$ | $\delta_1$               | $\delta_2$ | $\delta_3$ |
| 1                   | 2 369 004                      | -3.56         | 5.31     | -9.88    | 0.177                    | 0.341      | 0.182      |
| 2                   | 4 242 883                      | -4.92         | 4.54     | -11.15   | 0.139                    | 0.148      | 0.077      |
| 3                   | 7 986 142                      | -4.44         | 4.05     | -12.50   | 0.027                    | 0.025      | 0.023      |
| 4                   | 9 747 773                      | -4.32         | 3.96     | -12.09   |                          |            |            |

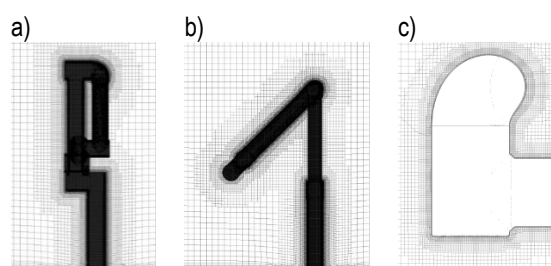


Fig. 4. Details of computational grid near and on the surface of the manipulator

In this research emphasis was placed on the calculations of moments of hydrodynamic forces exerted by the current of water about three  $z$  axis in local reference frames assigned to

the arm links, as they are shown in Fig. 1. Going from top to bottom, the moment  $\tau_3$  was calculated taking into account pressure and shear stress distributions along the surface of upper link about  $z_3$  axis. The moment  $\tau_2$  includes hydrodynamic effects (due to pressure and shear stresses) on the two upper links with respect to  $z_2$  axis and the moment  $\tau_1$  – describes the action of water on the whole manipulator about  $z_1$  axis. They can be considered as joint torques experienced by the manipulator placed into the current of water and which have to be compensated by motors in order to maintain the positions of the links.

Incompressible fluid flow surrounding the robotic arm, when temperature effect is neglected, is governed by the set of continuity equation and Navier-Stokes equation of motion.

For 3D problems, the governing equations can be described as:

– the continuity equation:

$$\nabla \cdot \vec{V} = 0; \quad (3)$$

– the Navier-Stokes equation of motion:

$$\frac{\partial \vec{V}}{\partial t} + (\vec{V} \cdot \nabla) \vec{V} = -\frac{1}{\rho} \nabla p + \frac{\mu}{\rho} \nabla^2 \vec{V} + f, \quad (4)$$

where:  $\vec{V} = [V_x, V_y, V_z]$  is the velocity vector,  $\rho$  is the density of fluid,  $p$  is the pressure,  $\mu$  – the viscosity,  $f$  – the body force (in this case – apparent weight) per unit mass, and  $\nabla$  is the vector differential operator (gradient).

The present considerations were bounded to the computational domain in the shape of a box of 8m long, 3m wide and 2.5m tall, depicted in Fig. 2. The manipulator was attached to the solid base in the middle of the width of the base at a distance of 2.5m from free current inlet, as it is shown in Fig. 2. The other sides of computational domain were in contact with surrounding flowing water with the assumption that the backflow into the domain was allowed and computed using the direction of the flow in the cell layer adjacent to these sides (pressure outlet boundary conditions).

Gulf Stream, Kuroshio, Agulhas, Brazil, and East Australian Currents flow at speeds up to 2.5 m/s. It was decided to limit the velocity to 1.5 m/s at most. This was the maximum current speed far away from the base in free stream of water. Reynolds number computed with respect to the links diameters and the maximum current speed was equal to 126 000. The 1/7th power law was used to specify turbulent velocity profile near the solid base at the inlet to the domain (see Fig. 2).

The considerations were carried out for two cases investigating two different current disturbances. The first one concerned the change in the direction of the current with respect to the position of the robotic arm. The second one examined the properties of the flow, when the speed of the current changes in time. The investigations of the current direction effect on the load on the manipulator were performed as steady-state, whilst the second ones, dealing with the time dependence of the current speed, were considered as transient problem. The change in the direction of the current with respect to the fixed robotic arm was modeled as the change in position of the arm (its rotation about vertical axis) to the unchanged current direction, because it was the easiest way to maintain the shape of the computational domain unchanged. The relative positions of the robotic arm and the direction of the current are indicated in Fig. 3 as the angles of rotation  $\theta_1$  about vertical axis with respect to the initial position, when the third upper link is inclined exactly towards the current ( $\theta_1 = 0$ ).

Tab. 2. Resolving moments into components due to viscosity  $\tau_v$  and pressure  $\tau_p$

|                  | $\theta_1$        | 0°      | 45°      | 90°      | 135°    | 180°    | 225°    | 270°    | 315°    |
|------------------|-------------------|---------|----------|----------|---------|---------|---------|---------|---------|
| $\tau_1$<br>[Nm] | $\tau_v$          | -0.0497 | 0.0996   | 0.1724   | 0.1833  | 0.0483  | -0.0877 | -0.1379 | -0.1854 |
|                  | $\tau_p$          | -4.2703 | 0.5536   | 4.2854   | 5.5586  | 1.0702  | -3.0283 | -5.4013 | -5.4408 |
|                  | $\tau_v / \tau_p$ | 0.012   | 0.179    | 0.040    | 0.033   | 0.045   | 0.029   | -0.026  | 0.034   |
| $\tau_2$<br>[Nm] | $\tau_v$          | 0.407   | 0.2793   | 0.00276  | -0.3426 | -0.4648 | -0.3354 | 0.0229  | 0.3255  |
|                  | $\tau_p$          | 3.548   | 3.3682   | -0.4384  | -6.0219 | -8.8238 | -7.4930 | -0.0560 | 3.4445  |
|                  | $\tau_v / \tau_p$ | 0.115   | 0.083    | -0.006   | 0.057   | 0.053   | 0.045   | -0.409  | 0.094   |
| $\tau_3$<br>[Nm] | $\tau_v$          | -0.215  | -0.1721  | -0.00012 | 0.1555  | 0.1849  | 0.1511  | 0.0038  | -0.1492 |
|                  | $\tau_p$          | -11.872 | -10.2525 | 0.04047  | 4.2664  | 5.1017  | 3.7452  | -0.1965 | -7.6076 |
|                  | $\tau_v / \tau_p$ | 0.018   | 0.017    | -0.003   | 0.036   | 0.036   | 0.040   | -0.019  | 0.019   |

The ANSYS CFD (ANSYS, Canonsburg, PA) software was used to conduct simulations. For the computational domain with different manipulator positions to the current the set of eight meshes of approx.  $9\,500\,00 \div 10\,500\,000$  elements were generated using cut-cell method. Simulations were executed in Parallel Fluent 16.0 (which implements the finite volume method) with twelve parallel processes utilizing a second order spatial pressure discretization and second order upwind discretization schemes for momentum equations and for the model of turbulence. In steady-state simulations the SIMPLE algorithm (Semi-Implicit Method for Pressure Linked Equations) was used as the method of solution, whilst in transient simulation – the PISO (Pressure Implicit with Splitting of Operators) scheme was applied with second order implicit transient formulation and 20 iterations per time step equal to 0.01s.

Grid independence analysis was carried out for steady-state flow and initial arm position, i.e. for the rotation angle  $\theta_1 = 0$ , comparing resulting torques  $\tau_1$ ,  $\tau_2$ ,  $\tau_3$ , obtained for meshes of different resolutions, as it is shown in Tab. 1. Grid independence factor was defined as

$$\delta_j = \left| \frac{\tau_j(i) - \tau_j(4)}{\tau_j(4)} \right|, \quad (5)$$

where:  $j$  is an indicator of the torque (1, 2 or 3),  $i$  – stands for a serial number of the mesh (Tab. 1),  $\tau_j(4)$  is the “ $j$ ” torque computed for the reference grid No. 4 of maximum number of cells. As one can see in Tab. 1, grid independence factor constantly decreases with increasing number of cells and for two finest meshes of cell numbers 7 986 142 and 9 747 773, the relative differences of the torques were less than 3%. In order to better capture the flow structures, the finest mesh (No. 4) was chosen and, consequently, the number of cells for all computational cases was kept in the range of  $950000 \div 10500000$ . Fig. 4 depicts some details of the computational grid near and on the surface of the manipulator.

## 4. RESULTS AND DISCUSSION

A number of steady-state numerical simulations were conducted under a series of various environmental disturbances caused by different current directions. The influence of changing with time current speed has been studied utilizing transient simu-

lations for the initial position of the arm ( $\theta_1 = 0^\circ$ ). The effects of these environmental disturbances on hydrodynamic load on the robotic arm are analyzed in the following subsections.

### 4.1. The effect of current direction change

Several numerical calculations were carried out for eight different relative positions of the arm and the current direction indicated by the angle  $\theta_1$  ( $0^\circ$ ,  $45^\circ$ ,  $90^\circ$ ,  $135^\circ$ ,  $180^\circ$ ,  $225^\circ$ ,  $270^\circ$ ,  $315^\circ$ ). The angle  $\theta_1$  is measured from the x0 axis directed opposite the flow as it is depicted in Fig. 1. The results are gathered and presented in Fig. 5 in terms of hydrodynamic torques  $\tau_1$ ,  $\tau_2$ ,  $\tau_3$  plotted against the angle  $\theta_1$ . All the moments were calculated in local reference frames shown in Fig. 1.

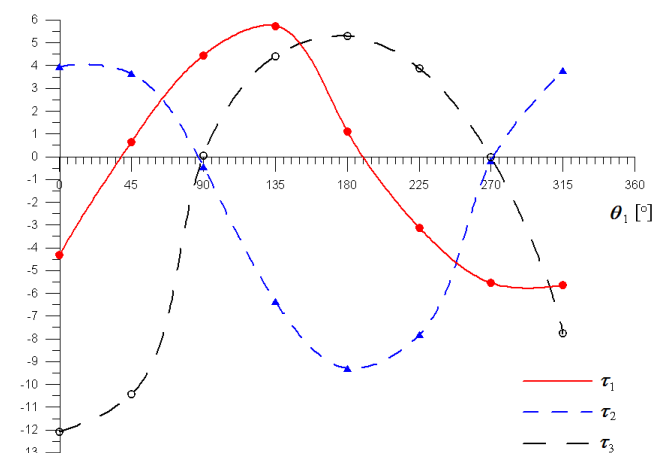


Fig. 5. Hydrodynamic torques vs. the angle  $\theta_1$

The torque  $\tau_1$  of the whole manipulator around vertical z1 axis vanishes changing its direction at  $\theta_1 = 38^\circ$  and  $190^\circ$  mainly due to dissymmetry of the arm. It is a common practice for underwater vehicles and manipulator systems (UVMS) to align them with the current in order to minimize the drag forces, but in our case the torque  $\tau_1$  at the position aligned with the flow ( $\theta_1 = 0^\circ$ ) was only a little less than maximum absolute value achieved. Taking into account, that drag forces are usually estimated only approximately, neglecting some geometric details of the system disturbing the

symmetry of the structure, one has to be aware of inaccuracies induced by this practice. Even that dissymmetry of the structure, as we have in the case of our manipulator located at the initial position, can cause unanticipated increase of the joint torque required to maintain the position of the arm.

The maximum magnitude of  $\tau_1$  was obtained for  $\theta_1 = 135^\circ$  and between  $270^\circ \div 315^\circ$ . It is worth mentioning, that  $\tau_1$  takes

unexpectedly different values at corresponding positions with respect to the current, e.g. at  $\theta_1$  equal to  $135^\circ$  and  $225^\circ$  or  $45^\circ$  and  $315^\circ$ . The behavior of  $\tau_2$  and  $\tau_3$  is more predictable and intuitive. They are equal to zero for  $\theta_1 = 90^\circ$  and  $270^\circ$ . Their plots are almost symmetrical with respect to  $\theta_1 = 180^\circ$  and they take approximately the same values for corresponding positions.

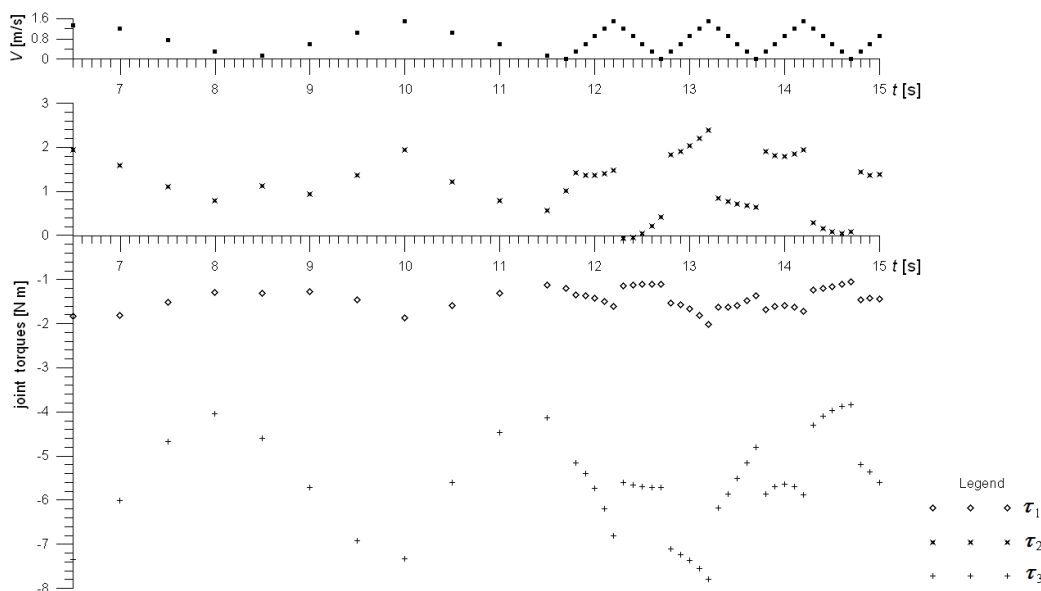


Fig. 6. Time history of joint torques  $\tau_1$ ,  $\tau_2$ ,  $\tau_3$

Moments of hydrodynamic forces appear mainly due to the pressure distribution around the links. Tab. 2 shows moments  $\tau_1$ ,  $\tau_2$ ,  $\tau_3$  broken into components  $\tau_v$  and  $\tau_p$ , generated due to shear and pressure forces, respectively. Maximum magnitude of viscous  $\tau_v$  equal to about 0.5 Nm acted on the two upper links with respect to  $z_2$  axis (Fig. 1) at position of the arm indicated by  $\theta_1 = 180^\circ$  (Fig. 3), but in most cases they were less than 0.1 Nm and made significant fraction of pressure induced moments ( $\tau_v/\tau_p$ ) only when the pressure component notably decreases due to flow conditions (for example  $\tau_1$  at the position indicated by  $\theta_1 = 45^\circ$ ).

#### 4.2. The effect of changing with time current speed

The effect of current speed was examined applying transient CFD simulation for time dependent inlet velocity to the domain. At the inlet to the computational domain turbulent velocity profile has been changing with time according to the saw function shown at the top of Fig. 6. For the sake of clarity only a part of time history of joint torques  $\tau_1$ ,  $\tau_2$ ,  $\tau_3$  is displayed, although simulation was performed over time duration of 17s and above, starting from initial conditions obtained from steady-state calculations for arm initial position denoted in Fig. 3 as  $\theta_1 = 0$ . The free stream speed has been changing linearly from zero to 1.5m/s there and back again with two different periods of change. In the first interval (below 11.7s) the period of speed change was equal to 3.33s, and after that it has been reduced to 1.0s.

As one can see from plots in Fig. 6, the torques  $\tau_1$ ,  $\tau_2$ ,  $\tau_3$  follow the changes of inlet velocity. It is especially clearly seen for the first time interval (below 11.7s), when speed frequency was

fairly low. After reducing the time period to 1.0s, the behavior of the plots is not so obvious, but it can be observed, that the magnitudes of torques are increasing with increasing velocity and, in most cases, decreasing with decreasing speed, but changes become more irregular and violent. Velocity distributions depicted in Fig. 7 for time instances 14.2s and 14.7s, that is, when current speed sharply starts dropping or rising, respectively, show how agitated becomes the flow after increasing the frequency of inlet velocity changes (upstream the manipulator) compared with that of lower frequency (downstream the arm).

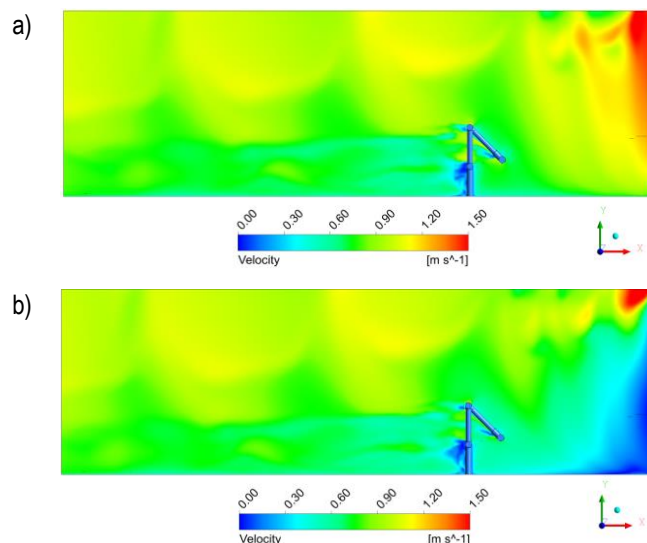
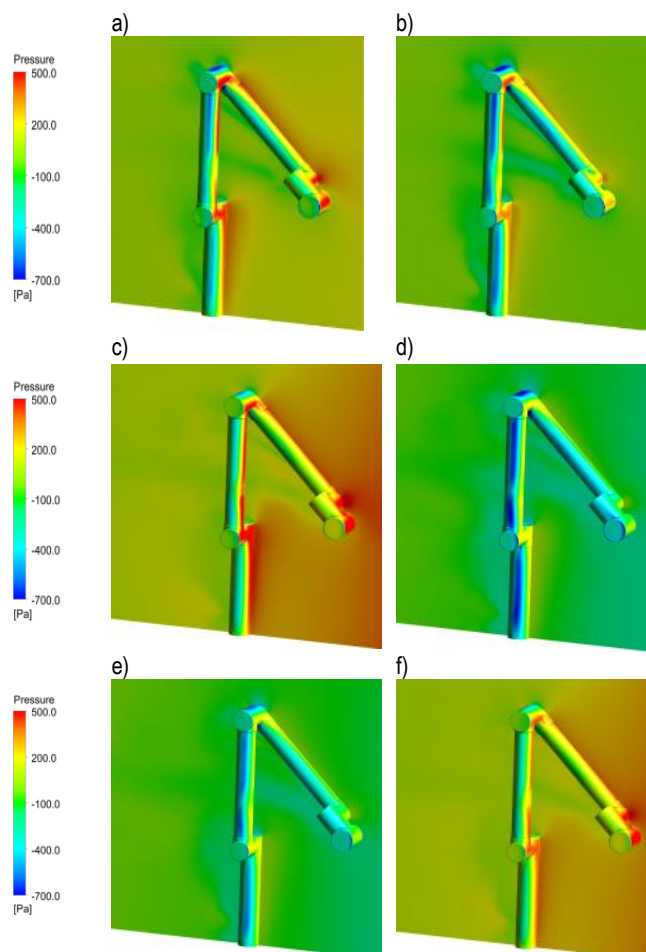


Fig. 7. Velocity distributions in the midplane of the domain of solution: a)  $t = 14.2s$ ; b)  $t = 14.7s$

In the second interval (beyond 11.7s), when the time period was very short (1.0s), sharp and sudden changes of torques magnitudes can be observed for sharp changes of speed, e.g. in  $t = 14.2$ s and 14.7s. For lower frequency at an earlier time (below 11.7s), such phenomena were not discovered. The hydrodynamic loads expressed in terms of joint torques changed gradually with speed changes, much smoother than for higher speed frequency.



**Fig. 8.** Pressure (gauge pressure) distributions on the robotic arm and in the midplane of the domain in selected time points: a)  $t = 10.0$ s; b)  $t = 10.1$ s; c)  $t = 14.2$ s; d)  $t = 14.3$ s; e)  $t = 14.7$ s; f)  $t = 14.8$ s

The explanation to that flow behavior comes from pressure distribution analysis carried out on the basis of plots shown in Fig. 8. Suffice it to compare the pressure distributions on and in the vicinity of the manipulator, drawn for two subsequent time points, when the speed starts dropping for higher and lower frequency. For example, the pressure maps presented in Fig. 8c) and 8d), drawn for time  $t = 14.2$ s and  $t = 14.3$ s, respectively, reveal much more intense changes in pressure than in corresponding situation for lower frequency (compare Fig. 8a and 8b). The same conditions, but in opposite direction of pressure change, are when current speed starts rising, e.g. from the time point  $t = 14.7$ s to  $t = 14.8$ s, for which pressure distributions are presented in Fig. 8e) and 8f), respectively. More intense pressure changes caused by greater acceleration of water for higher frequency induce sharp and sudden changes in joint torques depicted

in Fig. 7. The fast variations in velocity always cause great variations in pressure in the surroundings, which cannot be reduced by the viscous damping of water. This type of flow behavior may happen due to sudden changes in flow velocity during, for example, the gate opening or closing in structured underwater environment.

It should be added at the end of this section, that in the kind of time dependent flow presented in this paper, periodically decreasing velocity causes the great reduction of the magnitude of hydrodynamic moments experienced by the manipulator. For example, the greatest magnitude of  $\tau_1$  exceeds 12 Nm in steady flow, whilst in time dependent flow it takes the values not more than 8 Nm.

The results obtained for changing current direction are more general than those for changing current speed. The latter ones depend strongly on the geometry of the computational domain, and especially on the distance of the manipulator from the source of disturbances (inlet), however they may serve as an example showing qualitatively the impact of such changeable environmental conditions as current speed.

## 5. CONCLUSIONS

In this paper attention is given to the physics of the problem of disturbances influencing underwater robotic arm, caused by varying current direction and speed. Realistic predictions of environmental loads are needed to identify operational limitations and set proper operating ranges while doing a task. Usually they are assessed applying simplified theories and experimental studies. Compared to experiments, CFD software offers a less expensive alternative, and can serve as a useful and very promising tool to solve this problem. There are several works carried out in the area of CFD modeling of underwater vehicles performed in order to predict hydrodynamic load or hydrodynamic coefficients, e.g. Zhang et al. (2013), Joung et al. (2014), Bettel et al. (2014), Kumar et al. (2015), Luo and Lyu (2015), expressing the need for the synergy between lumped and continuum mechanics approaches.

Although the usage of CFD analysis to the subsea vehicles problems grows steadily, there are little works in the literature concerning numerical analysis of underwater manipulators, and especially we have not found any papers relating to the effects of current disturbances on the moments experienced by the manipulator joints. The present work was prepared with the intention to fill the gap in this area and to give a deeper insight into physics of the environmental disturbances caused by water current. Numerical simulations, performed by the use of ANSYS Fluent software, enabled us to observe the effects of such disturbances as changes in the current velocity direction and its magnitude on the moments experienced by the manipulator joints. The investigations of the current direction effect on the load on the manipulator were carried out as steady-state whilst those for the time dependent current speed, were considered as transient problem.

As a result of investigations the joint moments of hydrodynamic forces were plotted as a function of relative angle between the manipulator and the current and analyzed, showing that even small dissymmetry of the structure can cause unanticipated increase of the joint torque required to maintain the position of the arm. The time history of joint torques due to periodically varying with time current speed reveals that load variations follow gradually the variation of current speed for lower speed frequency, but



when the period of change becomes short enough, the hydrodynamic load may change very sharply and violently due to the sudden pressure variations associated with changes of velocity field. These flow phenomena, which may strongly affect the underwater manipulators control, can be predicted quantitatively through appropriate experiments, still - CFD analysis may be considered as a useful and less expensive research tool in this regard. The present study is just a first step in modeling of hydrodynamic load on the underwater arm. The next step will focus on the problem of making the manipulator move through the application of dynamic meshes.

## REFERENCES

1. **ANSYS Inc.** (2015), ANSYS FLUENT Theory Guide, Release 16.0, Canonsburg, USA.
2. **Antonelli G.** (2006), *Underwater Robots* (Springer Tracts in Advanced Robotics), Second edition, Springer.
3. **Bettle M.C., Gerber A.G., Watt G.D.** (2014), Using reduced hydrodynamic models to accelerate the predictor-corrector convergence of implicit 6-DOF URANS submarine manoeuvring simulations, *Computers & Fluids*, 102, 215-236.
4. **Fossen T.I.** (1994), *Guidance and Control of Ocean Vehicles*, John Wiley & Sons, Chichester, United Kingdom.
5. **Herman P.** (2009), Decoupled PD set-point controller for underwater vehicles, *Ocean Engineering*, 36, 529-534.
6. **Joung T.-H., Choi H.-S., Jung S.-K., Sammut K., He F.** (2014), Verification of CFD analysis method for predicting the drag force and thrust power of an underwater disc robot, *International Journal of Naval Architecture and Ocean Engineering*, 6, 269-281.
7. **Kumar M.S., Raja S.C., Kumar M.N.S., Gowthamraj B.** (2015), A synergic approach to the conceptual design of Autonomous Underwater Vehicle, *Robotics and Autonomous Systems*, 67, 105-114.
8. **Leabourne K.N., Rock S.M.** (1998), Model Development of an Underwater Manipulator for Coordinated Arm-Vehicle Control, *Proceedings of the OCEANS 98 Conference*, Nice, France, 2, 941-946.
9. **Luo W., Lyu W.** (2015), An application of multidisciplinary design optimization to the hydrodynamic performances of underwater robots, *Ocean Engineering*, 104, 686-697.
10. **McLain T.W., Rock S.M.** (1998), Development and Experimental Validation of an Underwater Manipulator Hydrodynamic Model, *The International Journal of Robotics Research*, 17, 748-759.
11. **Pazmino R. S., Garcia Cena C.E., Alvarez Arocha C., Santoja R.A.** (2011), Experiences and results from designing and developing a 6DoF underwater parallel robot, *Robotics and Autonomous System*, 59, 101-112.
12. **Richard M.J., Levesque B.** (1996), Stochastic dynamic modelling of an open-chain manipulator in a fluid environment, *Mechanism and Machine Theory*, 31(5), 561-572.
13. **Santhakumar M., Kim J.** (2012), Indirect adaptive control of an autonomous underwater vehicle-manipulator system for underwater manipulation tasks, *Ocean Engineering*, 54, 233-243.
14. **Vossoughi G.R., Meghdari A., Borhan H.** (2004), Dynamic modeling and robust control of an underwater ROV equipped with a robotic manipulator arm, *Proceedings of 2004 JUSFA, @004 Japan-USA Symposium on Flexible Automation*, Denver, Colorado.
15. **Wang Z.** (2012), An interactive virtual prototyping platform considering environment effect described by fluid dynamics, *Robotics and Computer-Integrated Manufacturing*, 28, 316-325.
16. **Zhang S., Yu J., Zhang A., Zhang F.** (2013), Spiraling motion of underwater gliders: Modeling, analysis, and experimental results, *Ocean Engineering*, 60, 1-13.

This work has been supported by the Bialystok University of Technology grant No. S/WM/1/2012.

# THRUST POROUS BEARING WITH ROUGH SURFACES LUBRICATED BY A ROTEM-SHINNAR FLUID

Anna WALICKA\*, Edward WALICKI\*

\*Faculty of Mechanical Engineering, ul. Szafrana 2, P.O.Box 47, University of Zielona Góra, 65-516 Zielona Góra, Poland

[A.Walicka@ijame.uz.zgora.pl](mailto:A.Walicka@ijame.uz.zgora.pl), [E.Walicki@ijame.uz.zgora.pl](mailto:E.Walicki@ijame.uz.zgora.pl)

received 13 June 2014, revised 10 February 2016, accepted 23 February 2016

**Abstract:** In the paper the influence of both bearing surfaces roughness and porosity of one bearing surface on the pressure distribution and load-carrying capacity of a thrust bearing surfaces is discussed. The equations of motion of a pseudo-plastic fluid of Rotem-Shinnar, are used to derive the Reynolds equation. After general considerations on the flow in a bearing clearance and in a porous layer using the Morgan-Cameron approximation and Christensen theory of hydrodynamic lubrication the modified Reynolds equation is obtained. The analytical solutions of this equation for the cases of squeeze film bearing and externally pressurized bearing are presented. As a result one obtains the formulae expressing pressure distribution and load-carrying capacity. Thrust radial bearing with squeezed film is considered as a numerical example.

**Key words:** Pseudo-Plastic Fluid, Rotem-Shinnar Model, Thrust Bearing, Porous Layer, Christensen Roughness

## 1. INTRODUCTION

Viscosity of lubricating oils decreases with an increase of temperature. This viscosity increases with the additives concentration and it is relatively independent on temperature and usually exhibits a non-linear relation between the shear stress and the rate of shear in shear flow. There is no generally acceptable theory taking into account the flow behavior of non-Newtonian lubricants. Studies have been done on fluid film lubrication employing several models such as micropolar (see e.g.: Walicka, 1994), couple-stress (Walicki and Walicka, 1998), mixture (Khonsari and Dai, 1992), viscoplastic (Lipscomb and Denn, 1984; Dorier and Tichy, 1992), pseudo-plastic (Wada and Hayashi, 1971; Swamy et al., 1975; Rajalingam et al., 1978). Naturally, this list is not complete and given only to present possibility of mathematical modeling. More complete list may be found in (Walicka, 2002; Walicki, 2005).

In recent years, a considerable amount of tribology research has been devoted to the study of the effect of surface roughness or geometric imperfections on hydrodynamic lubrication because the bearings surfaces, in practice, are all rough and the height of the roughness asperities may have the same order as the mean bearing clearance. Under these conditions, the surface roughness affects the bearing performance considerably.

The work in this area has mainly been confined to impermeable surfaces. The well-established stochastic theory of hydrodynamic lubrication of rough surfaces developed by Christensen (1970) formed the basis of this paper. In a series of works (Bujurke et al., 2007; Lin, 2000; 2001; Prakash and Tiwari, 1985; Walicka 2009; 2012; Walicka and Walicki, 2002a; 2002b) the model was applied to the study of the surface roughness of various geometrical configurations.

Porous bearings have been widely used in industry for a long time. Basing on the Darcy model, Morgan and Cameron (1957)

first presented theoretical research on these bearings. To get a better insight into the effect of surface roughness in porous bearings, Prakash and Tiwari (1984) developed a stochastic theory of hydrodynamic lubrication of rough surfaces proposed by Christensen (1970).

The modified Reynolds equation (Gurujan and Prakash, 1999) applicable to two types of directional roughness structure were used by Walicka and Walicki (2002a; 2002b) to find bearing parameters for the squeeze film between two curvilinear surface.

In this paper the Rotem-Shinnar fluid model is used to describe the pseudo-plastic behaviour of a lubricant. The modified Reynolds equation is derived and its solution for the curvilinear thrust bearing is presented. The analysis is based on the assumption that the porous matrix consists of a system of capillaries of very small radii which allows a generalization of the Darcy law and use of the Morgan-Cameron approximation for the flow in a porous layer. According to Christensen's stochastic model (1970), different forms of Reynolds equations are derived to take account of various types of surface roughness. Analytical solutions for the film pressure are presented for the longitudinal and circumferential roughness patterns.

## 2. DERIVATION OF THE REYNOLDS EQUATION FOR A ROTEM-SHINNAR FLUID

It may be assumed that lubricating oils, with a viscosity index improver added, exhibit the same characteristics as pseudo-plastic fluids. Rotem and Shinnar (1961) proposed a method for expressing empirically the relation between the stress and the shear rate as

$$\frac{dy}{dt} = \frac{\tau}{\mu} \left( 1 + \sum_{i=1}^n k_i \tau^{2i} \right). \quad (1)$$

Retaining only the first order term ( $i = 1$ ) the above equation reduces to

$$\mu \frac{d\gamma}{dt} = \tau + k\tau^3. \quad (2)$$

Typical flow curves are shown in Fig.1. Since  $\mu$  is the tangent at the original point of the flow curves, shown in Fig.1,  $\mu$  is the initial viscosity. If the values of  $\mu$  do not vary, the non-linearity of the flow curve increases with the value of  $k$ , which means the coefficient of pseudo-plasticity. In pseudo-plastic fluids  $k \neq 0$  and in Newtonian fluids  $k = 0$ .

Therefore, in Newtonian fluids, the initial viscosity becomes the viscosity given by Newton's law.

The three-dimensional notation of Eq.(2) may be expressed as (Walicka, 2002)

$$\mu \mathbf{A}_1 = \Lambda(1 + k\Lambda^2) \quad \text{where} \quad \Lambda = \left[ \frac{1}{2} \text{tr}(\mathbf{A}^2) \right]^{\frac{1}{2}} \quad (3)$$

is the magnitude of the second-order shear stress tensor  $\mathbf{A}$ , but  $\mathbf{A}_1$  is the first Rivlin-Ericksen kinematic tensor.

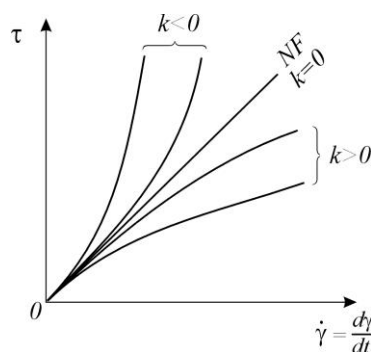


Fig. 1. Flows curves of a Rotem-Shinnar fluid of the first order ( $i = 1$ ); symbol NF means a Newtonian fluid

Let us consider a thrust bearing with a curvilinear profile of the working surfaces shown in Fig.2. The upper bound of a porous layer is described by the function  $R(x)$  which denotes the radius of this bound. The nominal bearing clearance thickness is given by the function  $h(x, t)$ , while the porous layer thickness is given by  $H_p = \text{const.}$

The expression for the film thickness is considered to be made up of two parts.

$$H = h(x, t) + h_s(x, \vartheta, \xi), \quad (4)$$

where:  $h(x, t)$  represents the nominal smooth part of the film geometry, while  $h_s = \delta_r + \delta_s$  denotes the random part resulting from the surface roughness asperities measured from the nominal level,  $\xi$  describes a random variable which characterizes the definite roughness arrangement. An intrinsic curvilinear orthogonal coordinate system  $x, \vartheta, y$  linked with the upper surface of a porous layer is also presented in Fig.2.

Taking into account the considerations of the works (Walicka, 2002; Walicki, 2005) one may present the equation of continuity and the equations of motion of a Rotem-Shinnar fluid for axial symmetry in the form

$$\frac{1}{R} \frac{\partial(Rv_x)}{\partial x} + \frac{\partial v_y}{\partial y} = 0, \quad (5)$$

$$\frac{\partial \Lambda_{xy}}{\partial y} = \frac{\partial p}{\partial x}, \quad \frac{\partial p}{\partial y} = 0. \quad (6)$$

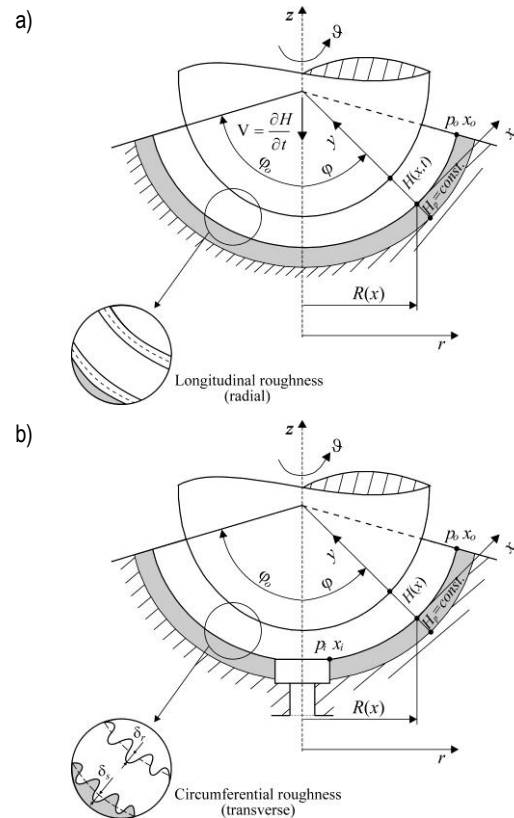


Fig. 2. Geometry of a curvilinear thrust bearing; (a) squeeze film bearing, (b) externally pressurized bearing

The constitutive equation (3) takes the form:

$$\mu \frac{\partial v_x}{\partial y} = \Lambda_{xy} + k\Lambda_{xy}^3. \quad (7)$$

The problem statement is complete after specification of boundary conditions. These conditions for velocity component are stated as follows:

$$v_x(x, 0, t) = 0, \quad v_x(x, H, t) = 0, \quad (8)$$

$$v_y(x, 0, t) = V_H, \quad v_y(x, H, t) = \frac{\partial H}{\partial t} = \dot{H}. \quad (9)$$

Solving the equations of motion (5), (6) and the constitutive taking into account equation (7) one obtains the Reynolds equation [detailed solution may be found in works (Walicka, 2002; Walicki, 2005)]

$$\frac{1}{R} \frac{\partial}{\partial x} R H^3 \left[ \frac{\partial p}{\partial x} + \frac{3}{20} k H^2 \left( \frac{\partial p}{\partial x} \right)^3 \right] = 12\mu \left( \frac{\partial H}{\partial t} - V_H \right) \quad (10)$$

for a lubricating pseudo-plastic fluid of Rotem-Shinnar. If  $k = 0$ , the above equation is identical to the Reynolds equation for Newtonian lubricant (Walicki, 1977).

### 3. MODIFIED REYNOLDS EQUATION FOR A BEARING WITH A POROUS PAD

To solve Eq.(10) let us study the flow of a Rotem-Shinnar fluid in the porous layer. Assume that this layer consists a system of capillaries with an average radius  $r_c$  and porosity  $\phi_p$ . Let the porous layer be homogeneous and isotropic and let the flow within the layer satisfy the modified Darcy's law. Thus one has (Walicki, 2005):

$$\begin{aligned}\bar{v}_x &= \frac{\Phi_p}{\mu} \left( -\frac{\partial \bar{p}}{\partial x} \right) + \frac{\Phi_p}{\mu} \frac{kr_c^2}{6} \left( -\frac{\partial \bar{p}}{\partial x} \right)^3, \\ \bar{v}_y &= \frac{\Phi_p}{\mu} \left( -\frac{\partial \bar{p}}{\partial y} \right) + \frac{\Phi_p}{\mu} \frac{kr_c^2}{6} \left( -\frac{\partial \bar{p}}{\partial y} \right)^3,\end{aligned}\quad (11)$$

where:  $\bar{v}_x, \bar{v}_y$  are velocity components in the porous layer and

$$\Phi_p = \frac{\phi_p r_c^2}{8} \quad (12)$$

is a permeability of the porous layer but  $\phi_p$  is a coefficient of porosity.

Since the cross velocity component  $\bar{v}_y$  must be continuous at the porous wall-fluid film interface and must be equal to  $V_H$ , we have then – by virtue of Eqs (10) and (11) – the following form of the modified Reynolds equation

$$\begin{aligned}\frac{1}{R} \frac{\partial}{\partial x} RH^3 \left[ \frac{\partial p}{\partial x} + \frac{3}{20} kH^2 \left( \frac{\partial p}{\partial x} \right)^3 \right] = \\ = 12\mu \left[ \frac{\partial H}{\partial t} - \frac{\Phi_p}{\mu} \left\{ \left( -\frac{\partial \bar{p}}{\partial y} \right) + \frac{kr_c^2}{6} \left( -\frac{\partial \bar{p}}{\partial y} \right)^3 \right\} \right]_{y=0}.\end{aligned}\quad (13)$$

Using the Morgan-Cameron approximation (Morgan and Cameron, 1957) one obtains

$$\begin{aligned}\left\{ \left( -\frac{\partial \bar{p}}{\partial y} \right) + \frac{kr_c^2}{6} \left( -\frac{\partial \bar{p}}{\partial y} \right)^3 \right\} \Big|_{y=0} = \\ = -\frac{H_p}{R} \frac{\partial}{\partial x} R \left\{ \left( \frac{\partial p}{\partial x} \right) + \frac{kr_c^2}{6} \left( \frac{\partial p}{\partial x} \right)^3 \right\}.\end{aligned}\quad (14)$$

When formula (14) is inserted into Eq.(13) the modified Reynolds equation takes the form:

$$\begin{aligned}\frac{1}{R} \frac{\partial}{\partial x} R \left[ \left( H^3 + \frac{3}{2} \Phi_p r_c^2 H_p \right) \frac{\partial p}{\partial x} + \right. \\ \left. + \frac{3k}{20} \left( H^5 + \frac{5}{3} \Phi_p r_c^4 H_p \right) \left( \frac{\partial p}{\partial x} \right)^3 \right] = 12\mu \frac{\partial H}{\partial t}.\end{aligned}\quad (15)$$

If the film thickness is regarded as a random quantity, a height distribution function must be associated. Many real bearing surfaces show a roughness height distribution which is closely Gaussian, at least up to three standard deviations. From a practical point of view, the Gaussian distribution is rather inconvenient and therefore a polynomial form of its approximation is chosen. Following Christensen (1970; 1971; 1973) such a probability density function is

$$f(h_s) = \begin{cases} \frac{35}{32c^7} (c^2 - h_s^2)^3, & -c \leq h_s \leq +c \\ 0, & \text{elsewhere} \end{cases} \quad (16)$$

where  $c$  is the half total range of the random film thickness variable. The function terminates at  $c = \pm 3\sigma$ , where  $\sigma$  is the standard deviation.

Inserting expected values in Eq.(15) we get the general form of the stochastic Reynolds equation

$$\begin{aligned}\frac{1}{R} \frac{\partial}{\partial x} \left( E \left\{ R \left[ \left( H^3 + \frac{3}{2} \Phi_p r_c^2 H_p \right) \frac{\partial p}{\partial x} + \right. \right. \right. \\ \left. \left. \left. + \frac{3k}{20} \left( H^5 + \frac{5}{3} \Phi_p r_c^4 H_p \right) \left( \frac{\partial p}{\partial x} \right)^3 \right] \right\} \right) = 12\mu \frac{\partial E(H)}{\partial t}\end{aligned}\quad (17)$$

where  $E(\cdot)$  is the expectancy operator defined by

$$E(\cdot) = \int_{-c}^{+c} (\cdot) f(h_s) dh_s. \quad (18)$$

The problem is now reduced to devising means of evaluating the left-hand side of Eq.(17) subject to the specific model of roughness.

The calculation of the mean film pressure distribution would require the evaluation of the expected value of various film thickness functions.

The forms of the distribution function described by Eq.(18) are given in (Walicka, 2012).

#### 4. SOLUTIONS TO THE MODIFIED REYNOLDS EQUATION

In the present study two types of roughness structure are of interest: the longitudinal (radial) one-dimensional roughness pattern, having the form of long narrow ridges and valleys running in the  $x$  direction, and the circumferential (transverse) one-dimensional roughness pattern, having the form of long narrow ridges and valleys running in the  $\vartheta$  direction (Walicka and Walicki, 2002a; 2002b; Walicka, 2009).

For the longitudinal one-dimensional roughness

$$H = h(x, t) + h_s(\vartheta, \xi) \quad (19)$$

the stochastic Reynolds equation is

$$\begin{aligned}\frac{1}{R} \frac{\partial}{\partial x} \left( R \left\{ \left[ E(H^3) + \frac{3}{2} \Phi_p r_c^2 H_p \right] \frac{\partial(Ep)}{\partial x} + \right. \right. \\ \left. \left. + \frac{3k}{20} \left[ E(H^5) + \frac{5}{3} \Phi_p r_c^4 H_p \right] \left[ \frac{\partial(Ep)}{\partial x} \right]^3 \right\} \right) = 12\mu \frac{\partial E(H)}{\partial t},\end{aligned}\quad (20)$$

but for the circumferential one-dimensional roughness

$$H = h(x, t) + h_s(x, \xi) \quad (21)$$

the stochastic Reynolds equation is

$$\begin{aligned}\frac{1}{R} \frac{\partial}{\partial x} \left( R \left\{ \left[ \frac{1}{E(H^{-3})} + \frac{3}{2} \Phi_p r_c^2 H_p \right] \frac{\partial(Ep)}{\partial x} + \right. \right. \\ \left. \left. + \frac{3k}{20} \left[ \frac{1}{E(H^{-5})} + \frac{5}{3} \Phi_p r_c^4 H_p \right] \left[ \frac{\partial(Ep)}{\partial x} \right]^3 \right\} \right) = 12\mu \frac{\partial E(H)}{\partial t}.\end{aligned}\quad (22)$$

Note that it may present both Eqs (20) and (22) in one common form as follows:

$$\begin{aligned}\frac{1}{R} \frac{\partial}{\partial x} \left( R \left\{ \left[ H_j^{(3)} + \frac{3}{2} \Phi_p r_c^2 H_p \right] \frac{\partial(Ep)}{\partial x} + \right. \right. \\ \left. \left. + \frac{3k}{20} \left[ H_j^{(5)} + \frac{5}{3} \Phi_p r_c^4 H_p \right] \left[ \frac{\partial(Ep)}{\partial x} \right]^3 \right\} \right) = 12\mu \frac{\partial E(H)}{\partial t},\end{aligned}\quad (23)$$

where

$$\begin{aligned}H_j^{(3)} &= \begin{cases} E(H^3) & \text{for } j = l, \\ \frac{1}{E(H^{-3})} & \text{for } j = c, \end{cases} \\ H_j^{(5)} &= \begin{cases} E(H^5) & \text{for } j = l, \\ \frac{1}{E(H^{-5})} & \text{for } j = c \end{cases}\end{aligned}$$

the case  $j = l$  refers to the longitudinal one-dimensional roughness, but the case  $j = c$  – to the circumferential one-dimensional roughness.

Consider the case of the Rotem-Shinnar fluid of frequent occurrence for which the factor  $k\Lambda_{xy}^2 < 1$ ; the value of this factor



indicates that the solutions to the Reynolds equation (23) may be searched in a form of the sum:

$$Ep = Ep^{(0)} + Ep^{(1)}. \quad (24)$$

Assuming that  $Ep^{(1)} \ll Ep^{(0)}$  and substituting Eq.(24) into Eq.(23) we arrive at two linearized equations, the first one

$$\frac{1}{R} \frac{\partial}{\partial x} \left\{ R \left[ H_j^{(3)} + \frac{3}{2} \Phi_p r_c^2 H_p \right] \frac{\partial(Ep^{(0)})}{\partial x} \right\} = 12\mu \frac{\partial E(H)}{\partial t}, \quad (25)$$

and the second

$$\begin{aligned} \frac{1}{R} \frac{\partial}{\partial x} \left\{ R \left[ H_j^{(3)} + \frac{3}{2} \Phi_p r_c^2 H_p \right] \frac{\partial(Ep^{(1)})}{\partial x} \right\} = \\ = - \frac{3k}{20} \frac{1}{R} \frac{\partial}{\partial x} \left\{ R \left[ H_j^{(5)} + \frac{5}{3} \Phi_p r_c^4 H_p \right] \left[ \frac{\partial(Ep^{(0)})}{\partial x} \right]^3 \right\}. \end{aligned} \quad (26)$$

The boundary conditions for pressure are:

– for squeeze film bearing  $\left(\frac{\partial H}{\partial t} \neq 0\right)$

$$\begin{aligned} \left. \frac{\partial Ep^{(0)}}{\partial x} \right|_{x=0} = 0, \quad Ep^{(0)}(x_o) = p_o, \\ \left. \frac{\partial Ep^{(1)}}{\partial x} \right|_{x=0} = Ep^{(1)}(x_o) = 0, \end{aligned} \quad (27)$$

– for externally pressurized bearing  $\left(\frac{\partial H}{\partial t} = 0\right)$

$$\begin{aligned} Ep^{(0)}(x_i) = p_i, \quad Ep^{(0)}(x_o) = p_o, \\ Ep^{(1)}(x_i) = Ep^{(1)}(x_o) = 0. \end{aligned} \quad (28)$$

The solutions of Eqs (25) and (26) are given, respectively, as follows:

$$Ep(x, t) = p_o - 12\mu[F_o - F(x, t)] \quad (29)$$

and

$$\begin{aligned} Ep(x) = - \frac{3kC^3}{20} G(x) + \frac{[A(x) - A_o] \left( p_i + \frac{3kC^3}{20} G_i \right)}{A_i - A_o} - \\ - \frac{[A(x) - A_i] \left( p_o + \frac{3kC^3}{20} G_o \right)}{A_i - A_o}, \end{aligned} \quad (30)$$

where:

$$\begin{aligned} I(x, t) &= \int \frac{R \frac{\partial E(H)}{\partial t} dx}{R \left[ H_j^{(3)} + \frac{3}{2} \Phi_p r_c^2 H_p \right]}, \\ J(x, t) &= \int \left\{ \frac{\left[ H_j^{(5)} + \frac{5}{3} \Phi_p r_c^4 H_p \right]}{R^3 \left[ H_j^{(3)} + \frac{3}{2} \Phi_p r_c^2 H_p \right]^4} \left[ \int R \frac{\partial E(H)}{\partial t} dx \right]^3 \right\} dx, \\ F(x, t) &= I(x, t) - \frac{108k\mu^2}{5} J(x, t), \quad F_o = F(x_o, t); \\ A(x) &= \int \frac{dx}{R \left[ H_j^{(3)} + \frac{3}{2} \Phi_p r_c^2 H_p \right]}, \quad A_i = A(x_i), \\ A_o &= A(x_o), \quad C = \frac{p_i - p_o}{A_i - A_o}, \\ G(x) &= \int \frac{\left[ H_j^{(5)} + \frac{5}{3} \Phi_p r_c^4 H_p \right] dx}{R^3 \left[ H_j^{(3)} + \frac{3}{2} \Phi_p r_c^2 H_p \right]^4}, \\ G_i &= G(x_i), \quad G_o = G(x_o). \end{aligned} \quad (31)$$

The load-carrying capacity is defined by

$$N = 2\pi \int_0^{x_o} (Ep - p_o) R \cos \phi dx \quad (31a)$$

or

$$N = \pi R_i^2 p_i + 2\pi \int_{x_i}^{x_o} Ep R \cos \phi dx \quad (31b)$$

the sense of angle  $\phi$  arises from Fig. 2.

The calculation of the mean film pressure distribution would require the calculation of the expected value for various film thickness. For the distribution function given by Eq. (17) we have (Walicka, 2012):

$$\begin{aligned} E(H) &= h, \quad E(H^3) = h^3 \left( 1 + \frac{1}{3} Y^2 \right), \\ E(H^5) &= h^5 \left( 1 + \frac{10}{9} Y^2 + \frac{5}{33} Y^4 \right), \\ E(H^{-3}) &= \frac{1}{h^3} \left[ 1 + \sum_{n=1}^{\infty} \frac{105(n+1)Y^{2n}}{(2n+3)(2n+5)(2n+7)} \right], \\ E(H^{-5}) &= \frac{1}{h^5} \left[ 1 + \sum_{n=1}^{\infty} \frac{35(n+1)(n+2)Y^{2n}}{2(2n+5)(2n+7)} \right], \quad Y = \frac{c}{h}. \end{aligned} \quad (32)$$

## 5. RADIAL THRUST BEARING WITH SQUEEZED FILM

The radial thrust bearing with squeezed film of lubricant is modelled by two parallel disks (Fig. 3).

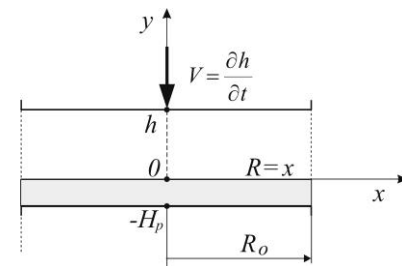


Fig. 3. Squeeze film in a radial thrust bearing

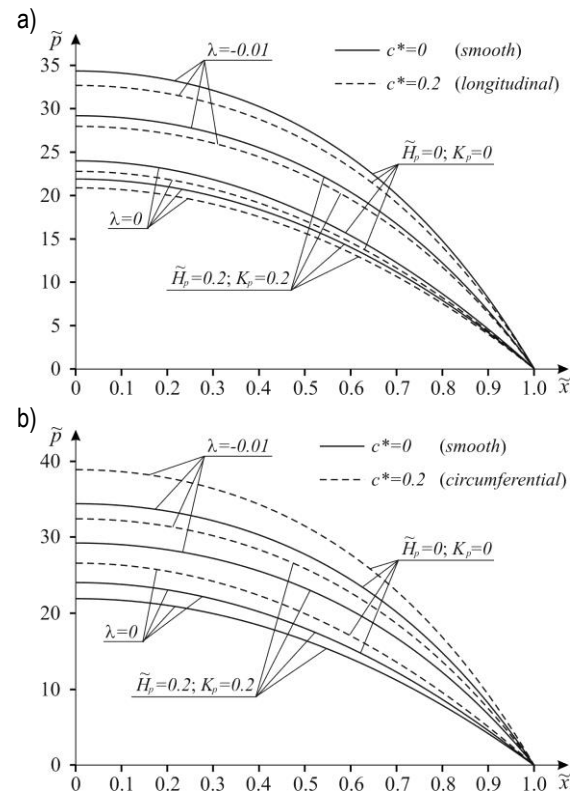


Fig. 4. Dimensionless pressure distribution in the squeeze film thrust bearing with rough surfaces for  $\tilde{H}_p = 0.2$ ,  $K_p = 0.2$ ,  $\lambda = -0.01$  and  $\lambda = 0$  and  $\varepsilon = 0.5$ ; (a) longitudinal roughness and (b) circumferential roughness

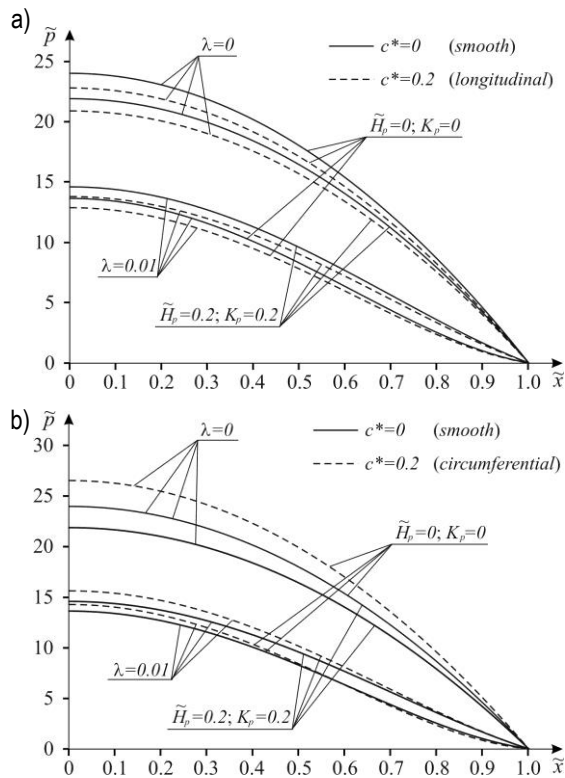


Fig. 5. Dimensionless pressure distribution in the squeeze film thrust bearing with rough surfaces for  $\tilde{H}_p = 0.2$ ,  $K_p = 0.2$ ,  $\lambda = 0$  and  $\lambda = 0.01$  and  $\varepsilon = 0.5$ ; (a) longitudinal roughness and (b) circumferential roughness

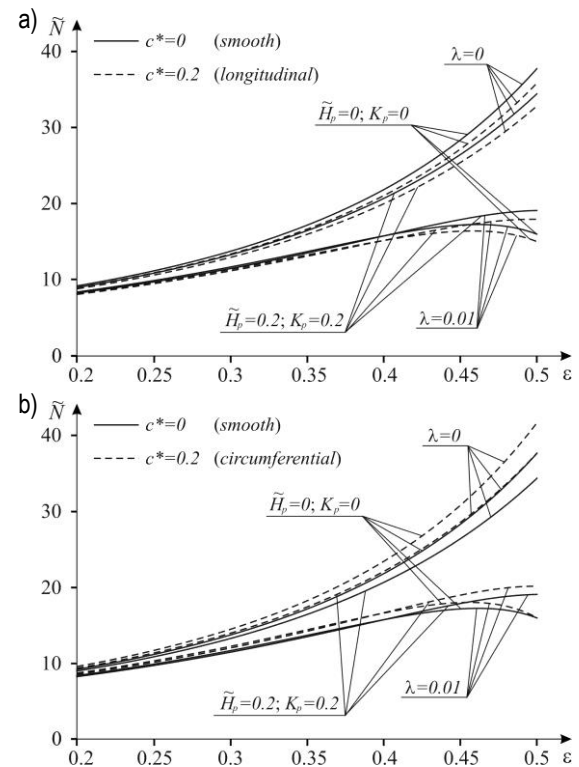


Fig. 7. Load-carrying capacity for the squeeze film thrust bearing with rough surfaces for  $\tilde{H}_p = 0.2$ ,  $K_p = 0.2$ ,  $\lambda = 0$  and  $\lambda = 0.01$  and  $\varepsilon = 0.5$ ; (a) longitudinal roughness and (b) circumferential roughness

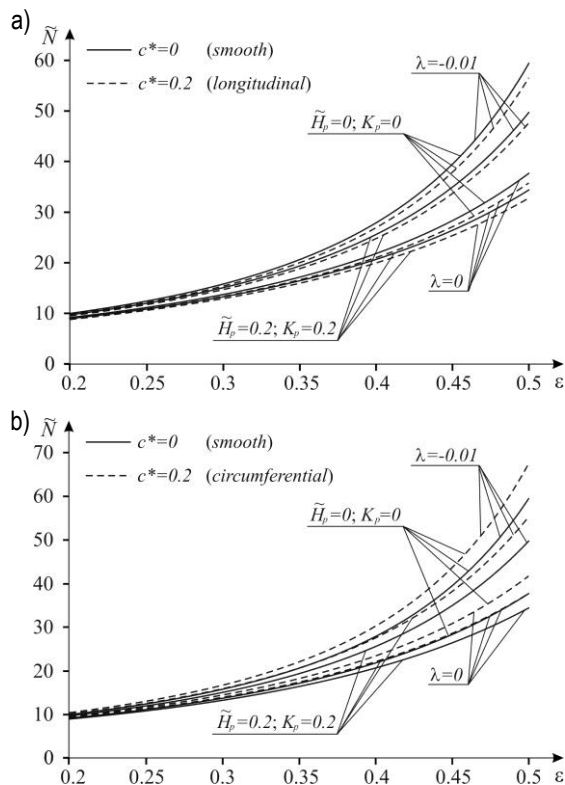


Fig. 6. Load-carrying capacity for the squeeze film thrust bearing with rough surfaces for  $\tilde{H}_p = 0.2$ ,  $K_p = 0.2$ ,  $\lambda = -0.01$  and  $\lambda = 0$  and  $\varepsilon = 0.5$ ; (a) longitudinal roughness and (b) circumferential roughness

Introducing the following parameters:

$$\begin{aligned}\tilde{x} &= \frac{x}{R_o}, \quad x = R, \quad \tilde{R} = \frac{R}{R_o}, \quad \tilde{h} = \frac{h}{h_o} = e(t), \\ e(t) &= 1 - \varepsilon(t), \quad K_p = \frac{r_c}{h_o}, \quad \tilde{H}_p = \frac{\Phi_p H_p}{h_o}, \\ \tilde{p} &= \frac{(E p - p_o)}{\mu \dot{\varepsilon}} \left( \frac{h_o}{x_o} \right)^2, \quad \dot{\varepsilon} = \frac{d\varepsilon}{dt}, \quad \tilde{N} = \frac{N h_o^2}{\mu \dot{\varepsilon} x_o^4}, \\ \lambda &= k \left( \frac{\mu \dot{\varepsilon} x_o}{h_o} \right)^2\end{aligned}\quad (33)$$

we will obtain the formulae for the dimensionless pressure distribution and load-carrying capacity for the radial thrust bearing with a squeeze film of the Rotem-Shinnar type lubricant:

$$\tilde{p} = \frac{3}{M_j^{(3)}} \left[ 1 - \tilde{x}^2 - \frac{27}{10} \lambda \frac{M_j^{(5)}}{(M_j^{(3)})^3} (1 - \tilde{x}^4) \right], \quad (34)$$

$$\tilde{N} = \frac{3\pi}{2M_j^{(3)}} \left[ 1 - \frac{18}{5} \lambda \frac{M_j^{(5)}}{(M_j^{(3)})^3} \right], \quad (35)$$

where:

$$\begin{aligned}M_j^{(3)} &= \tilde{H}_j^{(3)} + \frac{3}{2} K_p^2 H_p, \quad M_j^{(5)} = \tilde{H}_j^{(5)} + \frac{5}{3} K_p^4 H_p, \\ c^* &= \frac{c}{h_o},\end{aligned}\quad (36)$$

$$\tilde{H}_j^{(3)} = \begin{cases} e^3 \left[ 1 + \frac{1}{3} \left( \frac{c^*}{e} \right)^2 \right] & \text{for } j = l, \\ \left( \frac{1}{e^3} \left[ 1 + \frac{2}{3} \left( \frac{c^*}{e} \right)^2 \right] \right)^{-1} & \text{for } j = c, \end{cases}$$

$$\tilde{H}_j^{(5)} = \begin{cases} e^5 \left[ 1 + \frac{10}{9} \left( \frac{c^*}{e} \right)^2 \right] & \text{for } j = l, \\ \left( \frac{1}{e^5} \left[ 1 + \frac{5}{3} \left( \frac{c^*}{e} \right)^2 \right] \right)^{-1} & \text{for } j = c. \end{cases}$$

## 6. CONCLUSIONS

The modified Reynolds equation for a Rotem-Shinnar type of pseudo-plastic lubricants flowing in a clearance of the thrust curvilinear bearing with rough surfaces is derived; to one bearing surface a porous layer adheres. As a result the general formulae for pressure distributions and load-carrying capacity are obtained.

It follows from carried out calculations and their graphic presentations that the both magnitudes are dependent on the signs of rheological parameters  $k$  or  $\lambda$ .

For squeeze film radial bearings the pressures and load-carrying capacities increase with a decrease of the  $\lambda$  values with respect to the suitable values of Newtonian lubricants.

Basing on the adequate formulae for thrust externally pressurized bearing it may conclude that this phenomenon should run inversely. Note the changes of the bearing parameters presented in this paper for rough surfaces and the Rotem-Shinnar lubricant are similar to those for smooth surfaces (Walicki, 2005). The bearing surfaces porosity, expressed as a product of the parameters  $\tilde{H}_p$  and  $K_p$ , results in some small decrease of the pressure and load-carrying capacity.

**Nomenclature:**  $A_1$  – the first Rivlin-Ericksen kinematic tensor,  $c$  – maximum asperity deviation,  $c^*$  – nondimensional roughness parameter,  $e(t)$  – bearing squeezing,  $E(\bullet)$  – expectancy operator,  $f(h_s)$  – probability density distribution function,  $h(x, t)$  – nominal film thickness,  $h_s(x, \vartheta, \xi)$  – random deviation of film thickness,  $H$  – film thickness,  $H_p$  – porous pad thickness,  $k, k_i$  – pseudo-plasticity coefficients,  $N$  – load-carrying capacity,  $p$  – pressure,  $r$  – radius,  $R, R(x)$  – local radius of the lower bearing surface,  $v_x, v_y$  – velocity components,  $x, y$  – orthogonal coordinate,  $\varepsilon(t)$  – squeezing ratio,  $\vartheta$  – angular coordinate,  $\mu$  – coefficient of viscosity,  $\xi$  – random variable,  $\rho$  – fluid density.

## REFERENCES

- Bujurke N.M., Kudenatti R.B., Awati V.B. (2007), Effect of surface roughness on squeeze film poroelastic bearings with special reference to synovial joints, *Mathematical Biosciences*, 209, 76-89.
- Christensen H. (1970), Stochastic model for hydrodynamic lubrication of rough surfaces, *Proc. Inst. Mech. Engrs*, 184, No. 1, 1013-1022.
- Christensen H., Tønder K. (1971), The hydrodynamic lubrication of rough bearing surfaces of finite width, *ASME, J. Lubric. Technol.*, 93(2), 324-330.
- Christensen H., Tønder K. (1973), The hydrodynamic lubrication of rough journal bearings, *ASME, J. Lubric. Technol.*, 95(1), 166-172.
- Dorier C., Tichy J. (1992), Behaviour of a Bingham-like viscous fluid in lubrication flows, *J. Non-Newt. Fluid Mech.*, 45(3), 291-350.
- Gururajan K., Prakash J. (1999), Surface roughness effects in infinitely long porous journal bearing, *Journal of Tribology, Trans. ASME*, 121(1), 139-147.
- Khonsari M.M., Dai F. (1992), On the mixture flow problem in lubrication of hydrodynamic bearing: small solid volume fraction, *STLE Trib. Trans.*, 35(1), 45-52.
- Lin J.-R. (2000), Surfaces roughness effect on the dynamic stiffness and damping characteristics of compensated hydrostatic thrust bearings, *Int. J. Machine Tools Manufact.*, 40, 1671-1689.
- Lin J.-R. (2001), The effect of couple stresses in the squeeze film behavior between isotropic rough rectangular plates, *Int. J. Appl. Mech. Eng.*, 6(4), 1007-1024.
- Lipscomb C.C., Denn M.M. (1984), Flow of Bingham fluids in complex geometries, *J. Non-Newt. Fluid Mech.*, 14(3), 337-349.
- Morgan V.T., Cameron A. (1957), Mechanismus of lubrication in porous metal bearings, *Proc. Conf. on Lubrication and Wear, Inst. Mech. Eng.*, 151-157, London.
- Prakash J., Tiwari K. (1984), An analysis of the squeeze film between rough porous rectangular plates with arbitrary porous wall thickness, *Journal of Tribology, Trans. ASME*, 106(2), 218-222.
- Prakash J., Tiwari K. (1985), Effects of surface roughness on the squeeze film between rectangular porous annular disc with arbitrary porous wall thickness, *Int. J. Mech. Sci.*, 27(3), 135-144.
- Rajalingam C., Rao B.V.A., Prabu S. (1978), The effect of a non-Newtonian lubricant on piston ring lubrication, *Wear*, 50, 47-57.
- Rotem Z., Shinnar R. (1961), Non-Newtonian flow between parallel boundaries in linear movements, *Chem. Eng. Sie.*, 15, 130-143.
- Swamy S.T.N., Prabhu B.S., Rao B.V.A. (1975), Stiffness and damping characteristics of finite width journal bearing with a non-Newtonian film and their application to instability prediction, *Wear*, 32, 379-390.
- Wada S., Hayashi H. (1971), Hydrodynamic lubrication of journal bearings by pseudo-plastic lubricants, Pt 1, Theoretical studies, Pt 2, Experimental studies, *Bull. JSME*, 14(69), 268-286.
- Walicka A. (1989), Accurate and Asymptotic Solution of Simplified Sets of Equations Describing the Motion of Viscous Fluids in a Slot Bounded by Two Co-axial Surfaces of Revolution (in Polish), PWN, Warszawa.
- Walicka A. (1994), *Micropolar flow in a Slot Between Rotating Surfaces of Revolution*, TU Press, Zielona Gora.
- Walicka A. (2002), *Rotational Flows of Rheologically Complex Fluids in Thin Channels* (in Russian), University Press, Zielona Gora.
- Walicka A. (2009), Surface roughness effects in a curvilinear squeeze film bearing lubricated by a power-law fluid, *Int. J. Appl. Mech. Engng*, 14(1), 277-293.
- Walicka A. (2012), Porous curvilinear squeeze film bearing with rough surfaces lubricated by a power-law fluid, *Journal of Porous Media*, 15(1), 29-49.
- Walicka A., Walicki E. (2002a), Surface roughness effect on the pressure distribution in curvilinear thrust bearings, *Exploitation Problems of Machines*, 131(3), 157-167.
- Walicka A., Walicki E. (2002b), Couple stress and surface roughness effects in curvilinear thrust bearings, *Int. J. Appl. Mech. Engng*, Vol. 7, Spec. Issue: SITC, 109-117.
- Walicki E. (1975), Viscous fluid flow in a slot of the curvilinear thrust bearing, *Rev. Roum. Sci. Techn. - Mech. Appl.*, 20(4), 483-493.

# APPLICATION OF A SPH COUPLED FEM METHOD FOR SIMULATION OF TRIMMING OF ALUMINUM AUTOBODY SHEET

Łukasz BOHDAL\*

\*Faculty of Mechanical Engineering, Koszalin University of Technology, Raclawicka 15-17 str., 75-620 Koszalin, Poland

[lukasz.bohdal@tu.koszalin.pl](mailto:lukasz.bohdal@tu.koszalin.pl)

received 5 April 2015, revised 23 February 2016, accepted 24 February 2016

**Abstract:** In this paper, the applications of mesh-free SPH (Smoothed Particle Hydrodynamics) continuum method to the simulation and analysis of trimming process is presented. In dealing with shearing simulations for example of blanking, piercing or slitting, existing literatures apply finite element method (FEM) to analysis of this processes. Presented in this work approach and its application to trimming of aluminum autobody sheet allows for a complex analysis of physical phenomena occurring during the process without significant deterioration in the quality of the finite element mesh during large deformation. This allows for accurate representation of the loss of cohesion of the material under the influence of cutting tools. An analysis of state of stress, strain and fracture mechanisms of the material is presented. In experimental studies, an advanced vision-based technology based on digital image correlation (DIC) for monitoring the cutting process is used.

**Key words:** Trimming, Smoothed Particle Hydrodynamics, Digital Image Correlation

## 1. INTRODUCTION

The process of forming parts from sheet metal using shearing frequently includes blanking, piercing, slitting, and trimming operations. This operations realized with high speed, are a very complicated technological processes in which material undergoes plastic deformations. The main challenge when analyzing trimming is to obtain high quality products characterized optimum sheared edge condition, freedom from burrs and residual stresses. In the automotive industry for instance, burrs formed in the trimming process often scratch the surface of the formed parts in the downstream processes. In order to satisfy the existing standards of quality and to meet customer satisfaction requirements, stamped parts frequently need an additional deburring operation. Therefore, deburring adds significantly to the cost of a stamped part (Golovashchenko, 2006).

Knowledge of the trimming process is based mainly on experimental methods, which are often expensive and unable to be extrapolated to other cutting configurations. Trimming modelling is becoming an increasingly important tool in gaining understanding and improving this process. At the moment the trimming numerical models are based on Lagrangian or Arbitrary Lagrangian Eulerian (ALE) Finite Element Methods (FEM) (Golovashchenko, 2007; Hilditch and Hodgson, 2005b).

The operation of trimming has been studied with respect to sheared edge morphology (Golovashchenko, 2006; Li, 2000) shearing parameters optimization (Ilinichet al., 2011), residual stress analysis, or forming defects using FEM (Hilditch and Hodgson, 2005b; Golovashchenko, 2007). An analysis of the current literature suggests that these approaches imply difficulties. The difficulty in modeling this kind of process using FEM is that all the stages of the material behavior have to be represented: elastoplasticity, damage, crack initiation and propagation, and failure.

Many of problems are resulted from the use of mesh, which should always ensure that the numerical compatibility condition is the same as the physical compatibility condition for a continuum. Hence, the use of grid/mesh can lead to various difficulties in dealing with problems with free surface, deformable boundary, moving interface, and extremely large deformation and crack propagation. Moreover, for problems with complicated geometry, the generation of a quality mesh has become a difficult, time-consuming and costly process.

Mentioned disadvantages of the finite element models can be eliminated using following mesh-free methods: smoothed particle hydrodynamics (SPH), element - free Galerkin method, amongst others (Heisel et al., 2013). SPH-method is used not only to describe the behavior of fluids and granular materials, but also for the modeling of large plastic deformation of solids, such as simulation of the orthogonal cutting processes (Bagci, 2011; Xi et al., 2014; Heisel et al., 2013) shoot peening (Jianming et al., 2011), or guillotining (Gąsiorek, 2013).

In this paper, the applications of mesh-free SPH methodology to the simulation and analysis of 3-D trimming process is presented. At the moment in current literature applications of mesh-free methods to modeling of trimming process is lacking. Developed model is used to analysis of residual stresses in workpiece during and after process under different conditions. Next, the model is validated with experimental research by using vision-based solutions. The proposed advanced vision-based technology is a modern tool which provide accurate measurement of sheet surface shape or deformation (displacement).

## 2. BASIS OF THE SPH METHOD

SPH is total Langrangian and is a truly mesh-free technique



initially developed by Gingold and Monaghan (1977) for the analysis and simulation of astrophysics problems. The idea of this method is to divide a continuum into discrete elements, called particles which are placed at some distance  $d$  from each other. This distance is called particle density  $d$  (Fig. 1).

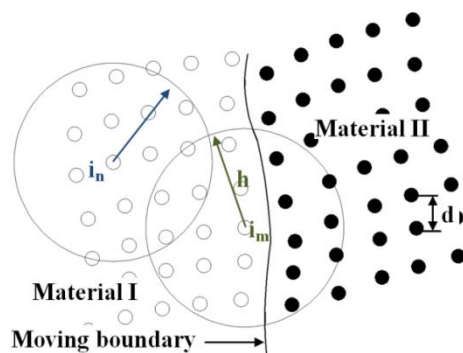


Fig. 1. Smoothing kernel in material volume and at the boundary

The smoothing of field variables is performed in the area with radius  $h$ , called the smoothing length, over which the variables are smoothed by a kernel function. This means that the value of a variable in any spatial point can be obtained by adding the relevant values of the variables within two smoothed circles. Sometimes relative to particle density smoothing length  $\bar{h} = h/d$  is used. In contrast to mesh methods such as, e.g., the FEM, in which the mesh distorts in the case of large deformations, the SPH method can be used to model processes accompanied by large deformations. The SPH approximation of the searched function for continuum mechanics uses the following approaches. A function  $f(x)$  is substituted by its approximation  $A_f(x, h)$ , characterising a body condition. For example, the velocities of a body's points in a particular area are approximated with the following expression:

$$A_f(x, h) = \int f(y) \cdot W(x, h) dy, \quad (1)$$

where:  $W(x, h)$  is a smoothed kernel function (Heisel et al., 2013). The size of the smoothing kernel is defined by the function of  $\Theta$ :

$$W(x, h) = \left( \frac{1}{h(x)^p} \right) \cdot \Theta(x), \quad (2)$$

where:  $p$  is the dimension of space (Das and Cleary, 2007).

The majority of the smoothing kernels used in the SPH method is represented as cubic B-spline, determining the selection of the function  $\Theta$  as follows:

$$\Theta(x) = C \cdot \begin{cases} 1 - \frac{3}{2} \cdot x^2 + \frac{3}{4} \cdot x^3, & \text{if } |x| \leq 1 \\ \frac{1}{4} \cdot (2 - x)^3, & \text{if } 1 \leq |x| \leq 2 \\ 0 & \text{if } 2 \leq |x| \end{cases} \quad (3)$$

where:  $C$  is the normalisation constant. Integration time step can be determined by following equation:

$$\Delta\tau = C_{\Delta\tau} \cdot \min_i \left( \frac{h_i}{C_i + v_i} \right), \quad (4)$$

where:  $i$  is the particle number;  $C_{\Delta\tau}$  is the timestep increase coefficient (in this work  $C_{\Delta\tau} = 0.2$ );  $v_i$  is the velocity of particle  $i$ . It is important to notice that coefficient  $C_{\Delta\tau}$  directly influences the integration time step.

The smoothing length in LS-DYNA solver used in this work dynamically varies so that the number of neighbouring particles remains relatively constant. It is realized by recalculating the smoothing length in accordance with the average particle density:

$$h = h_0 \left( \frac{d_0}{d_i} \right)^{1/p}, \quad (5)$$

or by solving the continuity equation:

$$\frac{dh}{dt} = \frac{1}{d} \cdot \frac{h}{d} \cdot \frac{\partial d}{\partial t}, \quad (6)$$

where:  $d_0$  and  $h_0$  are the initial density and the initial smoothing length.

A quadratic approximation of the particle motion is mainly used for the SPH method. A motion of the particles can be described here with the following equation:

$$\frac{\partial v_i^\alpha}{\partial t} = \sum_{j=1}^N m_j \cdot \left( \frac{\sigma_i^{\alpha\beta}}{d_i^2} + \frac{\sigma_j^{\alpha\beta}}{d_j^2} + A_{ij} \right) \cdot \frac{\partial W_{ij}}{\partial x_i^\beta}, \quad (7)$$

where:  $j$  is particle number;  $N$  is the number of neighbouring particles;  $d_i$  and  $d_j$  are the densities of  $i$  and  $j$  particles respectively;  $A_{ij}$  are the specific external forces;  $W_{ij} = W(x_i - x_j, h)$  is the smoothing kernel;  $v_i^\alpha = \frac{dx_i^\alpha}{dt}$  is the velocity of particle  $i$ ;  $m_j$  is the mass of particle  $j$ ;  $\sigma_i^{\alpha\beta}$ ,  $\sigma_j^{\alpha\beta}$  are the stress tensors of  $i$  and  $j$  particles respectively (Heisel et al., 2013).

### 3. CONSTITUTIVE MODEL FOR MATERIAL

In trimming models, accurate and reliable flow stress models are considered as highly necessary to represent workpiece materials' constitutive behavior, the constitutive material model reported by Johnson and Cook (1985) was employed in this study, it is often used for ductile materials in cases where strain rate vary over a large range and where adiabatic temperature increase due to plastic heating cause material softening. The model can be represented by Eq (8):

$$\sigma_Y = [A + B(\bar{\epsilon}^p)^n][1 + C \ln \dot{\epsilon}^*][1 - (T^*)^m], \quad (8)$$

where:  $A$ ,  $B$ , and  $n$  are strain hardening constants;  $C$  is the strain rate hardening constant,  $\sigma_Y$  is the equivalent flow stress,  $\bar{\epsilon}^p$  is the equivalent plastic strain and  $m$  is the thermal softening constant that modifies the homologous temperature term,  $T^*$ . The homologous temperature is defined as,  $T^* = \frac{T - T_r}{T_m - T_r}$ , where  $T$  is the temperature of the material,  $T_r$  is a reference temperature (typically room temperature), and  $T_m$  is the melt temperature of the material. The term,  $\dot{\epsilon}^*$ , is the normalized strain rate of the material or  $\dot{\epsilon}^* = \frac{\dot{\epsilon}^p}{\dot{\epsilon}_0}$ , where  $\dot{\epsilon}_0 = 1.0s^{-1}$ .

Tab. 1. The Johnson-Cook constitutive model constants for AA6111-T4

| $A$ [MPa] | $B$ [MPa] | $C$   | $n$  | $m$  |
|-----------|-----------|-------|------|------|
| 324.1     | 113.8     | 0.002 | 1.34 | 0.42 |

The failure model must accurately predict the material equivalent plastic failure strain for various stress states, strain rates, and temperatures. The Johnson Cook failure model is:

$$\bar{\epsilon}_f^p = [D_1 + D_2 e^{D_3 \sigma^*}][1 + D_4 \ln \dot{\epsilon}^*][1 + D_5 T^*], \quad (9)$$

where:  $D_1, D_2, D_3, D_4$  and  $D_5$  are material specific constants,  $\bar{\varepsilon}_f^p$  is the equivalent plastic failure strain of the material and  $\sigma^*$  is the stress triaxiality factor defined as  $\sigma^* = \frac{\sigma_m}{\bar{\sigma}}$ , where  $\sigma_m$  is the average of the three principle stresses. Aluminum alloy AA6111-T4, which is often employed for exterior panels in the automotive industry, is used to simulate typical production conditions. For AA6111-T4:  $D_1 = -0.77$ ;  $D_2 = 1.45$ ;  $D_3 = -0.47$ ;  $D_4 = 0$ ;  $D_5 = 1.6$ .

#### 4. COUPLED SPH+FEM MODEL

In the suggested approach to the modeling of the trimming process, a coupling of the FEM model and the model based on hydrodynamic particles (the SPH method) has been proposed. The one big disadvantage of meshless methods over the Lagrangian models is their computational demand. For that reason, in the trimming model, only an area in which there is a direct interaction between the upper knife and the sheet metal is modeled with SPH particles (Fig. 2). In the case of the SPH approach, the particles are tied to the Lagrangian portion of domain using tied types of the contact. The implementation of the SPH method in LS-DYNA allows for seamless transition between the two domains without resorting to the contact definitions. A three-dimensional model of trimming is built in LS - DYNA solver. Numerical calculations are performed for the 3D state of strain and 3D state of stress in this model.

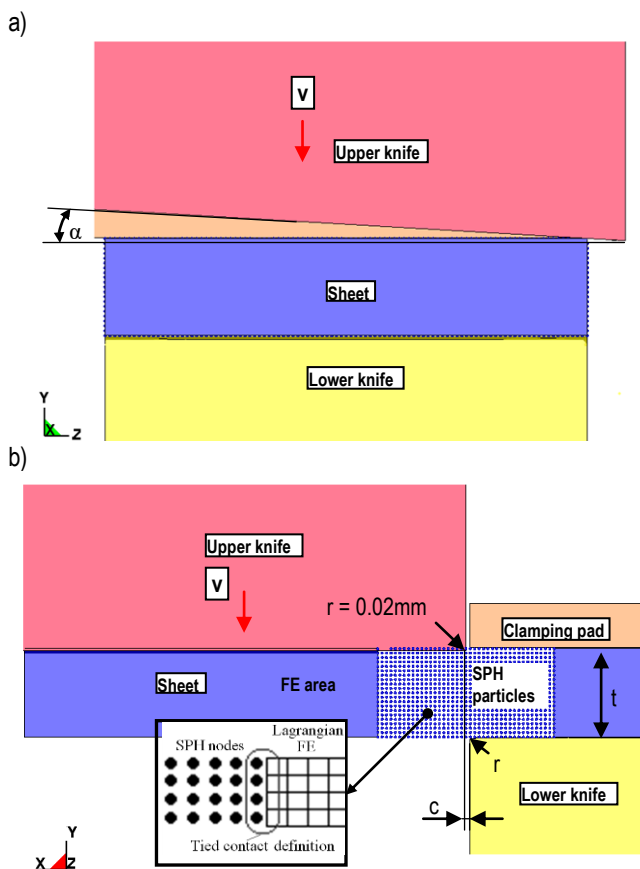


Fig. 2. FEM+SPH coupled model: a) side view; b) front view

Aluminum alloy with thickness of  $t = 1$  mm is used as the material to be cut in the numerical and experimental studies. A velocity of  $v = 100$  mm/s is applied to the upper knife in the y direction. The contact between ideally rigid tools and the deformable sheet metal is described using Coulomb's friction model, and constant coefficients of static friction  $\mu_s = 0.08$  and kinetic friction  $\mu_d = 0.009$  are accepted. A rake angle of upper knife is set about  $\alpha = 3^\circ$  and clearance  $c = 0.1$  mm.

#### 5. RESULTS AND DISCUSSION

##### 5.1. Analysis of trimming mechanism

Sample results of numerical and experimental investigations at various stages of the trimming process are shown in Figs. 3–5. At the beginning of the cutting process during the elastic-plastic phase the plasticised zone occurs only at the highest concentration of stresses, that is in direct contact with the cutting edges of tools. During the second phase the intensive plastic flow of the material in the surroundings of the cutting surface can be observed (Fig. 3a). A characteristic distortion of SPH particles in this areas can be seen. The highest stresses occurs near the cutting edges of the tools in this phase ( $\sigma_{max} = 411$  MPa). Figure 3b shows the image from a high-speed camera i-SPEED TR in the same phase of process.

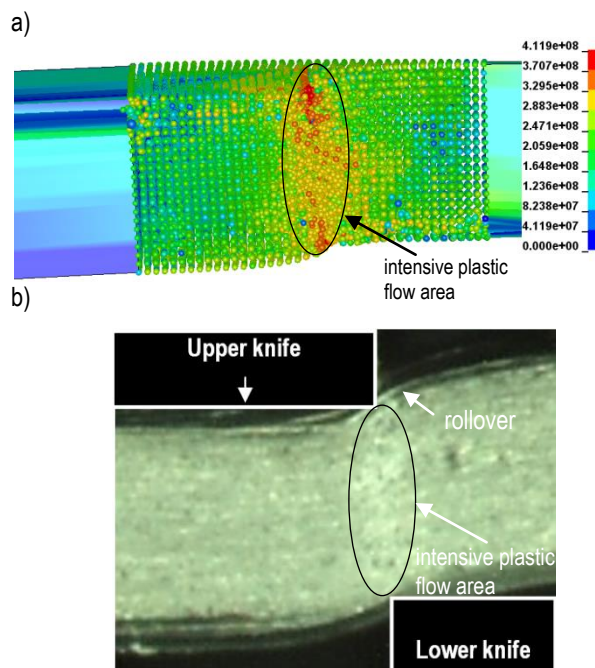
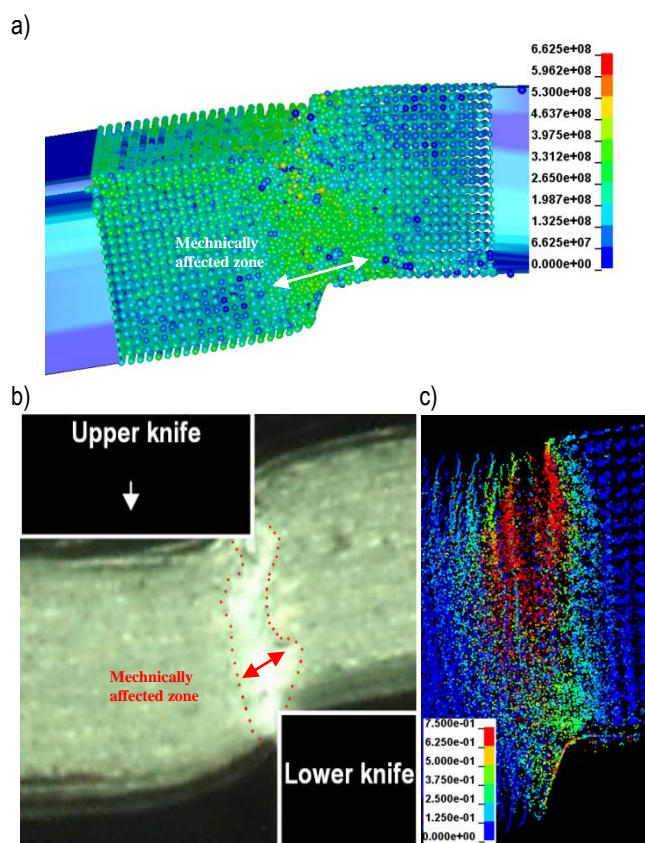


Fig. 3. Comparison of the numerical and experimental results for upper knife penetration  $w = 0.25$  mm: a) FEM+SPH model (equivalent stress distribution [Pa]), b) recorded image from a high-speed camera

During the trimming process, a camera together with a computer record a set of consecutive images of the sample surface. To quantify the displacements of material, a digital image correlation technique (DIC) is used (Domski and Katzer, 2013). In two-dimensional digital image correlation, displacements are directly detected from digital images of the surface of an object (speci-

men) (Kozicki and Teichman, 2007). Then, the images on the surface of the object, one before and another after deformation are recorded and saved in a computer as digital images. These images are compared to detect displacements by searching a characteristic features from one image to another. This features might be material texture, machining marks (for example an area of multiple pixel points), oxide deposits, finishing/polishing marks. Using this method it is possible to determine the areas of strong nonlinearities and deformation of material structure (Fig. 3b). The formation of rollover can be identified.

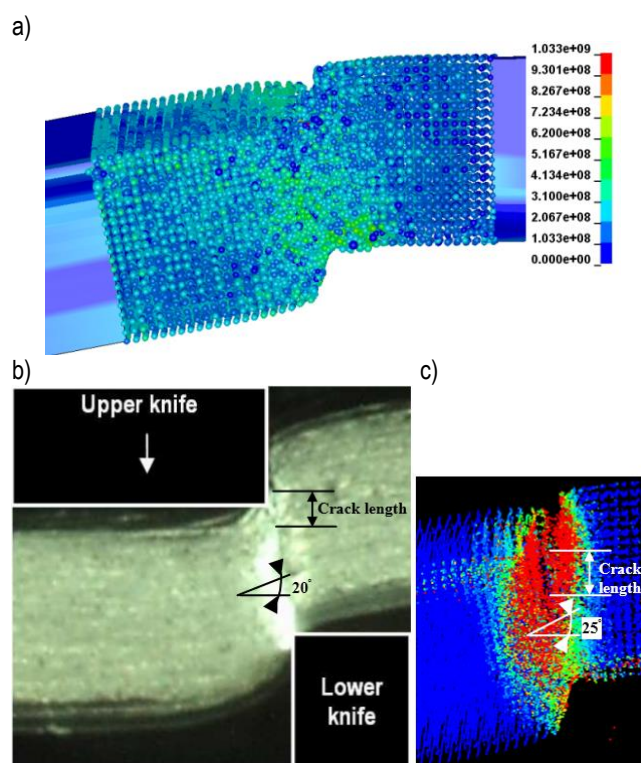
Both in numerical model and experimental investigations the plastic strain localization zones propagate much faster from the moving (upper knife) blade than from the bottom stationary blade (Fig 4c). The deformation zone is non-symmetric with respect to the top and bottom blades (Fig. 4). According to work (Li, 2000) this is not due to dynamic (or inertial) effects but rather to the shearing configuration of the experimental setup. It can be observed the large distortions of the SPH particles near the bottom edge of sheet just before burr formation (Fig. 4a). The mechanically affected zone in this area is extended along the  $x$  direction (Figs. 4a and b).



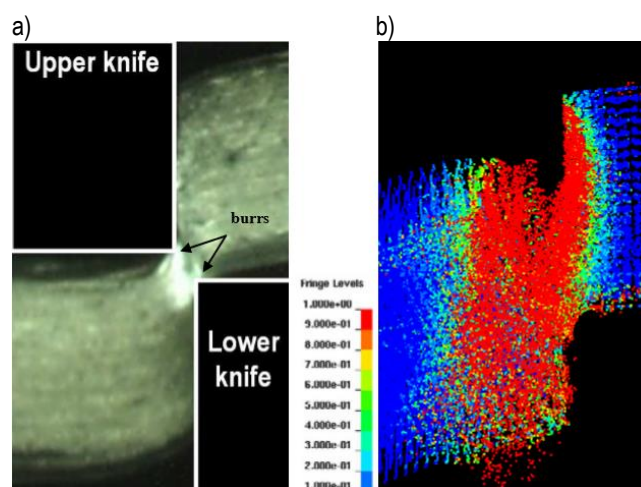
**Fig. 4.** Comparison of the numerical and experimental results for upper knife penetration  $w = 0.35$  mm: a) FEM+SPH model (equivalent stress distribution), b) recorded image from a high-speed camera (deformation zone is extended on a whole sheet thickness and along  $x$  direction which is observed as an area with high light intensity), c) FEM+SPH model (equivalent strain distribution in contact zone)

Fig. 5 shows the equivalent stress and strain distribution during the cracking phase. Since the crack will initiate and propagate through the localization zone, the cut surface will be curved and the burr will form because the crack will not run to the bottom

blade tip. This trend is evident in both the numerical model as well as experimental studies (Fig. 5). Results in the study by Golovashchenko (2006, 2007) and Hilditch (2005a), show that no burr formation occurs at clearances below 5% of the sheet thickness, attributed to the crack initiation in the sheet at the bottom blade tip. In mechanically affected zone a characteristic material flow along the crack path can be observed. To accurately measure the material flow on the surface of an object using DIC, a texture patterns need to be related to small group areas. Obtained results are in agreement with these experimental observations with approximately error margin about  $5^\circ$  in flowing angle measurement.



**Fig. 5.** Comparison of the numerical and experimental results for upper knife penetration  $w = 0.45$  mm: a) FEM+SPH model (equivalent stress distribution), b) recorded image from a high-speed camera, c) FEM+SPH model (equivalent strain distribution in contact zone)



**Fig. 6.** Comparison of the numerical and experimental results at final separation: a) recorded image from a high-speed camera, b) FEM+SPH model (equivalent strain distribution in contact zone)



## 5.2. Sheared edge quality

The quality of the sheared edge produced from the trimming of the sheet would depend upon the damage caused to the edge, the extent of the damage around the edge and burr height. The extent of the mechanically affected region can be quantified through the equivalent plastic strain state. Strain measurements are made at three locations on the cut surface: without burr side, middle and burr side (Fig. 7).

An analysis of strain state shows that the maximum values of plastic strain occurs at the edge and then gradually decreases with increasing distance from the cut edge until it reaches a low constant value (Fig. 8). The measured results indicate that the maximum strain has reached a value of 1.5 at the middle of cut surface, and it exponentially decays away from the edge. The lowest values of strain occur in the upper part of the sample. The width of the deformed area is small and carry out approximately 0.1 mm.

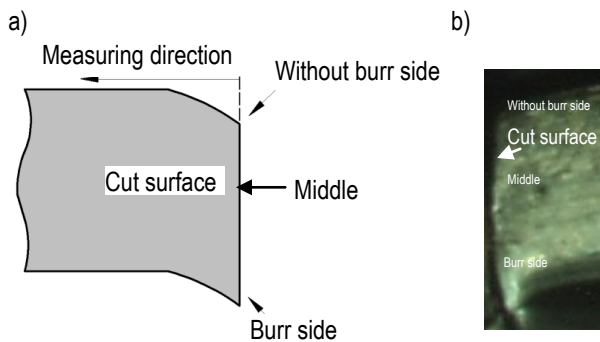


Fig. 7. Strain measurement areas at cut surface: a) schematic diagram, b) experimental profile

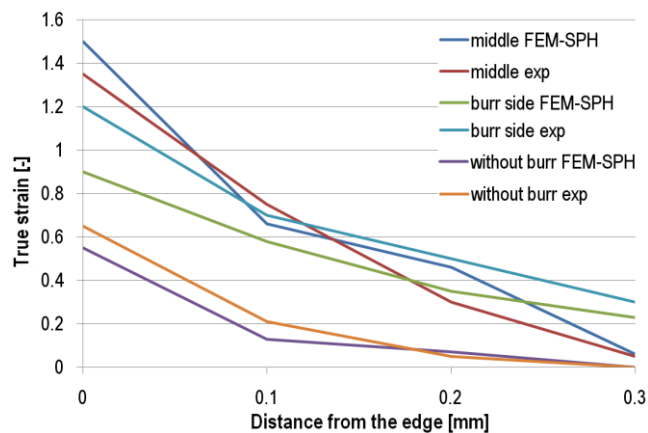


Fig. 8. Results of the true strain measured in sheared edge

Analysis of residual stress state in cut surface is presented on Fig 9. In the following, the von Mises equivalent stress is used to define and compare the residual stress state (Achouri et al., 2014) which is by definition is a complex three-dimensional stress state with interaction between the components of the stress tensor. In each analyzed cut surface area a high increase of stresses at a small tool penetration can be seen. In the initial phases of the cutting process the maximum stress values occur at the edge of cut surface and then decreases with increasing distance from the

cut edge. During the workpiece forming large oscillations in stress values in unsteady state of process are observed. Stabilization of stresses occur after complete separation of the material and depends on distance from the edge. At any measured areas stress after stabilization did not exceed 200 MPa.

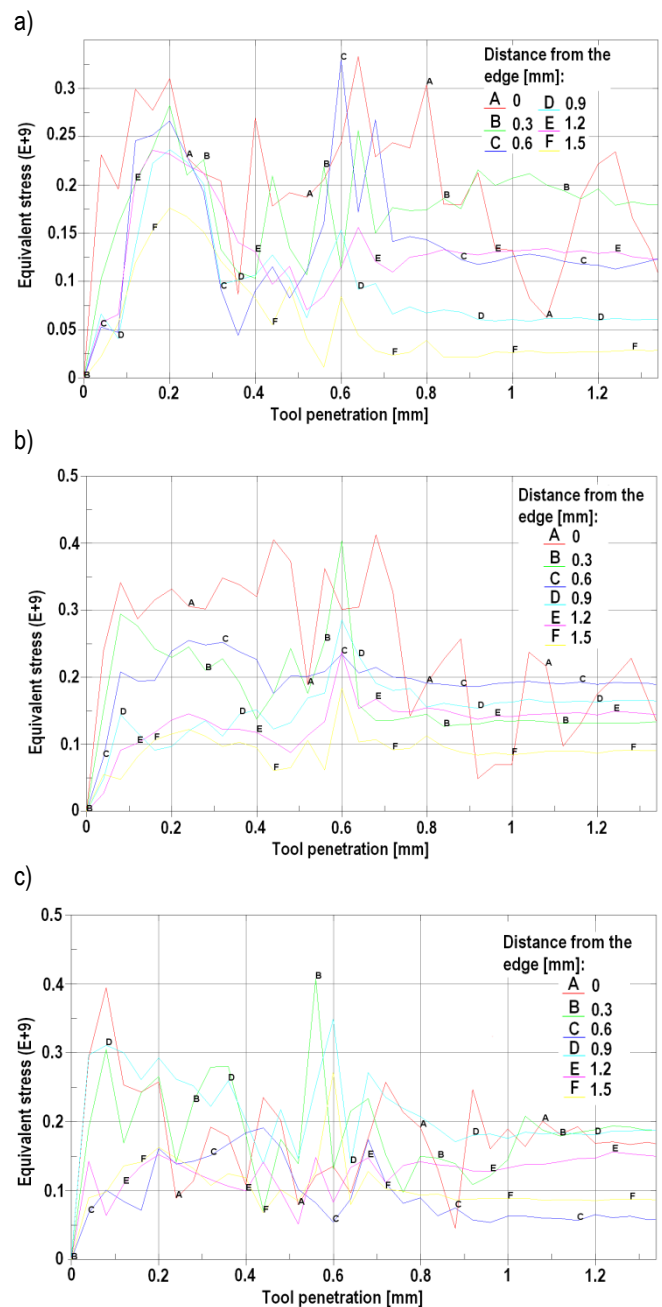


Fig. 9. Results of the equivalent stress measured in sheared edge during process [Pa]: a) without burr side, b) middle, c) burr side

Comparison of the characteristic features of cut surface obtained from numerical model and experiment shows good agreement in the depth angle and the burr height. Some differences occurs in the measurement of the rollover of the upper edge of workpiece (Fig. 10). Developed 3D FEM-SPH model of the trimming process allows for the observation of non-uniform burr at selected locations along the cutting line. From the results obtained it can be seen that the fracture process because less steady and progresses in a non-uniform manner in some locations along the



shearing line. The transition of the material fracture from the “shear mode” to the “shear and tear mode” is observed.

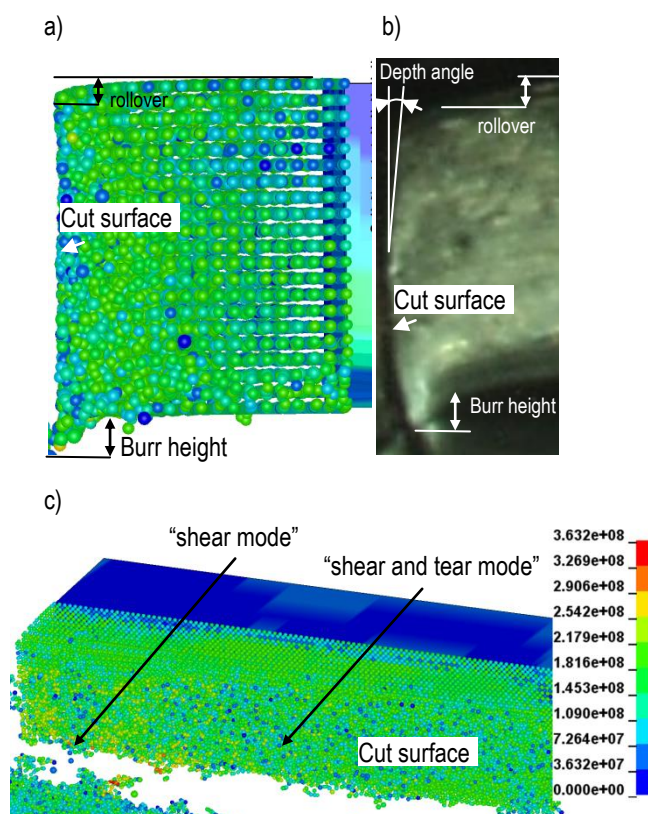


Fig. 10. Characteristic features of the sheared edge: a) FEM+SPH model (equivalent stress distribution – front view), b) experimental profile, c) FEM+SPH model (equivalent stress distribution - side view)

## 6. CONCLUSIONS

This paper presents a SPH coupled FEM method to simulate the trimming process. The application of SPH method is fairly new in metal forming simulations. Its features are not fully understood and the most effective means to exploit it are still being discovered. A hybrid approach that used the SPH formulation in the shearing zone with high material distortion and the Lagrangian formulation in the region away from the highly distorted zone is very robust and reliable. It reduces the simulation time needed to obtain the results. The FEM-SPH method is validated using the advanced vision based system and DIC method. Based on the experimental data, the model has been shown to be able to provide adequate estimation of the deformation state of material and might be used for process control as well as optimizing the trimming parameters. The good agreement between simulation results and the experimental data have confirmed the correctness and credibility of the model. Additionally, next paper will be focused on examination and analysis of influence of process technological parameters for example: the clearance, tool geometry, cutting velocity on residual stresses and quality of cut surface using the SPH method.

## REFERENCES

1. Achouri M., Gildemyn E., Germain G., Dal Santo P., Potiron A. (2014), Influence of the edge rounding process on the behavior of blanked parts: numerical predictions with experimental correlation, *International Journal of Advanced Manufacturing Technology*, 71, 1019-1032.
2. Bagci E. (2011), 3-D numerical analysis of orthogonal cutting process via mesh-free method, *International Journal of Physical Sciences*, 6, 1267-1282.
3. Das R., Cleary P.W. (2007), Modeling plastic deformation and thermal response in welding using smoothed particle hydrodynamics, *16th Australasian fluid mechanics conference*, 2–7 December 2007.
4. Domski J., Katzer J. (2013), Load-deflection characteristic of fibre concrete based on waste ceramic aggregate, *Annual Set The Environment Protection* 15, 213-230.
5. Gąsiorek D. (2013), The application of the smoothed particle hydrodynamics (SPH) method and the experimental verification of cutting of sheet metal bundles using a guillotine, *Journal of Theoretical and Applied Mechanics*, 51 (4), 1053-1065.
6. Gingold R.A., Monaghan J.J. (1977), Smooth particle hydrodynamics: theory and application to non-spherical stars, *Monthly Notices of the Royal Astronomical Society*, 181, 375-389.
7. Golovashchenko S.F. (2006), A study on trimming of aluminum autobody sheet and development of a new robust process eliminating burrs and slivers, *International Journal of Mechanical Sciences*, 48, 1384-1400.
8. Golovashchenko S.F. (2007), Analysis of Trimming of Aluminum Closure Panels, *JMEPEG*, 16, 213-219.
9. Heisel U., Zaloga W., Krivoruchko D., Storchak M., Goloborodko L. (2013), Modelling of orthogonal cutting processes with the method of smoothed particle hydrodynamics, *Production Engineering Research and Development*, 7, 639-645.
10. Hilditch T.B., Hodgson P.D. (2005a), Development of the sheared edge in the trimming of steel and light metal sheet, Part 1 - Experimental observations, *Journal of Materials Processing Technology*, 169, 184-191.
11. Hilditch T.B., Hodgson P.D. (2005b), Development of the sheared edge in the trimming of steel and light metal sheet, Part 2 – Mechanisms and modeling, *Journal of Materials Processing Technology*, 169, 192-198.
12. Ilinich A.M., Golovashchenko S.F., Smith L.M. (2011), Material anisotropy and trimming method effects on total elongation in DP500 sheet steel, *Journal of Materials Processing Technology*, 211, 441-449.
13. Jianming W., Feihong L., Feng Y., Gang Z. (2011), Shot peening simulation based on SPH method, *International Journal of Advanced Manufacturing Technology*, 56, 571-578.
14. Johnson G.R., Cook W.H. (1985), Fracture characteristics of three metals subjected to various strains, strain rates, temperatures and pressures, *Engineering Fracture Mechanics*, 21(1), 31-48.
15. Kozicki J., Teichman J. (2007), Experimental investigations of strain localization in concrete using digital image correlation (DIC) technique, *Archives of Hydro-Engineering and Environmental Mechanics*, 54(1), 3-24.
16. Li M. (2000), Micromechanisms of deformation and fracture in shearing aluminum alloy sheet, *International Journal of Mechanical Sciences*, 42, 907-923.
17. Xi Y., Bermingham M., Wang G., Dargusch M. (2014), SPH/FE modeling of cutting force and chip formation during thermally assisted machining of Ti6Al4V alloy, *Computational Materials Science*, 84, 188-197.

## LOW CYCLE FATIGUE OF STEEL IN STRAIN CONTROLLED CYCLIC BENDING

Anna KULESA\*, Andrzej KUREK\*, Tadeusz ŁAGODA\*, Henryk ACHEŁLIK\*, Krzysztof KLUGER\*

\*Faculty of Mechanical Engineering, Department of Mechanics and Machine Design,  
Opole University of Technology, ul. Mikołajczyka 5, 45-271 Opole, Poland[a.kulesa@po.opole.pl](mailto:a.kulesa@po.opole.pl), [a.kurek@po.opole.pl](mailto:a.kurek@po.opole.pl), [t.lagoda@po.opole.pl](mailto:t.lagoda@po.opole.pl), [h.achtełlik@po.opole.pl](mailto:h.achtełlik@po.opole.pl), [k.kluger@po.opole.pl](mailto:k.kluger@po.opole.pl)

received 5 April 2015, revised 22 February 2016, accepted 25 February 2016

**Abstract:** The paper presents a comparison of the fatigue life curves based on test of 15Mo3 steel under cyclic, pendulum bending and tension-compression. These studies were analyzed in terms of a large and small number of cycles where strain amplitude is dependent on the fatigue life. It has been shown that commonly used Manson-Coffin-Basquin model cannot be used for tests under cyclic bending due to the impossibility of separating elastic and plastic strains. For this purpose, some well-known models of Langer and Kandil and one new model of authors, where strain amplitude is dependent on the number of cycles, were proposed. Comparing the results of bending with tension-compression it was shown that for smaller strain amplitudes the fatigue life for both test methods were similar, for higher strain amplitudes fatigue life for bending tests was greater than for tension-compression.

**Key words:** Lifetime, Strain Control, Bending, Push-Pull, Tension-Compression

## 1. INTRODUCTION

Most often fatigue tests for a range of low number of cycles (Low Cycle Fatigue) are performed at a controlled strain (Walat et al., 2015) and the high range of cycles (High Cycle Fatigue) tests are characterized by a study in strength-controlled environment (Karolczuk et al., 2015). Such tests are carried out for tension-compression and torsion of thin specimens. However, in the case of bending or torsion of full specimens, as is the case of many experimental studies, the torque causing bending or torsion is controlled and therefore the tests are conducted in terms of large number of cycles (Achtełlik et al., 1996). In the literature to describe the fatigue test results for tension-compression both stress and strain models are used (Niesłony et al., 2012; Zhao et al., 2007; Shul'ginov 2008, Lee, Song, 2006). However there is a significant amount of fatigue tests for bending, often pendulum rather than rotary. It turns out that for bending, due to the stress (strain) gradient, those two types of models are not equal. There aren't many studies comparing stress and strain fatigue curves (models). For stress curves some comparison might be found in (Manson and Muralidharan, 1987; Troschenko, 1996, Megahed 1990). While in (Krzyżak et al., 2014) authors prove that changes in bending plane has an effect on fatigue strength relative to the constant surface bending (pendulum bending). Results from these comparisons show that on the level of fatigue limit the loading method does not affect fatigue life. However for higher stress levels fatigue strength obtained from bending tests is higher than corresponding push-pull results. There is no comparison of this kind for strain curves.

Therefore, the present study compares the fatigue life curves of 15Mo3 steel obtained from new test stand capable of conducting pendulum bending with controlled strain amplitude with push-pull results. The results for push-pull tests were taken from the literature (Boller and Seeger, 1987).

## 2. STRAIN-LIFE CURVES

The most well-known equation allowing to describe fatigue properties from strain-controlled tests is proposed by Manson-Coffin-Basquin (MCB) for the strain-life curve ( $\varepsilon_a - N_f$ ):

$$\varepsilon_{at} = \varepsilon_{ap} + \varepsilon_{ae} = \varepsilon'_f (2N_f)^c + \frac{\sigma'_f}{E} (2N_f)^b, \quad (1)$$

where:  $E$  – Young's modulus;  $\varepsilon'_f$ ,  $c$  – coefficient and exponent of the plastic strain, respectively;  $\sigma'_f$ ,  $b$  – coefficient and exponent of the fatigue strength, respectively.

This model (1) can only be used when it is possible to distinguish elastic  $\varepsilon_{ae}$  and plastic  $\varepsilon_{ap}$  parts of the strain amplitude  $\varepsilon_{at}$  (Niesłony et al., 2008, Basan et al., 2011).

Then for cyclic loadings we get:

$$\varepsilon_{ae} = \frac{\sigma_a}{E} \quad (2)$$

and

$$\varepsilon_{ap} = \varepsilon_{at} - \varepsilon_{ae}. \quad (3)$$

The relation between stress and strain amplitude is described with Ramberg-Osgood equation:

$$\varepsilon_{at} = \frac{\sigma_a}{E} + \left( \frac{\sigma_a}{K'} \right)^{1/n'}. \quad (4)$$

where:  $K'$  – coefficient of cyclic strength;  $n'$  – exponent of cyclic hardening.

However we often face the problem with distinguishing elastic and plastic parts of strain amplitude. This problem occurs for example when the stress amplitude  $\sigma_a$  is greater than twice yield strength of the material  $2R_e$  (Marcisz et al., 2012)

$$\varepsilon_{at} = \varepsilon_{ap} + \varepsilon_{ae} + \varepsilon_{ane} = \varepsilon_a = \frac{\sigma_a}{E} + \left( \frac{\sigma_a}{K'} \right)^{1/n'} + \left( \frac{\sigma_a}{K''} \right)^{1/n''}, \quad (5)$$

where:  $\varepsilon_{ane}$  – unelastic strain amplitude.

Another problem is shown in (Radhakrishnan, 1992), where authors prove that the importance of plastic deformation amplitude in the expression (1) depends on fatigue life, therefore  $c$  is not a constant value.

Furthermore different authors have proposed different empiric models subordinating total strain amplitude on the number of cycles.

Langer's (1962) proposal can be one of the examples. It is commonly used in many studies and is prompted by Manson (1965, 1979) and Chopra (1999)

$$\log N_f = A - B \log(\varepsilon_{at} - C), \quad (6)$$

where:  $A, B, C$  – material constants.

Another model was proposed by Kandil (2000) and Gorash and Chen (2013):

$$\log \varepsilon_{at} = A - B \log(N_f) + C \log^2(N_f), \quad (7)$$

where:  $A, B, C$  – material constants.

As in the case of cyclic bending tests where there is no possibility to distinguish elastic and plastic parts of total strain amplitude the MCB model (1) cannot be used. However both (6) and (7) or any other empirical form of strain-life model can be used. It can be for example combination of (6) and (7):

$$\log(\varepsilon_{at} - D) = A - B \log(N_f) + C \log^2(N_f), \quad (8)$$

where:  $A, B, C, D$  – material constants.

Very rich overview of fatigue life models can be found among others in (Kurek et al., 2015).

The newly proposed form of the strain-life curve model (8) requires the calculation of four material constants as well as the popular MCB model (1).

### 3. EXPERIMENT

In this paper we will present new test stand for fatigue tests under bending and capable of experimental studies with controlled strain in the range of a small number of cycles (LCF). Operation of the machine was verified on the basis of experimental tests on specimens made of steel commonly used in the power industry – 15Mo3 (16Mo3, 1.5415) (Boller and Seeger, 1987). Finally the strain controlled experimental data for tension-compression and pendulum bending was compared.

The Manson-Coffin-Basquin curve (1) for tension-compression on the basis of results from three different tests collected in (Boller and Seeger, 1987) can be written as:

$$\varepsilon_{at} = 0.229(2N_f)^{-0.470} + \frac{766.5}{210000}(2N_f)^{-0.094}, \quad (9)$$

and Ramberg-Osgood curve (4) as:

$$\varepsilon_{at} = \frac{\sigma_a}{210000} + \left(\frac{\sigma_a}{1035}\right)^{1/0.202}. \quad (10)$$

Our studies were performed on the newly constructed machine, as shown in Fig. 1.

The idea behind this machine is that using the screw on the eccentric we can set the deflection of machine arm acting on the specimen, that deflection is set as constant and controlled by the micrometer. This way we obtain a constant strain amplitude on specimen. One of those specimens after experiment is shown in Fig. 2.

Additionally, during the test, bending torque is monitored. At the time, when this torque drops significantly, the initiation

of fatigue crack occurs but further tests allow us to obtain total fatigue life of the tested specimen.



Fig. 1. Strain controlled stand for bending loading

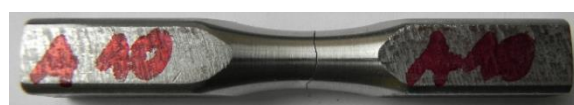


Fig. 2. Specimen with fracture after bending loading

The study determined the fatigue life both to the initiation point and total fatigue life. At the fatigue crack initiation point there is a sharp drop of the bending moment acting on specimen which correlate with the appearance of visible cracks on a specimen of a size of less than 1 mm.

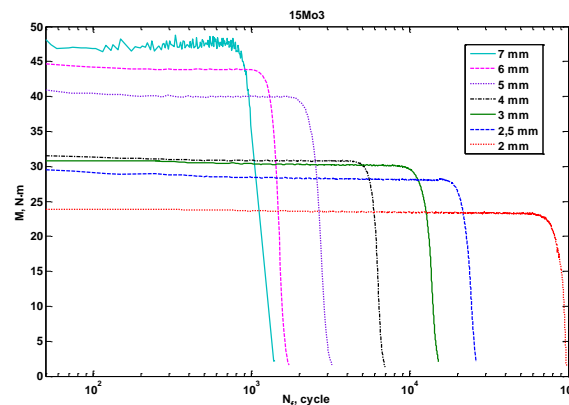


Fig. 3. Change of the moments causing bending as a function of number of cycles at a constant strain amplitudes

In the Fig. 3 change of the moment depending on time at fixed arm deflection amplitudes, which means a constant strain, was presented. The graph shows that the material slightly weakens cyclically. From the analysis of moment changes it can be seen that for larger deflection amplitudes we obtain larger amplitudes of bending moment and consequently lower fatigue durability.

This quantity of cycles is adopted as an initiation of a fatigue crack. In the Fig. 4 strain amplitudes as a function of number of cycles leading to initiation for material 15Mo3 were established. The data come from literature for tension-compression and own research for oscillatory bending as a function of number of cycles for initial bending and total lifetime.

Cross-section of the specimen after fatigue tests under pendulum bending is shown in Fig. 5. The photograph clearly shows

a neutral plane of bending and the symmetry of the fatigue crack process.

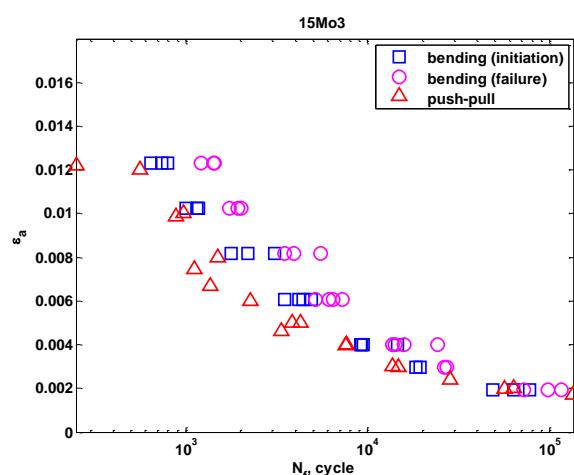


Fig. 4. Experimental strain amplitudes as a function of number of cycles

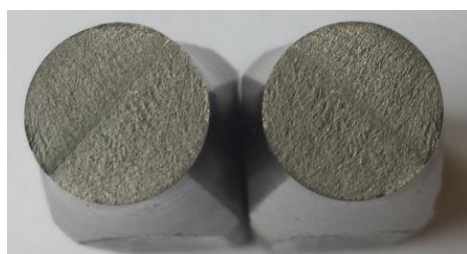


Fig. 5. Cross-section of the specimen after fatigue tests under pendulum bending

#### 4. COMPARISON OF FATIGUE LIFE CURVES

Fig. 6 shows the fatigue strain-life curves for pendulum bending and tension-compression according to the Kandil proposal (7) and Fig. 7 as proposed by Langer (6). In addition the calculation of the model proposed by the authors (8) is shown in Fig. 8.

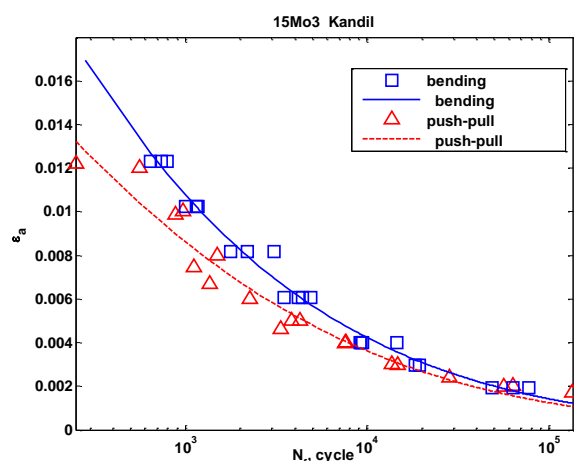


Fig. 6. Strain-life curves according to Kandil's model for both push-pull and bending tests

Then, for all analyzed curves the correlation parameter R-squared was determined both for tension-compression (Tab. 1) and bending (Tab. 2). From the analysis of data it should be noted

that relatively similar statistical parameters were obtained for the analyzed models. By analyzing the shapes of fatigue curves it can be seen that for Langer's proposal for higher strain amplitudes both curves for bending and push-pull tests are very close. The two other models lack this flaw. What is more, author's proposal (8) is shaped like a letter 'S' which is sometimes advised for stress-life models (Kurek et al., 2015).

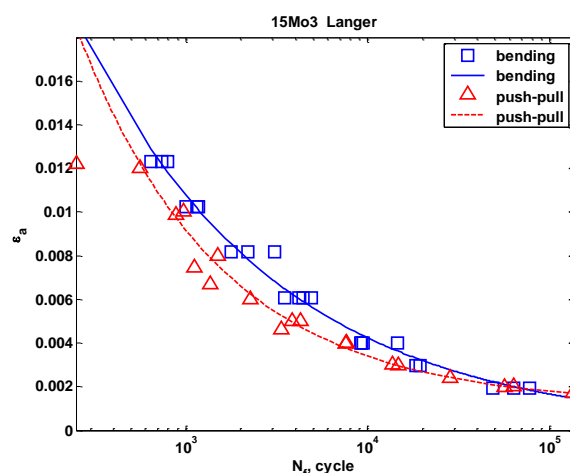


Fig. 7. Strain-life curves according to Langer's model for both push-pull and bending tests

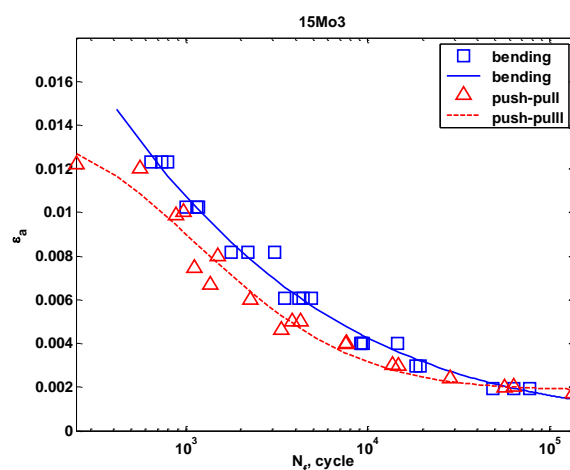


Fig. 8. Strain-life curves according to Author's model

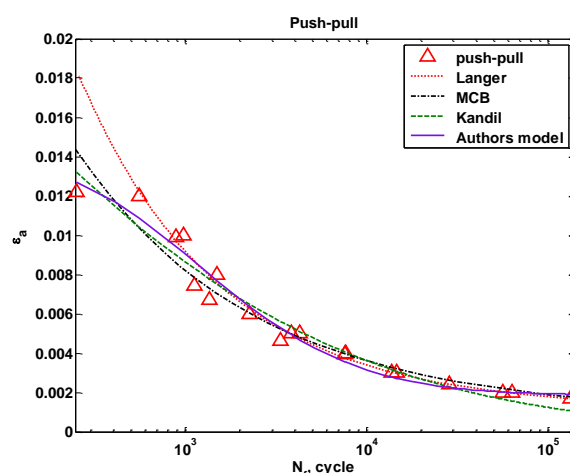


Fig. 9. Strain-life curves for push-pull tests



In addition, Fig. 9 and 10 summarize the characteristics appropriate for tension-compression and pendulum bending to compare the curve shapes obtained for different states of the load. In the case of tension-compression most popular Manson-Coffin-Basquin (1) curve was added to the comparison.

Tab. 1. Push-pull

| Model   | R <sup>2</sup> |
|---------|----------------|
| Kandil  | 0.9488         |
| Langer  | 0.9438         |
| Authors | 0.9676         |

Tab. 2. Bending

| Model   | R <sup>2</sup> |
|---------|----------------|
| Kandil  | 0.9857         |
| Langer  | 0.9843         |
| Authors | 0.9854         |

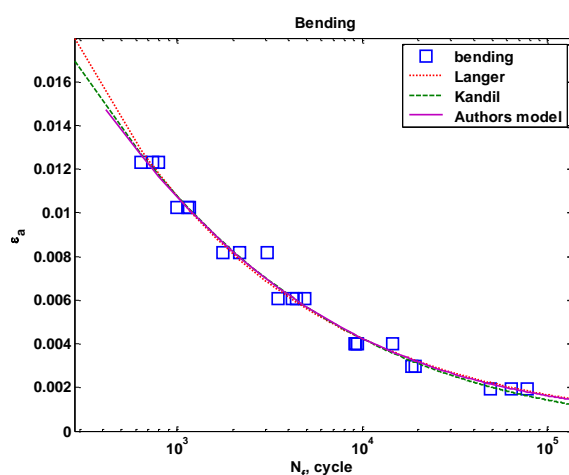


Fig. 10. Strain-life curves for bending tests

## 5. CONCLUSIONS

1. The newly designed and built test stand is capable of experimental studies with controlled strain for bending in the range of a small number of cycles (LCF).
2. Preliminary experimental studies of pendulum bending, with controlled strain amplitude, have shown that fatigue life for bending is close to tension-compression tests for small loading and larger for high strain.
3. Further verification of the correlation between the bending fatigue curves for other materials is necessary.
4. In the future strain-controlled test for pure torsion and combination of bending and torsion should be performed.

## REFERENCES

1. Achteik H., Lachowicz C., Łagoda T., Macha E. (1997), Life time of the notched specimens of 10HNAF steel under proportional bending with torsion, *Proceedings and presented in 1st annual fatigue group meeting of Copernicus Contract CIPA*, Smolenice, 60-69.
2. Basan R., Franulović M., Prebil I., Črnjarić-Žic N. (2011), Analysis of strain-life fatigue parameters and behaviour of different groups of metallic materials, *International Journal of Fatigue*, 33, 484-491.
3. Boller C., Seeger T. (1987), Materials Data for Cyclic Loading, *Materials Science, Monographs*, 42, Elsevier Publisher.
4. Chopra O.K. (1998), *Effects of LWR coolant environments of fatigue design curves of austenitic stainless steels*, U.S. Nuclear Regulatory Commission, NUREG/CR-5704, ANL-98/31.
5. Gorash Y., Chen H. (2013), On creep-fatigue endurance of TIG-dressed weldments using the linear matching method, *Engineering Failure Analysis*, 34, 308-323.
6. Kandil F.A. (2000), *The Determination of Uncertainties in Low Cycle Fatigue Testing*, Standards Measurement & Testing Project No. SMT4-CT97-2165, 1, 1-26.
7. Karolczuk A., Kurek M., Łagoda T. (2015), Fatigue life of aluminium alloy 6082 T6 under constant and variable amplitude bending with torsion, *J. of Theoretical and Applied Mechanics*, 53(2), 521-430.
8. Krzyżak D., Kurek M., Łagoda T., Sówka D. (2014), Influence of changes of the bending plane position on the fatigue life, *Materialwissenschaft und Werkstofftechnik*, 45(11), 1018-1029.
9. Kurek A., Kulesa A., Łagoda T. (2015), Stress-life curve for a range of low and high number of cycles (in Polish), 54. *Symposium „Modelowanie w Mechanice”*, 87-88.
10. Langer B.F. (1962), Design of Pressure Vessels for Low-Cycle Fatigue, *ASME Journal of Basic Engineering*, 84, 389-402.
11. Lee K. S., Song J. H. (2006), Estimation methods for strain-life fatigue properties from hardness, *International Journal of Fatigue*, 28, 386-400.
12. Manson S.S. (1979), Inversion of the strain-life and strain-stress relationships for use in metal fatigue analysis, *Fatigue of Engineering Materials and Structures*, 1, 37-57.
13. Manson S.S. (1965), Fatigue: A complex subject-some simple approximations, *Experimental Mechanics*, 5(4), 193-226.
14. Manson S.S., Muralidharan U. (1987) Fatigue life prediction in bending from axial fatigue information, *Fatigue & Fracture Engineering Materials & Structures*, 9(5), 357-372.
15. Marcisz E., Niesłony A., Łagoda T. (2012), Concept of fatigue for determining characteristics of materials with strengthening, *Material Science Forum*, 726, 43-48.
16. Megahed M.M. (1990), Prediction of bending fatigue behaviour by the reference stress approach, *Fatigue & Fracture of Engineering Materials & Structures*, 13(4), 361-374.
17. Niesłony A., el Dsoki C., Kaufmann H., Krug P. (2008), New method for evaluation of the Manson-Coffin-Basquin and Ramberg-Osgood equations with respect to compatibility, *International Journal of Fatigue*, 30, 1967-1977.
18. Niesłony A., Kurek A., EL Dsoki Ch., Kaufmann H. (2012), A Study of Compatibility Between two ical Fatigue Curve Models based on Some Selected Structural Materials, *International Journal of Fatigue*, 39, 88-94.
19. Radhakrishnan V.M. (1992), *On bilinearity of Manson-Coffin low-cycle-fatigue relationship*, NASA Technical Memorandum 105840, NASA-TM-105840, E-7283, NAS 1.15:105840, 11.
20. Shul'ginov B. S. (2008), Determination of parameters of an exponential function in the description of a fatigue curve, *Strength of Materials*, 50(3), 343-349.
21. Troschenko V. (1996), *High-cycle fatigue and Inelasticity of Metals, Multiaxial and Fatigue Design*, ESIS 21, (Edited by A. Pineau, G. Cailletaud and T. C. Lindley), Mechanical Engineering Publications, London, 335-348.
22. Walat K., Łagoda T., Kurek M. (2015), Life time assessment for and aluminium alloy under complex low cycle fatigue loadings, *Materials Testing*, 57, 160-164.
23. Zhao Y. X., Yang B., Zhai Z. Y. (2007), The framework for a strain-based fatigue reliability analysis, *International Journal of Fatigue*, 30, 493-501.

## BOUNDARY INTEGRAL EQUATIONS FOR AN ANISOTROPIC BIMATERIAL WITH THERMALLY IMPERFECT INTERFACE AND INTERNAL INHOMOGENEITIES

Heorhiy SULYM\*, Iaroslav PASTERNAK\*\*, Mykhailo TOMASHIVSKYY\*\*\*

\*Bialystok University of Technology, ul. Wiejska 45C, 15-351 Bialystok, Poland

\*\*Lutsk National Technical University, Lvivska Str. 75, 43018 Lutsk, Ukraine

\*\*\*Ivan Franko National University of Lviv, Universytetska Str. 1, 79000 Lviv, Ukraine

[h.sulym@pb.edu.pl](mailto:h.sulym@pb.edu.pl), [yaroslav.pasternak@gmail.com](mailto:yaroslav.pasternak@gmail.com), [tomashmyh@gmail.com](mailto:tomashmyh@gmail.com)

received 4 May 2015, revised 25 February 2016, accepted 26 February 2016

**Abstract:** This paper studies a thermoelastic anisotropic bimaterial with thermally imperfect interface and internal inhomogeneities. Based on the complex variable calculus and the extended Stroh formalism a new approach is proposed for obtaining the Somigliana type integral formulae and corresponding boundary integral equations for a thermoelastic bimaterial consisting of two half-spaces with different thermal and mechanical properties. The half-spaces are bonded together with mechanically perfect and thermally imperfect interface, which model interfacial adhesive layers present in bimaterial solids. Obtained integral equations are introduced into the modified boundary element method that allows solving arbitrary 2D thermoelasticity problems for anisotropic bimaterial solids with imperfect thin thermo-resistant interfacial layer, which half-spaces contain cracks and thin inclusions. Presented numerical examples show the effect of thermal resistance of the bimaterial interface on the stress intensity factors at thin inhomogeneities.

**Key words:** Bimaterial, Imperfect Interface, Thermoelastic, Anisotropic, Crack, Thin Inclusion

### 1. INTRODUCTION

Bimaterial parts and structures with different thermal and mechanical properties of their components are widely used in modern engineering design due to their useful anisotropic properties, which thus operate different way in different directions. As a result of such bondage of different materials a thin interfacial layer with finite thickness appears at the interface, which affects the temperature and stress fields in the obtained bimaterial solid. In modeling of the effect of this layer, due to small thickness of the latter it can be reduced to consideration of certain boundary conditions of imperfect interface at the surface of material bondage. However, besides the imperfect interface, another inhomogeneities (such as cracks, thin inclusions etc.) are usually present in structural materials. Therefore, in the study of bimaterial solids one should account for both. Thus, the development of effective methods for modeling of thermal and mechanical fields' distribution in bimaterial solids with imperfect interface and internal thin inhomogeneities is an important practical problem.

Development of efficient techniques for analysis of thermoelasticity problems is very important in the study of contact and friction problems, especially those accounting for thermal emission. Polish scientists vastly develop these studies. Those are Z. Baczynski, J. Ignaczak, A. Kaczynski, M. Kuciej, S.J. Matysiak, V. Pauk, E. Wierzbicki, A. Yevtushenko (e.g. see the recent review by Yevtushenko and Kuciej (2012) and monograph Jewtusheko et al (2014)).

The study of bimaterial solids is widely covered in scientific literature (Benveniste, 2006, Kattis and Mavroyannis, 2006, Pan and Amadei, 1999, Pasternak et al., 2014, Qin, 2007, Wang and

Pan, 2010). In particular, Pan and Amadei (1999) developed an efficient boundary element approach for defective elastic anisotropic bimaterial solids. Hwu (1992) obtained analytic solutions for interfacial cracks in thermoelastic anisotropic dissimilar media. Wang and Pan (2010) derived thermoelastic Green's functions for anisotropic thermoelastic bimaterial with Kapitza-type and spring-type imperfect interface. Pasternak et al. (2014) obtained truly boundary integral equations for 2D thermoelectroelasticity of a defective bimaterial solid with a perfect interface.

However, the thermoelasticity of anisotropic bimaterial solids with imperfect interface containing internal inhomogeneities is less studied. In general, there are mainly two types of imperfect interfaces in the context of heat conduction (Benveniste, 2006, Chen, 2001, Kattis and Mavroyannis, 2006), namely the weakly conducting interface (or the well known Kapitza thermal contact resistance model) and the highly conducting interface. At a weakly conducting interface it is assumed that the normal heat flux is continuous across the interface, and the temperature possesses an interfacial discontinuity, which is proportional to the normal heat flux (Wang and Pan, 2010).

Therefore, this paper studies the thermoelastic anisotropic bimaterial with thermally imperfect and mechanically perfect interface. It is assumed the weakly temperature conducting interface, as in Ref (Wang and Pan, 2010), and tractions and displacements are assumed to be continuous across the interface (perfect mechanical contact). The general complex variable approach of Pasternak et al. (2014) is used to derive closed-form boundary integral formulae and equations for a bimaterial solid with thermally imperfect interface.

## 2. GOVERNING EQUATIONS OF PLANE ANISOTROPIC THERMOELASTICITY AND THE EXTENDED STROH FORMALISM

In a fixed rectangular system of coordinates  $Ox_1x_2x_3$  the equilibrium, heat balance, and constitutive equations of plane (in a plane  $Ox_1x_2$ ) strain and plane heat conduction for a linearly thermoelastic anisotropic solid can be written as (Hwu, 2010, Pasternak, 2012, Ting, 1996):

$$\sigma_{ij,j} = 0, \quad h_{i,i} = 0 \quad (i, j = 1, 2, 3); \quad (1)$$

$$\sigma_{ij} = C_{ijkl} \varepsilon_{kl} - \beta_{ij} \theta, \quad h_i = -k_{ij} \theta_{,j}, \quad (2)$$

where:  $\varepsilon_{ij} = (u_{i,j} + u_{j,i})/2$  is a strain tensor;  $\sigma_{ij}$  is a stress tensor;  $h_i$  is a heat flux;  $u_i$  is a displacement vector;  $\theta$  is a temperature change with respect to the reference one;  $C_{ijkl}$  are elastic moduli;  $k_{ij}$  are heat conduction coefficients;  $\beta_{ij} = C_{ijkl} \alpha_{km}$  ( $i, j, k, m = 1, \dots, 3$ ) are thermal moduli;  $\alpha_{ij}$  are thermal expansion coefficients. Tensors  $C_{ijkl}$ ,  $k_{ij}$ ,  $\alpha_{ij}$ , and  $\beta_{ij}$  are fully symmetric. Here and further, the Einstein summation convention is used. A comma at subscript denotes differentiation with respect to a coordinate indexed after the comma, i.e.  $u_{i,j} = \frac{\partial u_i}{\partial x_j}$ .

According to the extended Stroh formalism (Hwu, 2010, Ting, 1996) the general homogeneous solution of Eqs (1), (2) writes as:

$$\begin{aligned} \theta &= 2\operatorname{Re}\{g'(z_t)\}, \quad \vartheta = 2k_t \operatorname{Im}\{g'(z_t)\}, \\ h_1 &= -\vartheta_{,2}, \quad h_2 = \vartheta_{,1}, \quad k_t = \sqrt{k_{11}k_{22} - k_{12}^2}, \\ \mathbf{u} &= 2\operatorname{Re}[\mathbf{A}\mathbf{f}(z_*) + \mathbf{c}g(z_t)], \\ \phi &= 2\operatorname{Re}[\mathbf{B}\mathbf{f}(z_*) + \mathbf{d}g(z_t)], \\ \sigma_{i1} &= -\varphi_{i,2}, \quad \sigma_{i2} = \varphi_{i,1}, \\ z_t &= x_1 + p_t x_2, \quad z_\alpha = x_1 + p_\alpha x_2, \\ \mathbf{f}(z_*) &= [F_1(z_1), F_2(z_2), F_3(z_3)]^T, \end{aligned} \quad (3)$$

where:  $\vartheta$  is a heat flux function;  $F_\alpha(z_\alpha)$  and  $g(z_t)$  are complex analytic functions with respect to their arguments; the complex constant  $p_t$  is a root (with a positive imaginary part) of the characteristic equation for heat conduction  $k_{22}p_t^2 + 2k_{12}p_t + k_{11} = 0$ . Constant complex matrices  $\mathbf{A}$ ,  $\mathbf{B}$ , vectors  $\mathbf{c}$ ,  $\mathbf{d}$ , and scalars  $p_\alpha$  ( $\alpha = 1, 2, 3$ ) are determined from the extended Stroh eigenvalue problem (Ting, 1996).

Vector  $\mathbf{f}(z_*)$  of Stroh complex functions is related to the real-valued stress and displacement functions as (Pasternak, 2012):

$$\begin{aligned} \mathbf{f}(z_*) &= \mathbf{B}^T \mathbf{u} + \mathbf{A}^T \phi - \mathbf{B}^T \mathbf{u}^t - \mathbf{A}^T \phi^t, \\ \mathbf{u}^t &= 2\operatorname{Re}\{\mathbf{c}g(z_t)\}, \quad \phi^t = 2\operatorname{Re}\{\mathbf{d}g(z_t)\}. \end{aligned} \quad (4)$$

According to Eq (3), the Stroh temperature function  $g'(z_t)$  is related to the heat flux and temperature functions as:

$$g'(z_t) = \frac{1}{2} \left( \theta + i \frac{\vartheta}{k_t} \right). \quad (5)$$

## 3. DERIVATION OF THE INTEGRAL FORMULAE FOR A BIMATERIAL SOLID

Consider plane strain of a medium consisting of two thermoelastic anisotropic half-spaces  $S_1$  ( $x_2 > 0$ ) and  $S_2$  ( $x_2 < 0$ ) (see Fig. 1). Along the line  $x_2 = 0$  (actually, the plane  $Ox_2x_3$ ), which

is a bondage line, the conditions of imperfect thermal contact are satisfied:

$$\begin{aligned} \theta^{(1)}(x_1, x_2) \Big|_{x_2=0} &= \\ \theta^{(2)}(x_1, x_2) \Big|_{x_2=0} - \rho_0 \left( \vartheta_{,1}^{(2)}(x_1, x_2) \right) \Big|_{x_2=0}, \end{aligned} \quad (6)$$

$$\vartheta^{(1)}(x_1, x_2) \Big|_{x_2=0} = \vartheta^{(2)}(x_1, x_2) \Big|_{x_2=0}, \quad (7)$$

and perfect mechanical contact holds

$$\begin{aligned} \phi^{(1)}(x_1, x_2) \Big|_{x_2=0} &= \phi^{(2)}(x_1, x_2) \Big|_{x_2=0}, \\ \mathbf{u}^{(1)}(x_1, x_2) \Big|_{x_2=0} &= \mathbf{u}^{(2)}(x_1, x_2) \Big|_{x_2=0}. \end{aligned} \quad (8)$$

Here and further superscripts 1 or 2 denote corresponding half-space  $S_1$  or  $S_2$ , respectively, which the field quantity belongs to. Boundary conditions (6) and (7) from the physical point of view correspond to a model of a thin layer, for which according to Fourier law of heat conduction the temperature difference at the bimaterial interface is proportional to the heat flux through it. Thus, the parameter  $\rho_0$  in Eq (6) is a thermal resistance of the above-mentioned layer, and as a consequence, a thermal resistance of the bimaterial interface. As  $\rho_0 \rightarrow 0$  or  $\rho_0 \rightarrow \infty$  one obtains perfect thermal contact or thermally insulated bimaterial interface (adiabatic contact), respectively.

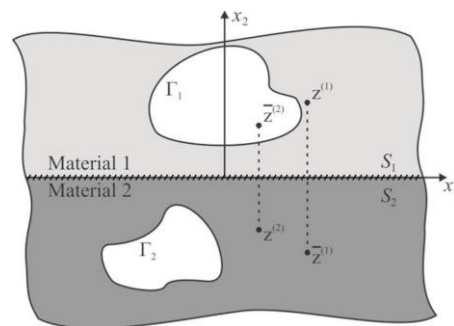


Fig. 1. Thermoelastic anisotropic bimaterial medium

It is considered that each of the half-spaces contains systems of cylindrical holes, which are represented with plane contours  $\Gamma_1 = \cup_i \Gamma_i^{(1)}$  and  $\Gamma_2 = \cup_i \Gamma_i^{(2)}$ , respectively.

For derivation of the integral formulae for the Stroh complex functions for bonded half-spaces one can use the Cauchy integral formula (Muskhelishvili, 2008), which relates values of an arbitrary analytic function  $\phi(\tau)$  at the boundary  $\partial S$  of the domain  $S$  with its value inside this domain:

$$\frac{1}{2\pi i} \int_{\partial S} \frac{\phi(\tau) d\tau}{\tau - z} = \begin{cases} \phi(z) & \forall z \in S, \\ 0 & \forall z \notin S, \end{cases} \quad (9)$$

where  $\tau, z \in \mathbb{C}$  are complex variables, which define the position of the source and field points, respectively. Herewith, if the domain  $S$  is infinite it is assumed that the function  $\phi(z)$  vanishes at  $z \rightarrow \infty$ .

### 3.1. Heat conduction

Due to the linearity of the problem of heat conduction one can present its solution as a superposition of the homogeneous solu-

tion given by the functions  $g_{1\infty}(z_t^{(1)})$  and  $g_{2\infty}(z_t^{(2)})$  (which should definitely satisfy the boundary conditions (6)), and the perturbed solution caused by the presence of the contours  $\Gamma_1$  and  $\Gamma_2$ .

Denote the Cauchy integrals of the complex temperature functions  $g'_i(z_t^{(i)})$  as:

$$q_t^{(i)}(z_t^{(j)}) = \int_{\Gamma_i} \frac{g'_i(\tau_t^{(i)}) d\tau_t^{(i)}}{\tau_t^{(i)} - z_t^{(j)}}, \quad (10)$$

$$\bar{q}_t^{(i)}(z_t^{(j)}) = \int_{\Gamma_i} \frac{\overline{g'_i(\tau_t^{(i)})} d\tau_t^{(i)}}{\bar{\tau}_t^{(i)} - z_t^{(j)}}$$

and the improper integrals over the infinite path  $-\infty < x_1 < +\infty$  as

$$m_t(z_t^{(j)}) = \int_{-\infty}^{+\infty} \frac{\vartheta(x_1) dx_1}{x_1 - z_t^{(j)}}, \quad (11)$$

$$p_t(z_t^{(j)}) = \int_{-\infty}^{+\infty} \frac{\vartheta^{(2)}(x_1) dx_1}{x_1 - z_t^{(j)}}.$$

Integration by parts of the improper integral gives:

$$\int_{-\infty}^{+\infty} \frac{\vartheta_1(x_1)}{x_1 - z_t^{(j)}} dx_1 = \frac{\vartheta(x_1)}{x_1 - z_t^{(j)}} \Big|_{-\infty}^{+\infty} + \int_{-\infty}^{+\infty} \frac{\vartheta(x_1)}{(x_1 - z_t^{(j)})^2} dx_1 = m'_t(z_t^{(j)}). \quad (12)$$

Accounting for the thermal balance conditions, the function  $\vartheta(x_1)$  tends to zero at the infinity, therefore the first term in Eq (12) vanishes, and the second term is a derivative of a function  $m'_t(z_t^{(j)})$ . Thus,

$$\int_{-\infty}^{+\infty} \frac{\vartheta_1(x_1)}{x_1 - z_t^{(j)}} dx_1 = m'_t(z_t^{(j)}). \quad (13)$$

Utilizing Eqs (5), (9)–(11), (13) and accounting for the boundary conditions at the bimaterial interface the Cauchy integral formulae for the functions  $g'_1(z_t^{(1)})$  and  $g'_2(z_t^{(2)})$  write as

$$g'_1(z_t^{(1)}) = g'_{1\infty}(z_t^{(1)}) + \frac{1}{2\pi i} q_t^{(1)}(z_t^{(1)}) + \frac{1}{4\pi i} p_t^{(1)}(z_t^{(1)}) + \frac{1}{4\pi k_t} m_t^{(1)}(z_t^{(1)}) - \frac{\rho_0}{4\pi i} m'_t(z_t^{(1)}),$$

$$\forall \text{Im}(z_t^{(1)}) > 0 \quad (14)$$

$$g'_2(z_t^{(2)}) = g'_{2\infty}(z_t^{(2)}) + \frac{1}{2\pi i} q_t^{(2)}(z_t^{(2)}) - \frac{1}{4\pi i} p_t(z_t^{(2)}) - \frac{1}{4\pi k_t^{(2)}} m_t(z_t^{(2)}), \forall \text{Im}(z_t^{(2)}) < 0$$

and for determination of the improper integrals (11) through the Cauchy integrals (10) one obtains the following system of first-order ordinary differential equations:

$$\forall \text{Im}(z_t^{(1)}) > 0: q_t^{(2)}(z_t^{(1)}) - \frac{1}{2} p_t(z_t^{(1)}) - \frac{i}{2k_t^{(2)}} m_t(z_t^{(1)}) = 0, \quad (15)$$

$$\bar{q}_t^{(1)}(z_t^{(1)}) + \frac{1}{2} p_t(z_t^{(1)}) - \frac{i}{2k_t^{(1)}} m_t(z_t^{(1)}) - \frac{\rho_0}{2} m'(z_t^{(1)}) = 0,$$

$$\forall \text{Im}(z_t^{(2)}) < 0: \bar{q}_t^{(2)}(z_t^{(2)}) - \frac{1}{2} p_t(z_t^{(2)}) + \quad (16)$$

$$\frac{i}{2k_t^{(2)}} m_t(z_t^{(2)}) = 0,$$

$$\bar{q}_t^{(1)}(z_t^{(2)}) + \frac{1}{2} p_t(z_t^{(2)}) + \frac{i}{2k_t^{(1)}} m_t(z_t^{(1)}) - \frac{\rho_0}{2} m'(z_t^{(2)}) = 0.$$

Satisfying an evident condition that  $m_t(z_t^{(j)}) \rightarrow 0$  as  $z_t^{(j)} \rightarrow \infty$  one obtains the solution of systems (15), (16) as:

$$p_t(z_t^{(1)}) = 2 \cdot q_t^{(2)}(z_t^{(1)}) + \frac{2i}{\rho_0 k_t^{(2)}} [e_t^{(2)}(z_t^{(1)}) + \bar{e}_t^{(1)}(z_t^{(1)})], \quad (17)$$

$$m_t(z_t^{(1)}) = -\frac{2}{\rho_0} [e_t^{(2)}(z_t^{(1)}) + \bar{e}_t^{(1)}(z_t^{(1)})],$$

$$p_t(z_t^{(2)}) = 2 \cdot \bar{q}_t^{(2)}(z_t^{(2)}) - \frac{2i}{\rho_0 k_t^{(2)}} [e_t^{(1)}(z_t^{(2)}) + \bar{e}_t^{(2)}(z_t^{(2)})], m_t(z_t^{(2)}) = -\frac{2}{\rho_0} [e_t^{(1)}(z_t^{(2)}) + \bar{e}_t^{(2)}(z_t^{(2)})]. \quad (18)$$

New functions  $e_t^{(i)}(z_t^{(j)})$  and  $\bar{e}_t^{(i)}(z_t^{(j)})$  are defined though the following integral formulae

$$e_t^{(i)}(z_t^{(j)}) = \int_{\Gamma_i} g'_i(\tau_t^{(i)}) K(B^{(j)}(\tau_t^{(i)} - z_t^{(j)})) d\tau_t^{(i)}, \quad (19)$$

$$e_t^{(i)}(z_t^{(j)}) = \int_{\Gamma_i} g'_i(\tau_t^{(i)}) K(B^{(j)}(\tau_t^{(i)} - z_t^{(j)})) d\tau_t^{(i)}, \quad (20)$$

where:  $K(z) = e^z E_1(z)$ ,

$$B^{(1)} = \frac{i}{\rho_0} \frac{k_t^{(1)} + k_t^{(2)}}{k_t^{(1)} \cdot k_t^{(2)}}, \quad (21)$$

$$B^{(2)} = -\frac{i}{\rho_0} \frac{k_t^{(1)} + k_t^{(2)}}{k_t^{(1)} \cdot k_t^{(2)}}$$

and  $E_1(z)$  is an exponential integral defined as

$$E_1(z) = \int_z^\infty \frac{e^{-t}}{t} dt. \quad (22)$$

Substituting obtained solution into Eq (14) one can derive the integral formulae for the Stroh complex temperature functions  $g'_1(z_t^{(1)})$  and  $g'_2(z_t^{(2)})$ , which do not contain the improper integrals over the infinite bimaterial interface:

$$\forall \text{Im}(z_t^{(1)}) > 0: g'_1(z_t^{(1)}) = g'_{1\infty}(z_t^{(1)}) + \frac{1}{2\pi i} [q_t^{(1)}(z_t^{(1)}) - \bar{q}_t^{(1)}(z_t^{(1)}) + \frac{2i}{\rho_0 k_t^{(1)}} (e_t^{(2)}(z_t^{(1)}) + \bar{e}_t^{(1)}(z_t^{(1)}))] , \quad (23)$$

$$\forall \text{Im}(z_t^{(2)}) > 0: g'_2(z_t^{(2)}) = g'_{2\infty}(z_t^{(2)}) + \frac{1}{2\pi i} [q_t^{(2)}(z_t^{(2)}) - \bar{q}_t^{(2)}(z_t^{(2)}) - \frac{2i}{\rho_0 k_t^{(2)}} (e_t^{(1)}(z_t^{(2)}) + \bar{e}_t^{(2)}(z_t^{(2)}))] . \quad (24)$$

Using (5) one can derive the integral formulae for the functions  $g'_1(z_t^{(1)})$  and  $g'_2(z_t^{(2)})$  relating them with the boundary values of temperature  $\theta$  and normal component  $h_n = h_i n_i$  of a heat flux vector ( $n_i$  is a unit outwards normal vector to a curve  $\Gamma_i$  at its certain point).

According to Eqs (5), (23), and (24), one can obtain the inte-



gral formulae for temperature and heat flux at the arbitrary point  $\xi$  of a bimaterial solid:

$$\theta(\xi) = \begin{cases} 2\operatorname{Re}\{g'_1(Z_t^{(1)}(\xi))\} (\forall \xi \in S_1), \\ 2\operatorname{Re}\{g'_2(Z_t^{(2)}(\xi))\} (\forall \xi \in S_2), \end{cases} = \int_{\Gamma} [\Theta^{ITC*}(\mathbf{x}, \xi) h_n(\mathbf{x}) - H^{ITC*}(\mathbf{x}, \xi) \theta(\mathbf{x})] ds(\mathbf{x}) + \theta^\infty(\xi), \quad (25)$$

$$h_i(\xi) = \begin{cases} 2k_t^{(1)} \operatorname{Im}\{(\delta_{2i} - \delta_{1i} p_t^{(1)}) g''_1(Z_t^{(1)}(\xi))\} (\forall \xi \in S_1), \\ 2k_t^{(2)} \operatorname{Im}\{(\delta_{2i} - \delta_{1i} p_t^{(2)}) g''_2(Z_t^{(2)}(\xi))\} (\forall \xi \in S_2), \end{cases} = \int_{\Gamma} [\Theta_i^{ITC**}(\mathbf{x}, \xi) h_n(\mathbf{x}) - H_i^{ITC**}(\mathbf{x}, \xi) \theta(\mathbf{x})] ds(\mathbf{x}) + h_i^\infty(\xi), \quad (26)$$

where: the functions  $\theta^\infty(\xi)$  and  $h_i^\infty(\xi)$  define the homogeneous solution for the unnotched bimaterial

$$\theta^\infty(\xi) = \begin{cases} 2\operatorname{Re}[g'_{1\infty}(Z_t^{(1)}(\xi))] & \forall \xi \in S_1, \\ 2\operatorname{Re}[g'_{2\infty}(Z_t^{(2)}(\xi))] & \forall \xi \in S_2, \end{cases} \quad (27)$$

$$h_i^\infty(\xi) = \begin{cases} 2k_t^{(1)} \operatorname{Im}[(\delta_{2i} - \delta_{1i} p_t^{(1)}) g''_{1\infty}(Z_t^{(1)}(\xi))] & \forall \xi \in S_1, \\ 2k_t^{(2)} \operatorname{Im}[(\delta_{2i} - \delta_{1i} p_t^{(2)}) g''_{2\infty}(Z_t^{(2)}(\xi))] & \forall \xi \in S_2. \end{cases} \quad (28)$$

According to Eqs (3), (23), (24) the kernels of the heat conduction integral formulae are as follows:

$$\begin{aligned} \mathbf{x} \in S_1 \wedge \xi \in S_1: \\ \Theta^{ITC*}(\mathbf{x}, \xi) &= \frac{1}{2\pi k_t^{(1)}} \operatorname{Re}\{\ln W_t^{(1,1)} + \ln \bar{W}_t^{(1,1)} \\ &+ (K-1)L^{(1)}(\bar{W}_t^{(1,1)})\}, \\ H^{ITC*}(\mathbf{x}, \xi) &= \frac{1}{2\pi} \operatorname{Im}\left\{\frac{n_t^{(1)}}{W_t^{(1,1)}} - \frac{\bar{n}_t^{(1)}}{\bar{W}_t^{(1,1)}} + \frac{2i\bar{n}_t^{(1)}}{\rho_0 k_t^{(1)}} K(B^{(1)}\bar{W}_t^{(1,1)})\right\}, \\ \Theta_i^{ITC**}(\mathbf{x}, \xi) &= -\frac{1}{2\pi} \operatorname{Im}\left\{\delta_t^{(1)} \left(\frac{1}{W_t^{(1,1)}} + \frac{1}{\bar{W}_t^{(1,1)}}\right) \right. \\ &\left. - \frac{2i}{\rho_0 k_t^{(1)}} K(B^{(1)}\bar{W}_t^{(1,1)})\right\}, \\ H_i^{ITC**}(\mathbf{x}, \xi) &= -\frac{k_t^{(1)}}{2\pi} \operatorname{Re}\left\{\delta_t^{(1)} \left(\frac{n_t^{(1)}}{(W_t^{(1,1)})^2} - \frac{\bar{n}_t^{(1)}}{(\bar{W}_t^{(1,1)})^2}\right) \right. \\ &\left. + \frac{2i\bar{n}_t^{(1)}}{\rho_0 k_t^{(1)}} \left(B^{(1)}K(B^{(1)}\bar{W}_t^{(1,1)}) - \frac{1}{\bar{W}_t^{(1,1)}}\right)\right\}; \end{aligned}$$

$$\begin{aligned} \mathbf{x} \in S_2 \wedge \xi \in S_1: \\ \Theta^{ITC*}(\mathbf{x}, \xi) &= \frac{1-K}{2\pi k_t^{(2)}} \operatorname{Re}\{\ln W_t^{(2,1)} + K(B^{(1)}W_t^{(2,1)})\}, \\ H^{ITC*}(\mathbf{x}, \xi) &= \frac{1}{\rho_0 \pi k_t^{(1)}} \operatorname{Im}\{in_t^{(2)} K(B^{(1)}W_t^{(2,1)})\}, \\ \Theta_i^{ITC**}(\mathbf{x}, \xi) &= -\frac{1}{\rho_0 \pi k_t^{(2)}} \operatorname{Im}\{i\delta_t^{(1)} K(B^{(1)}W_t^{(2,1)})\} \\ , H_i^{ITC**}(\mathbf{x}, \xi) &= \frac{1}{\rho_0 \pi} \operatorname{Re}\left\{\delta_t^{(1)} n_t^{(2)} \left(iB^{(1)}K(B^{(1)}W_t^{(2,1)}) - \frac{1}{W_t^{(2,1)}}\right)\right\}; \\ \mathbf{x} \in S_1 \wedge \xi \in S_2: \\ \Theta^{ITC*}(\mathbf{x}, \xi) &= \frac{1+K}{2\pi k_t^{(1)}} \operatorname{Re}\{\ln W_t^{(1,2)} + K(B^{(2)}W_t^{(1,2)})\}, \\ H^{ITC*}(\mathbf{x}, \xi) &= -\frac{1}{\rho_0 \pi k_t^{(2)}} \operatorname{Im}\{in_t^{(1)} K(B^{(2)}W_t^{(1,2)})\}, \end{aligned}$$

$$\begin{aligned} \Theta_i^{ITC**}(\mathbf{x}, \xi) &= \frac{1}{\rho_0 \pi k_t^{(1)}} \operatorname{Im}\{i\delta_t^{(2)} K(B^{(2)}W_t^{(1,2)})\}, \\ H_i^{ITC**}(\mathbf{x}, \xi) &= -\frac{1}{\rho_0 \pi} \operatorname{Re}\left\{\delta_t^{(2)} n_t^{(1)} \left(iB^{(2)}K(B^{(2)}W_t^{(1,2)}) - \frac{1}{W_t^{(1,2)}}\right)\right\}; \\ \mathbf{x} \in S_2 \wedge \xi \in S_2: \\ \Theta^{ITC*}(\mathbf{x}, \xi) &= \frac{1}{2\pi k_t^{(2)}} \operatorname{Re}\{\ln W_t^{(2,2)} + \ln \bar{W}_t^{(2,2)} \\ &- (K+1)L^{(2)}(\bar{W}_t^{(2,2)})\}, \\ H^{ITC*}(\mathbf{x}, \xi) &= \frac{1}{2\pi} \operatorname{Im}\left\{\frac{n_t^{(2)}}{W_t^{(2,2)}} - \frac{\bar{n}_t^{(2)}}{\bar{W}_t^{(2,2)}} - \frac{2i\bar{n}_t^{(2)}}{\rho_0 k_t^{(2)}} K(B^{(2)}\bar{W}_t^{(2,2)})\right\}, \\ \Theta_i^{ITC**}(\mathbf{x}, \xi) &= -\frac{1}{2\pi} \operatorname{Im}\left\{\delta_t^{(2)} \left(\frac{1}{W_t^{(2,2)}} + \frac{1}{\bar{W}_t^{(2,2)}} + \frac{2i}{\rho_0 k_t^{(2)}} K(B^{(2)}\bar{W}_t^{(2,2)})\right)\right\} \\ H_i^{ITC**}(\mathbf{x}, \xi) &= \frac{-k_t^{(1)}}{2\pi} \operatorname{Re}\left\{\delta_t^{(2)} \left(\frac{n_t^{(2)}}{(W_t^{(2,2)})^2} - \frac{\bar{n}_t^{(2)}}{(\bar{W}_t^{(2,2)})^2}\right) \right. \\ &\left. - \frac{2i\bar{n}_t^{(2)}}{\rho_0 k_t^{(2)}} \left(B^{(2)}K(B^{(1)}\bar{W}_t^{(2,2)}) - \frac{1}{\bar{W}_t^{(2,2)}}\right)\right\}, \end{aligned} \quad (29)$$

where:

$$\begin{aligned} W_t^{(i,j)} &= Z_t^{(i)}(\mathbf{x}) - Z_t^{(j)}(\xi), \bar{W}_t^{(i,j)} = \bar{Z}_t^{(i)}(\mathbf{x}) - \bar{Z}_t^{(j)}(\xi), \\ n_t^{(i)} &= n_2(\mathbf{x}) - p_t^{(i)} n_1(\mathbf{x}), \delta_t^{(j)} = \delta_{i2} - p_t^{(j)} \delta_{i1}, \\ L^{(i)}(z) &= K(B^{(i)}z) + \ln z. \end{aligned}$$

According to Eqs (3) and (4), for derivation of integral formulae for extended displacement and extended stress function one should evaluate the anti-derivatives of functions  $g'_i(z_t^{(i)})$ ,  $m_t(z)$ , and  $p_t(z)$  as:

$$g_i(z_t^{(j)}) = \int g'_i(z_t^{(j)}) dz_t^{(j)}, \quad (30)$$

$$M_t(z) = \int m_t(z) dz = -\int_{-\infty}^{+\infty} \ln(x_1 - z) \vartheta(x_1) dx_1, \quad (31)$$

$$P_t(z) = \int p_t(z) dz = -\int_{-\infty}^{+\infty} \ln(x_1 - z) \theta(x_1) dx_1. \quad (32)$$

Utilizing Eqs (23), (24), one obtains:

$$\begin{aligned} \forall \operatorname{Im}(z_t^{(1)}) > 0: \\ g_1(z_t^{(1)}) &= g_{1\infty}(z_t^{(1)}) + \frac{1}{2\pi i} [Q_t^{(1)}(z_t^{(1)}) - K\bar{Q}_t^{(1)}(z_t^{(1)}) \\ &+ (1-K)Q_t^{(2)}(z_t^{(1)}) + (K-1)(e_t^{(2)}(z_t^{(1)}) + \bar{e}_t^{(1)}(z_t^{(1)}))], \\ P_t(z_t^{(1)}) &= (1-K)Q_t^{(2)}(z_t^{(1)}) - (1+K)\bar{Q}_t^{(1)}(z_t^{(1)}) \\ &+ (1+K)(e_t^{(2)}(z_t^{(1)}) + \bar{e}_t^{(1)}(z_t^{(1)})), \\ M_t(z_t^{(1)}) &= -2ik_t^{(1)}(1-K)[\bar{Q}_t^{(1)}(z_t^{(1)}) + Q_t^{(2)}(z_t^{(1)}) \\ &- (e_t^{(2)}(z_t^{(1)}) + \bar{e}_t^{(1)}(z_t^{(1)}))]; \end{aligned} \quad (33)$$

$$\begin{aligned} \forall \operatorname{Im}(z_t^{(2)}) < 0: \\ g_2(z_t^{(2)}) &= g_{2\infty}(z_t^{(2)}) + \frac{1}{2\pi i} [Q_t^{(2)}(z_t^{(2)}) + K\bar{Q}_t^{(2)}(z_t^{(2)}) \\ &+ (1+K)Q_t^{(1)}(z_t^{(2)}) - (K+1)(e_t^{(1)}(z_t^{(2)}) + \bar{e}_t^{(2)}(z_t^{(2)}))], \\ P_t(z_t^{(2)}) &= (1-K)\bar{Q}_t^{(2)}(z_t^{(2)}) - (1+K)Q_t^{(1)}(z_t^{(2)}) \\ &+ (1+K)(e_t^{(1)}(z_t^{(2)}) + \bar{e}_t^{(2)}(z_t^{(2)})), \end{aligned}$$

$$M_t(z_t^{(2)}) = 2ik_t^{(2)}(1 + K)[\bar{Q}_t^{(2)}(z_t^{(2)}) + Q_t^{(1)}(z_t^{(2)}) - (e_t^{(1)}(z_t^{(2)}) + \bar{e}_t^{(2)}(z_t^{(2)}))], \quad (34)$$

where according to Eqs (5) and (28), (29),

$$\begin{aligned} \bar{Q}_t^{(i)}(z) &= \int \bar{q}_t^{(i)}(z) dz = \frac{i}{2k_t^{(i)}} \int_{\Gamma_i} f^*(\bar{\tau}_t^{(i)}(s) - z) h_n(s) ds \\ &+ \frac{1}{2} \int_{\Gamma_i} (n_2(s) - \bar{p}_t^{(i)} n_1(s)) \ln(\bar{\tau}_t^{(i)}(s) - z) \theta(s) ds, \quad (35) \\ Q_t^{(i)}(z) &= \int q_t^{(i)}(z) dz = \frac{-i}{2k_t^{(i)}} \int_{\Gamma_i} f^*(\tau_t^{(i)}(s) - z) h_n(s) ds \\ &+ \frac{1}{2} \int_{\Gamma_i} (n_2(s) - p_t^{(i)} n_1(s)) \ln(\tau_t^{(i)}(s) - z) \theta(s) ds, \\ f^*(z) &= z(\ln(z) - 1), \quad K = (k_t^{(1)} - k_t^{(2)}) / (k_t^{(1)} + k_t^{(2)}). \end{aligned}$$

### 3.2. Thermoelasticity of an anisotropic bimaterial

For obtaining the integral formulae of thermoelectroelasticity one should write the Cauchy integral formula (9) for the Stroh complex vector functions  $f^{(1)}(z_*^{(1)})$  and  $f^{(2)}(z_*^{(2)})$ , which are analytic in the domains  $S_1$  and  $S_2$ , respectively. Since the Cauchy integral formula define the analytic function that vanishes at the infinity, the complete solution of the problem can be presented as a sum of the perturbed solution defined by the Cauchy formula and a homogeneous solution given by the functions  $f_\infty^{(1)}(z_*^{(1)})$  and  $f_\infty^{(2)}(z_*^{(2)})$ , which satisfy boundary conditions (8). Consequently, one obtains

$$\begin{aligned} \mathbf{f}^{(1)}(z_*^{(1)}) &= \mathbf{f}_\infty^{(1)}(z_*^{(1)}) + \frac{1}{2\pi i} \left[ \int_{\Gamma_1} \left\langle \frac{d\tau_*^{(1)}}{\tau_*^{(1)} - z_*^{(1)}} \right\rangle \mathbf{f}^{(1)}(\tau_*^{(1)}) \right. \\ &\left. + \int_{-\infty}^{+\infty} \left\langle \frac{dx_1}{x_1 - z_*^{(1)}} \right\rangle \mathbf{f}^{(1)}(x_1) \right] \quad (\text{Im} z_*^{(1)} > 0), \quad (36) \end{aligned}$$

$$\text{Im} z_\beta^{(1)} > 0:$$

$$\int_{\Gamma_1} \left\langle \frac{d\tau_*^{(1)}}{\tau_*^{(1)} - z_\beta^{(1)}} \right\rangle \mathbf{f}^{(1)}(\tau_*^{(1)}) + \int_{-\infty}^{+\infty} \frac{dx_1}{x_1 - z_\beta^{(1)}} \mathbf{f}^{(1)}(x_1) = 0, \quad (37)$$

$$\int_{\Gamma_2} \left\langle \frac{d\tau_*^{(2)}}{\tau_*^{(2)} - z_\beta^{(1)}} \right\rangle \mathbf{f}^{(2)}(\tau_*^{(2)}) - \int_{-\infty}^{+\infty} \frac{dx_1}{x_1 - z_\beta^{(1)}} \mathbf{f}^{(2)}(x_1), \quad (38)$$

$$\begin{aligned} \mathbf{f}^{(2)}(z_*^{(2)}) &= \mathbf{f}_\infty^{(2)}(z_*^{(2)}) + \frac{1}{2\pi i} \left[ \int_{\Gamma_2} \left\langle \frac{d\tau_*^{(2)}}{\tau_*^{(2)} - z_*^{(2)}} \right\rangle \mathbf{f}^{(2)}(\tau_*^{(2)}) \right. \\ &\left. - \int_{-\infty}^{+\infty} \left\langle \frac{dx_1}{x_1 - z_*^{(2)}} \right\rangle \mathbf{f}^{(2)}(x_1) \right] \quad (\text{Im} z_*^{(2)} < 0); \quad (39) \end{aligned}$$

$$\text{Im} z_\beta^{(2)} < 0:$$

$$\int_{\Gamma_1} \left\langle \frac{d\tau_*^{(1)}}{\tau_*^{(1)} - z_\beta^{(2)}} \right\rangle \mathbf{f}^{(1)}(\tau_*^{(1)}) + \int_{-\infty}^{+\infty} \frac{dx_1}{x_1 - z_\beta^{(2)}} \mathbf{f}^{(1)}(x_1) = 0; \quad (40)$$

$$\int_{\Gamma_2} \left\langle \frac{d\tau_*^{(2)}}{\tau_*^{(2)} - z_\beta^{(2)}} \right\rangle \mathbf{f}^{(2)}(\tau_*^{(2)}) - \int_{-\infty}^{+\infty} \frac{dx_1}{x_1 - z_\beta^{(2)}} \mathbf{f}^{(2)}(x_1), \quad (41)$$

where:  $\langle F(z_*) \rangle = \text{diag}[F_1(z_1), F_2(z_2), F_3(z_3)]$ ,

$$z_\beta^{(i)} = x_1 + p_\beta^{(i)} x_2 \quad (\beta = 1, \dots, 3).$$

Utilizing Eqs (4) and (8), the improper integrals in Eqs (36)–(41) can be rewritten as follows:

$$\begin{aligned} \int_{-\infty}^{+\infty} \frac{f^{(j)} dx_1}{x_1 - z_\beta^{(i)}} &= \mathbf{A}_j^T \mathbf{m}(z_\beta^{(i)}) + \mathbf{B}_j^T \mathbf{p}(z_\beta^{(i)}) \\ &- 2 \int_{-\infty}^{+\infty} \frac{(\mathbf{A}_j^T \text{Re}[\mathbf{d}_j g_j(x_1)] + \mathbf{B}_j^T \text{Re}[\mathbf{c}_j g_j(x_1)]) dx_1}{x_1 - z_\beta^{(i)}}, \quad (42) \end{aligned}$$

where

$$\begin{aligned} \mathbf{m}(z_\beta^{(j)}) &= \int_{-\infty}^{+\infty} \frac{\phi(x_1) dx_1}{x_1 - z_\beta^{(j)}}, \\ \mathbf{p}(z_\beta^{(j)}) &= \int_{-\infty}^{+\infty} \frac{\mathbf{u}(x_1) dx_1}{x_1 - z_\beta^{(j)}}. \quad (43) \end{aligned}$$

Integrating by parts the second term in Eq (42) and accounting for Eq (4), one can obtain that

$$\begin{aligned} \int_{-\infty}^{+\infty} \frac{f^{(1)} dx_1}{x_1 - z_\beta^{(i)}} &= \mathbf{A}_1^T \mathbf{m}(z_\beta^{(i)}) + \mathbf{B}_1^T \mathbf{p}(z_\beta^{(i)}) + \mu_1 M_t(z_\beta^{(i)}) \\ &- \lambda_1 P_t(z_\beta^{(i)}) + \rho_0 \lambda_1 m_t(z_\beta^{(i)}) \quad (44) \end{aligned}$$

$$\begin{aligned} \int_{-\infty}^{+\infty} \frac{f^{(2)} dx_1}{x_1 - z_\beta^{(i)}} &= \mathbf{A}_2^T \mathbf{m}(z_\beta^{(i)}) + \mathbf{B}_2^T \mathbf{p}(z_\beta^{(i)}) + \mu_2 M_t(z_\beta^{(i)}) \\ &- \lambda_2 P_t(z_\beta^{(i)}) \quad (45) \end{aligned}$$

where the complex constants  $\mu_i$  and  $\lambda_i$  are defined as:

$$\mu_i = \frac{1}{k_t^{(i)}} (\mathbf{A}_i^T \text{Im}[\mathbf{d}_i] + \mathbf{B}_i^T \text{Im}[\mathbf{c}_i]), \quad (46)$$

$$\lambda_i = \mathbf{A}_i^T \text{Re}[\mathbf{d}_i] + \mathbf{B}_i^T \text{Re}[\mathbf{c}_i]$$

Denoting the Cauchy integrals of the Stroh complex functions as:

$$\begin{aligned} \mathbf{q}_j(z_\beta^{(i)}) &= \int_{\Gamma_j} \left\langle \frac{d\tau_*^{(j)}}{\tau_*^{(j)} - z_\beta^{(i)}} \right\rangle \mathbf{f}^{(j)}(\tau_*^{(j)}) \\ \bar{\mathbf{q}}_j(z_\beta^{(i)}) &= \int_{\Gamma_j} \left\langle \frac{d\tau_*^{(j)}}{\tau_*^{(j)} - z_\beta^{(i)}} \right\rangle \overline{\mathbf{f}^{(j)}(\tau_*^{(j)})}. \quad (47) \end{aligned}$$

Eqs (36)–(41) can be rewritten as follows:

$$\begin{aligned} \mathbf{f}^{(1)}(z_*^{(1)}) &= \mathbf{f}_\infty^{(1)}(z_*^{(1)}) + \frac{1}{2\pi i} [\mathbf{q}_1(z_*^{(1)}) \\ &+ \sum_{\beta=1}^3 \mathbf{I}_\beta (\mathbf{A}_1^T \mathbf{m}(z_\beta^{(1)}) + \mathbf{B}_1^T \mathbf{p}(z_\beta^{(1)}))] \quad (48) \end{aligned}$$

$$\begin{aligned} &+ \langle M_t(z_*^{(1)}) \rangle \mu_1 - \langle P_t(z_*^{(1)}) \rangle \lambda_1 + \rho_0 \langle m_t(z_*^{(1)}) \rangle \lambda_1; \\ \bar{\mathbf{q}}_1(z_\beta^{(1)}) &+ \bar{\mathbf{A}}_1^T \mathbf{m}(z_\beta^{(1)}) + \bar{\mathbf{B}}_1^T \mathbf{p}(z_\beta^{(1)}) + M_t(z_\beta^{(1)}) \bar{\mu}_1 \\ &- P_t(z_\beta^{(1)}) \bar{\lambda}_1 + \rho_0 m_t(z_\beta^{(1)}) \bar{\lambda}_1 = 0; \quad (49) \end{aligned}$$

$$\begin{aligned} \mathbf{q}_2(z_\beta^{(1)}) &- \mathbf{A}_2^T \mathbf{m}(z_\beta^{(1)}) - \mathbf{B}_2^T \mathbf{p}(z_\beta^{(1)}) - M_t(z_\beta^{(1)}) \mu_2 \\ &+ P_t(z_\beta^{(1)}) \lambda_2 = 0; \quad (50) \end{aligned}$$

$$\begin{aligned} \mathbf{f}^{(2)}(z_*^{(2)}) &= \mathbf{f}_\infty^{(2)}(z_*^{(2)}) + \frac{1}{2\pi i} [\mathbf{q}_2(z_*^{(2)}) \\ &- \sum_{\beta=1}^3 \mathbf{I}_\beta (\mathbf{A}_2^T \mathbf{m}(z_\beta^{(2)}) + \mathbf{B}_2^T \mathbf{p}(z_\beta^{(2)}))] \\ &- \langle M_t(z_*^{(2)}) \rangle \mu_2 + \langle P_t(z_*^{(2)}) \rangle \lambda_2; \quad (51) \end{aligned}$$

$$\mathbf{q}_1(z_\beta^{(2)}) + \mathbf{A}_1^T \mathbf{m}(z_\beta^{(2)}) + \mathbf{B}_1^T \mathbf{p}(z_\beta^{(2)}) + M_t(z_\beta^{(2)}) \mu_1 - P_t(z_\beta^{(2)}) \lambda_1 + \rho_0 m_t(z_\beta^{(2)}) \lambda_1 = 0; \quad (52)$$

$$\bar{\mathbf{q}}_2(z_\beta^{(2)}) - \bar{\mathbf{A}}_2^T \mathbf{m}(z_\beta^{(2)}) - \bar{\mathbf{B}}_2^T \mathbf{p}(z_\beta^{(2)}) - M_t(z_\beta^{(2)}) \bar{\mu}_2 + P_t(z_\beta^{(2)}) \bar{\lambda}_2 = 0, \quad (53)$$

where:  $\mathbf{I}_1 = \text{diag}[1,0,0]$ ,  $\mathbf{I}_2 = \text{diag}[0,1,0]$ ,  $\mathbf{I}_3 = \text{diag}[0,0,1]$ .

Eqs (49), (50), (52), (53) allow to express the improper integrals (43) along the infinite path through the path integrals over the contours  $\Gamma_j$ :

$$\begin{aligned} \mathbf{m}(z_\beta^{(1)}) &= (\bar{\mathbf{A}}_1 \bar{\mathbf{B}}_1^{-1} - \mathbf{A}_2 \mathbf{B}_2^{-1})^{-T} (\bar{\mathbf{B}}_1^{-T} \mathbf{y}_1(z_\beta^{(1)}) - \mathbf{B}_2^{-T} \mathbf{y}_2(z_\beta^{(1)})), \\ \mathbf{p}(z_\beta^{(1)}) &= (\bar{\mathbf{B}}_1 \bar{\mathbf{A}}_1^{-1} - \mathbf{B}_2 \mathbf{A}_2^{-1})^{-T} (\bar{\mathbf{A}}_1^{-T} \mathbf{y}_1(z_\beta^{(1)}) - \mathbf{A}_2^{-T} \mathbf{y}_2(z_\beta^{(1)})), \\ \mathbf{y}_1(z_\beta^{(1)}) &= -\bar{\mathbf{q}}_1(z_\beta^{(1)}) - M_t(z_\beta^{(1)}) \bar{\mu}_1 + P_t(z_\beta^{(1)}) \bar{\lambda}_1 - \rho_0 m_t(z_\beta^{(1)}) \bar{\lambda}_1, \\ \mathbf{y}_2(z_\beta^{(1)}) &= \mathbf{q}_2(z_\beta^{(1)}) - M_t(z_\beta^{(1)}) \mu_2 + P_t(z_\beta^{(1)}) \lambda_2, \end{aligned} \quad (54)$$

$$\begin{aligned} \mathbf{m}(z_\beta^{(2)}) &= (\bar{\mathbf{A}}_2 \bar{\mathbf{B}}_2^{-1} - \mathbf{A}_1 \mathbf{B}_1^{-1})^{-T} (\bar{\mathbf{B}}_2^{-T} \mathbf{y}_3(z_\beta^{(2)}) - \mathbf{B}_1^{-T} \mathbf{y}_4(z_\beta^{(2)})), \\ \mathbf{p}(z_\beta^{(2)}) &= (\bar{\mathbf{B}}_2 \bar{\mathbf{A}}_2^{-1} - \mathbf{B}_1 \mathbf{A}_1^{-1})^{-T} (\bar{\mathbf{A}}_2^{-T} \mathbf{y}_3(z_\beta^{(2)}) - \mathbf{A}_1^{-T} \mathbf{y}_4(z_\beta^{(2)})), \\ \mathbf{y}_3(z_\beta^{(2)}) &= \bar{\mathbf{q}}_2(z_\beta^{(2)}) - M_t(z_\beta^{(2)}) \bar{\mu}_2 + P_t(z_\beta^{(2)}) \bar{\lambda}_2, \\ \mathbf{y}_4(z_\beta^{(2)}) &= -\mathbf{q}_1(z_\beta^{(2)}) - M_t(z_\beta^{(2)}) \mu_1 + P_t(z_\beta^{(2)}) \lambda_1 - \rho_0 m_t(z_\beta^{(2)}) \lambda_1. \end{aligned} \quad (55)$$

Substituting Eqs (54), (55) into Eqs (48), (51), accounting for Eq (35), one can obtain the integral formulae for the Stroh complex vector-functions of thermoelastic anisotropic bimaterial with thermally imperfect interface, which do not contain the improper integrals over the infinite path (bimaterial interface):

$$\begin{aligned} \mathbf{f}^{(1)}(z_*^{(1)}) &= \mathbf{f}_\infty^{(1)}(z_*^{(1)}) + \frac{1}{2\pi i} [\mathbf{q}_1(z_*^{(1)}) + \sum_{\beta=1}^3 \mathbf{I}_\beta (\mathbf{G}_1^{(1)} \bar{\mathbf{q}}_1(z_\beta^{(1)}) + \mathbf{G}_2^{(1)} \mathbf{q}_2(z_\beta^{(1)})) \\ &+ \langle \bar{Q}_t^{(1)}(z_*^{(1)}) \rangle \delta_1^{(1)} + \langle Q_t^{(2)}(z_*^{(1)}) \rangle \delta_2^{(1)} + \langle e_t^{(2)}(z_*^{(1)}) + \bar{e}_t^{(1)}(z_*^{(1)}) \rangle \kappa^{(1)}], \end{aligned} \quad (56)$$

$$\begin{aligned} \mathbf{f}^{(2)}(z_*^{(2)}) &= \mathbf{f}_\infty^{(2)}(z_*^{(2)}) + \frac{1}{2\pi i} [\mathbf{q}_2(z_*^{(2)}) - \sum_{\beta=1}^3 \mathbf{I}_\beta (\mathbf{G}_1^{(2)} \mathbf{q}_1(z_\beta^{(2)}) + \mathbf{G}_2^{(2)} \bar{\mathbf{q}}_2(z_\beta^{(2)})) \\ &+ \langle Q_t^{(1)}(z_*^{(2)}) \rangle \delta_1^{(2)} + \langle \bar{Q}_t^{(2)}(z_*^{(2)}) \rangle \delta_2^{(2)} + \langle e_t^{(1)}(z_*^{(2)}) + \bar{e}_t^{(2)}(z_*^{(2)}) \rangle \kappa^{(2)}], \end{aligned} \quad (57)$$

where the constants  $\mathbf{G}_i^{(j)}$  and  $\delta_i^{(j)}$  are the same as in Ref (Pas-

ternak et al., 2014), and

$$\kappa^{(1)} = -\delta_2^{(1)} + 2\mathbf{G}_2^{(1)} \lambda_2; \kappa^{(2)} = -\delta_1^{(2)} - 2\mathbf{G}_1^{(2)} \lambda_1. \quad (58)$$

Derived equations (56) and (57) for the Stroh complex functions allow writing the integral formulae relating the latter at the arbitrary point of the bimaterial solid with the boundary values of temperature, heat flux, displacement and traction at the contours  $\Gamma_i$ . Therefore, using Eqs (3), (4), (56), (57) and (Pasternak, 2012, Ting, 1996) one can obtain the following extended Somigliana integral identity for a thermoelastic bimaterial solid with imperfect thermal contact at its interface:

$$\begin{aligned} \mathbf{u}(\xi) &= \mathbf{u}^\infty(\xi) + \int_\Gamma \mathbf{U}^{\text{bm}}(\mathbf{x}, \xi) \mathbf{t}(\mathbf{x}) ds(\mathbf{x}) - \int_\Gamma \mathbf{T}^{\text{bm}}(\mathbf{x}, \xi) \mathbf{u}(\mathbf{x}) ds(\mathbf{x}) + \int_\Gamma \mathbf{r}^{\text{ITC}}(\mathbf{x}, \xi) \theta(\mathbf{x}) ds(\mathbf{x}) + \int_\Gamma \mathbf{v}^{\text{ITC}}(\mathbf{x}, \xi) h_n(\mathbf{x}) ds(\mathbf{x}), \\ \sigma_j(\xi) &= \sigma_j^\infty(\xi) + \int_\Gamma \mathbf{D}_j^{\text{bm}}(\mathbf{x}, \xi) \mathbf{t}(\mathbf{x}) ds(\mathbf{x}) - \int_\Gamma \mathbf{S}_j^{\text{bm}}(\mathbf{x}, \xi) \mathbf{u}(\mathbf{x}) ds(\mathbf{x}) + \int_\Gamma \mathbf{q}_j^{\text{ITC}}(\mathbf{x}, \xi) \theta(\mathbf{x}) ds(\mathbf{x}) + \int_\Gamma \mathbf{w}_j^{\text{ITC}}(\mathbf{x}, \xi) h_n(\mathbf{x}) ds(\mathbf{x}), \end{aligned} \quad (59)$$

where: the kernels  $\mathbf{U}^{\text{bm}}(\mathbf{x}, \xi)$ ,  $\mathbf{T}^{\text{bm}}(\mathbf{x}, \xi)$ ,  $\mathbf{D}_j^{\text{bm}}(\mathbf{x}, \xi)$ ,  $\mathbf{S}_j^{\text{bm}}(\mathbf{x}, \xi)$  are the same as those derived by Pasternak et al. (2014) for a thermoelectroelastic bimaterial with perfect thermal and mechanical interface, and others kernels are defined by the following equations:

$\mathbf{x} \in S_1 \wedge \xi \in S_1$ :

$$\begin{aligned} \mathbf{r}^{\text{ITC}}(\mathbf{x}, \xi) &= -\frac{1}{\pi} \text{Im} \left\{ \mathbf{A}_1 \left( \left\langle \ln W_*^{(1,1)} \right\rangle \mathbf{n}^{(1)} + \sum_{\beta=1}^3 \left\langle \ln \bar{W}_\beta^{(1,1)} \right\rangle \mathbf{G}_1^{(1)} \mathbf{I}_\beta \bar{\mathbf{n}}^{(1)} - \frac{\bar{n}_t^{(1)}}{2} \left( \left\langle \ln \bar{W}_{t*}^{(1,1)} \right\rangle \delta_1^{(1)} - \left\langle K(B^{(1)} \bar{W}_{t*}^{(1,1)}) \right\rangle \mathbf{k}^{(1)} \right) + \frac{c_1}{2} (K-1) \bar{n}_t^{(1)} L^{(1)}(\bar{W}_t^{(1,1)}) - \frac{c_1}{2} (n_t^{(1)} \ln W_t^{(1,1)} - \bar{n}_t^{(1)} \ln \bar{W}_t^{(1,1)}) \right\}, \\ \mathbf{v}^{\text{ITC}}(\mathbf{x}, \xi) &= \frac{1}{\pi} \text{Im} \left\{ \mathbf{A}_1 \left[ -\left\langle f^*(W_*^{(1,1)}) \right\rangle \mu_1 - \sum_{\beta=1}^3 \left\langle f^*(\bar{W}_\beta^{(1,1)}) \right\rangle \mathbf{G}_1^{(1)} \mathbf{I}_\beta \bar{\mu}_1 + \frac{i}{2k_t^{(1)}} \left\langle f^*(\bar{W}_{t*}^{(1,1)}) \right\rangle \delta_1^{(1)} - \frac{\rho_0(1-K)}{4} L^{(1)}(\bar{W}_{t*}^{(1,1)}) \kappa^{(1)} \right] - \frac{ic_1}{2k_t^{(1)}} [f^*(W_t^{(1,1)}) + K f^*(\bar{W}_t^{(1,1)})] + \frac{\rho_0 c_1 (K-1)^2}{4} L^{(1)}(\bar{W}_t^{(1,1)}) \right\}, \\ \mathbf{q}_j^{\text{ITC}}(\mathbf{x}, \xi) &= \frac{1}{\pi} \text{Im} \left\{ \mathbf{B}_1 \delta_*^{(1)} \left[ \left\langle \frac{1}{W_*^{(1,1)}} \right\rangle \mathbf{n}^{(1)} + \sum_{\beta=1}^3 \left\langle \frac{1}{\bar{W}_\beta^{(1,1)}} \right\rangle \mathbf{G}_1^{(1)} \mathbf{I}_\beta \bar{\mathbf{n}}^{(1)} - \frac{1}{2} \bar{n}_t^{(1)} \left( \left\langle \frac{1}{\bar{W}_{t*}^{(1,1)}} \right\rangle (\delta_1^{(1)} + \kappa^{(1)}) - B^{(1)} \left\langle K(B^{(1)} \bar{W}_{t*}^{(1,1)}) \right\rangle \kappa^{(1)} \right) \right] - \frac{\mathbf{d}_1}{2} \delta_t^{(1)} \left( \left[ \frac{n_t^{(1)}}{W_t^{(1,1)}} - \frac{\bar{n}_t^{(1)}}{\bar{W}_t^{(1,1)}} \right] + \frac{2i\bar{n}_t^{(1)}}{\rho_0 k_t^{(1)}} K(B^{(1)} \bar{W}_t^{(1,1)}) \right) \right\}, \\ \mathbf{w}_j^{\text{ITC}}(\mathbf{x}, \xi) &= \frac{1}{\pi} \text{Im} \left\{ \mathbf{B}_1 \delta_*^{(1)} \left[ \left\langle \ln W_*^{(1,1)} \right\rangle \mu_1 + \sum_{\beta=1}^3 \left\langle \ln \bar{W}_\beta^{(1,1)} \right\rangle \mathbf{G}_1^{(1)} \mathbf{I}_\beta \bar{\mu}_1 - \frac{i}{2k_t^{(1)}} \left( \left\langle \ln \bar{W}_{t*}^{(1,1)} \right\rangle \delta_1^{(1)} - \left\langle K(B^{(1)} \bar{W}_{t*}^{(1,1)}) \right\rangle \kappa^{(1)} \right) \right] + \frac{id_1}{2k_t^{(1)}} \delta_t^{(1)} (\ln W_t^{(1,1)} + \ln \bar{W}_t^{(1,1)} + (K-1) L^{(1)}(\bar{W}_t^{(1,1)})) \right\}; \end{aligned} \quad (60)$$

$\mathbf{x} \in S_2 \wedge \xi \in S_1$ :

$$\begin{aligned} \mathbf{r}^{ITC}(\mathbf{x}, \xi) &= -\frac{1}{\pi} \operatorname{Im} \left\{ \mathbf{A}_1 \left[ \sum_{\beta=1}^3 \left\langle \ln W_{\beta}^{(2,1)} \right\rangle \mathbf{G}_2^{(1)} \mathbf{I}_{\beta} \mathbf{n}^{(2)} \right. \right. \\ &\quad \left. \left. - \frac{1}{2} n_t^{(2)} \left( \left\langle \ln W_{t*}^{(2,1)} \right\rangle \delta_2^{(1)} \right) - \left\langle K(B^{(1)} W_{t*}^{(2,1)}) \right\rangle \kappa^{(1)} \right] \right. \\ &\quad \left. + \frac{c_1}{2} (K-1) n_t^{(2)} L^{(1)}(W_t^{(2,1)}) \right\}, \\ \mathbf{v}^{ITC}(\mathbf{x}, \xi) &= -\frac{1}{\pi} \operatorname{Im} \left\{ \mathbf{A}_1 \left[ \sum_{\beta=1}^3 \left\langle f^*(W_{\beta}^{(2,1)}) \right\rangle \mathbf{G}_2^{(1)} \mathbf{I}_{\beta} \mu_2 \right. \right. \\ &\quad \left. \left. + \frac{i}{2k_t^{(2)}} \left\langle f^*(W_{t*}^{(2,1)}) \right\rangle \delta_2^{(1)} - \frac{\rho_0(1+K)}{4} L^{(1)}(W_{t*}^{(2,1)}) \kappa^{(1)} \right] \right. \\ &\quad \left. + \frac{i c_1 (1-K)}{2k_t^{(2)}} f^*(W_t^{(2,1)}) - \frac{\rho_0 c_1 (K^2-1)}{4} L^{(1)}(W_t^{(2,1)}) \right\}, \\ \mathbf{q}_j^{ITC}(\mathbf{x}, \xi) &= \frac{1}{\pi} \operatorname{Im} \left\{ \mathbf{B}_1 \delta_*^{(1)} \left[ \sum_{\beta=1}^3 \left\langle \frac{1}{W_{\beta}^{(2,1)}} \right\rangle \mathbf{G}_2^{(1)} \mathbf{I}_{\beta} \mathbf{n}^{(2)} \right. \right. \\ &\quad \left. \left. - \frac{1}{2} n_t^{(2)} \left( \left\langle \frac{1}{W_{t*}^{(2,1)}} \right\rangle (\delta_2^{(1)} + \kappa^{(1)}) - B^{(1)} \left\langle K(B^{(1)} W_{t*}^{(2,1)}) \right\rangle \kappa^{(1)} \right) \right] \right. \\ &\quad \left. - \frac{i d_1}{\rho_0 k_t^{(1)}} n_t^{(2)} \delta_t^{(1)} K(B^{(1)} W_t^{(2,1)}) \right\} \\ \mathbf{w}_j^{ITC}(\mathbf{x}, \xi) &= \frac{1}{\pi} \operatorname{Im} \left\{ \mathbf{B}_1 \delta_*^{(1)} \left[ \sum_{\beta=1}^3 \left\langle \ln W_{\beta}^{(2,1)} \right\rangle \mathbf{G}_2^{(1)} \mathbf{I}_{\beta} \mu_2 \right. \right. \\ &\quad \left. \left. + \frac{i}{2k_t^{(2)}} \left( \left\langle \ln W_{t*}^{(2,1)} \right\rangle \delta_2^{(1)} - \left\langle K(B^{(1)} W_{t*}^{(2,1)}) \right\rangle \kappa^{(1)} \right) \right] \right. \\ &\quad \left. + \frac{i d_1}{k_t^{(1)} + k_t^{(2)}} \delta_t^{(1)} L^{(1)}(W_t^{(2,1)}) \right\}; \end{aligned} \quad (61)$$

$\mathbf{x} \in S_1 \wedge \xi \in S_2$ :

$$\begin{aligned} \mathbf{r}^{ITC}(\mathbf{x}, \xi) &= \frac{1}{\pi} \operatorname{Im} \left\{ \mathbf{A}_2 \left[ \sum_{\beta=1}^3 \left\langle \ln W_{\beta}^{(1,2)} \right\rangle \mathbf{G}_1^{(2)} \mathbf{I}_{\beta} \mathbf{n}^{(2)} \right. \right. \\ &\quad \left. \left. + \frac{1}{2} n_t^{(1)} \left( \left\langle \ln W_{t*}^{(1,2)} \right\rangle \delta_1^{(2)} - \left\langle K(B^{(1)} W_{t*}^{(1,2)}) \right\rangle \kappa^{(2)} \right) \right] \right. \\ &\quad \left. + \frac{c_2}{2} (K+1) n_t^{(1)} L^{(2)}(W_t^{(1,2)}) \right\}, \\ \mathbf{v}^{ITC}(\mathbf{x}, \xi) &= \frac{1}{\pi} \operatorname{Im} \left\{ \mathbf{A}_1 \left[ \sum_{\beta=1}^3 \left\langle f^*(W_{\beta}^{(1,2)}) \right\rangle \mathbf{G}_1^{(2)} \mathbf{I}_{\beta} \mu_1 \right. \right. \\ &\quad \left. \left. - \frac{i}{2k_t^{(1)}} \left\langle f^*(W_{t*}^{(1,2)}) \right\rangle \delta_1^{(2)} - \frac{\rho_0(1-K)}{4} L^{(2)}(W_{t*}^{(1,2)}) \kappa^{(2)} \right] \right. \\ &\quad \left. - \frac{i c_2}{2k_t^{(1)}} (1+K) f^*(W_t^{(1,2)}) - \frac{\rho_0 c_2 (K^2-1)}{4} L^{(2)}(W_t^{(1,2)}) \right\}, \\ \mathbf{q}_j^{ITC}(\mathbf{x}, \xi) &= -\frac{1}{\pi} \operatorname{Im} \left\{ \mathbf{B}_2 \delta_*^{(2)} \left[ \sum_{\beta=1}^3 \left\langle \frac{1}{W_{\beta}^{(1,2)}} \right\rangle \mathbf{G}_1^{(2)} \mathbf{I}_{\beta} \mathbf{n}^{(1)} \right. \right. \\ &\quad \left. \left. + \frac{1}{2} n_t^{(1)} \left( \left\langle \frac{1}{W_{t*}^{(1,2)}} \right\rangle (\delta_1^{(2)} + \kappa^{(2)}) \right) \right] \right. \\ &\quad \left. + B^{(2)} \left\langle K(B^{(2)} W_{t*}^{(1,2)}) \right\rangle \kappa^{(2)} \right] \right. \\ &\quad \left. - \frac{i d_2}{\rho_0 k_t^{(2)}} n_t^{(1)} \delta_t^{(2)} K(B^{(2)} W_t^{(1,2)}) \right\}, \\ \mathbf{w}_j^{ITC}(\mathbf{x}, \xi) &= -\frac{1}{\pi} \operatorname{Im} \left\{ \mathbf{B}_2 \delta_*^{(2)} \left[ \sum_{\beta=1}^3 \left\langle \ln W_{\beta}^{(1,2)} \right\rangle \mathbf{G}_1^{(2)} \mathbf{I}_{\beta} \mu_1 \right. \right. \\ &\quad \left. \left. - \frac{i}{2k_t^{(1)}} \left( \left\langle \ln W_{t*}^{(1,2)} \right\rangle \delta_1^{(2)} - \left\langle K(B^{(2)} W_{t*}^{(1,2)}) \right\rangle \kappa^{(2)} \right) \right] \right. \\ &\quad \left. - \frac{i d_2}{k_t^{(1)} + k_t^{(2)}} \delta_t^{(2)} L^{(2)}(W_t^{(1,2)}) \right\}; \end{aligned} \quad (62)$$

$\mathbf{x} \in S_2 \wedge \xi \in S_2$ :

$$\begin{aligned} \mathbf{r}^{ITC}(\mathbf{x}, \xi) &= -\frac{1}{\pi} \operatorname{Im} \left\{ \mathbf{A}_2 \left[ \left\langle \ln W_*^{(2,2)} \right\rangle \mathbf{n}^{(2)} \right. \right. \\ &\quad \left. \left. - \sum_{\beta=1}^3 \left\langle \ln \bar{W}_{\beta}^{(2,2)} \right\rangle \mathbf{G}_2^{(2)} \mathbf{I}_{\beta} \bar{\mathbf{n}}^{(2)} - \frac{1}{2} \bar{n}_t^{(2)} \left( \left\langle \ln \bar{W}_{t*}^{(2,2)} \right\rangle \delta_2^{(1)} \right. \right. \right. \\ &\quad \left. \left. - \left\langle K(B^{(2)} \bar{W}_{t*}^{(2,2)}) \right\rangle \kappa^{(2)} \right) \right] - \frac{c_2}{2} \bar{n}_t^{(2)} L^{(2)}(\bar{W}_t^{(2,2)}) \right. \\ &\quad \left. - \frac{c_2}{2} (n_t^{(2)} \ln W_t^{(2,2)} - \bar{n}_t^{(2)} \ln \bar{W}_t^{(2,2)}) \right\}, \\ \mathbf{v}^{ITC}(\mathbf{x}, \xi) &= \frac{1}{\pi} \operatorname{Im} \left\{ \mathbf{A}_2 \left[ -\left\langle f^*(W_*^{(2,2)}) \right\rangle \mu_2 \right. \right. \\ &\quad \left. \left. + \sum_{\beta=1}^3 \left\langle f^*(\bar{W}_{\beta}^{(2,2)}) \right\rangle \mathbf{G}_2^{(2)} \mathbf{I}_{\beta} \bar{\mu}_2 \right. \right. \\ &\quad \left. \left. + \frac{i}{2k_t^{(2)}} \left\langle f^*(\bar{W}_{t*}^{(2,2)}) \right\rangle \delta_2^{(2)} + \frac{\rho_0(1+K)}{4} L^{(2)}(\bar{W}_{t*}^{(2,2)}) \kappa^{(2)} \right] \right. \\ &\quad \left. - \frac{i c_2}{2k_t^{(2)}} [f^*(W_t^{(2,2)}) - K f^*(\bar{W}_t^{(2,2)})] \right. \\ &\quad \left. - \frac{\rho_0 c_2 (K+1)^2}{4} L^{(2)}(\bar{W}_t^{(2,2)}) \right\}, \\ \mathbf{q}_j^{ITC}(\mathbf{x}, \xi) &= \frac{1}{\pi} \operatorname{Im} \left\{ \mathbf{B}_2 \delta_*^{(2)} \left[ \left\langle \frac{1}{W_*^{(2,2)}} \right\rangle \mathbf{n}^{(2)} \right. \right. \\ &\quad \left. \left. - \sum_{\beta=1}^3 \left\langle \frac{1}{\bar{W}_{\beta}^{(2,2)}} \right\rangle \mathbf{G}_2^{(2)} \mathbf{I}_{\beta} \bar{\mathbf{n}}^{(2)} - \frac{1}{2} \bar{n}_t^{(2)} \left( \left\langle \frac{1}{\bar{W}_{t*}^{(2,2)}} \right\rangle (\delta_1^{(2)} + \kappa^{(2)}) \right. \right. \right. \\ &\quad \left. \left. + B^{(2)} \left\langle K(B^{(2)} \bar{W}_{t*}^{(2,2)}) \right\rangle \kappa^{(2)} \right) \right] \right. \\ &\quad \left. - \frac{d_2}{2} \delta_t^{(2)} \left( \left[ \frac{n_t^{(2)}}{W_t^{(2,2)}} - \frac{\bar{n}_t^{(2)}}{\bar{W}_t^{(2,2)}} \right] - \frac{2i}{\rho_0 k_t^{(2)}} \bar{n}_t^{(2)} K(B^{(2)} \bar{W}_t^{(2,2)}) \right) \right\}, \\ \mathbf{w}_j^{ITC}(\mathbf{x}, \xi) &= \frac{1}{\pi} \operatorname{Im} \left\{ \mathbf{B}_2 \delta_*^{(2)} \left[ \left\langle \ln W_*^{(2,2)} \right\rangle \mu_2 \right. \right. \\ &\quad \left. \left. - \sum_{\beta=1}^3 \left\langle \ln \bar{W}_{\beta}^{(2,2)} \right\rangle \mathbf{G}_2^{(2)} \mathbf{I}_{\beta} \bar{\mu}_2 - \frac{i}{2k_t^{(2)}} \left( \left\langle \ln \bar{W}_{t*}^{(2,2)} \right\rangle \delta_2^{(2)} \right. \right. \right. \\ &\quad \left. \left. - \left\langle K(B^{(2)} \bar{W}_{t*}^{(2,2)}) \right\rangle \kappa^{(2)} \right) \right] \right. \\ &\quad \left. + \frac{i d_2}{2k_t^{(2)}} \delta_t^{(2)} \left( \ln W_t^{(2,2)} - \ln \bar{W}_t^{(2,2)} - (1+K) L^{(2)}(\bar{W}_t^{(2,2)}) \right) \right\}. \end{aligned} \quad (63)$$

The following constants and functions are used for contracting the notations:

$$\begin{aligned} \rho_j &= \mathbf{A}_j^T \operatorname{Re}[p_t^{(j)} \mathbf{d}_j] + \mathbf{B}_j^T \operatorname{Re}[p_t^{(j)} \mathbf{c}_j], \\ \mathbf{n}^{(i)} &= \lambda_i n_2(\mathbf{x}) - \rho_i n_1(\mathbf{x}), Z_*^{(i)}(\mathbf{x}) = x_1 + p_*^{(i)} x_2, \\ W_*^{(i,j)} &= Z_*^{(i)}(\mathbf{x}) - Z_*^{(j)}(\xi), W_{\beta}^{(i,j)} = Z_{\beta}^{(i)}(\mathbf{x}) - Z_{\beta}^{(j)}(\xi), \\ \bar{W}_{\beta}^{(i,j)} &= \bar{Z}_{\beta}^{(i)}(\mathbf{x}) - \bar{Z}_{\beta}^{(j)}(\xi), W_{t*}^{(i,j)} = Z_t^{(i)}(\mathbf{x}) - Z_*^{(j)}(\xi), \\ \bar{W}_{t*}^{(i,j)} &= \bar{Z}_t^{(i)}(\mathbf{x}) - \bar{Z}_*^{(j)}(\xi), \delta_*^{(j)} = \left\langle \delta_{i2} - \delta_{i1} p_*^{(j)} \right\rangle. \end{aligned} \quad (64)$$

The proposed complex variable approach allow not only to derive the boundary integral formulae for anisotropic thermoelasticity, but also to derive singular boundary integral equations for solving the boundary value problems for thermoelastic bimaterial solids with thermally imperfect interface. In particular, for derivation of the boundary integral equations it is convenient to apply the Sokhotskii-Plemelj formula (Muskhelishvili, 2008), which relates the limit value of the Cauchy integral over a smooth closed contour with its principal value. Thus, according to Eq (59) and (Muskhelishvili, 2008, Pasternak, 2012), for a smooth closed contours  $\Gamma$  in a thermoelastic bimaterial one can obtain the following boundary integral equations for determination of the unknown boundary functions:



$$\begin{aligned} \frac{1}{2}\theta(\mathbf{y}) &= \theta^\infty(\mathbf{y}) + \text{RPV} \int_{\Gamma} \Theta^{ITC*}(\mathbf{x}, \mathbf{y}) h_n(\mathbf{x}) ds(\mathbf{x}) - \\ &\text{CPV} \int_{\Gamma} H^{ITC*}(\mathbf{x}, \mathbf{y}) \theta(\mathbf{x}) ds(\mathbf{x}), \\ \frac{1}{2}\mathbf{u}(\mathbf{y}) &= \mathbf{u}^\infty(\mathbf{y}) + \text{RPV} \int_{\Gamma} \mathbf{U}^{\text{bm}}(\mathbf{x}, \mathbf{y}) \mathbf{t}(\mathbf{x}) ds(\mathbf{x}) - \\ &\text{CPV} \int_{\Gamma} \mathbf{T}^{\text{bm}}(\mathbf{x}, \mathbf{y}) \mathbf{u}(\mathbf{x}) ds(\mathbf{x}) + \\ &\text{RPV} \int_{\Gamma} \mathbf{r}^{ITC}(\mathbf{x}, \mathbf{y}) \theta(\mathbf{x}) ds(\mathbf{x}) + \\ &\int_{\Gamma} \mathbf{v}^{ITC}(\mathbf{x}, \mathbf{y}) h_n(\mathbf{x}) ds(\mathbf{x}), \end{aligned} \quad (65)$$

where RPV stands for a Riemann Principal Value and CPV for a Cauchy Principal Value of an integral.

The integral equations (65) degenerate, when separate closed contours  $\Gamma_j$  of a line  $\Gamma$  are the faces of mathematical cuts  $\Gamma_{Cj}$  (the simple opened arcs). In this case it is necessary to apply the theory of dual hypersingular integral equations (Pasternak et al., 2013a, Pasternak, 2012).

According to (Pasternak et al., 2013a), the stress and displacement discontinuity functions at the tips of thin inhomogeneities, which are not placed at the bimaterial interface, possess square root singularity. And the stress field in the vicinity of inclusion's tip is completely defined by the generalized stress intensity factors. The latter are related to the displacement and stress discontinuities at thin inhomogeneity with the following equations

$$\mathbf{k}^{(1)} = \lim_{s \rightarrow 0} \sqrt{\frac{\pi}{8s}} \mathbf{L} \cdot \Delta \mathbf{u}(s), \quad \mathbf{k}^{(2)} = -\lim_{s \rightarrow 0} \sqrt{\frac{\pi s}{2}} \Sigma \mathbf{t}(s), \quad (66)$$

where:  $\mathbf{k}^{(1)} = [K_{21}, K_{11}, K_{31}]^T$ ,  $\mathbf{k}^{(2)} = [K_{12}^{(2)}, K_{22}^{(2)}, K_{32}]^T$ ;  $K_{ij}$  are generalized stress intensity factors (SIF) (Pasternak et al., 2013b, Sulym, 2007); and  $\mathbf{L} = -2\sqrt{-1}\mathbf{B}\mathbf{B}^T$  is a real Barnett – Lothe tensor (Sulym et al., 2014).

Obtained dual boundary integral equations along with the models of thin thermoelastic inclusions (Pasternak et al., 2013a) allow solving thermoelastic problems for a bimaterial solid with thermally imperfect interface, which components contain thin inhomogeneities.

#### 4. NUMERICAL EXAMPLES

Similarly to (Pasternak et al., 2013a, Pasternak, 2012), obtained integral formulae and equations (25), (26), (59) are introduced entered into the computational algorithm of the modified boundary element method (Pasternak et al., 2013a, 2014) that allows numerical solution of a wide range of 2D problems for an anisotropic thermoelastic bimaterial solid with thermally imperfect interface containing internal inhomogeneities. Several numerical examples are considered here for a bimaterial containing thin thermoelastic inclusions. The boundary element mesh consists of only 20 discontinuous three-node boundary elements including two special for convenient determination of stress intensity factors at inclusion's tips.

Consider an anisotropic thermoelastic bimaterial (Fig. 2) consisting of two half-space that have identical mechanical and thermal properties. The bimaterial contains a thin rectilinear elastic isotropic inclusion of length  $2a$  and thickness  $2h = 0.02a$  placed at the upper half-space  $x_2 > 0$  parallel to the interface. The centre of the inclusion is placed at the distance  $d$  to the bimaterial interface. In the lower half-space  $x_2 < 0$  at the distance  $d/2$  to the interface and at the distance  $a$  to the central vertical axis a heat source and a heat drain both of the same magnitude

are placed. The half-spaces of the bimaterial possess the same thermal and mechanical properties of glass/epoxy:  $E_1 = 55$  GPa,  $E_2 = 21$  GPa,  $G_{12} = 9.7$  GPa,  $\nu_{12} = 0.25$ ,  $\alpha_{11} = 6.3 \cdot 10^{-6}$  K<sup>-1</sup>,  $\alpha_{22} = 2.0 \cdot 10^{-5}$  K<sup>-1</sup>,  $k_{11} = 3.46$  W/(m·K),  $k_{22} = 0.35$  W/(m·K). Material symmetry axes coincide with the reference coordinates. Plane stress is considered.

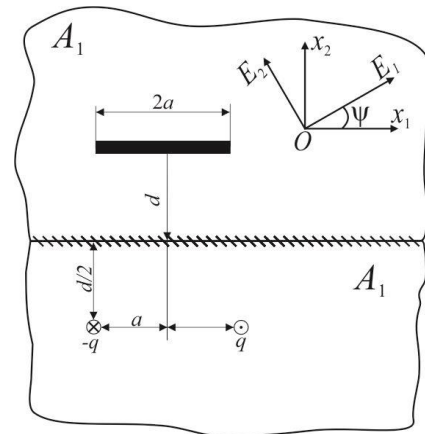


Fig. 2. Bimaterial with identical properties of half-spaces

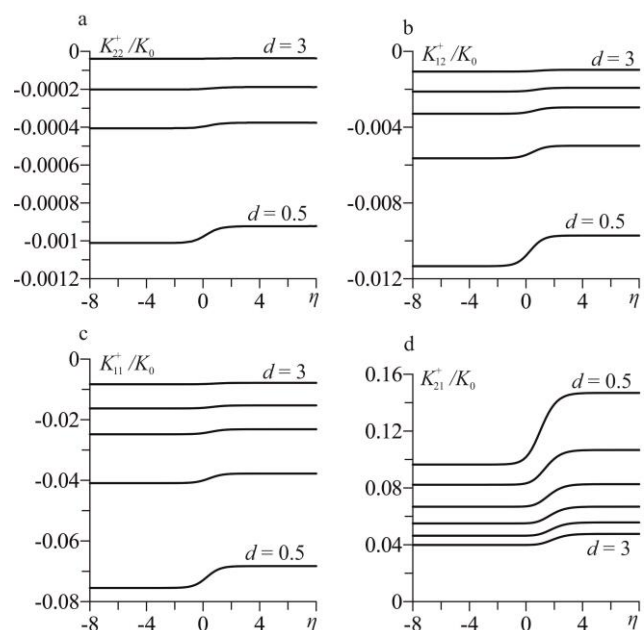
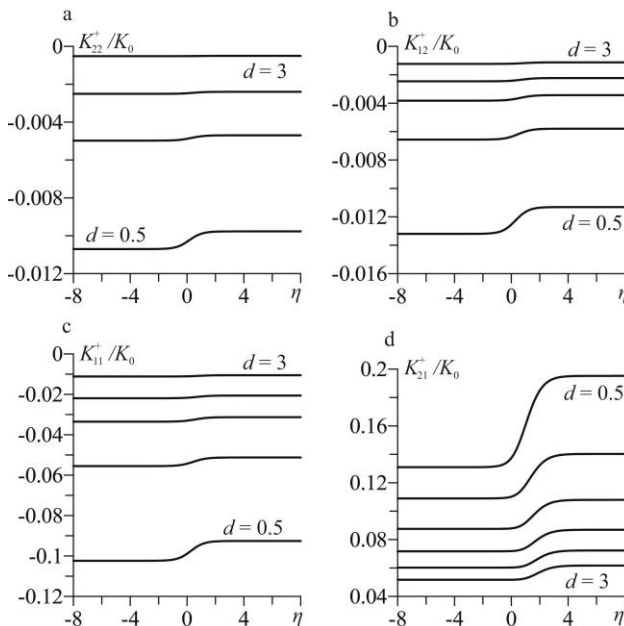


Fig. 3. Generalized stress intensity factors at the right tip of the inclusion, which relative rigidity is  $10^2$  (a-b) or  $10^{-2}$  (c-d)

Fig. 3 presents the dependence of the generalized stress intensity factors (SIF) at the right tip of the inclusion on the parameter  $\eta$ , which define the thermal resistance of the interface as  $\rho_0 = \alpha/k_{11} \cdot 10^\eta$ . The normalization factor is equal to  $K_0 = \sqrt{\pi a} \cdot E_1 \cdot \alpha_{11}/k_{11} \cdot q$ . Plots are obtained for different values of the parameter  $d$  and the relative rigidity  $k = G^i/G_{12}$  of the inclusion, where  $G^i$  is a shear modulus of inclusion's material. It is assumed that the inclusion does not possess thermal expansion.

One can see in Fig. 3 that the closer are the heat sources and the inclusion to the bimaterial interface, the higher are the values of generalized SIF. Decrease in inclusion's rigidity considerably increases stress intensity. It should be mentioned that the

most significant growth of all generalized SIF occurs, when the parameter  $\eta$  of normalized thermal resistance of the bimaterial interface is near zero.



**Fig. 4.** Generalized stress intensity factors at the right tip of the inclusion, which relative rigidity is  $10^5$  (a-b) or  $10^{-5}$  (c-d)

The increase in inclusion's relative rigidity (Fig. 4, a-b) causes a significant growth in the magnitude of the generalized SIF, and, in general, their behavior is the same, as well as in case of a softer inclusion. The same conclusion can be made, when relative rigidity of inclusion is equal to  $10^{-5}$ .

## 5. CONCLUSION

The paper presents a general complex variable straightforward approach for obtaining the boundary integral equations and integral formulae for a defective bimaterial solid with thermally imperfect interface. The kernels of these equations are obtained explicitly and in closed-form that allows developing the efficient boundary element approach for the analysis of thermoelastic anisotropic bimaterial solids with imperfect interface containing internal inhomogeneities. The influence of the thermal resistance of the interface on the field intensity factors at the tips of thin inhomogeneities is studied. It is shown that thermal resistance of the interface causes significant influence on the stress intensity at the tips of cracks even in the bimaterial consisting of two half-spaces with identical thermal and mechanical properties. Also several examples are considered for bimaterials with thin thermoelastic inclusions, and the intensity of heat flux and stress at their tips is studied.

## REFERENCES

1. Benveniste Y. (2006), A general interface model for a three-dimensional curved thin anisotropic interphase between two anisotropic media, *J. Mech. Phys. Solids*, 54, 708–734.
2. Chen T. (2001), Thermal conduction of a circular inclusion with variable interface parameter, *Int. J. Solids. Struct.*, 38, 3081–3097.
3. Hwu C. (1992), Thermoelastic interface crack problems in dissimilar anisotropic media, *Int. J. Solids. Struct.*, 18, 2077–2090.
4. Hwu C. (2010), *Anisotropic elastic plates*, Springer, London.
5. Jewtuszenko O., Adamowicz F., Grzes P., Kuciej M., Och E. (2014) Analytic and numerical modeling of the process of heat transfer in parts of disc of the brake systems, Publishing House of BUT (in Polish).
6. Kattis M. A., Mavroyannis G. (2006), Feeble interfaces in bimaterials, *Acta Mech.*, 185, 11–29.
7. Muskhelishvili N.I. (2008), *Singular integral equations*, Dover publications, New York.
8. Pan E., Amadei B. (1999), Boundary element analysis of fracture mechanics in anisotropic bimaterials, *Engineering Analysis with Boundary Elements*, 23, 683–691.
9. Pasternak Ia. (2012), Boundary integral equations and the boundary element method for fracture mechanics analysis in 2D anisotropic thermoelasticity, *Engineering Analysis with Boundary Elements*, 36(12), 1931–1941.
10. Pasternak Ia., Pasternak R., Sulym H. (2013a), A comprehensive study on the 2D boundary element method for anisotropic thermoelectroelastic solids with cracks and thin inhomogeneities, *Engineering Analysis with Boundary Elements*, 37, No. 2, 419–433.
11. Pasternak Ia., Pasternak R., Sulym H. (2013b), Boundary integral equations for 2D thermoelasticity of a half-space with cracks and thin inclusions, *Engineering Analysis with Boundary Elements*, 37, 1514–1523.
12. Pasternak Ia., Pasternak R., Sulym H. (2014), Boundary integral equations and Green's functions for 2D thermoelectroelastic bimaterial, *Engineering Analysis with Boundary Elements*, 48, 87–101.
13. Qin Q.H. (2007), *Green's function and boundary elements of multifield materials*, Elsevier, Oxford.
14. Sulym H.T. (2007), Bases of mathematical theory of thermo-elastic equilibrium of solids containing thin inclusions, *Research and Publishing center of NTSh*, 2007 (in Ukrainian).
15. Sulym H.T., Pasternak Ia., Tomashivsky M. (2014), Boundary element analysis of anisotropic thermoelastic half-space containing thin deformable inclusions, *Terнопіль Іван Пулюй Національний Технічний Університет*, 2014 (in Ukrainian).
16. Ting T.C.T. (1996), *Anisotropic elasticity: theory and applications*, Oxford University Press, New York.
17. Wang X., Pan E. (2010), Thermal Green's functions in plane anisotropic bimaterials with spring-type and Kapitza-type imperfect interface, *Acta Mech.*, 209, 115–128.
18. Yevtushenko A. A., Kuciej M. (2012), One-dimensional thermal problem of friction during braking: The history of development and actual state, *International Journal of Heat and Mass Transfer*, 55, 4148–4153.